TRIBOELECTRIC NANOGENERATORS

A Dissertation
Presented to
The Academic Faculty

by

Jun Chen

In Partial Fulfillment
of the Requirements for the Degree
Doctor of Philosophy in the
School of Materials Science and Engineering

Georgia Institute of Technology
May 2016

TRIBOELECTRIC NANOGENERATORS

Approved by:

Dr. Zhong Lin (Z.L.) Wang, Advisor
School of Materials Science and
Engineering
Georgia Institute of Technology

Dr. David McDowell
The George W. Woodruff School of
Mechanical Engineering
Georgia Institute of Technology

Dr. Preet Singh
School of Materials Science and
Engineering
Georgia Institute of Technology

Dr. Meilin Liu
School of Materials Science and
Engineering
Georgia Institute of Technology

Dr. Yulin Deng
School of Chemical and Biomolecular
Engineering
Georgia Institute of Technology

Date Approved: February 8, 2016

ACKNOWLEDGEMENTS

This dissertation would not have been completed without the efforts of a few key individuals, to whom I can never express enough gratitude.

First and foremost, I would like to express my deepest and sincerest gratitude to my major advisor Dr. Zhong Lin Wang for his continuous support of my Ph.D study, for his trust, dedicated guidance, immense knowledge, fabulous life wisdom to me throughout the last four years. His attitude towards life and scientific research really inspired me a lot, which will keep motivating me to become a person with love, integrity, and goal. And his encouraging words are always invaluable and endless driving force to me whenever I felt frustrated. The collaboration work with him in Georgia Institute of Technology will be a valuable and beneficial experience in my life.

Besides, I also would love to show my sincere thanks to Dr. David McDowell, Dr. Meilin Liu, Dr. Preet Singh, Dr. Yulin Deng, for their encouragement, insightful guidance and advices, with great kindness and tremendous patience.

Furthermore, my sincere thanks also go to Dr. Guang Zhu, Dr. Weiqing Yang, Dr. Jin Yang, Dr. Xing Fan, Dr. Huiliang Wang, Dr. Jianguo Fan, Dr. Caofeng Pan, who helped me not only academically, but also mentally. Just like my brothers, their great kindness as well as encouragement accompanied and led me through a lot of depressions and frustrations in my life. In the meanwhile, I could not go without acknowledging my fellow labmates, specifically including Zhaoling Li, Yuanjie Su, Hulin Zhang, Qingshen Jing, Peng Bai, Simiao Niu, Ruomeng Yu, Hengyu Guo, Zhen Wen, Haiyang Zou, Ruiyuan Liu, Yunlong Zi, Changsheng Wu, Fang Yi, Long Lin, Sihong Wang, Xiaonan Wen, Yusheng Zhou, Li Zheng, Gang Cheng, Ying Wu, Zong-Hong Lin, Yannan Xie, Ya Yang, Youfan

iii

Hu and so on. They are an integral part to my PhD research, tremendously helpful and supportive.

Last but not least, I would like to thank my deeply beloved ones. My family have been supporting me spiritually throughout my life. Their love is absolutely unconditioned, invaluable and leads me through all the hard times. Finally, I am grateful for my girlfriend, Chenchen Hu, for her lighting up my life journey after walking alone a long time in darkness. Her emergence has brought sunshine into my life and colored my grayscale sky. I thank her with all my heart for her trust, braveness, continuous love and confidence in me.

Jun Chen
February, 2016
Atlanta, Georgia

TABLE OF CONTENTS

LIST OF FIGURES

LIST OF TABLES

SUMMARY

With the threatening of global warming and energy crises, searching for renewable and green energy resources with reduced carbon emissions is one of the most urgent challenges to the sustainable development of human civilization. In the past decades, increasing research efforts have been committed to seek for clean and renewable energy sources as well as to develop renewable energy technologies.

Mechanical motion ubiquitously exists in ambient environment and people's daily life. In recent years, it becomes an attractive target for energy harvesting as a promising supplement to traditional fuel sources and a potentially alternative power source to battery-operated electronics. Until recently, the mechanisms of mechanical energy harvesting are limited to transductions based on piezoelectric effect, electromagnetic effect, electrostatic effect and magnetostrictive effect. Widespread usage of these techniques is likely to be shadowed by possible limitations, such as structure complexity, low power output, fabrication of high-quality materials, reliance on external power sources and little adaptability on structural design for different applications. In 2012, triboelectric nanogenerator (TENG), a creative invention for harvesting ambient mechanical energy based on the coupling between triboelectric effect and electrostatic effect has been launched as a new and renewable energy technology. The concept and design presented in this thesis research can greatly promote the development of TENG as both sustainable power sources and self-powered active sensors. And it will greatly help to define the TENG as a fundamentally new green energy technology, featured as being simple, reliable, cost-effective as well as high efficiency.

CHAPTER 1

INTRODUCTION

1.1 Mechanical energy harvesting

With the threatening of global warming and energy crises, searching for renewable and green energy resources with reduced carbon emissions is one of the most urgent challenge to the sustainable development of human civilization.[1-3] In the past decades, increasing research efforts have been committed to seek for clean and renewable energy sources as well as to develop renewable energy technologies. In the meanwhile, the tremendous development of portable electronics and sensor networks necessitates sustainable and stable energy sources for them.

Mechanical motion ubiquitously exists in ambient environment and people's daily life. In recent years, it becomes an attractive target for energy harvesting as a promising supplement to traditional fuel sources and a potentially alternative power source to battery-operated electronics. Until recently, the mechanisms of mechanical energy harvesting are limited to transductions based on electromagnetic effect,[4-6] electrostatic effect,[7-9] piezoelectric effect.[10-15]

Based on the electromagnetic effect, an electromagnetic generator is capable of converting mechanical energy into electrical power for use in an external circuit. It usually consists of a magnet on a polyimide spring. It is the current technology for large-scale mechanical energy harvesting. However, an obvious disadvantage of this technology was that the output voltage was very low, due to the single current path through the magnetic flux. Furthermore, it has a very low power output when miniaturized and little adaptability

on structural design for various applications. The device structure of a typical example of electromagnetic generator was shown in Figure 1.1a.[5] It consisted of four magnets, which were attached to both the top and bottom surfaces of a cantilever beam. Designed for ambient vibration energy harvesting, its electrical output was illustrated in Figure 1.1b. And an output power of 10.82 µW was delivered at a beam vibration frequency of 58.5 Hz.
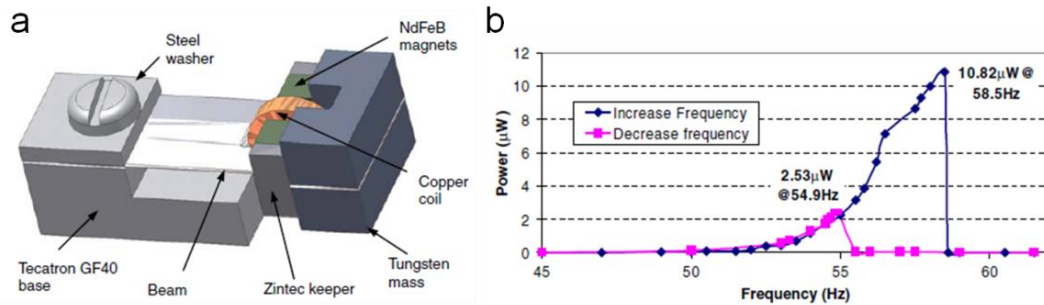
Figure 1.1 (a) A sketch showing the structural design of a typical electromagnetic generator for ambient vibration energy harvesting. (b) The excitation frequency depended power output of the micro-electromagnetic generator.[5]

By utilizing the electrostatic effect, an electrostatic generator develops electrostatic charges of opposite signs rendered to two conductors. And the external mechanical motions can carry electric charge to a high potential electrode, in this processing, it converts the mechanical motions into electricity. Wehrsen Machine and the Van de Graaff generator are popular traditional electrostatic generators. Recent efforts have been committed to minimize the total size of the device in the field of electrostatic generator. In this regards, separated by a passive spacing gap, an in-plane electrostatic generator based on electrets materials were develpped.[8] As shown in Figure 1.2a, a repulsive electrostatic force was induced by a patterned electrets material, while a dual-phase electrode arrangement is adopted for reducing the horizontal electrostatic damping force. As demonstrated in Figure 1.2b, a power output of 0.56 µW was delivered by the reported electrostatic generator.

2
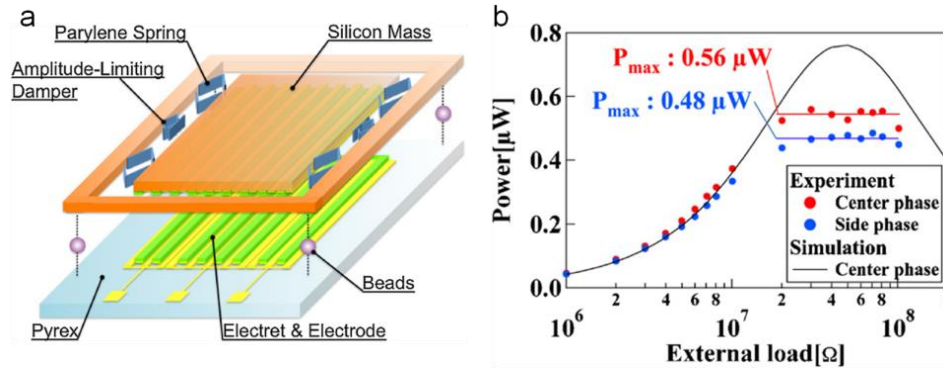
Figure 1.2 (a) The schematic structural design of an electrostatic generator. (b) Dependence of the output power on the external loading resistances.[8]

While for the piezoelectric effect based generator, it harnesses the strain induced piezoelectric polarization in certain crystals, such as ZnO and PZT, the potential created by polarization charges can drive the flow of electrons across two electrodes placed on the top and bottom surfaces of the crystal. In this processing, the mechanical motion is thus converted into the electricity in the external circuit.

In summary, widespread usage of these techniques is likely to be shadowed by possible limitations. For both the electromagnetic-based and electrostatic generator, they deliver low power output when miniaturized, and they both have little adaptability on structural design for various applications. With sophisticated structure and special fabrication materials, they also suffer from high manufacturing cost. And for electrostatic-based generator, it needs external DC voltage to maintain the static charge. While regarding the piezoelectric effect based generator, the low power output greatly limited its practical applications as sustainable power sources.

1.2 Triboelectric nanogenerators

In 2012, triboelectric nanogenerator (TENG), a creative invention for harvesting ambient mechanical energy based on triboelectric effect,[16, 17] has been launched as a new and renewable energy technology. The first triboelectric nanogenerator is demonstrated in Figure 1.3.[18]
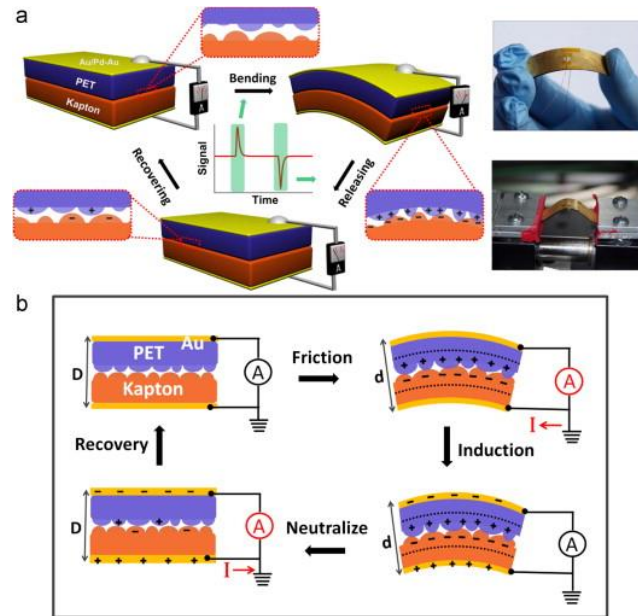
Figure 1.3 A schematic illustration of the device structure and working principle of the first triboelectric generator. (a) The structure of the triboelectric nanogenerator in bending and releasing process and experimental setup for electrical measurement. (b) An illustration of the working principle of the first triboelectric nanogenerator.[18]

The first-reported triboelectric nanogenerator has a multilayer structure. Due to the coupling between triboelectric effect and electrostatic induction, the periodic contact and separation between PET and Kapton, triggered by external mechanical motion, alternatingly drives the induced electrons between electrodes. And a peak voltage of 3.3 V, a current of 0.6 μA with a peak power density of 10.4 mW/cm^3 was delivered. In this process, the mechanical energy is effectively converted into electricity.

Since the launching of the first triboelectric nanogenerator, it attracts growing scientific attentions, and has been proved to be a cost-effective, simple and robust technique in the field of mechanical energy harvesting.[19-28] The past three years has witnessed the remarkable progress in the triboelectric nanogenerator based self-powered devices and systems.[29-31] Currently, four fundamental operation modes of the triboelectric nanogenerator have been systematically developed, which respectively are vertical contact-separation mode,[26-28] in-plane linear sliding mode,[32, 33] single electrode mode,[34, 35] and freestanding triboelectric-layer mode,[36] as schematically shown in Figure 1.4.
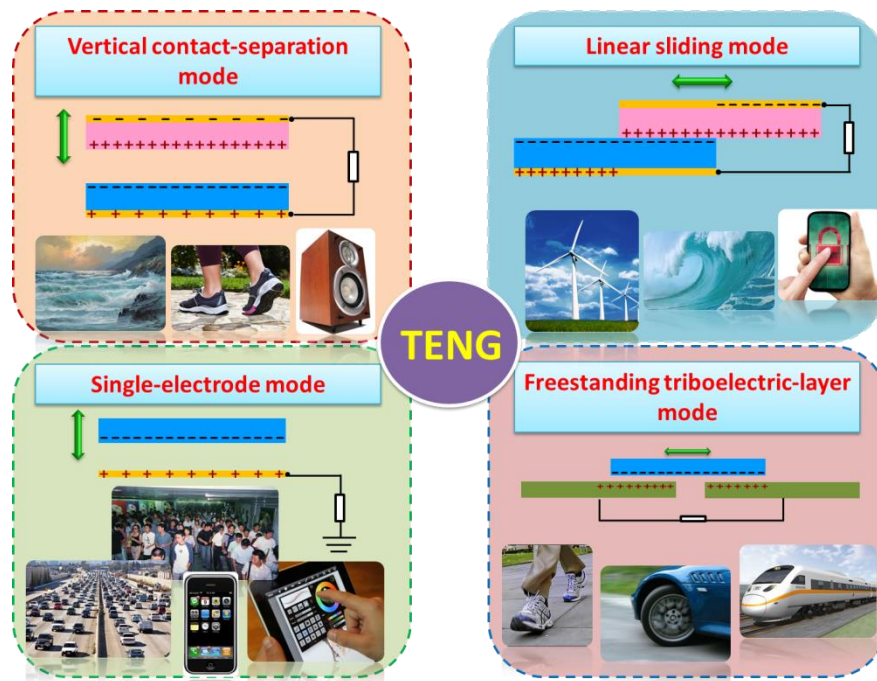
Figure 1.4 The working mechanism of four modes of triboelectric nanogenerator.[31]

In the following sections, we will elaborate each operation mode of the triboelectric nanogenerator in details as well as introduce corresponding unique applications.

1.2.1 The vertical contact-separation mode

The vertical contact-separation mode is the first invented operation mode for the triboelectric nanogenerator. A physical contact between the two dielectric films with different electron affinity creates oppositely charged surfaces. Once the two surfaces are separated by a gap, a potential drop is created between electrodes deposited on the top and the bottom surfaces of two dielectric films, as shown in Figure 1.5a.[28] If the two electrodes are electrically connected by a load, free electrons in one electrode would flow to the other electrode in order to balance the electrostatic field, as demonstrated in Figure 1.5b. Once the gap is closed, the triboelectric charge created potential disappears, the electrons flow back. In a word, the periodic contact and separation between two materials alternatingly drives induced electrons between electrodes.
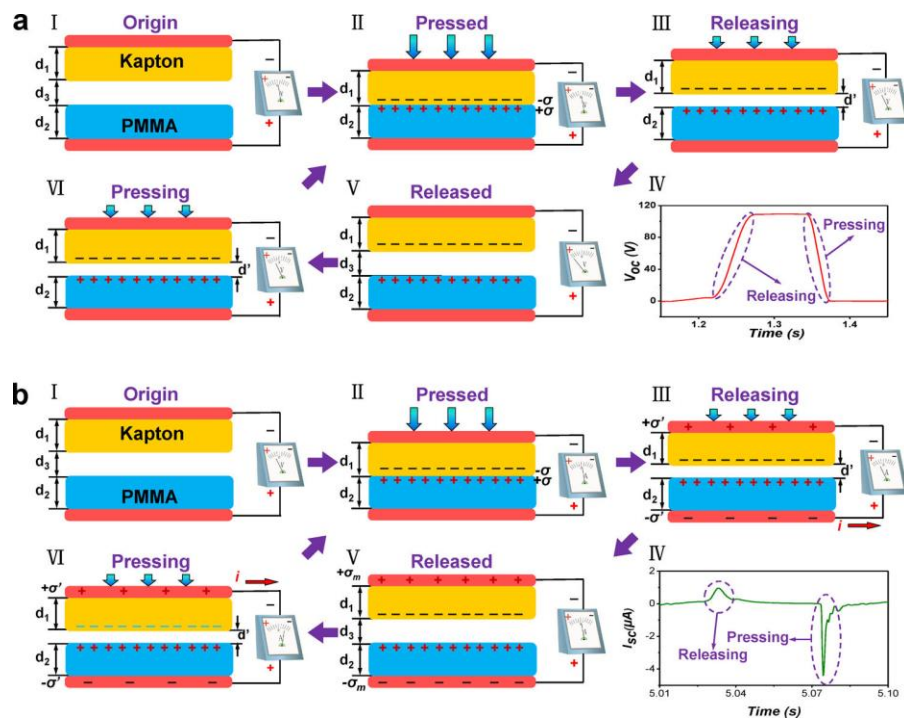
Figure 1.5 Sketches that illustrate the working principle of a typical vertical contact-separation mode triboelectric nanogenerator. (a) Open-circuit condition. (b) Short-circuit condition. [28]

1.2.2 The in-plane sliding mode

The structure to start with is the same as that for the vertical contact-separation mode. When two materials with opposite triboelectric polarities, for instance PTFE and aluminum, are brought into contact, surface charge transfer takes place due to the triboelectric effect. Since PTFE is much more triboelectrically negative than aluminum, electrons are injected from aluminum into PTFE, as shown in Figure 1.6.[33]
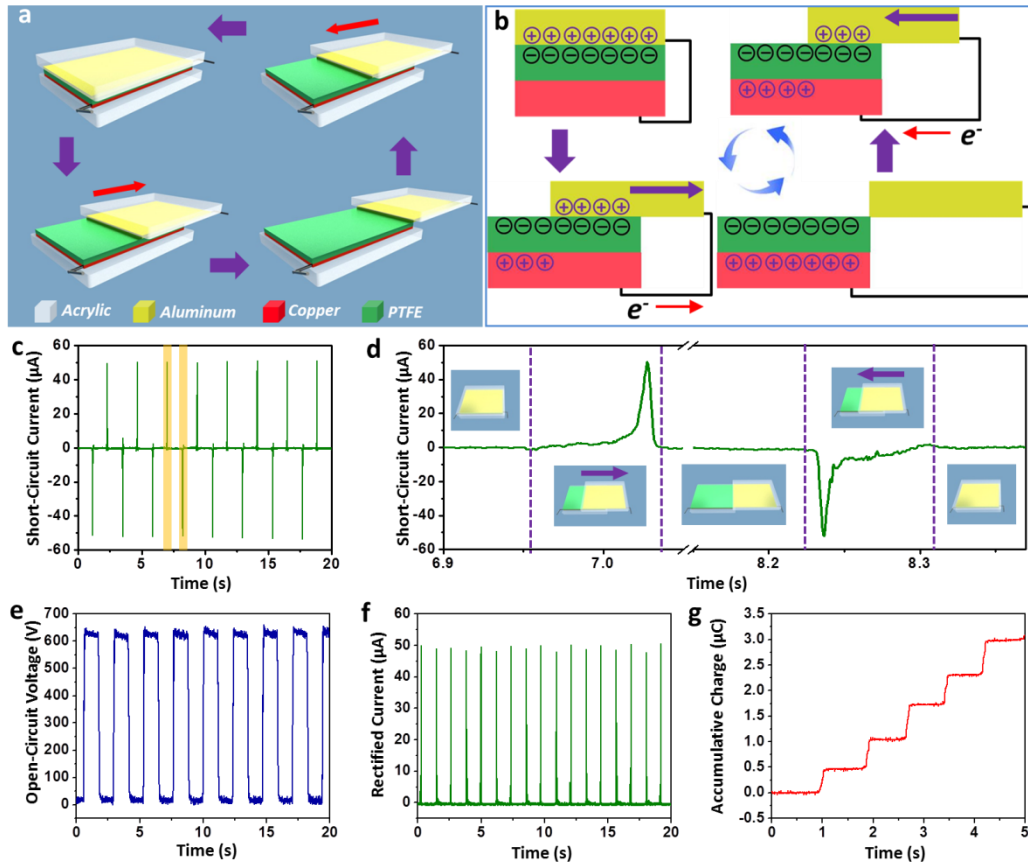
Figure 1.6 Triboelectric nanogenerator based on sliding electrification. (a) Schematic of the operation process of an in-plane sliding triboelectric nanogenerator. (b) A cycle of electricity generation process for illustrating the mechanism of the TENG.Electrical measurement results of an in-plane sliding triboelectric nanogenerator. (c) Short-circuit current and enlarged view of a cycle (d) highlighted in (c). Insets: relative positions between the two sliding surfaces that correspond to the current output. (d) Open-circuit voltage. (e) Rectified current by a full-wave diode bridge. (f) Accumulative inductive charges generated by the TENG.[33]

At aligned position, though triboelectric charges present on the surfaces, positive ones on aluminum are fully compensated by the negative ones on PTFE, producing no electric field in surrounding space if the electric field at the edge is ignored. Once a relative displacement is introduced by an externally applied force in the direction parallel to the surfaces, triboelectric charges are not compensated at the displaced/mismatched areas, resulting in the creation of an effective dipole polarization parallel to the direction of the displacement. Therefore, the uncompensated charges generate electric potential difference across the two electrodes, which will repulsively drive free electrons on the copper electrode to the aluminum electrode, neutralizing the positive triboelectric charges and leaving behind positive inductive charges. The flow of inductive electrons lasts until the displacement reaches the maximum. As the displacement is diminished by the reciprocating force, the inductive electrons flow back to the copper electrode until the fully aligned position is restored. Therefore, in the entire process, alternating current is produced through the external load.

1.2.3 The single-electrode mode

For both the vertical contact-separation mode and in-plane sliding mode triboelectric nanogenerators, the moving objects need to be bonded with an electrode and a lead wire. Such a device configuration largely limits TENGs' versatility and applicability for harvesting energy from an arbitrary moving object, because the object has to be connected to the entire system by an interconnect. With this regards, the single electrode mode triboelectric nanogenerator was developed.[34] A typical example of single-

electrode TENGs is shown in Figure 1.7. In the original position, PTFE and aluminum fully

contact each other, which will result in that electrons are injected from aluminum to PTFE,
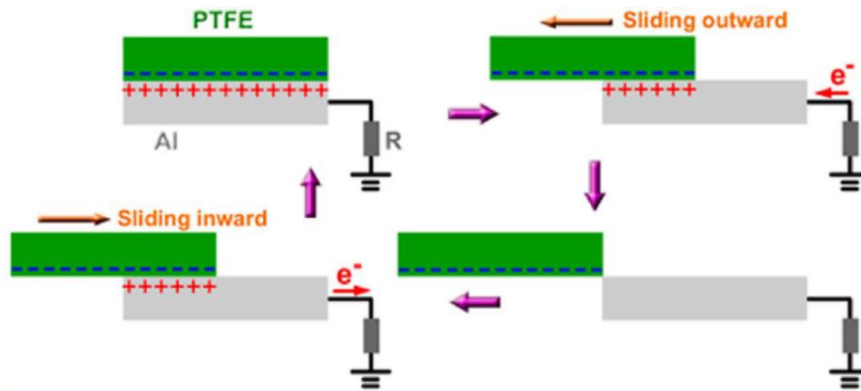
Figure 1.7 Sketches that illustrate the working principle of a typical single electrode mode triboelectric nanogenerator.[34]

since PTFE is much more triboelectrically negative than aluminum. Once the negatively

charged PTFE slides apart, a decrease of the induced positive charges on the Al will occur,

and thus the electrons will flow from ground to aluminum till the two plates are entirely

separated. Then, when the PTFE slides backward, the induced positive charges on the

aluminum increase, driving the electrons to flow from aluminum to the ground till the two

plates fully overlapped. This is a full cycle of electricity generation process of the single-

electrode mode triboelectric nanogenerator.

1.2.4 The freestanding triboelectric-layer mode

The freestanding triboelectric-layer mode triboelectric nanogenerator is also

capable of scavenging energy from the mechanical motion without an attached electrode.

If we make a pair of symmetric electrodes underneath a dielectric layer and the size of the

9

electrodes and the gap distance between the two are of the same order as the size of the moving object, the object's approaching to and/or departing from the electrodes create an asymmetric charge distribution in the media, which causes the electrons to flow between the two electrodes to balance the local potential distribution.
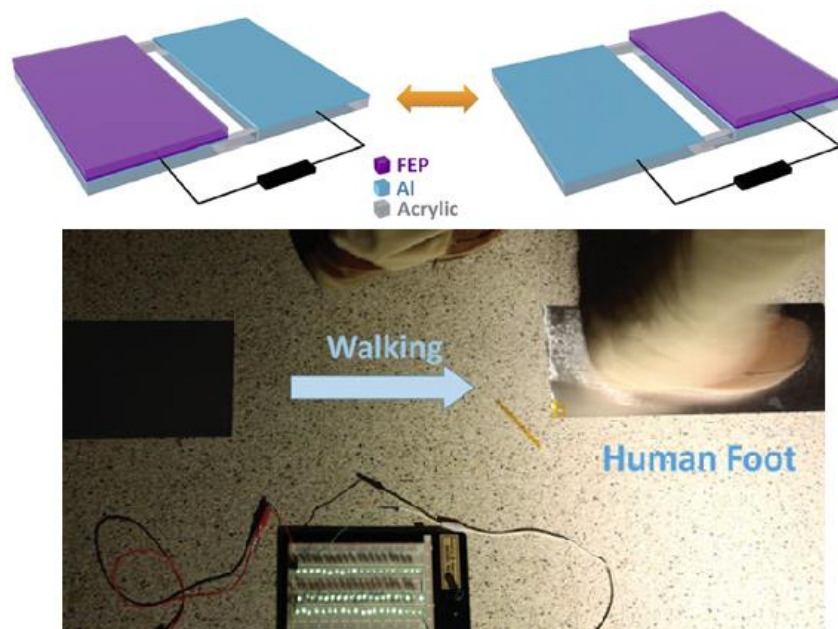
Figure 1.8 Sketch that illustrates the structure design of a typical freestanding triboelectric-layer mode triboelectric nanogenerator and its application in harvesting mechanical energy from human walking.[36]

The oscillation of the electrons between the pair electrodes produces electricity. One typical structure of freestanding triboelectric-layer mode triboelectric nanogenerator is shown in Figure 1.8.[36] Given the unique applicability resulting from distinctive mechanism and device structure, the freestanding triboelectric-layer mode triboelectric nanogenerator can be utilized to harvest energy from a walking human or a moving automobile.

1.3 Objective of the research

Mechanical motions, in various forms, is ubiquitous in ambient environment with wide-range of scale, from air flow, ocean wave to human activities such as walking, running, even heartbeat, throat vibration and breathing, from operating household appliances such as washing machines and refrigerators to bouncing automobile tires on a gravel road. With this regards, the objective of this thesis research is mainly devoted to developing and expanding the applicability of triboelectric nanogenerators, which is engaged in fundamental working mode development, functional materials synthesis as well as applications directed device design for various mechanical energy harvesting. The concept and design presented in this dissertation research can greatly promote the development of TENG as sustainable power sources and self-powered active sensors.

CHAPTER 2

TENG AS SUSTAINABLE POWER SOURCES

2.1 TENG for vibration energy harvesting

Vibration, as a type of common mechanical motion, ubiquitously exists in people's daily life. In recent years, it becomes an attractive target for energy harvesting as a potentially alternative power source to battery-operated electronics. Until recently, the mechanisms of vibrational energy harvesting are limited to transductions based on piezoelectric effect,[11] electromagnetic effect,[5] electrostatic effect[7]. Widespread usage of these techniques is likely to be shadowed by possible limitations, such as structure complexity,[37] fabrication of high-quality materials,[38] and reliance on external power source.[7] Furthermore, all of the mechanisms require energy harvesting devices to operate at or within a very narrow range around resonance frequency. However, the majority of the ambient vibrations have a wide distribution of frequency spectrum, which may even drift over time, making the conventional mechanisms unsuitable in most circumstance.[39] With this regards, we introduced a new principle in harvesting vibration energy by fabricating several triboelectric nanogenerators, as elaborated in the following sections.

2.1.1 Harmonic-resonator-based TENG

The harmonic-resonator-based TENG has a multilayer structure with acrylic as supporting substrates, as schematically shown in Figure 2.1a.[40] Acrylic was selected as the

structural material owing to its decent strength, light weight, good machinability and low cost. A photograph of an as-fabricated TENG is shown in Figure 2.1b.
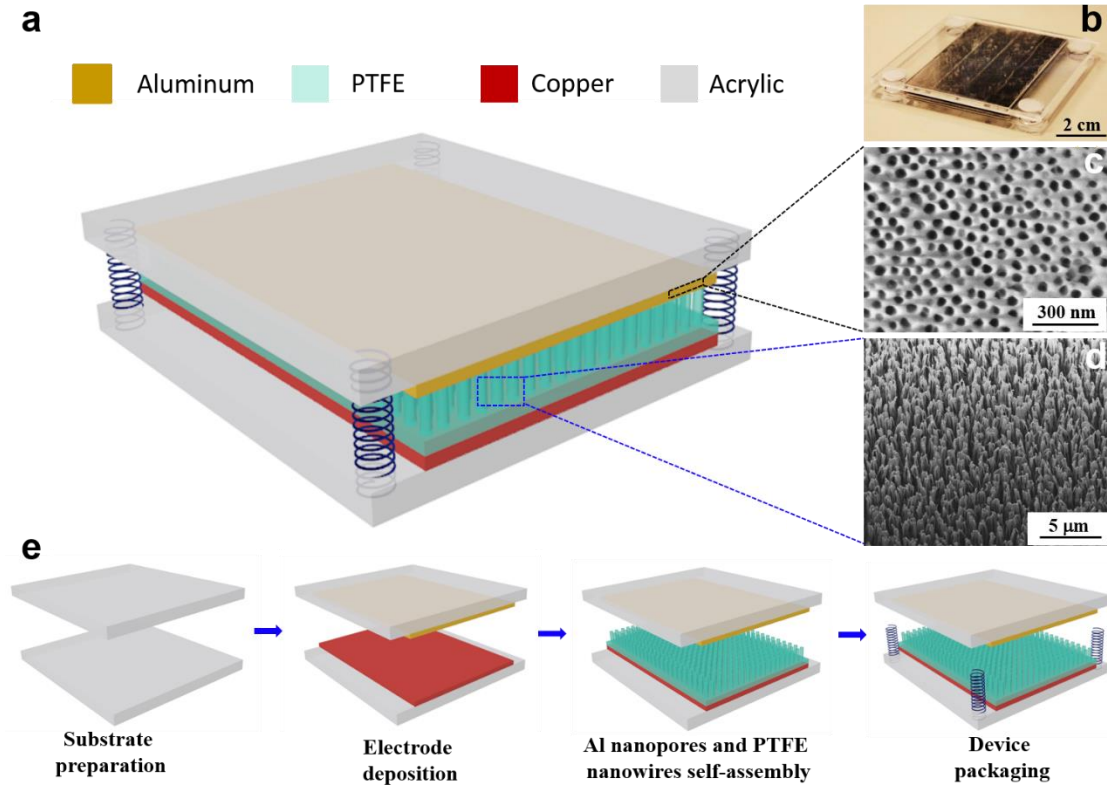
Figure 2.1 Harmonic Resonator Based Triboelectric Nanogenerator. (a) Sketch and (b) photograph of a typical harmonic resonator based TENG. (c) SEM image of nanopores on aluminum electrode. (d) SEM image of PTFE nanowires. (e) Process flow for fabricating the Harmonic Resonator Based TENG.[40]

On the upper substrate, aluminum thin film with nanoporous surface plays dual roles of an electrode and a contact surface. Scanning electron microscopy (SEM) image of nanopores on the aluminum is presented in Figure 2.1c. The average diameter of aluminum nanopores are 57 ± 5nm and a pore depth of 0.8 ± 0.2 μm with a distribution density of 212 per μm^2. A layer of polytetrafluoroethylene (PTFE) film was adhered to the lower substrate with deposited copper as another electrode. PTFE nanowires arrays were created on the exposed PTFE surface by a top-down method through reactive ion etching.[41] SEM image

13

of the PTFE nanowires is displayed in the Figure 2.1d. The average diameter of PTFE nanowires is 54$\pm$3 nm with an average length of 1.5$\pm$0.5 μm. A detailed fabrication process for the TENG is sketched in Figure 2.1e.

To investigate the TENG's performance of harvesting vibration energy, an electrodynamic shaker (Labworks Inc.) that provides sinusoidal wave was employed as a vibration source with tunable frequency and amplitude. The lower substrate of the TENG was anchored on the shaker, leaving the the upper part free-standing. At a fixed vibration amplitude, the reliance of electric output on the input vibration frequency is presented in Figure 2.2A and Figure 2.2B. The electric output can be measured with broad input frequency varying from 2 Hz to 200 Hz. Compared to state-of-the-art vibration energy harvesters that are based on nonlinear and topology variation,[42-44] it has a considerably wider working bandwidth 13.4 Hz.

Experimentally, both the open-circuit voltage (V_{oc}) and the short-ciruit current (I_{sc}) are maximized at the vibriation frequency of 14.5 Hz with maximum values of 287.4 V and 76.8 μA, respectively, indicating that 14.5 Hz is the resonance frequency of the TENG. Theoretically, for a single degree-of-freedom vibration system, the natural frequency is given by

$$f_0 = \frac{1}{2\pi}\sqrt{\frac{4k}{m_0}} \tag{2.1}$$

where f_0 is the natural frequency, m_0 is the mass of the upper substrate plus the aluminum film, and k is the stiffness coefficient of each spring. For the TENG, m_0 is 56.8 g, and spring stiffness coefficient is 112 N/m. Submitting the values into equation 2.1, we can obtain the natural frequency f_0 of 14.1Hz, which is well consistent with the experimental result.

At the resonance frequency, the V_{oc} is elaborated in Figure 2.2c. It has a uniform quasi-sinusoidal signal due to the fact that the upper substrate of the TENG vibrates in a harmonical manner. Theoretically, the harmonic-resonator-based TENG can be regarded as a damped system subjected to a harmonically varying force. Therefore, the maximum V_{oc} at the resonance frequency can be expressed as

$$V_{\text{oc-rf}} = \frac{\sigma}{\varepsilon_0} \cdot \frac{m_0 a}{2k\zeta} \tag{2.2}$$

where σ is the triboelectric charge density ($0.00281\,\mu\text{C/cm}^2$), ε_0 is the vacuum permittivty (8.85×10^{-12} F/m), ζ is the damping factor of the TENG system (0.34 by experimental measurement), and a is the acceleration of the electrodynamic shaker (a typical value of g/50 (g is the gravitational acceleration)).
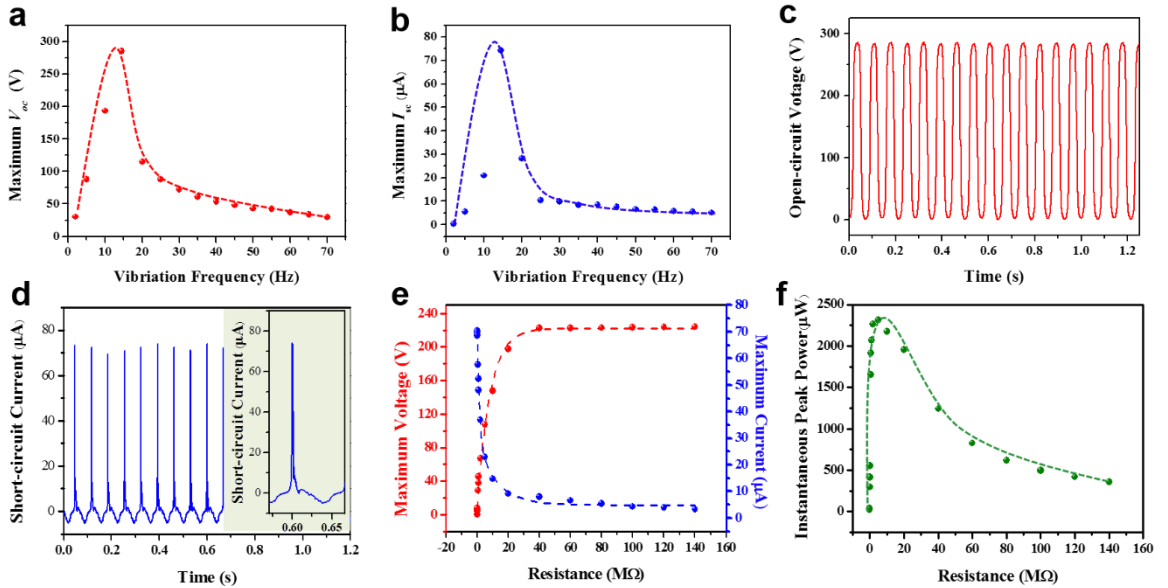
Figure 2.2 Electrical measurement results of a harmonic resonator based TENG. (a) Open-circuit voltage (V_{oc}) as a function of vibration frequency. The curve is the fitted result. (b) Short-circuit current (I_{sc}) as a function of vibration frequency. The curve is a fitted result. (c) Open-circuit voltage (V_{oc}) at vibration frequency of 14.5 Hz. (d) Short-circuit current (I_{sc}) at vibration frequency of 14.5 Hz. Inset: enlarged view if one cycle. (e) Dependence of the voltage and current output on the external load resistance. The points represent peak value of electric signals while the lines are the fitted results. (f) Dependence of the peak power output on the resistance of the external load, indicating maximum power output when R = 5 MΩ. The curve is fitted result.[40]

The theoretical result of the V_{oc} at the resonance frequency is calculated to be 464.2 V, which is larger than the experimental result of 287.4 V. The difference likely results from the assumptions made in the analytical model and non-ideal factors in the experiment. First, equation 2.2 is based on an assumption that the two contact surfaces are smooth. However, surface modification by nanomaterials is employed in the real case, leading to substantially enhanced contact area and thus higher triboelectric charge density. The value of triboelectric charge density submitted into equation 2.2 is obtained experimentally. Therefore, it is very likely to result in an overestimation of the theoretical V_{oc}. In addtion, non-ideal factors such as humidity and particle contaminations in the air, which are not considered in the theoretical model, may potentially have negative impact on the actual voltage output. As shown in Figure 2.2d, the output current at the resonance frequency has an alternating behavior with asymmetrical amplitudes. It is found that the larger peaks correspond to the process in which the two contact surfaces move apart after collision; while the smaller ones are generated as the two surfaces approach each other. Given the same amount of charges transported back and forth, the faster separation is expected to produce larger current peaks than the slower approach, leading to the asymmetry.

Resistors were utilized as external loads to further investigate the output power of the TENG at the resonance frequency. As displayed in Figure 2.2e, the current amplitude drops with increasing load resistance owing to the Ohmic loss, while the voltage follows a reverse trend. As a result, the instantanenous peak power (V^2_{peak}/R) is maximized at a load resistance of 5 MΩ, coresponding to a peak power density of 726.1 mW/m^2 (Figure 2.2f). To prove the capability of the harmonic resonator based TENG as a sustainable

power source and an active vibration sensor, four sets of practical applications were demonstrated.
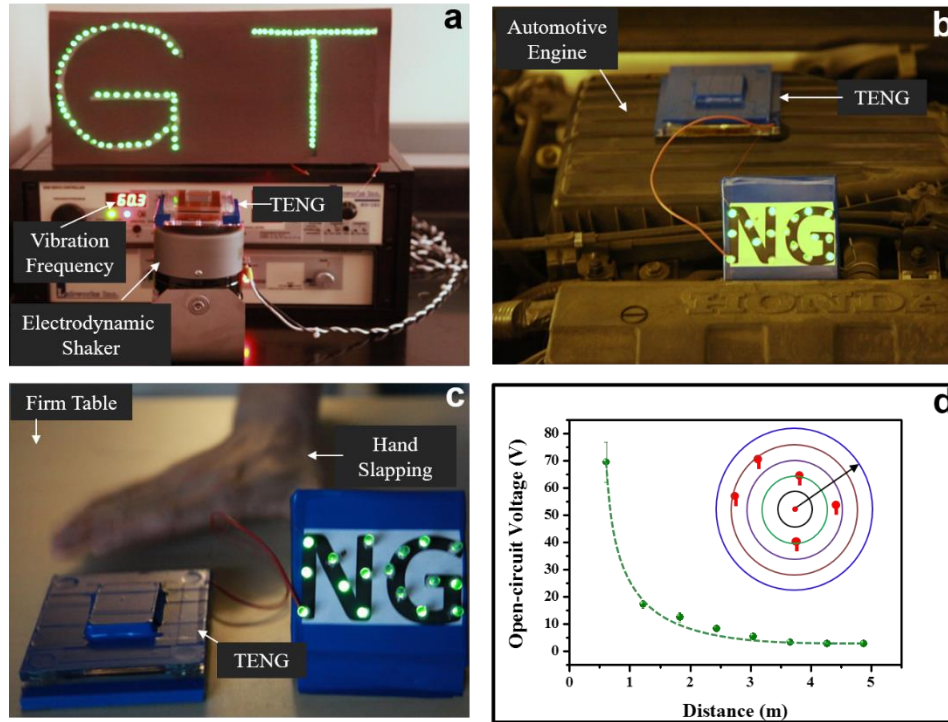
Figure 2.3. Demonstration of the harmonic resonator based TENG as a sustainable power source and self-powered active vibration sensor. (a) Photograph that shows TENG is working on an electrodynamic shaker at the vibration frequency of 60 Hz, which is the United States national power frequency. About 100 LEDs are being lighted up simultaneously without strobe perceived by a naked eye. (b) Photograph that shows TENG is working on an automotive engine. When the car starts up, the "NG" is being lighted up simultaneously. (c) Photograph that shows TENG works when a human hands slapping a firm table. Due to the table vibration, about 20 LEDs are being lighted up simultaneously. (d) TENG acts as active vibration sensor for distance measurement as well as ambient vibration detection. When a human walks naturally approaching the TENG, which is fixed on the floor, the output signal is exponentially increased.[40]

First, as shown in Figure 2.3a, the TENG was excited by an electrodynamic shaker at a vibration frequency of 60 Hz, lighting up almost 100 LED bulbs simultaneously and continuously without observable strobeflash. Secondly, shown in Figure 2.3b, the TENG was mounted onto an automotive engine. It sucessfully harvests vibrational energy from

the operating engine and powers about 20 LED bulbs simultaneously. The third practical application shows that the TENG, sitting on a table, generates electricity and drives small electronics as impact from a nearby human palm initiates vibration of the table (Figure 2.3c). Lastly, as demonstrated in Figure 2.3d, the TENG can also act as an active vibration sensor for detecting ambient vibration. When a human natually walks beside the TENG that is placed on the floor, electric output can be succesfully obtained. With the maximum effective range of 5 m, the electric output amplitude is exponentially related to the distance between the TENG and the footstep. These demonstrated applications prove that the TENG is sensitive to small ambient vibrations, making it suitable to a wide range of circumsntacnes for either energy-harvesting or sensing purposes, e.g. highways, bridges, and tunnels.

2.1.2 Three-dimensional TENG

Vibrations in our living environments are generally distributed over a wide frequency spectrum and exhibit multiple motion directions over time, which renders most of the current vibration energy harvesters unpractical for their purposes. With this regard, a three-dimensional triboelectric nanogenerator (3D-TENG) was developed, which can works in a hybridization mode of conjunctioning the vertical contact-separation mode and the in-plane sliding mode.[45] The innovative design facilitates harvesting random vibration energy in multiple directions over a wide bandwidth. The 3D-TENG has a multilayer structure with circular acrylic as supporting substrates, as schematically shown in Figure 2.4a. The cylindroid core of the 3D-TENG lies at the center of the acrylic substrate with a bottom diameter of 3 cm.
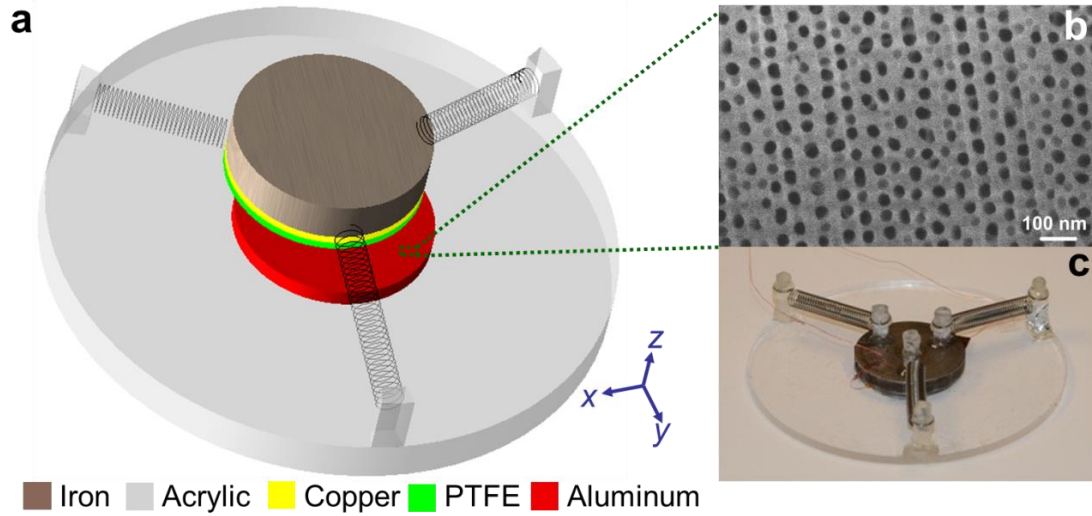
Figure 2.4 Three-dimensional triboelectric nanogenerator. (a) Schematic of a 3D-TENG. (b) SEM image of nanopores on aluminum electrode. (c) A photograph of the fabricated 3D-TENG.[45]

On the top of the core, an iron mass is mobile and suspended by three identical springs with an included angle of 120^0 between each other. The designed structural symmetry assures that the whole system has a constant resonant frequency at arbitrary in-plane directions. A layer of polytetrafluoroethylene (PTFE) film as one contact surface was adhered onto the bottom side of circular iron mass with deposited copper thin film as the back electrode. Attached to the bottom acrylic substrate, aluminum thin film with nanopores modification plays dual roles as a contact electrode and the other contact surface. The scanning electron microscopy (SEM) images of aluminum nanopores are shown in Figure 2.3b. Figure 2.3c is a photograph of the real 3D-TENG device.

To operate, an electrodynamic shaker is still used as an external vibration source with controlled amplitude and acceleration. The supporting acrylic substrate of the 3D-TENG is anchored on the shaker table to investigate the relationship between the electrical outputs and input frequency when it works in a vertical contact-separation mode.

19
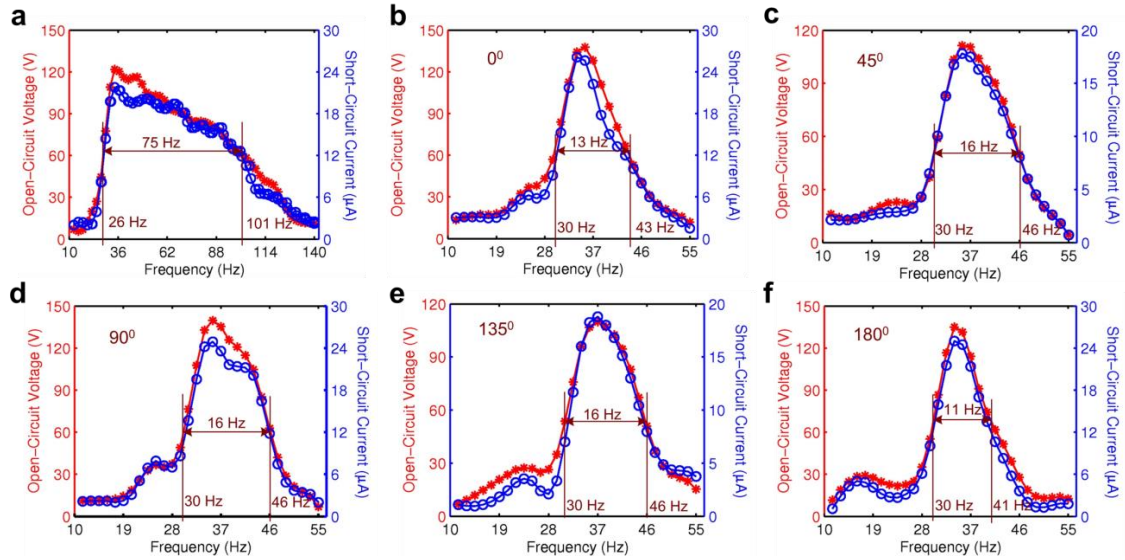
Figure 2.5 Frequency responses of the 3D-TENG. (a) Frequency response of 3D-TENG under out-of-plane excitation. (b-f) Frequency responses of 3D-TENG at in-plane excitation angles of 0^0, 45^0, 90^0, 135^0 and 180^0, respectively.[45]

As shown in Figure 2.5a, both the voltage and current present a rapid increasing with the increase of frequency from 10 to 36 Hz. The maximum values of the voltage and current respectively reach 123 V and 21 μA at the frequency of 36 Hz. Then, the voltage and current both gradually decrease to their minima as the frequency increases from 36 to 140 Hz. The larger separation at 36 Hz would cause a larger contacting force when the two objects impact together. Since the aluminum surface was patterned with nanopores, a larger impact will largely increase the effective contact area between the two surfaces, and thus the total electric output. In addition, if the half peak voltage point is adopted as the criteria of the working bandwidth, 3D-TENG shows an extremely wide working bandwidth up to 75 Hz in a low vibration frequency range under the out-of-plane excitation.

When it comes to the in-plane sliding mode, the electric outputs were measured with the input excitation frequencies in a range from 10 to 55 Hz at different in-plane

20

excitation angles (0^0, 45^0, 90^0, 135^0, 180^0), as shown in Figures 2.5 b-f. The results proved that the 3D-TENG is capable of harvesting vibration energy from all of the in-plane directions. Considered the non-ideal experimental factors, such as the variation of the spring stiffness factors and the deviation of the fabricated structure symmetry, the 3D-TENG has almost the same responses to the external vibrations at arbitrary in-plane directions. Furthermore, both the voltage and current are maximized at the frequency of 36 Hz at all excitation angles. And slightly nonlinear behaviors are observed in all of the output responses mainly owing to the non-linear topology structure of the spring vibration system. In addition, the 3D-TENG also shows a considerably wide working bandwidth of 14.4 Hz in a low vibration frequency range under the in-plane excitation.

The practicability of harvesting energy from multiple directions with considerably wide working bandwidth enable the 3D-TENG have tremendous applications of building up self-powered systems by harvesting ambient vibration energy. To prove the capability of the 3D-TENG as a sustainable power source, three sets of practical applications were demonstrated. First, as shown in Figure 2.6a, the 3D-TENG works on a national grid transmission line which can effectively harvest wind or rain droplet induced line vibration energy. Forty serial-connected commercial LEDs were lighted up due to the line oscillating. Figure 2.6b plots the output voltages of the 3D-TENG under different line swing amplitudes. It can be seen that the voltages present an obvious increasing tendency with the increased swing amplitudes. This is because larger swing amplitude of the line will contribute to a larger out-of-plane separation of the two contact surface in the 3D-TENG, leading to higher output voltage.

21
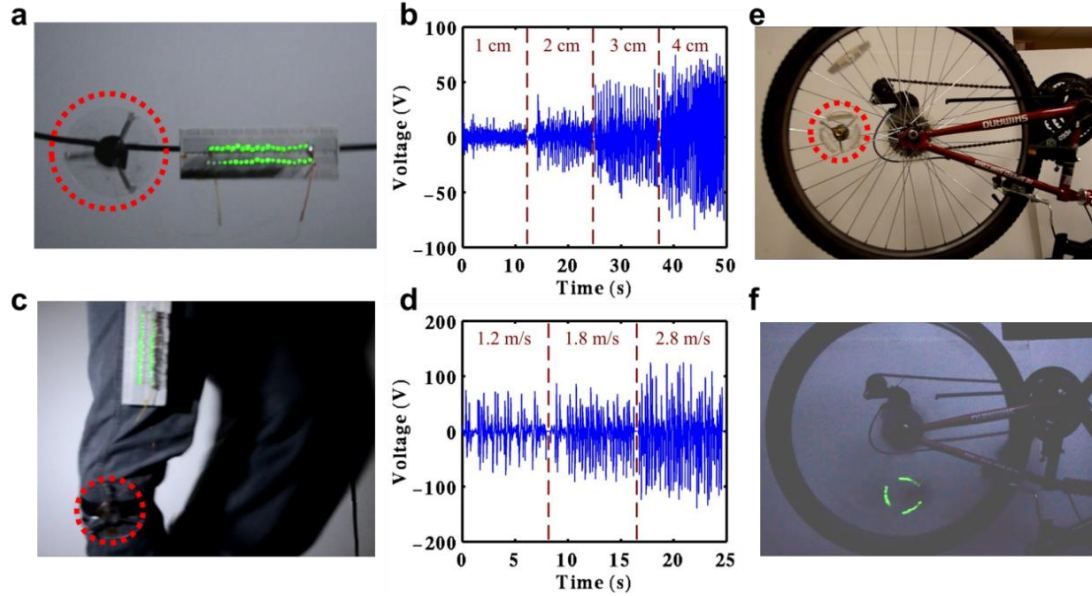
Figure 2.6 Demonstration of the 3D-TENG (marked in red circles) as a sustainable power source and self-powered active sensors. (a) The photograph of line vibration energy harvesting. Forty commercial LED bulbs were lighted up simultaneously. (b) The output voltage of the 3D-TENG under different line swing amplitudes. (c) The photograph of human walking energy harvesting. Forty commercial LED bulbs were lighted up simultaneously. (d) The output voltages at different walking speeds. (e) The photograph of 3D-TENG mounted on a still bicycle wheel. (f) Thirty commercial LED bulbs were lighted up simultaneously under the rotation of the bicycle wheel.[45]

Secondly, shown in Figure 2.6c, the 3D-TENG is mounted on a human trail leg to harvest the vibration energy from human walking. This human motion induced vibration can be used as an external excitation to the 3D-TENG and 40 serial-connected commercial LEDs were lighted up. Figure 2.6d plots the output voltages under different walk speeds, which indicates that a faster speed leads to a larger voltage output. A third practical application is shown in Figure 2.6e. The 3D-TENG was anchored on a bicycle wheel to harvest the rotation energy. And 30 serial-connected commercial LEDs were lighted up during the wheel rotating (Figure 2.6f). This demonstration proves that the 3D-TENG not only can harvest wheel rotation energy but also can be developed as self-powered sensing

system to monitor the tire-pressure of automobiles, airplanes and other wheel-based vehicles.

In a word, the 3D-TENG can effectively harvest ambient vibration energy in out-of-plane direction with extremely wide working bandwidth up to 75 Hz and in arbitrary in-plane directions with prepotent bandwidth of 14.4 Hz in low vibration frequency range. This superior capacity enable the 3D-TENG have tremendous practical applications, harvesting such as wind or rain droplet induced vibration energy from the national grid transmission lines, natural vibration energy from human walking, and rotation energy from the wheel-based vehicles. In addition, a large range of self-powered sensing systems can be also developed owing to the 3D-TENG's high sensitivity to the external vibrations. This TENG design will find applications in powering portable electronics, environmental/ infrastructure monitoring, security and more.

2.1.3 A triple-cantilever based TENG

Still, we demonstrate a rationally designed triple-cantilever based TENG for ambient vibration energy harvesting.[46] The basic structure of the triple-cantilever based TENG is shown in Figure 2.7a, in which, three metal plates of beryllium copper alloys foils are the three cantilevers. The bottom surface of the top cantilever and the top surface of the bottom cantilever are coated with Polydimethylsioxanes (PDMS) films.[47] The surfaces of the middle cantilever are covered by ZnO nanowire arrays grown by chemical approach,[48] on the top of which a layer of Cu was evaporated. A mass is also attached at its end for effectiveness of vibration. Photos of a real device are shown in Figure 2.7b and d. This device has three unique characteristics. Firstly, the middle cantilever has two chances to

contact the top and bottom cantilevers in each cycle of the vibration, doubling the vibration energy conversion efficiency. Secondly, the PDMS film can be easily deformed to increase the effective contact area of TENG.[25]
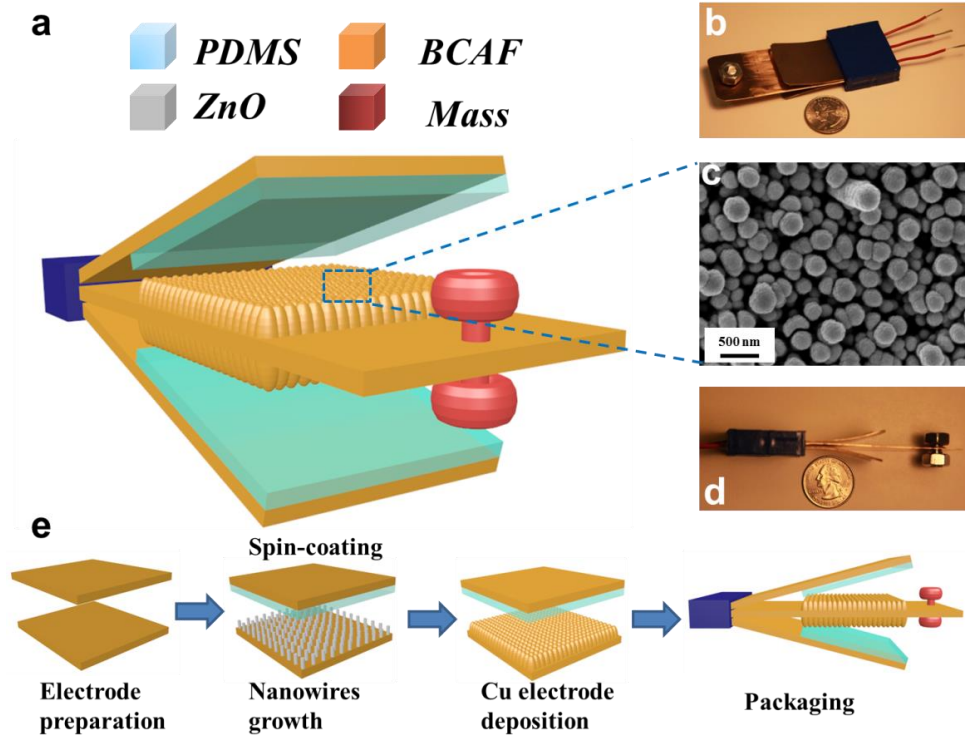
Figure 2.7 (a) Sketch and (b), (d) photographs of a typical triple-cantilever based TENG, with a size equivalent to a quarter. (c) SEM image of Cu film coated ZnO nanowire arrays. (e) Fabrication process of the TENG.[46]

Lastly, the nanowire-arrays based surface modification plays an important role for the output power enhancement (Figure 2.7c). The nanowire arrays can deeply insert into the PDMS to increase the effective contact area and thus a substantially higher electric output. As sketched in Figure 2.7e, the fabrication process is simple and straightforward, without involving any complicated equipment or procedures.

The triple-cantilever based TENG was tested by measuring its open-circuit voltages (V_{OC}) and rectified short-circuit current (I_{SC}) in a range of frequencies from 2.5 Hz to 5.0

Hz with the same amplitude. From Figure 2.8a and b, it is safe to conclude that the triple-cantilever based TENG is suitable to harvest the low-frequency vibration energy such as ocean waves, motor vibration, highway, bridge and tunnel vibration when vehicles passing by. In addition, we also investigated the reliance of the electric output power on the external load under the vibration frequency of 3.7 Hz. As indicated in Figure 2.8c, increasing the resistance of the external load, the maximum current and voltage decreased and increased, respectively. Correspondingly, the instantaneous output power density ($P_d = UI/S_{eff}$) as a function of the external resistance is shown in Fig. 4d. The peak power density of 252.3 mW/m^2 can be achieved at a load resistance of 0.25 MΩ.
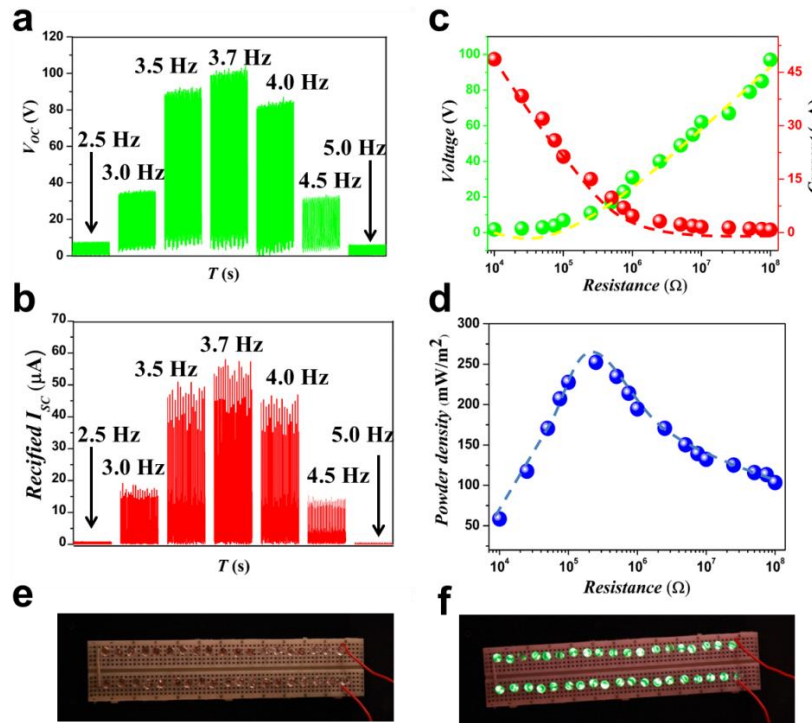
Figure 2.8 The triple-cantilever based TENG as a direct power source to power electronic devices. (a) Open-circuit voltage (V_{OC}) and (b) Rectified short-circuit current (I_{SC}) of vibration frequency from 2.5 Hz to 5.0 Hz, showing that 3.7 Hz is the resonant frequency of the TENG. (c, d) When the TENG a load with rectification, the dependence of (c) the output voltage, current, and (d) instantaneous power density on the resistance of the load. TENG simultaneously lights up 40 LEDs in real time. (e) Photographs of LEDs when there is no vibration and (f) lit up LEDs by a vibration at a frequency of 3.7 Hz.[46]

25

Indeed, non-ideal experimental factors, such as humidity and particle contaminations in the air, may potentially have negative impact on the electric performance and thus the longevity of the triple-cantilever based TENG. As a result, the device packaging is critical when the TENG is applied outdoor and even in circumstances with harsh environment, which would greatly extend the life time of the device up to even several years. The performance of the triple-cantilever based TENG is affected by three factors. First, by growing ZnO nanowire arrays on the surface of the middle cantilever, the output is dramatically enhanced. The peak value of the TENG without nanowires is only about 42.6 % of the TENG with the nanowires. Secondly, the usage of beryllium copper alloys foils with high elasticity as the vibration energy conversion medium is also very critical to harvest vibration energy in ambient environment. Lastly, the resonance state of the device maximizes the amplitude of vibration and thus enhances output power.The triple-cantilever based TENG aims at powering electronic devices by harvesting small-scale vibration energy. A total of 40 commercial LED bulbs were assembled in series on a piece of electric board (Figure 2.8e), connected to the triple-cantilever based TENG. As triggered by the shaker under a vibration frequency of 3.7 Hz, the TENG directly and simultaneously lights up all these forty LED bulbs (Figure 2.8f). The triple-cantilever based triboelectric nanogenerator provides a new approach for harvesting low-frequency vibration energy, opening its applications for self-powdered electronics and systems.

2.1.4 Three-Dimensional Stack Integrated TENG

The applications of a single-layer triboelectric nanogenerator for vibration energy harvesting may be challenged by its lower output current, and a possible solution is to use

three-dimensional (3D) stack integrated multilayered TENGs, but the most important point is to synchronize the outputs of all the TENGs so that the instantaneous output power can be maximized.[49] With this regard, we take a further step to develop a multi-layered stacked TENG as a cost-effective, simple and robust approach for harvesting ambient vibration energy. The 3D-TENG has a multilayered structure with acrylic as supporting substrates, as schematically shown in Figure 2.9a. Acrylic was selected as the structural material due to its decent strength, light weight, good machinability and low cost. A photograph of an as-fabricated TENG is shown in Figure 2.9b, in which, the total number of the unit cells can be expressed as:

$$N_{total} = 4n \tag{2.3}$$

where n is the number of pinned fingers of a TENG. Eight identical springs were employed to bridge the moveable and pinned fingers.
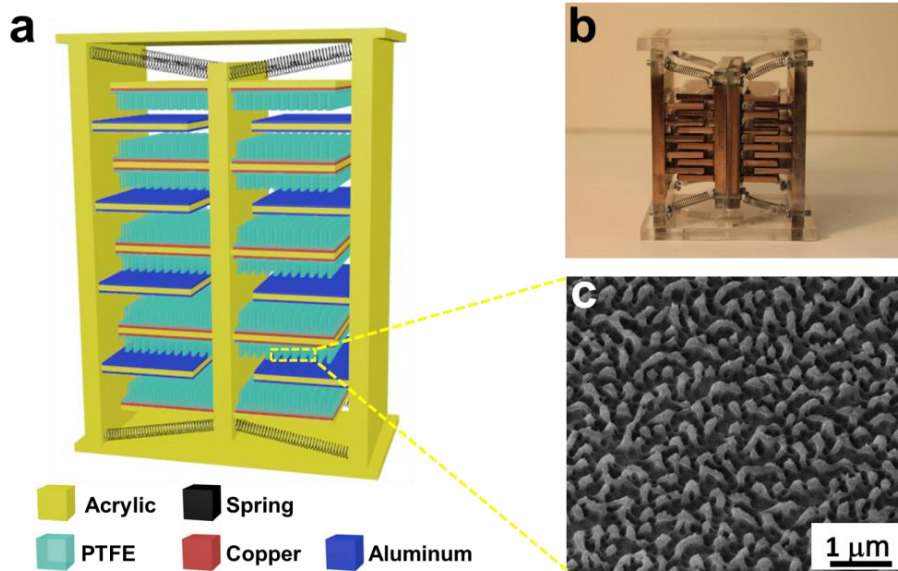
Figure 2.9 Three-dimensional stack triboelectric nanogenerator. (a) Schematic of a 3D-TENG. (b) SEM image of nanopores on aluminum electrode. (c) A photograph of the fabricated 3D-TENG.[49]

All fingers were made from acrylic sheets with a thickness of 3 mm and parallel to each other with identical but tuneable gap distance. The thickness of acrylic sheets is large enough to prevent the mutual charges influences among the unit cells. Moreover, all the unit cells are electrically connected in parallel. Aluminium thin films were deposited onto both sides of the pinned fingers, which played dual roles of a contact electrode and a contact surface. A layer of polytetrafluoroethylene (PTFE) film was adhered to the both sides of the movable fingers with deposited copper as another electrode. PTFE nanowires arrays were created on the exposed PTFE surface by a top-down method through reactive ion etching. SEM image of the PTFE nanowires is displayed in Figure 2.9c. Additionally, to promote the triboelectrification and to increase the effective contact area between the two contacting surfaces, PTFE nanowires are created as surface modifications, which greatly increases the triboelectric charges and thus the overall electrical output.

Theoretically, the short-circuit current of the 3D-TENG can be expressed as:

$$I_{SC} = \frac{\sigma s d_0 v}{\varepsilon_r [d + \frac{d_0}{\varepsilon_r}]^2} \tag{2.4}$$

where d_0 is the thickness of PTFE, ε_r is the relative permittivity of PTFE, s is the effective contact area and v is the relative velocity at which they will contact, whose motion direction determines the flowing direction of the induced charge, and thus the direction of the short circuit current. n is the number of pinned fingers, ΔS is the effective contact area and Δd is the gap distance between the two adjacent fingers.

To evaluate the TENG's performance for harvesting vibration energy, an electrodynamic shaker (Labworks Inc.) that provides sinusoidal wave was employed as an external vibration source with tunable frequency and amplitude. As shown in Figure 2.10a,

the voltage output is almost constant for 3D-TENG with $n = 1 \sim 5$, which is attributed to the electrically parallel connection among all the units. However, the current output is a monotonically increasing function of n throughout our experimental time window. And the current enhancement factor α is a function of n, $\alpha = bn$, the measured result b is very close to the ideal coefficient of 2. Such a high coefficient b is mainly owing to the operating synchronicity of all units, which convincingly demonstrates the effectiveness of our approach for current output enhancement. Likewise, a monotonically increasing relationship was observed between the current output and the effective contact area ΔS as well as parameter Δd, as shown in Figure 2.10b and c.
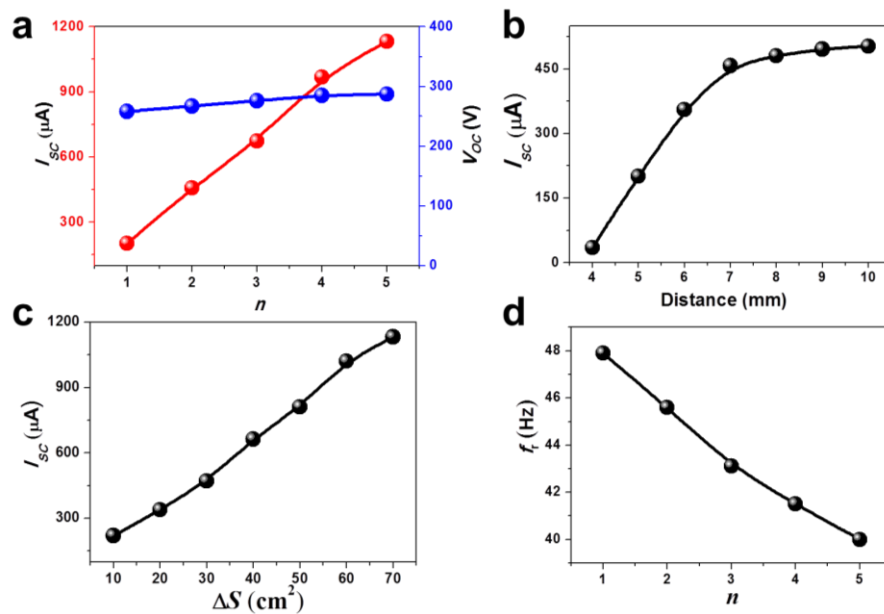
Figure 2.10 A systematical study of the reliance of current electric output on the design parameters. (a) Dependence of electric output on the number of pinned fingers n. (b) Dependence of the short-circuit current on the gap distance between two adjacent pinned fingers for the TENG with $n = 2$. (c) Dependence of short-circuit current on effective contact area (ΔS) of the TENG with $n = 5$. (d) The device natural frequency as a function of the number of pinned fingers n.[49]

A larger Δd will contribute to a larger relative velocity of the two contact plates, and thus renders us a higher output current, according to equation (2.4). In addition, as a vibration energy harvester, we also investigate the reliance of the natural frequency on the number of pinned fingers n for the 3D stack TENG. As indicated in Figure 2.10d, the resonance frequencies f_r decrease as increasing n, which is well consistent with a typical vibration system that a larger mass will lead to a smaller system natural frequency.[28-30]
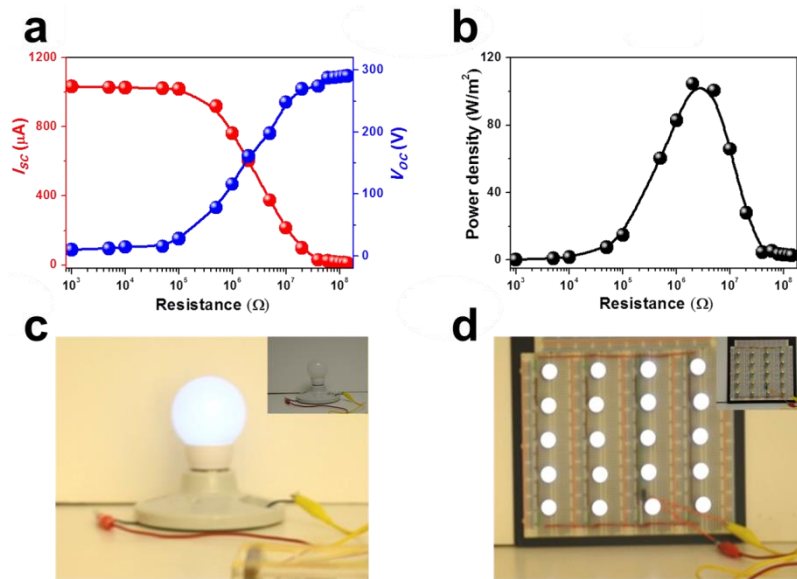
Figure 2.11 Demonstration of the 3D stack TENG as a direct power source. (A) Dependence of the voltage and current output on the external load resistance for the TENG with $n = 5$. (B) Dependence of the peak power output on the resistance of the external load for the TENG with $n = 5$, indicating maximum power output at $R = 2$ MΩ. The curve is a fitted result. (C) Photograph of a white G16 globe light that is directly powered by the TENG (Input frequency 40 Hz). Inset is a photograph when a white G16 globe light is off. (D) Photograph of 20 spot lights (0.6 W ea.) connected in series that are lighted up simultaneously and continuously without observable stroboflash by the TENG (Input frequency 40 Hz). Inset is a photograph when the spot lights are off.[49]

Resistors were utilized as external loads to further investigate the output power of the 3D-TENG at its resonance frequency. As displayed in Figure 2.11a, the current amplitude drops with increasing load resistance owing to the Ohmic loss, while the voltage

follows a reverse trend. Consequently, the instantanenous peak power ($P = I^2_{peak}R$) is maximized at a load resistance of 2 MΩ, coresponding to a peak power density ($P_d = I^2_{peak}R/\Delta S$) of 104.6 W m^{-2} (Figure 2.11b).

To prove the capability of the 3D-TENG as a sustainable power source, three sets of practical applications were demonstrated. First, as shown in Figure 2.11c, the TENG was excited by an electrodynamic shaker at a vibration frequency of 40 Hz, lighting up a white G16 globe light. Inset is a photograph when a white G16 globe light is off. Meanwhile, a total of 20 spot lights (0.6 W ea.) connected in series were lighted up simultaneously and continuously without observable flashing. Inset is a photograph when the spot lights are off. (Figure 2.11d).
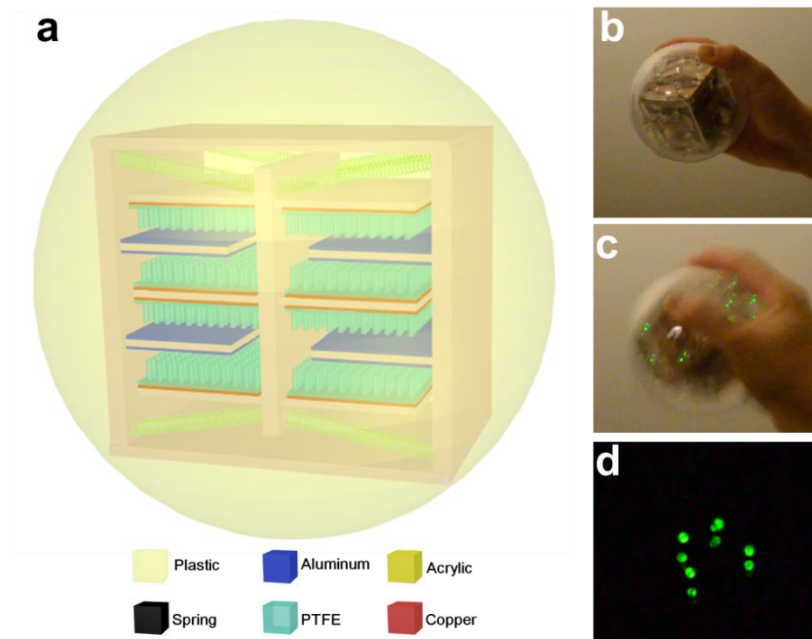
Figure 2.12 Demonstration of the 3D-TENG as it is equipped inside a ball, which has great potential of scavenging the kinetic energy when people play basketball, football, baseball and so on. Large amount of these self-powered balls can be also woven into webs for ocean wave energy harvesting, which can be potentially applied for large-scale energy generation. A sketch (a) and a photograph (b) of a self-powered ball. (c) When shaking the ball, about 32 commercial LEDs are lighted up simultaneously. (d) A photograph of 8 LEDs on a face of the device that are directly powered by the TENG in complete darkness (We equipped four faces of the devices with 8 LEDs on each face).[49]

In addition, with specific dimensional design, we integrated a 3D stack TENG into a ball with a diameter of 3 inches, as schematically shown in Figure 2.12a and a photograph of the as-fabricated devices in Figure 2.12b. In order to directly demonstrate the equipped ball as an energy harvester, we installed four faces of the inside TENG with 8 LEDs as indicators on each face. As shown in Figure 2.12c, the generated power by hand shaking simultaneously lighted up 32 commercial LEDs. And Figure 2.12d demonstrates that 8 LEDs on one of the four faces were lighted up in complete darkness. This practical application greatly demonstrated the capability of our 3D stack TENG for harvesting kinetic energy when people play various kinds of ball sports. It is worth noting that, large amount of these self-powered balls can also be woven into webs for ocean wave energy harvesting, which can be potentially applied for large-scale energy generation.

2.1.5 Integrated rhombic gridding based TENG

To enhance the output current for the vibration energy harvesting, here, we also demonstrated another rationally designed TENG with integrated rhombic gridding, which can greatly improve the total current output owing to the structurally multiplied unit cells connected in parallel.[50] The structure of integrated rhombic gridding based TENG is shown in Figure 2.13a, in which, the total number of unit cells in one TENG can be expressed as:

$$N_{\text{total}} = 2n^2 \tag{2.5}$$

where n is the number of unit cells along the edge length. The plastic sheets of polyethylene terephthalate (PET) with a thickness of 600 μm are utilized. Each PET sheet is cut half through and then lock into each other to form the framework of TENG. On one side of the PET substrate, aluminium thin film with nanoporous modification plays dual roles as a

contact electrode and a contact surface. A scanning electron microscopy (SEM) image of aluminium nanopores is shown in Figure 2.13b. A layer of PTFE film with nanowires arrays was adhered onto the other side of the PET substrate with deposited copper thin film as the back electrode. An SEM image of PTFE nanowires arrays is presented in Figure 2.13c. As demonstrated in Figure 2.13 d, e, f, there are 2, 8, and 18 unit cells in the TENGs (sketch and corresponding photograph of real devices) with n = 1, 2, and 3, respectively.
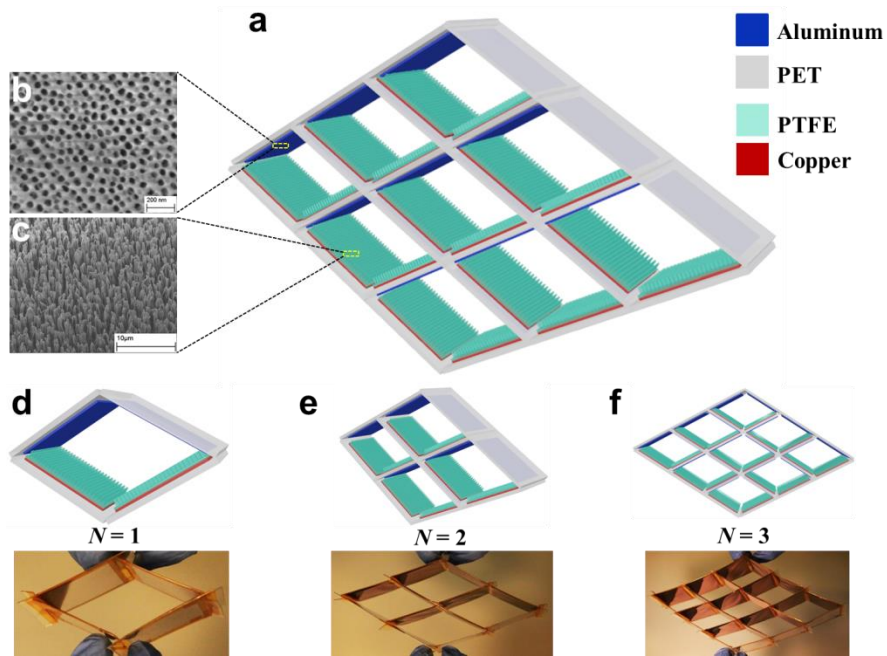
Figure 2.13 Integrated rhombic gridding based triboelectric nanogenerator. (a) Sketch of a typical TENG with n = 3. (b) SEM image of nanopores on aluminum electrode. (c) SEM image of PTFE nanowires. (d-f) Sketch and corresponding photograph of integrated rhombic gridding based TENG with n = 1, 2, 3, respectively.[50]

In order to enhance the total current output of the TENG, all of the unit cells are electrically connected in parallel. Under the fixed triggering frequencies and amplitude, the electric output measurement was performed on the integrated rhombic gridding based TENG with n = 1, 2, 3 (Figure 2.14). The effective contact area of TENG is $2n^2 \times 4.6$ cm $\times 4.6$ cm, which produces an open-circuit voltages (V_{OC}) 445 V at n = 1 (Figure 2.14a),

439 V at $n = 2$ (Figure 2.14b) and 428 V at $n = 3$ (Figure 2.14c). The voltage output is almost constant for all the measurements, which is because that all of the rhombic unit cells are electrically connected in parallel. As shown in the inset of Figure 2.14c, a positive voltage peak is generated due to the immediate charge separation at the departure of aluminum from PTFE. Since the electrons cannot flow back to screen the induced electric potential difference between the two electrodes under the open-circuit condition, the voltage holds at a plateau until the next contact emerges.[51-53]
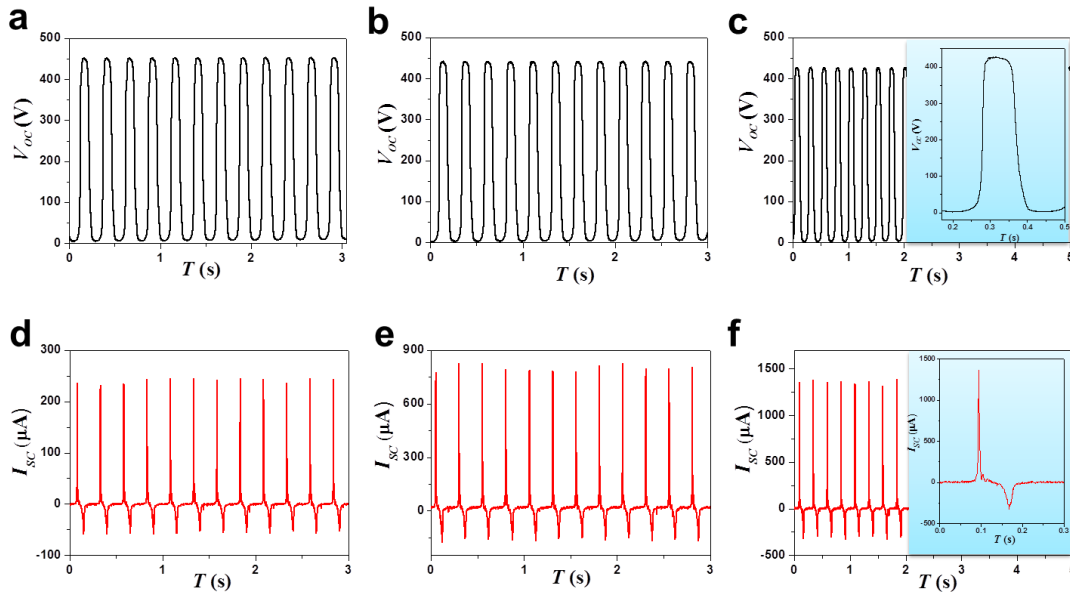
Figure 2.14 Electrical measurement of the integrated rhombic gridding based TENG. Open-circuit voltage (V_{OC}) (a, b, c) and short-circuit current (I_{SC}) (d, e, f) of the TENG with $n = 1$, 2 and 3, respectively. Insets of (c) and (f) are enlarged view of V_{OC} and I_{SC} in one cycle for the TENG with $n = 3$, respectively.[50]

Meanwhile, the peak values of the short-circuit current (I_{SC}) reach up to 245 μA at $n = 1$ (Figure 2.14d), 801 μA at $n = 2$ (Figure 2.14e) and 1.395 mA at $n = 3$ (Figure 2.14f). In addition, as shown in the inset of Figure 2.14f, the output current has an alternating behavior with asymmetrical amplitudes, with the larger peaks correspond to the process in which the two contact surfaces move towards each other, while the smaller ones are

34

generated as the two surfaces move apart, which is attributed to a faster approaching is expected to produce larger current peaks than the slower separation.
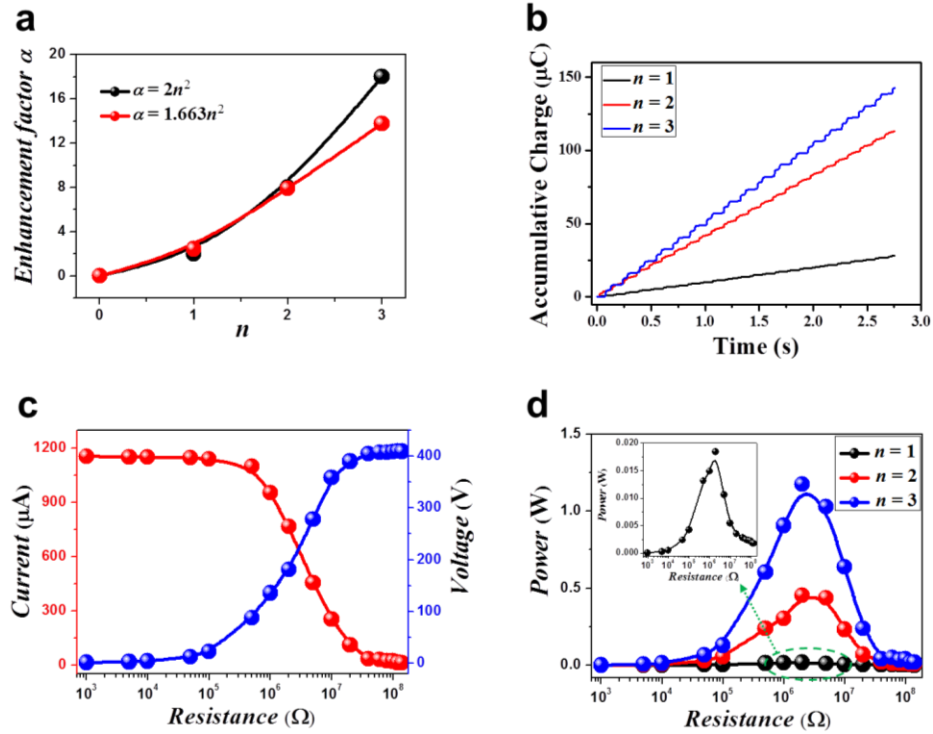
Figure 2.15. Electrical measurement of the integrated rhombic gridding based TENG. (a) The current's enhancement factor α is increasing as a function of number of unit cells along the edge length n. (b) Accumulative inductive charges generated by the TENG with $n = 1$, 2 and 3, respectively. (c) Dependence of the voltage and current output on the external load resistance for the TENG with $n = 3$. The lines are the fitted results. (d) Dependence of the peak power output on the resistance of the external load for the TENG with $n = 1$, 2, and 3, indicating maximum power output obtained at $R = 2$ MΩ. The curve is fitted result. Inset: an enlarged view of peak power output with $n = 1$.[50]

As indicated in Figure 2.15a, the current enhancement factor α is a function of the number of unit cells along the edge length, $\alpha = b\,n^2$. The fitting result renders the coefficient b a value of 1.66. Considering the non-ideal experimental factors, such as humidity, particle contaminations in the air, the imperfection from the device fabrication process, and the difficulty of working synchronization of all the device units, which may potentially have negative impact on the actual output, the experimental result of

enhancement factor is considerably approaching to the ideal value of $2n^2$, revealing that the integrated rhombic gridding structure can effectively enhance the total current output.

As illustrated in Figure 2.15b, the accumulative induced charges increases with n, which reaches up to 142.68 μC within 2.75 s when $n = 3$, further indicating that the integrated rhombic gridding structure can dramatically enhance the electric output of TENG. It is noteworthy that the accumulative induced charges are the sum of all the back-and-forth induced charges in the entire process of the TENG working as a "charge pump". Consequently, it is a monotonically increasing function of time throughout our experimental time window.

Resistors were utilized as external loads to further investigate the output power of the integrated rhombic gridding based TENG with $n = 3$. As displayed in Figure 2.15c, the current amplitude drops with increasing load resistance owing to the ohmic loss, while the voltage follows a reverse trend. As demonstrated in Figure 2.15d, all of the instantaneous peak power ($I^2_{peak}R$) for $n = 1$, 2, and 3 are maximized at a load resistance of 2 MΩ. Moreover, the peak power dramatically increases with the increase of n, which reaches up to 1.17 W at $n = 3$, corresponding to the peak power density and volumetric energy density of 30.7 W/m^2 and 1.54×10^4 W/m^3, respectively.

The integrated rhombic gridding based TENG demonstrated here has three unique characteristics. First, by using the novel integrated rhombic gridding structure, the total number N of unit cells, which are electrically connected in parallel, theoretically follows a rule of $N = 2n^2$. This is the key factor of dramatically enhancing the total electric output. Secondly, to promote the triboelectrification and to increase the effective contact area between the two contact surfaces, aluminum nanopores and PTFE nanowires are

36

simultaneously created as surface modifications. The rational design, coupled with nanomaterial modification, greatly increases the effective contact area and thus the triboelectric charges. Lastly, the structural coupling of nanopores and nanowires can also enhance the triboelectrification process for TENGs.
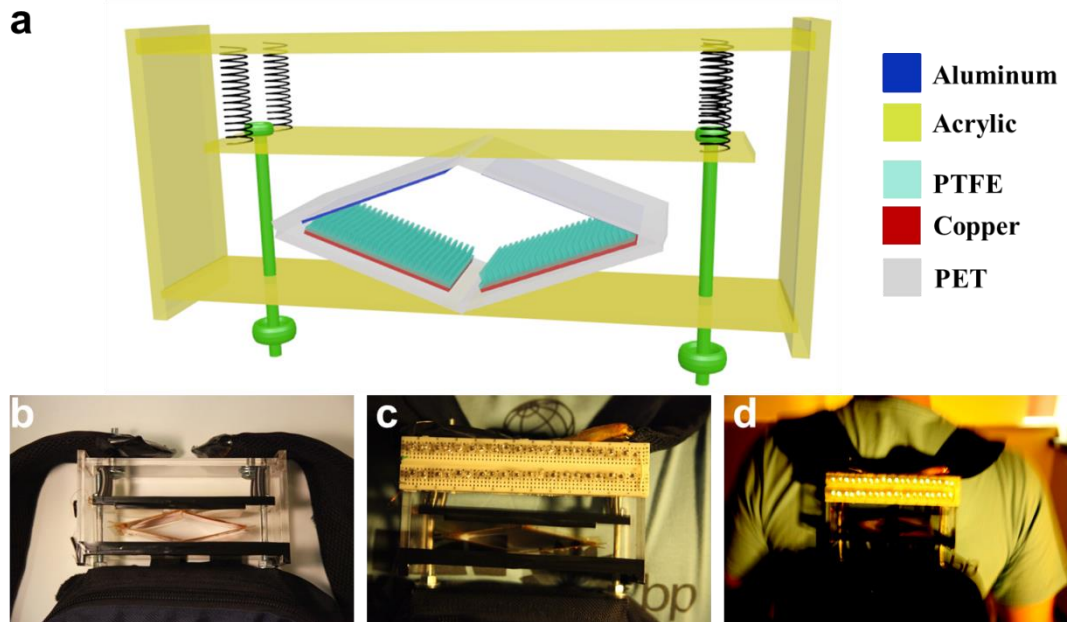
Figure 2.16 Sketch (a) and photograph (b) of a self-powered backpack which is developed based on the integrated rhombic gridding based TENG. (c) Photograph of the backpack on the shoulder with human standing still. (d) Photograph of the backpack under normal human walking. Forty Commercial LED bulbs were lighted up simultaneously.[50]

To prove the capability of the integrated rhombic gridding based TENG as a sustainable power source, a backpack was developed to harvest vibration energy from natural human walking. As indicated in Figure 2.16a, four acrylics plastics plates were built into a supporting shelf with a size of $5 \text{ cm} \times 7.5 \text{ cm} \times 20 \text{ cm}$, which bridged the backpack and its two straps using four springs and two long screw shanks. The integrated rhombic gridding based TENG with $n = 1$ is sandwiched between two acrylic sheets and the photograph of a real backpack is shown in Figure 2.16b. A total of forty commercial

LED bulbs were assembled in series on a piece of electric board (Figure 2.16c), electrically connected to the newly designed backpack. When a people walks naturally carrying the designed backpack with a total weight of 2.0 kilograms, the power harvested from the body vibration is high enough to simultaneously light up all the 40 LEDs (Figure 2.16d).

As an important figure of merit, we still investigated the vibration-to-electric energy conversion efficiency of the self-powered backpack. The conversion efficiency η_{direct} is defined as the ratio of the electric energy delivered to the vibration energy of the backpack triggered by human walking. And the electric energy delivered by the TENG can be expressed as,

$$E_{electric} = Q = \int_{t_1}^{t_2} I^2 \cdot R \cdot dt = R \cdot \int_{5.8217}^{5.8489} I^2 \cdot dt = 3.18 \ mJ \tag{2.6}$$

where Q is the Joule heating energy, I is the instantaneous current, and R is the load resistance, which is 2 MΩ in the experimental measurement. In the course of backpack vibration, its gravitational potential energy (E_G) is mainly converted into two parts, the elastic potential energy ($E_{elastic}$) and electric energy. The gravitational potential energy and elastic energy can be estimated as following,

$$E_G = mg\Delta x = 2.0 \ kg \times 9.8 \ N/kg \times 0.015 \ m = 294 \ mJ \tag{2.7}$$

$$E_{elastic} = \frac{1}{2} \cdot k \cdot \Delta x^2 \cdot N = 264.09 \ mJ \tag{2.8}$$

where m is the total weight of the backpack, Δx is the displacement of each spring, k is the spring stiffness factor ($k = 586.86$ N/m), and N is the number of springs ($N = 4$). Since the elastic energy stored in the springs has no loss during the backpack vibration, thus the direct energy conversion efficiency can be calculated as,

$$\eta_{direct} = \frac{E_{electric}}{E_G - E_{elastic}} \times 100\% = 10.6\% \tag{2.9}$$

Such high energy conversion efficiency of the TENG enables tremendous potential

applications for powering some small electronics by harvesting the vibration energy from human motions.

In summary, we demonstrated a novel integrated rhombic gridding based TENG. This innovative structure provides $2n^2$ unit cells electrically connected in parallel, which is able to greatly enhance the current output as well as the vibration-to-electric energy conversion efficiency. Based on the TENG, a self-powered backpack was developed with a considerably high vibration-to-electric energy conversion efficiency of 10.6%. When a people walks naturally carrying the designed backpack with a total weight of 2.0 kilograms, the power harvested from the body vibration is high enough to simultaneously light up all the 40 LEDs. Our newly designed TENG provides an innovative approach to effectively enhance the device current output and thus it is capable of harvesting vibration energy from natural human walking, which can have a range of applications for extending the lifetime of a battery as well as the possibility of replace battery for building self-powered systems.

2.2 TENG for rotary energy harvesting

Searching for renewable energy sources as well as to develop renewable energy technologies are urgent for the sustainable development of human civilization. Rotation, as a type of common mechanical motion, is ubiquitous in daily life, from operating household appliances, such as washing machines and electric fan, to automobile tires running on a road. Over the past decades, it has also become an attractive target for energy harvesting as a potentially alternative power source for battery-operated electronics.[54-58]

2.2.1 Radial-arrayed in-plane TENG

Here, we firstly provide a solution by designing a two-dimensional planar-structured triboelectric generator (TENG) on the basis of contact electrification, which is capable of producing energy from rotary surfaces with unprecedented performance. Enabled by a design of two radial-arrayed fine electrodes that are complementary on the same plane, the planar-structured TENG generates periodically changing triboelectric potential that induces alternating currents between electrodes.[59] A TENG has a multi-layered structure, which consists of mainly two parts, i.e., a rotator and a stator, as sketched in Figure 2.17a.
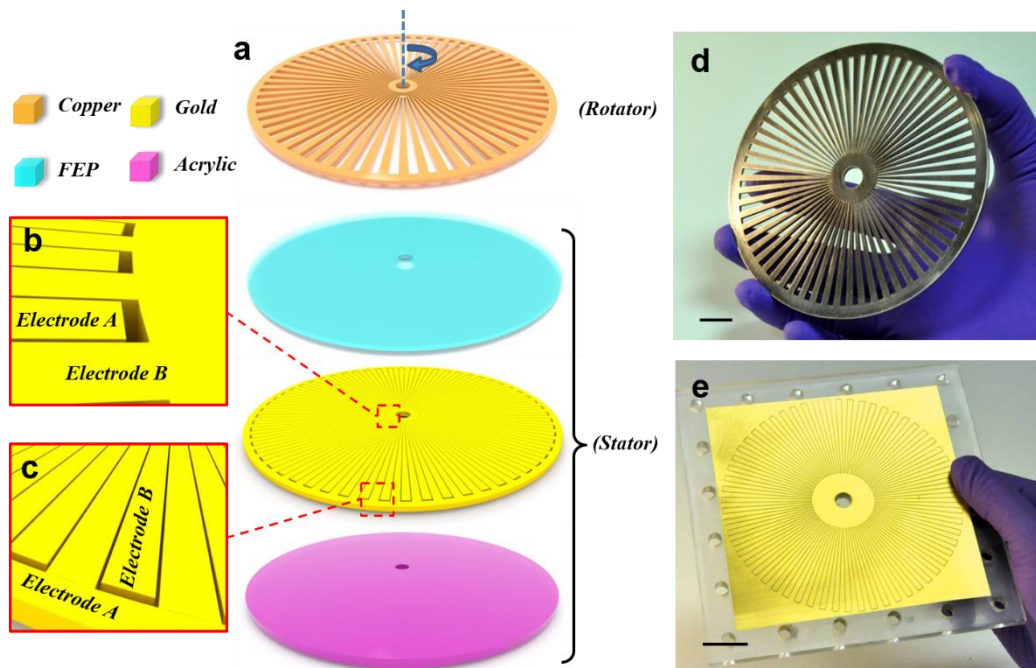
Figure 2.17 Structural design of the triboelectric generator. (a) Schematic illustrations of the triboelectric generator, which has two parts, i.e., a rotator and a stator. The zoomed-in illustrations at the inner end (b) and the outer end (c) reveal that the two electrodes have complementary patterns, which are separated by fine trenches in between. It is noted that these drawings do not scale. (d) Photograph of a rotator (scale bar: 1 cm). (e) Photograph of a stator, in which the through-holes along edges are for mounting purpose (scale bar: 2 cm).[59]

The rotator is a collection of radially-arrayed sectors separated by equal-degreed intervals in between. With each sector unit having a central angle of $3^{°}$, the rotator has a total of 60 units. For the stator, it is divided into three components. A layer of fluorinated ethylene propylene (FEP) as an electrification material, a layer of electrodes, and an underlying substrate are laminated along the vertical direction. The electrode layer is composed of two complementary-patterned electrode networks that are disconnected by fine trenches in between (Figure 2.17b and 2.17c). Having the same pattern as that of the rotator, each network is formed by a radial array of sectors that are mutually connected at one end. The electrode layer is fully imbedded and stationary. This rational design not only leads to structural simplicity but also accounts for excellent robustness, making the TENG practically reliable and durable. As exhibited in Figure 2.17d and e, both the rotator and the stator have two-dimensional planar structures, respectively, resulting in a small volume of the TENG.

The operation of the TENG relies on relative rotation between the rotator and the stator, in which a unique coupling between triboelectrification and electrostatic induction gives rise to alternating flows of electrons between electrodes. The electricity-generating process is elaborated through a basic unit in Figure 2.18. We define the initial state (Figure 2.18a) and the final state (Figure 2.18c) as the states when the rotator is aligned with electrode A and electrode B, respectively. The intermediate state (Figure 2.18b) represents the transitional process in which the rotator spins from the initial position to the final position. Since the rotator and the stator are in direct contact, triboelectrification creates charge transfer on contacting surfaces, with negative charges generated on the FEP and positive ones on the metal, as illustrated in the cross-sectional view defined by an arbitrary

intersection in Figure 2.18. Due to the law of charge conservation, the density of positive charges on the rotator is twice as much as that of negative ones on the stator because of unequal contact surface area of the two objects.
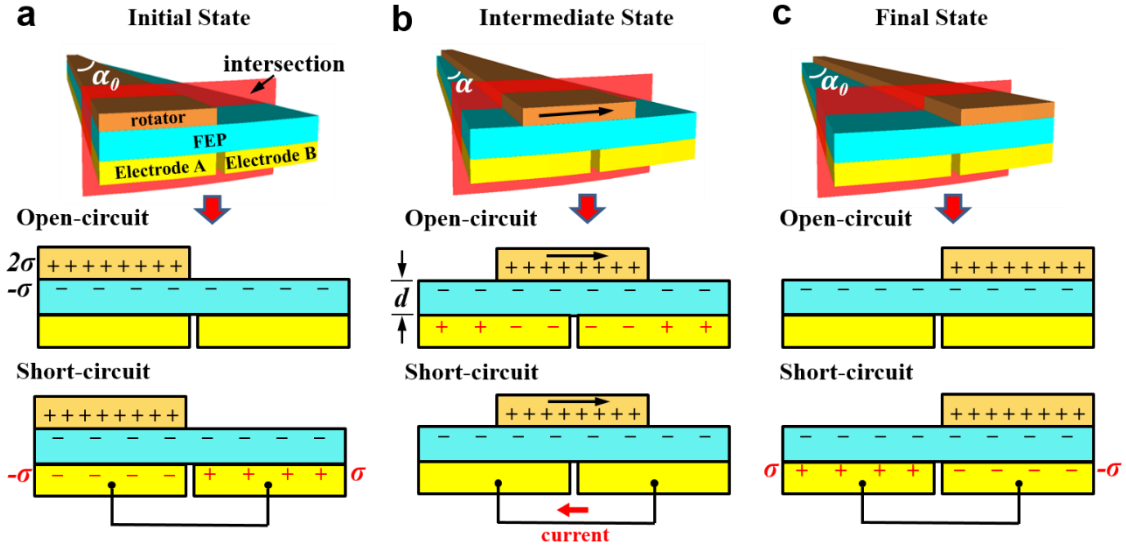
Figure 2.18. Schematics of operating principle of the triboelectric generator. (a) Initial state in which the rotator is in alignment with electrode A. The three sections from top to bottom illustrate the three-dimensional schematic, charge distribution in open-circuit condition, and charge distribution in short-circuit condition, respectively. (b)Intermediate state in which the rotator is spinning away from the initial position at an angle of α. (c) Final state in which the rotator is in alignment with electrode B. The rotator has rotated α_0 away from the initial position.[59]

In open-circuit condition, electrons cannot transfer between electrodes. The open-circuit voltage is then defined as the electric potential difference between the two electrodes, i.e. $V_{oc} = U_A - U_B$. The initial state corresponds to the maximum potential on electrode A and the minimum potential on electrode B, which results in the maximum V_{oc}. Such a voltage then diminishes as the rotator starts to spin. Once the rotator passes the middle position, V_{oc} with the opposite polarity starts to build up until the rotator reaches the final state. Further rotation beyond the final state induces the V_{oc} to change in a reversed way because of the periodic structure. Based on the assumption that the thickness of the

dielectric layer is far smaller than the width dimension in Figure 2.18, an analytical model can be established, in which any overlapped region between the rotator and the electrodes can be treated as a parallel-plate capacitor without consideration of edge effect.[60] Then the V_{oc} can be analytically expressed by the following equations using Gauss Theorem.

Initial state: $V_{oc}(0) = \frac{2d \cdot \sigma}{\varepsilon_0 \varepsilon_r}$ (2.10)

Intermediate state: $V_{oc}(\alpha) = \frac{d \cdot \sigma}{\varepsilon_0 \varepsilon_r} \cdot \left(\frac{\alpha_0 - \alpha}{\alpha} - \frac{\alpha}{\alpha_0 - \alpha} \right)$ (α approaches neither 0 nor α_0) (2.11)

Final state: $V_{oc}(\alpha_0) = -\frac{2d \cdot \sigma}{\varepsilon_0 \varepsilon_r}$ (2.12)

where d is the thickness of the FEP layer, σ is the triboelectric charge density on top of the FEP layer, ε_0 is the dielectric constant of vaccum, ε_r is the relative dielectric constant of FEP, α is the angle at which the rotator rotates away from the initial state, and α_0 is the central angle of a single rotator unit.

The equation (2.11) can only be used to illustrate the changing trend of the V_{oc}. The theoretical peak-to-peak value of the V_{oc} needs to be calculated by subtracting equation (2.12) from equation (2.10):

$V_{p-p} = \frac{4d \cdot \sigma}{\varepsilon_0 \varepsilon_r}$ (2.13)

By substituting the known parameters into equation (2.13) (d = 25 μm, σ = ~200 μCm^{-2}, ε_r = 2.1), [33] the V_{oc} (peak-to-peak) is theoretically estimated to be ~1000 V.

If the two electrodes are connected as shown by the bottom row in Figure 2.18, free charges can redistribute between electrodes due to electrostatic induction. At the initial state, induced charges accumulate on electrode A and electrode B with charge density of - σ and σ, respectively. As the rotation starts, free electrons keep flowing from electrode A to electrode B until the rotator reaches the final state where the charge density on both

43

electrodes is reversed in polarity compared to the initial state. As a result, the amount of charges in this transport process can be expressed by the following equation

$$Q = \frac{\alpha_0}{180} \cdot \sigma \cdot \pi(r_2^2 - r_1^2) \tag{2.14}$$

where r_2 and r_1 are the outer radius and inner radius of the TENG, respectively. Again, further rotation beyond the final state results in a current in the opposite direction. Therefore, alternating current is generated as a result of the periodically changing electric field, which has a frequency calculated as

$$f = \frac{180v}{\alpha_0} \tag{2.15}$$

where v is the roation rate (r/sec).
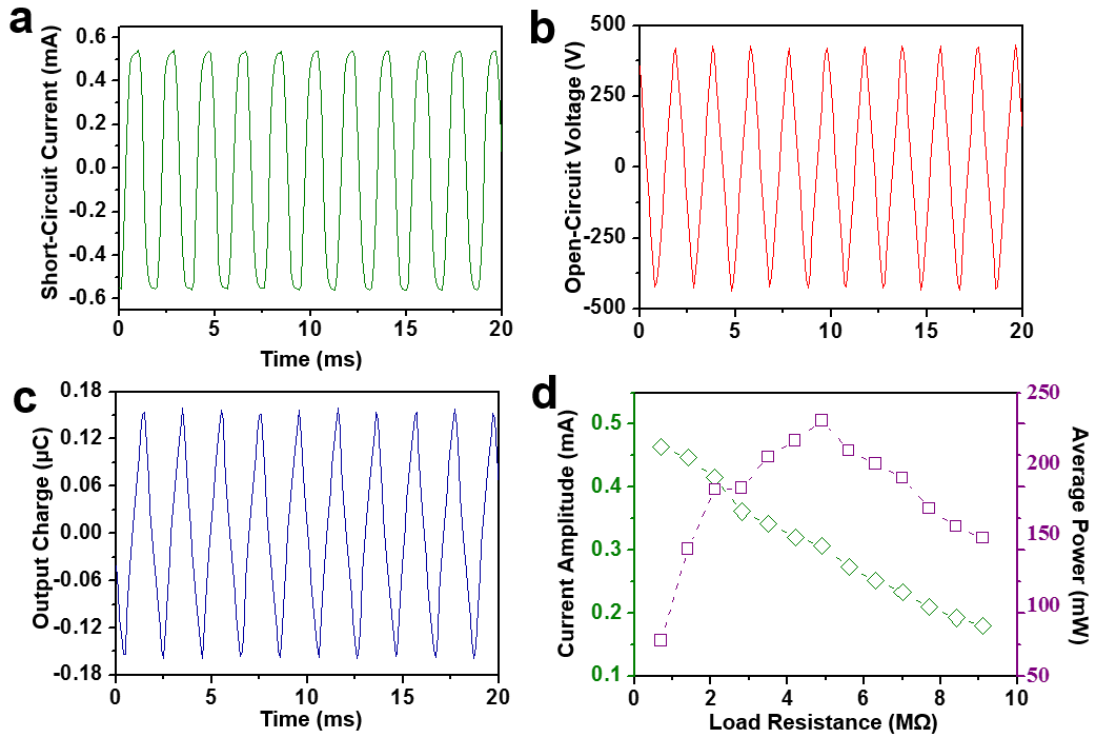
Figure 2.19 Results of electric measurements. (a) Open-circuit voltage (V_{oc}) at a rotation rate of 500 rmin^{-1}. (b) Short-circuit current (I_{sc}) at a rotation rate of 500 rmin^{-1}. (c) Output charge at a rotation rate of 500 rmin^{-1}. (d) Load matching test at a rotation rate of 500 rmin^{-1}. Maximum average output power is obtained at the matched load of 4.9 MΩ.[59]

To control the rotation rate for quantitative measurement, a programmable rotary motor was connected to the rotator that was in co-axial alignment with the stator. At a rotating rate of 500 rmin^{-1}, short-circuit current (I_{sc}) has a continuous AC output at an average amplitude of 0.5 mA (Figure 2.19a). The constant frequency of 500 Hz is consistent with the result calculated from equation (2.15). For open-circuit voltage (V_{oc}), it oscillates at the same frequency as that of I_{sc} with a peak-to-peak value of 870 V (Figure 2.19b), which corresponds well to the theoretical value obtained from equation (2.13) though the slight deviation is likely attributed to the fact that the actual contact area is less than the apparent device area because of surface roughness. In short-circuit condition, the amount of electrons in a single electron-transport process reaches 0.32 μC (Figure 2.19c), which corresponds to an effective DC current ($I_{dc}=\Delta Q/\Delta t$) of 0.32 mA. It is noticed that the duration of a current peak is determined by the ratio between the central angle of a sector and the rotation rate (Figure 2.19A). Once an external load is applied, the amplitude of the output current drops as the load resistance increases, as shown in Figure 2.19D. The average output power is equivalent to the Joule heating of the load resistor, which can be calculated as $I_{effective}^2 R$, where $I_{effective}$ is the effective current defined as the root mean square value of the current amplitude, and R is the load resistance. At the matched load of 4.9 MΩ, the average output power reaches 0.23 W at a rotation rate of 500 rmin^{-1} (Figure 2.19d).

Rotation rate is a major factor that determines electric output of the TENG. A linear relationship can be derived from Figure 2.20a between the amplitude of I_{sc} and the rotation rate since higher rate linearly shortens the duration of a current peak and thus boosts the current amplitude. In comparison, the amplitude of V_{oc} remains stable regardless of the

rotation rate (Figure 2.20a) because it is only dependent on the position of the rotator, as indicated in equation (2.11). It is found that the matched load is also a variable value, exhibiting a reversely proportional relationship with the rotation rate, as diagramed in Figure 2.20b. Consequently, linearly rising output power can be obtained at higher rotation rate (Figure 2.20b).
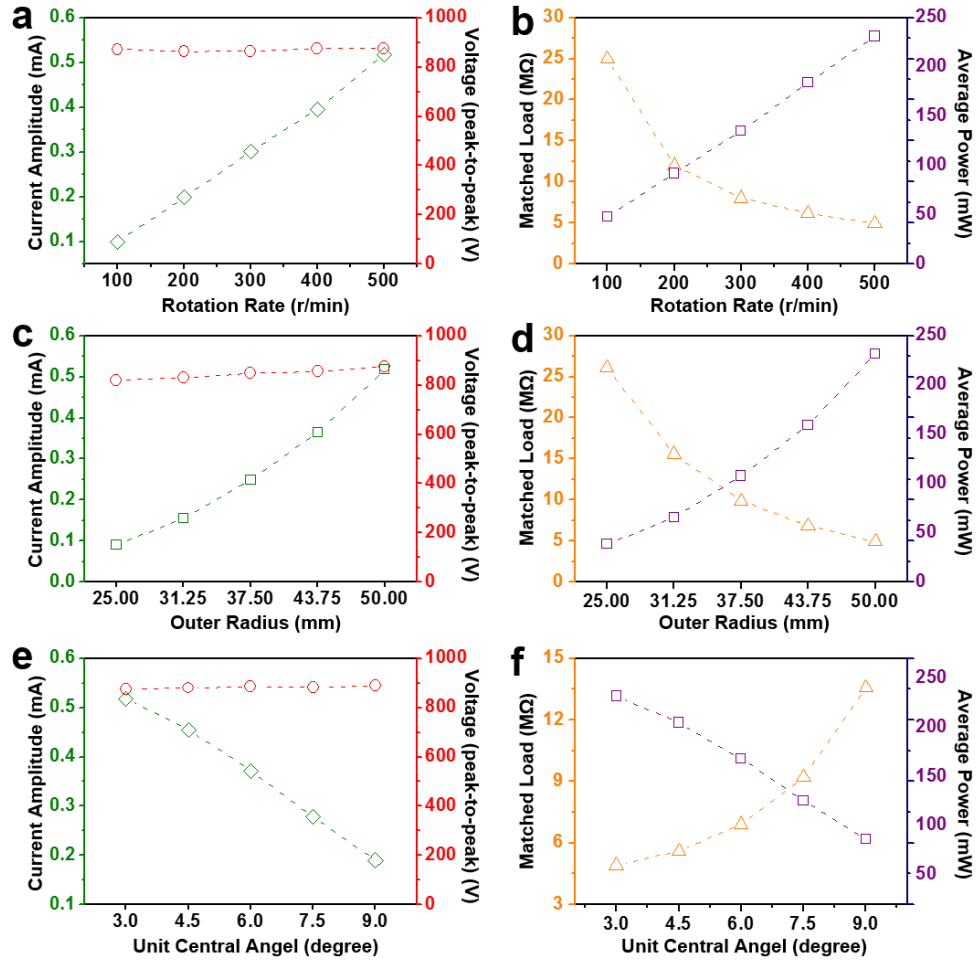
Figure 2.20 Factors that influence the electric output of the triboelectric generator. (a) Amplitude of I_{sc} and peak-to-peak value of V_{oc} with increasing rotation rate. (b) Matched load resistance and average output power with increasing rotation rate. (c) Amplitude of I_{sc} and peak-to-peak value of V_{oc} with increasing outer radius of the triboelectric generator (500 rmin[-1]). (d) Matched load resistance and average output power with increasing outer radius of the triboelectric generator (500 rmin[-1]). (e) Amplitude of I_{sc} and peak-to-peak value of V_{oc} with increasing central angle of a unit sector (500 rmin[-1]). (f) Matched load resistance and average output power with increasing central angle of a unit sector (500 rmin[-1]).[59]

Given the linear behavior of the TENG, it delivers an optimum average output power of ~1.5 W at the matched load of ~0.8 MΩ when operating at a rotation rate of 3000 rmin^{-1}, which corresponds to an average output power density of 19 mWcm^{-2}. For the first time, the output power from triboelectrification-based generators boosts to a level where it is sufficiently powerful to drive daily used electronics, immediately resolving the most critical concern for the concept of power generation *via* triboelectrification.

Design parameters, especially the size and the unit central angle, can largely influence the output power of TENG. Figure 2.20c shows an approximately quadratic dependence of the I_{sc} and independence of the V_{oc} on the radius of the TENG, which are consistent with the results in equations (2.13) and (2.14), respectively. With the matched load decreasing with the radius, the average output power exhibits a roughly quadratic relationship with the radius (Figure 2.20d). In other words, the output power linearly scales with the area of the TENG since the triboelectrification is a surface charging effect that is area-dependent. Compared to the device size, the unit central angle reversely affects the output power. As revealed in Figure 2.20e, the I_{sc} linearly drops as the central angle increases, while the V_{oc} still remains stable. Again, the measured results fit well with the theoretical model. Consequently, the average output power decreases in almost a linear way if devices with larger central angle are used. Therefore, fine feature size of the unit sector plays a key role in achieving high output power.

To demonstrate the capability of the TENG as a power source, it was directly connected to regular light bulbs without using a storage or power regulation unit. The rotation rate was set at 1000 rmin^{-1}. A total of 20 spot lights were simultaneously lighted up (Figure 2.21a), providing sufficient illumination even for reading printed text in

complete darkness (Figure 2.21b). Moreover, other types of light bulbs that could be driven

by the TENG included a white globe light (Figure 2.21c) and 10 multi-color decoration

candelabra lights (Figure 2.21d). It is noticed that the TENG has high voltage but relatively

low current, resulting in large output impedance and thus affecting its applicability as a

power source.
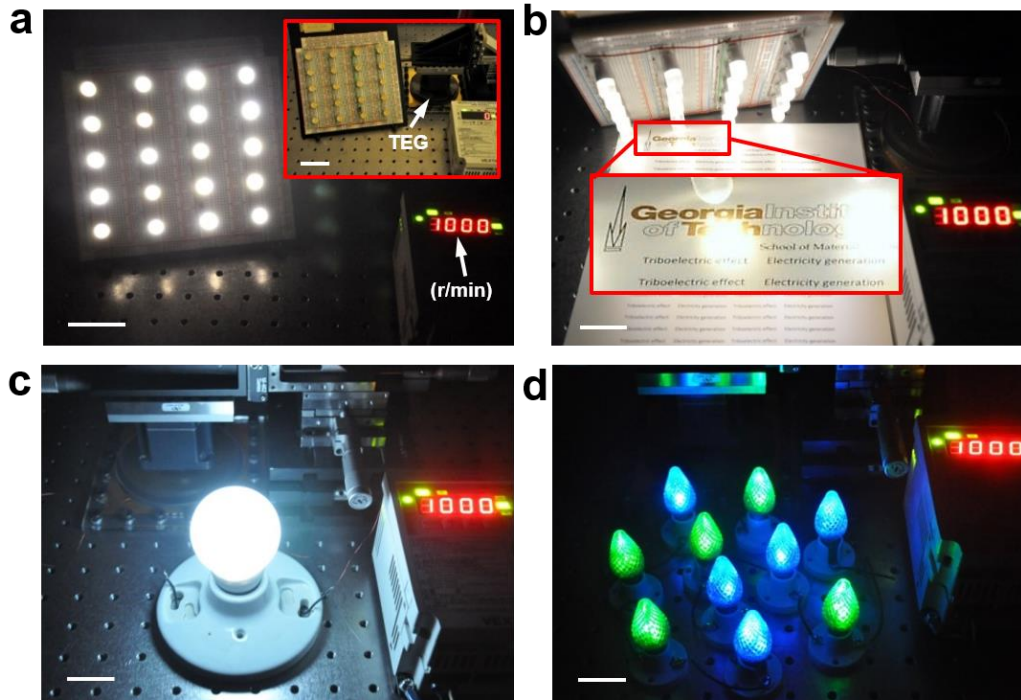
Figure 2.21 Demonstrations of the triboelectric generator as a practical power source. (a) Photograph of 20 spot lights that are directly powered by the triboelectric generator in complete darkness (rotation rate: 1000 rmin[-1]; scale bar: 5 cm). Inset: demonstration setup (scale bar: 5 cm). (b) Photograph of printed text on a paper illuminated by the 20 spot lights in complete darkness with the triboelectric generator as a direct power source (rotation rate: 1000 rmin[-1]; scale bar: 3 cm). The font size is 12 points. (c) Photograph of a G16 globe light that is directly powered by the triboelectric generator in complete darkness (rotation rate: 1000 rmin[-1]; scale bar: 3 cm). (d) Photograph of 10 multi-color decoration candelabra lights that are directly powered by the triboelectric generator in complete darkness (rotation rate: 1000 rmin[-1]; scale bar: 3 cm).[59]

Besides, fluctuation in output power and the AC output current are also concerns

in practical applications. These issues can be fully addressed by integrating the TENG with

a power management circuit to form a complete power-supplying system. Consisting of a transformer, a rectifier, a voltage regulator, and capacitors, the power management circuit as diagramed in Figure 2.22a can deliver a DC output at a constant voltage of 5 V in less than 0.5 sec after the TENG starts to operate (Figure 2.22b). The transformer shown in Figure 2.22a is able to tremendously boost the output current at the expense of the output voltage, which substantially reduces the output impedance of the TENG.
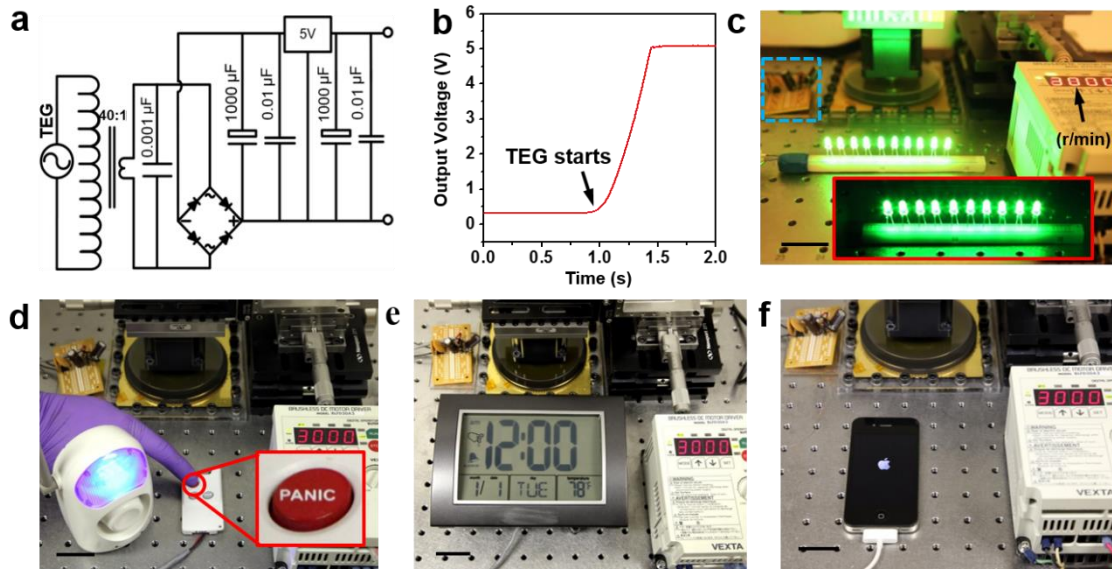
Figure 2.22 Demonstrations of the integrated power-supplying system for driving and charging electronics. (a) Circuit diagram of the complete power-supplying system that consists of a triboelectric generator and a power management circuit. (b) Output voltage of the system reaches a constant value of 5 V in less than 0.5 sec as the triboelectric generator starts to rotate at 3000 rmin^{-1}. (c) Photograph of 10 LEDs (0.75 mW ea.) in parallel that are powered to full brightness by the power-supplying system with ambient background lighting (rotation rate: 3000 rmin^{-1}; scale bar: 3 cm). The dashed blue box indicates the power management circuit. Inset: Photograph of the lighted LEDs in complete darkness. (d) Photograph of an alarm triggered by a wireless emitter that relies on the power-supplying system (scale bar: 3 cm). Inset: Photograph of the "panic" button that triggers the alarm. (e) Photograph of a multi-function digital clock driven by the power-supplying system (scale bar: 3 cm). (f) Photograph of a cellphone that is being charged by the power-supplying system (scale bar: 3 cm). As soon as the output voltage of the system reaches 5 V, the cellphone turns on automatically.[59]

The power-supplying system is suited to a variety of purposes. On one hand, it could provide a continuous uniform DC power to drive various commercial electronics. As demonstrated in Figure 2.22c, 10 LED bulbs (0.75 mW ea.) connected parallel were continuously powered with full brightness. Moreover, once the output voltage reaches 5 V, the power-supplying system could sustain wireless transitions for 5 times (Figure 2.22d) as well as continuous operation of a multi-function digital clock for 60 seconds (Figure 2.22e). On the other hand, the system is also able to serve as a charging source for batteries. Since 5 V is the standard charging voltage for most of the commercial portable electronics, a cellphone automatically turned on once the voltage output shot to 5 V due to the operation of the TENG, as visualized in Figure 2.22f.

In addition to being driven by an electric motor for quantitative measurement, the TENG was further tested in normal environment where a series of ambient mechanical energy was harvested. Firstly, energy harvesting from light air flow (wind) was demonstrated (Figure 2.23 a). Artificial breeze was generated at a speed of 6 m s^{-1} by an air mover. The wind perpendicularly blew on a miniaturized three-vane wind turbine (inset in Figure 2.23a). Driven by the turbine through a transmission shaft, the rotator of the TENG spun smoothly, directly providing a power source for lighting up an array of spot lights. Such a wind speed falls into class 4 defined by Beaufort scale and is much lower than the wind speed for normal operation of a large wind farm (~10 ms^{-1}), indicating the effectiveness of the TENG in addressing mild agitation from air flow. Secondly, water flow was successfully demonstrated as a target mechanical source (Figure 2.23b). The TENG was connected to the central shaft of a miniaturized water turbine (bottom inset in Figure 2.23b). Normal tap water at a flow rate of 5.5 Lmin^{-1} was directed into the turbine inlet

through a plastic pipe (top inset in Figure 2.23b), which served as a sufficient driving force for the TENG. Consequently, output power for the spot lights was continuously produced. Last but not least, the TENG could also effectively operate if the input mechanical energy originated from gentle body movement. As illustrated in Figure 2.23c, the compact-sized TENG in a hand had pieces of inertia mass fixed on the rotator. As the hand swung back and forth in small amplitude, asymmetric inertia resulting from the extra mass induced relative rotation between the hand-held stator and the free-standing rotator. The spot lights again served as an explicit indicator of the produced output power from the TENG.
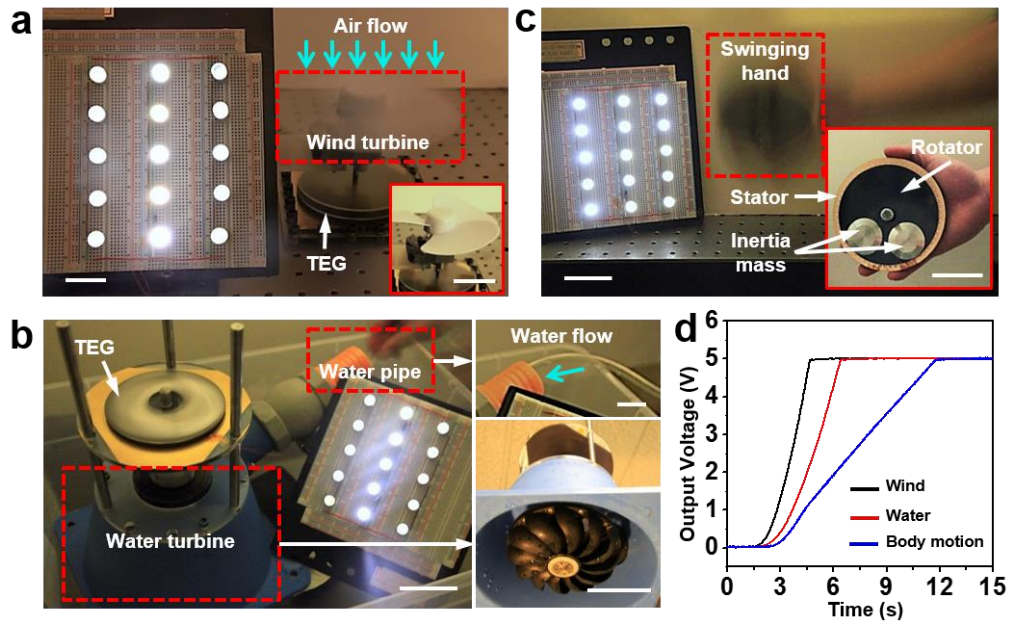
Figure 2.23 Demonstrations of the triboelectric generator for harvesting ambient energy. (a) Harvesting energy from light wind at a flow speed of 6 ms^{-1} by the triboelectric generator for powering an array of spot lights (scale bar: 3 cm). Inset: a wind turbine that transmits torque to the triboelectric generator (scale bar: 5 cm). (b) Harvesting energy from water flow at a flow rate of 5.5 Lmin^{-1} by the triboelectric generator for powering an array of spot lights (scale bar: 5 cm). Insets: tap water is directed into a water turbine through a water pipe (top; scale bar: 2 cm); upward view of the water turbine (bottom; scale bar: 7 cm). (c) Harvesting energy from body motion by the triboelectric generator that is being gentle swung with a hand for powering an array of spot lights (scale bar: 5 cm). Inset: the hand-held triboelectric generator with two pieces of inertia mass attached to the rotator (scale bar: 5 cm). (d) Output voltage of the power-supplying system when the triboelectric generator is driven by the above three types of ambient mechanical energy.[59]

Furthermore, with input mechanical energy fed from the above ambient motions, the power management circuit was still functional and showed a linearly increasing output voltage as it was being charged up by the TENG (Figure 2.23d). Therefore, these demonstrations firmly prove that the TENG can fully operate in normal environment by utilizing ambient mechanical energy from a variety of sources, indicating its widespread applications in harvesting human motions and even natural energy.

The efficiency of the TENG is defined as the ratio of the input mechanical power from the motor to the electric power that is delivered to the load. When driving the TENG at a rotation rate of 3000 $rmin^{-1}$, the motor exhibits a load factor of approximately 20 %, corresponding to an actual torque of 0.02 Nm delivered to the TENG. Then we can derive the power input from the motor to be 6.28 W by using the above values. Given the electric output power of 1.5 W at the same rotation rate, the efficiency is calculated to be ~24%. The reliability of the TENG, especially the resistance against mechanical wear, is important in evaluating its performance. Here, adhesive wear that occurs when two nominally flat solid bodies are in sliding contact applies to the TENG. Therefore, the adhesion of the deposited metal on the rotator largely determines the wear resistance. Special treatment was taken in fabricating the TENG, including adding an adhesion layer and surface plasma treatment before metal deposition.[61] As a result, the TENG shows excellent stability and durability. After continuously producing more than 10 million cycles of alternating current, the output current does not even exhibit any measurable decay or degradation, which firmly proves the reliability of the TENG as a feasible approach for practical applications.

Compared to other existing technologies for power generation, the TENG is distinct in basic mechanism from fundamental point of view. The usual electric generator mostly

relies on electromagnetic induction, an effect from the coupling between bulk magnetic materials and conductors. In comparison, our generator depends on triboelectrification, a universally applicable charging effect that is confined only at contact surfaces. Such a distinction in fundamental mechanism differentiates our generator from the traditional generator in a number of major aspects. In general, the TENG is a complementary approach in parallel to the traditional electric generator. Its uniqueness as well as real advantages is elaborated below.

From structure point of view, the usual generator has a bulky structure since the output power heavily depends on such factors as the number of coil turns, the diameter of metal coils, the coil geometry, and the size as well as weight of magnets. The shrinkage in size results in substantial deterioration in output power due to insufficient electromagnetic coupling and other parasitic effects. Therefore, the usual generator normally has relatively large size and weight for producing a decent output power. For example, our test on a commercial mini-sized generator of 8.2 cm^3 in volume and 29 g in weight showed an optimum output power of 0.13 W when rotating at 1800 rmin^{-1}. In comparison, our generator relies on triboelectrification, a surface charging effect. The simple stator-rotator structure has a two-dimensional planar configuration. In addition to using hard sheets as substrates, we can further extend the substrate materials to plastic thin-film materials that are flexible such as polyimide by using photolithography and laser patterning techniques (Figure 2.24). Having the same radius and radial periodicity as the device in Figure 2.17, the thin-film TENG gave the same level of output shown in Figure 2.18. It is only 75 μm in total thickness, 0.6 cm^3 in volume, and 1.1 g in weight, similar to the weight of a few goose feathers.
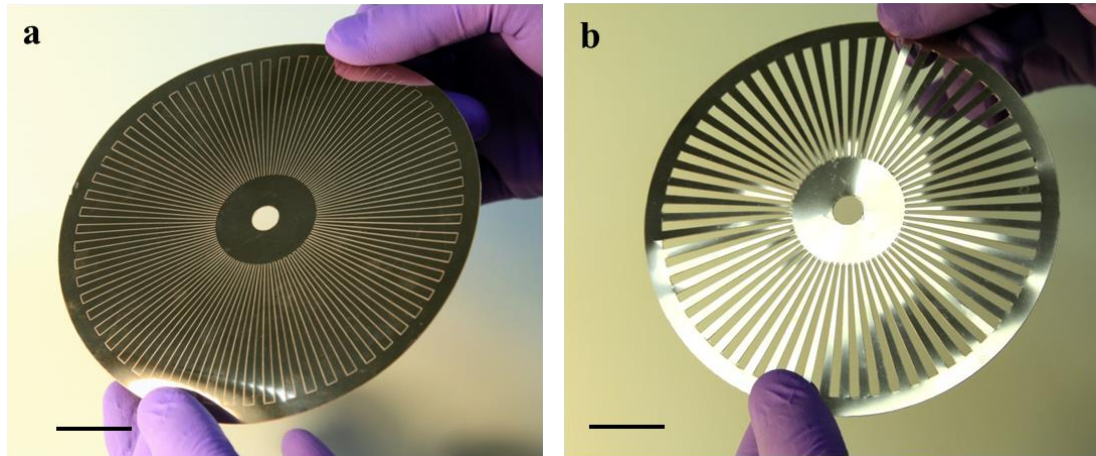
Figure 2.24. A thin-film based triboelectric generator fabricated on flexible polyamide substrate. (a) and (b) are stator and rotator (The scale bars are 2cm), respectively.[59]

From performance point of view, the TENG has substantially higher power density than the traditional generator in terms of both power-to-volume ratio and power-to-weight ratio due to much smaller volume and weight. The high power density imparts two major advantages to practical applications of the TENG. Firstly, it is superior to the conventional generator as a small-sized power source for self-powered electronics, e.g. harvesting human motions for powering or charging portable/wearable gadgets. In these applications, size and weight management become critical issues. Secondly, the significant power density makes the TENG potentially advantageous in large-scale power generation for stationary power plants, although the feasibility needs to be solidly validated with further investigations.

From cost point of view, the TENG based on surface charging effect only needs very small amount of materials. They are conventional thin-film insulating materials and metals of various kinds that are abundantly available. Besides, it has a simple structure and straightforward fabrication process. As a consequence, the TENG is extremely cost-

effective, which is an unparalleled advantage compared to any other power generation techniques. The significant low cost of the TENG is a key advantage for its potential widespread applications.

Last but not least, the unique 2D-planar generator owns distinctive applicability in a variety of circumstances. The usual generator has difficulty being made into a planar structure due to reasons such as poor properties of planar magnets, limited number of turns achievable with planar coils, and restricted amplitude of displacement. In comparison, the TENG offers a straightforward and even sole solution to addressing rotation sliding between two surfaces. For example, it can be possibly integrated into a brake system in automotive and other applications where a brake rotor and brake pads have relative contact rotation. Moreover, due to the simple rotator-stator structure, our generator provides a much easier and more convenient way to address common rotating motions. For example, with very little modification, the TENG can take advantage of rotating shafts that are commonly found in transmission systems, as clearly demonstrated in Figure 2.23. Besides, enabled by broad choices of materials, the TENG with particular properties can meet special needs. For instance, it can be fabricated from organic biocompatible materials for health care and other bio-related applications. Finally, it is the unique solution when installation space is constrained. Therefore, our generator enables unique applications in many circumstances where the usual generator cannot be implemented, although both of them utilize rotation for power generation.

In summary, we developed a new type of planar-structured electricity-generation method (TENG) that to convert rotary mechanical energy using triboelectrification effect, a universal phenomenon upon contact between two materials. Based on the stator-rotator

structure that has arrays of micro-sized radial sectors, the TENG produced significantly high output power for sufficiently powering as well as charging conventional consumer electronics. It could effectively harvest a variety of ambient energy from motions such as air flow, water flow, and even body motion. Furthermore, the combination of the TENG and a power management circuit demonstrated the immediate practicability of using TENG for everyday power needs. Given its exceptional power density, extremely low cost, and unique applicability, the TENG presented in this work is a practical approach in converting mechanical motions for self-powered electronics as well as possibly for producing electricity on a large scale.

2.2.2 Automatic mode transition enabled robust TENG

Although the TENG has been proven to be a renewable and effective route for ambient energy harvesting, its robustness remains a great challenge owning to the requirement of surface friction for a decent output, especially for the in-plane sliding mode TENG.[32, 33, 59, 62-65] Here, we present a rationally designed TENG for achieving a high output performance without compromising the device robustness through firstly converting the in-plane sliding electrification into contact-separation working mode, and secondly an automatic transition between a contact working state and a non-contact working state.[66] The magnets assisted automatic-transition triboelectric nanogenerator (AT-TENG) was developed to effectively harness various ambient rotational motions to generate electricity with greatly improved device robustness.

The device structure of the AT-TENG is schematically illustrated in Figure 2.25a, which mainly consists of two parts, a functional unit and a rotator. The functional unit has

a multilayer structure with acrylic as supporting substrates. Acrylic was selected as the structural material owing to its decent strength, light weight, good machinability and low cost.
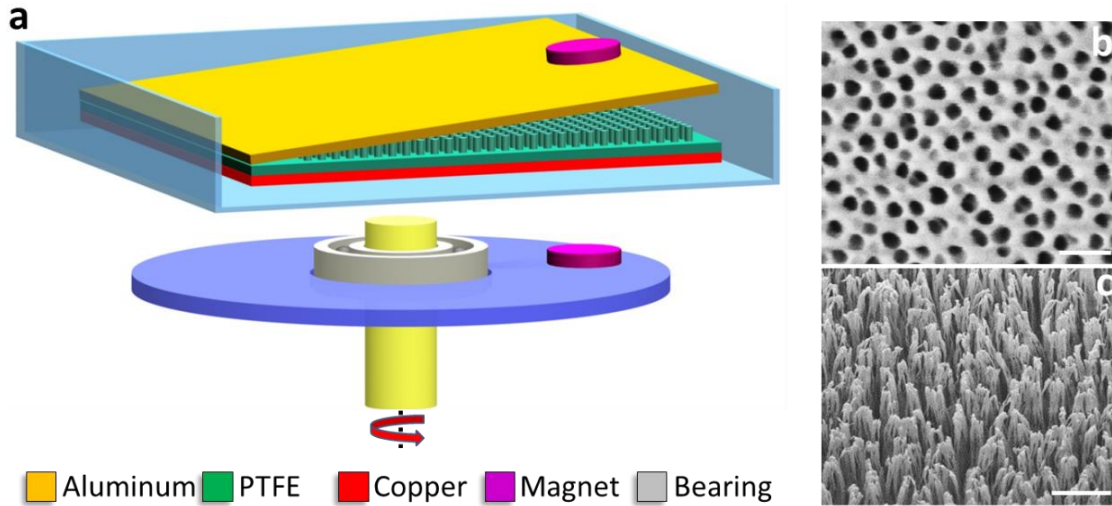
Figure 2.25 Structural design of the AT-TENG with one segment. (a) Schematic illustration of the triboelectric nanogenerator. (b) SEM image of the nanopores on aluminum electrode. The scale bar is 150 nm. (c) SEM image of the PTFE nanowires. The scale bar is 500 nm.[66]

The two triboelectric layers are laminated with a full contact at their initial states. One end of them is secured by a piece of rubber while the other end stays open. On the upper triboelectric layer, aluminum thin film with nanoporous surface plays dual roles of an electrode and a contact surface. Scanning electron microscopy (SEM) image of the nanopores on the aluminum is presented in Figure 2.25b. On the lower triboelectric layer, polytetrafluoroethylene (PTFE) film with deposited copper as back electrode was acting as another contact surface, and it was anchored onto the substrates. A top-down method through reactive ion etching was employed to create PTFE nanowires arrays on the PTFE surface.[41] An SEM image of the PTFE nanowires is displayed in Figure 2.25c. Here, a pair of magnets was respectively adhered onto the top triboelectric layer and the rotator plane

with a same pole facing each other. It is worth noting that, the functional unit of AT-TENG for electricity generation was fully enclosed, and its operation relies on the external rotator with a magnet. This novel structure design renders it capable of performing adequately in harsh environmental conditions.

The fundamental working principle of the AT-TENG is based on a two-way coupling of contact electrification and electrostatic induction.[67-72] As presented in Figure 2.26, both two-dimensional potential distribution by COMSOL (up) and schematic illustrations of charge distribution (down) were employed to elucidate the working principle of the AT-TENG, in which two working states were respectively depicted: contact working state (Figure 2.26a-c) and non-contact free-standing working state (Figure 2.26d-f).

Regarding the contact working state, the aluminum is initially aligned and in full contact with PTFE (Figure 2.26a). According to the triboelectric series, PTFE is much more triboelectrically negative than aluminum, electrons are injected from aluminum into PTFE, generating positive triboelectric charges on the aluminum and negative ones on the PTFE. When the external rotation brings the paired magnets to meet, the repulsion force will push the two triboelectric layers apart. The thus induced electric potential difference drives the electrons to flow from copper to aluminum (Figure 2.26b), screening the triboelectric charges and leaving behind the inductive charges. The flowing of electrons will be continued until the maximum separation distance was reached, and all the electrons are transferred from cooper to aluminum (Figure 2.26c). The increased separation distance between the layers leads the weakened magnetic repulsive force, thus, the restoring force of the elastic and the gravity of the top triboelectric layer will pull it downwards and back

to contact with the lower triboelectric layer. This is a full cycle of the operation for the AT-TENG in the contact working state.
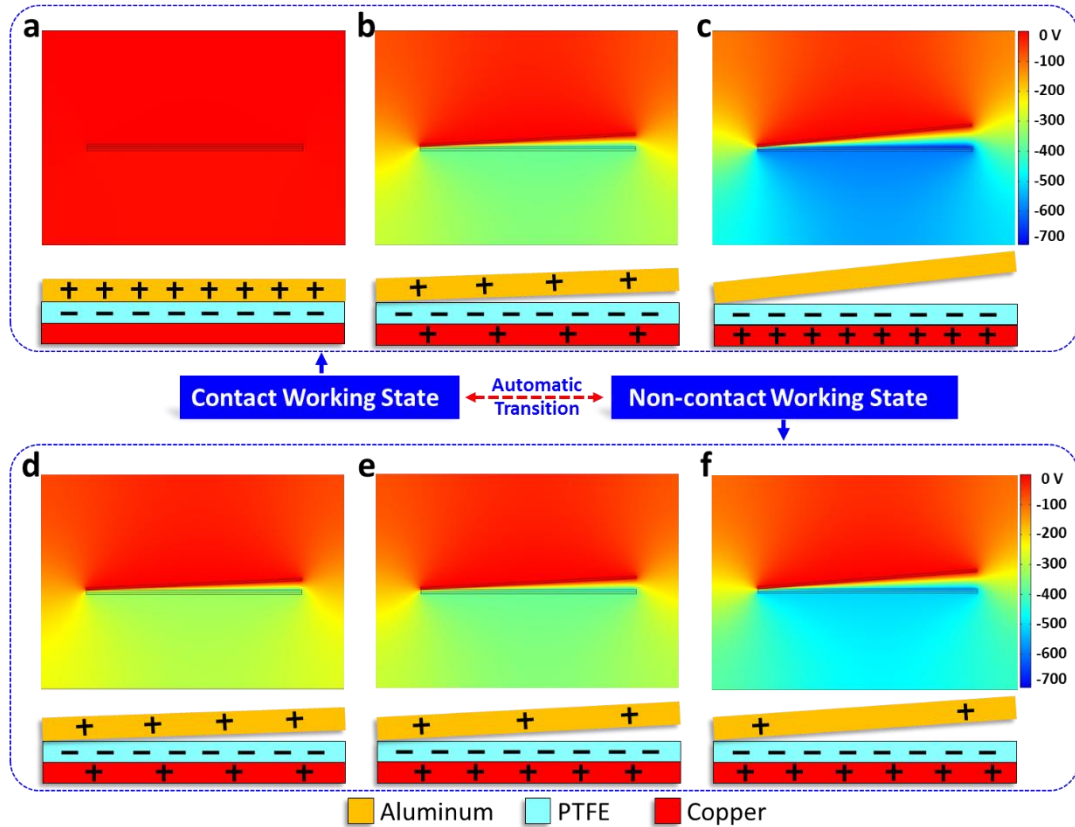
Figure 2.26 Schematics of the operating principle of the AT-TENG. Both two-dimensional potential distribution by COMSOL (up) and schematic illustrations of charge distribution (down) were employed to elucidate the working principle of the TENG. And two states were respectively elucidated: (a-c) Contact-Separation working state and (d-f) Non-contact free-standing working state. (a) Initial state in which the PTFE is negatively charged after contact with aluminum. (b) Magnetic repulsion force separates the PTFE and aluminum. Electric potential difference drives the electrons from copper to aluminum, screening the triboelectric charges and leaving behind the inductive charges. (c) With continuously increasing the separation, all the positive triboelectric charges gradually and almost entirely screened. When the magnetic repulsion force disappears, the top aluminum plate will be dragged back to contact again with the PTFE. While at a high rotation speed, another cycle of magnetic repulsion force will appear before the aluminum plate fully contact back with the PTFE. Under such a circumstance, the AT-TENG works in a Free-Standing state and the top aluminum will vibrate in a small range of separation distances with a high frequency. (d) At the minimum separation distance. (e) A transition state move upwards to the maximum separation state. (f) The top aluminum is raised up to the maximum separation distance.[66]

With further increasing the rotation speed, the AT-TENG can transit to a non-contact free-standing working mode. At a higher rotation rate, the magnetic repulsive force has a shorter exertion time, which produces a much smaller momentum to the upper triboelectric layer. Therefore, the upper triboelectric layer will be pulled downwards slightly with considering the joining effect of centrifugal force and gravitation. In the meanwhile, with considering the fast rotation speed, the upper triboelectric layer will soon be magnetically repulsive again before it falls back to contact with the bottom triboelectric layer. As a consequence, the upper triboelectric layer will vibrate around its equilibrium position at the frequency of the rotation, which will change the capacitance of the structure, resulting in an alternating current across the electrodes. As shown in Figure 2.26d, when the upper triboelectric layer falls to the lowest point at the minimum separation distance at a certain rotation rate, the electrons flowing from aluminum to copper will not fully screen the triboelectric charges in the copper electrode. When the repulsive force pushes the upper triboelectric layer to move upwards, the electrons will keep flowing from the copper to the aluminum (Figure 2.26e), until it reaches at the highest point, corresponding to a maximum separation distance between the two (Figure 2.26f).

To systematically investigate the performance of the AT-TENG as a new methodology in harvesting ambient mechanical energy, AT-TENGs with one segment and two segments were studied respectively. Figure 2.27a and 2.27b respectively show the dependence of the open-circuit voltage and short-circuit current on the rotation rate of the one-segment TENG. At a rotation rate lower than 240 rpm, the one-segment AT-TENG is in a contact-separation working state, and the open-circuit voltage is up to 530 V. The short-circuit current follows the same trend and constant around 0.26 mA.

60
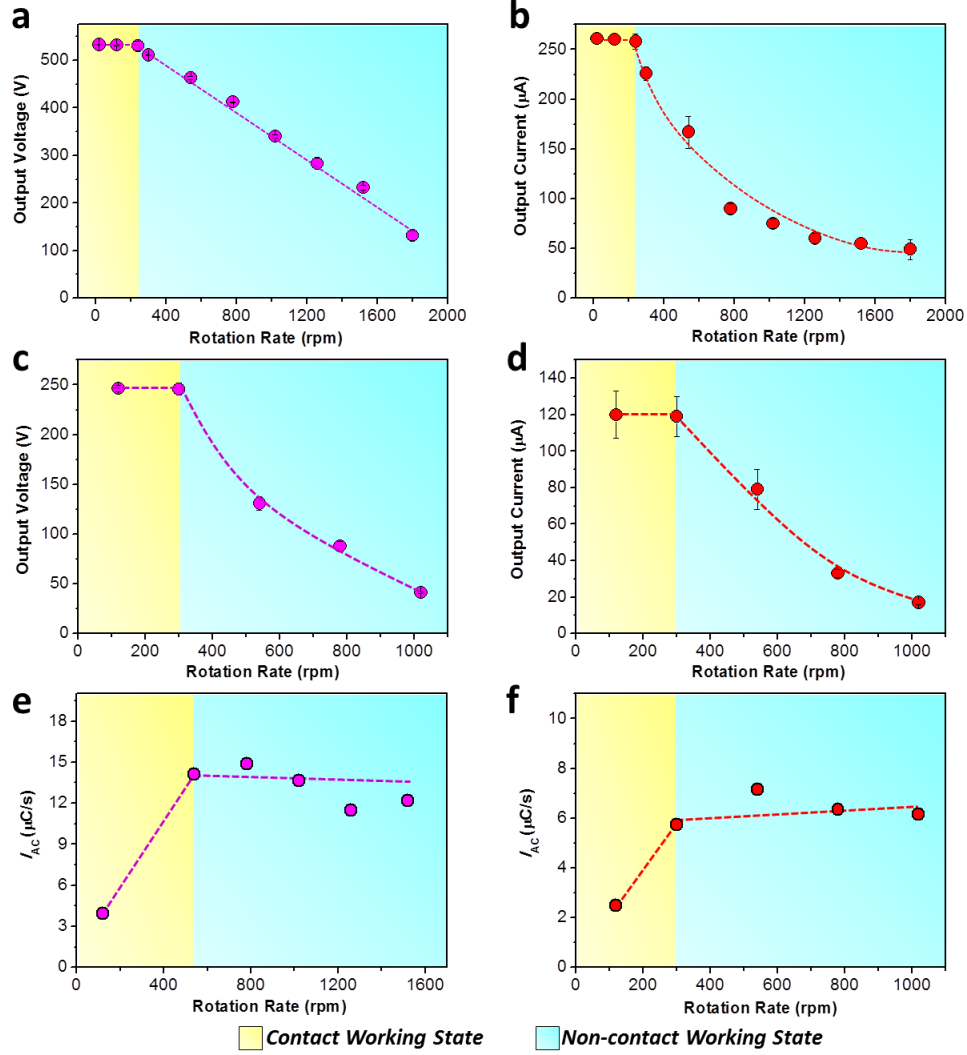
Figure 2.27 Electrical output characterization of the AT-TENGs. For a systematic investigation, two type of AT-TENGs: one-segment and two-segment were respectively studied. Dependence of the (a) open-circuit voltage and (b) short-circuit current on the rotation rate of the one-segment AT-TENG. Dependence of the (c) open-circuit voltage and (d) short-circuit current on the rotation rate of the two-segment AT-TENG. Dependence of the average charges transfer rate on the rotation rate for the (e) one segment AT-TENG and (f) two-segment AT-TENG.[66]

At this typical contact-separation working stage, the open-circuit voltage can be estimated as:

$$V_{oc} = \frac{\sigma d}{\varepsilon_o} \tag{2.16}$$

where ε_o is the vacuum permittivity and σ is the triboelectric charge density, d is the maximum separation of two triboelectric layers in a AT-TENG, which is designable and confined by the height of the device external packaging. Given a fabricated AT-TENG, d could be a fixed value, which determines the device output. At lower rotation rate, the AT-TENG works at the contact-separation mode and the upper triboelectric layer can obtain a larger momentum to move upwards. Thus, the separation distance between the two triboelectric layers is confined and equates to d at lower rotation rate, which explained a constant electric output at this stage.

With further increasing the rotation rate beyond the critical point, the AT-TENG will be automatically converted from the contact working state into a non-contact free-standing working state. For each AT-TENG, the critical rotational speed is designable and can be estimated as

$$\omega_{crs} = \sqrt{\frac{\frac{F}{M}(\Delta\theta)^2 - 4\pi g(\Delta\theta - \pi)}{8d}} \tag{2.17}$$

where F is the magnetical repulsion force, M is the total weight of the upper triboelectric layer, g is the gravitational acceleration, $\Delta\theta$ is field angle of the magnet on the rotator plane, which was determined by the magnet dimension. Based on the above analytical mode, it is safe to conclude that the critical rotational speed is highly correlated to a variety of parameters, including the weight of the upper substrate, the dimension and magnetism of the paired magnets, the height d of external package and so on.

As shown in Figure 2.27a and b, experimentally, the critical rotation rate of the as-fabricated AT-TENG with one-segment is measured to be 240 rpm. Beyond it, the AT-TENG operates in a non-contact working state in a wide range up to 1800 rpm. In this stage,

both the voltage and current amplitudes show a decreasing function of the rotation rate ω.
Here, theoretically, the open circuit voltage of the AT-TENG can be calculated as

$$V_{oc} = (\frac{\sigma}{\varepsilon_o})(\frac{\frac{F}{M}(\Delta\theta)^2 - 4\pi g(\Delta\theta - \pi)}{8\omega^2}) \tag{2.18}$$

According to equation (2.18), in the non-contact working state, the output voltage is also related to various parameters, such as the weight of the upper substrate, the dimension and magnetism of the paired magnets and so on. Particularly, it is also reversely proportional to the square of rotation rate, which is well consistent with the experimental observation.

For a systematical study of the presented methodology, the dependence of the open-circuit voltage and short-circuit current of the two-segment AT-TENG on the rotation rate were also investigated. As shown in Figure 2.27c and d, respectively, below the threshold rotation rate of 300 rpm, the two-segment AT-TENG was in a contact-separation working state. In this stage, similar to the one-segment case, the voltage and current are respectively constant at 246 V and 0.12 mA. With further increasing the rotation rate beyond 300 rpm, the AT-TENG with two-segment is working in a non-contact free-standing mode, and the peak amplitudes of the electrical output were decreasing with increase of the rotation rate, which shares a same trend of that with the one-segment AT-TENG. This is mainly attributed to the reduced separation distance between the two triboelectric layers of the AT-TENGs at higher rotation rates.

Here, it is worth noting that, for both one-segment and two-segment AT-TENGs, the reduced electric output amplitudes do not mean a reduction of the capability of the device for energy harvesting at higher rotation rates. Firstly, the peak density of the device electric output is dramatically increased with the increasing of the rotation rates. This leads

to an increasing amount of the transferred triboelectric charges across the electrodes. The dependence of the average charge transfer rate (I_{AC}) on the rotation rate for the two types AT-TENGs are respectively presented in Figure 2.27e and f. Here, I_{AC} is defined as the total transferred charges across the electrodes per unit operation time. As shown, at higher rotation rates beyond critical point, the devices are working at a non-contact state, they maintained a higher charge transfer rate than that in the contact working state. As a consequence, the capability of the AT-TENG for energy harvesting is actually enhanced at higher rotation rates. Furthermore, the dependence of the accumulative transferred charges (C_{AT}) on the rotation rate for the two types of AT-TENG were also measured and respectively plotted in Figure 2.28a and b. Likewise, much higher C_{AT} values were maintained for the AT-TENG in the non-contact working state, and especially at the rotation rates around the critical point or in the short range above it.

Resistors were utilized as external load to further investigate the output power of the AT-TENG around the critical rotation rate. As displayed in Figure 2.28c, the instantaneous peak power is maximized at a load resistance of 1 MΩ, corresponding to a peak power density of 1 W/m^2. The superior robustness is also an advantageous feature of the reported AT-TENG. As shown in Figure 2.28e, there is no observable output degradation after 300,000 cycles' continuous operations when the AT-TENG is in the non-contact free-standing working state, and a minor fluctuation of less than 6% was observed for the contact-separation working mode. However, an obvious degradation up to 26% of the electric output for the in-plane sliding mode was observed. As a consequence, on one hand, by converting the in-plane sliding electrification into the contact-separation mode, the device robustness of the AT-TENG was greatly improved. On the other hand, as long

as the AT-TENG works at the critical point or in the short-rang above critical point with an occasional transition into contact state for charge replenishment, the AT-TENGs could pave itself a way of keeping both high electric output and superior device robustness.
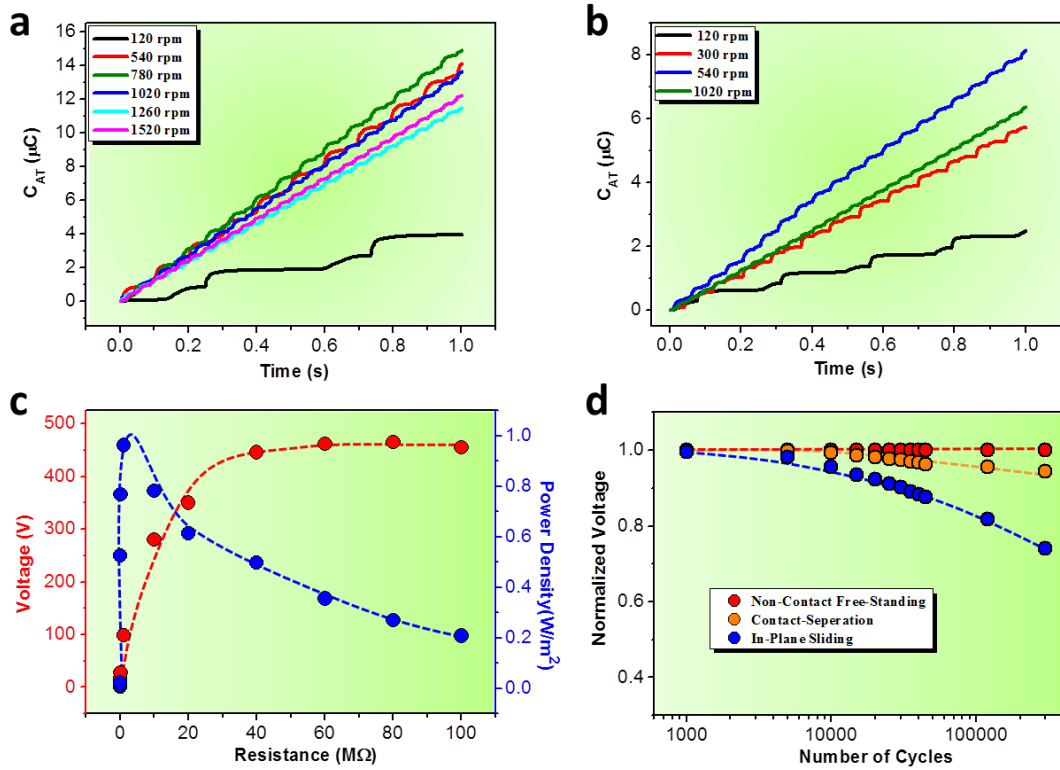
Figure 2.28 Accumulative transferred charges and the delivered power of the AT-TENGs. Dependence of the accumulative transferred charges across the electrodes on the rotation rate for the (a) one segment AT-TENG and (b) two-segment AT-TENG. (c) Dependence of the peak power output on the external load resistances for the one-segment TENG at a rotation rate around 240 rpm, indicating maximum power output at R =1MΩ. (d) Working state depended device robustness investigation.[66]

To prove it as a robust and sustainable energy technology, the AT-TENG was demonstrated to efficiently harness various ambient mechanical motions for long-time continuous operations. Here, the first step was taken to develop the AT-TENG into a wind energy harvester by equipping it with a wind cup.
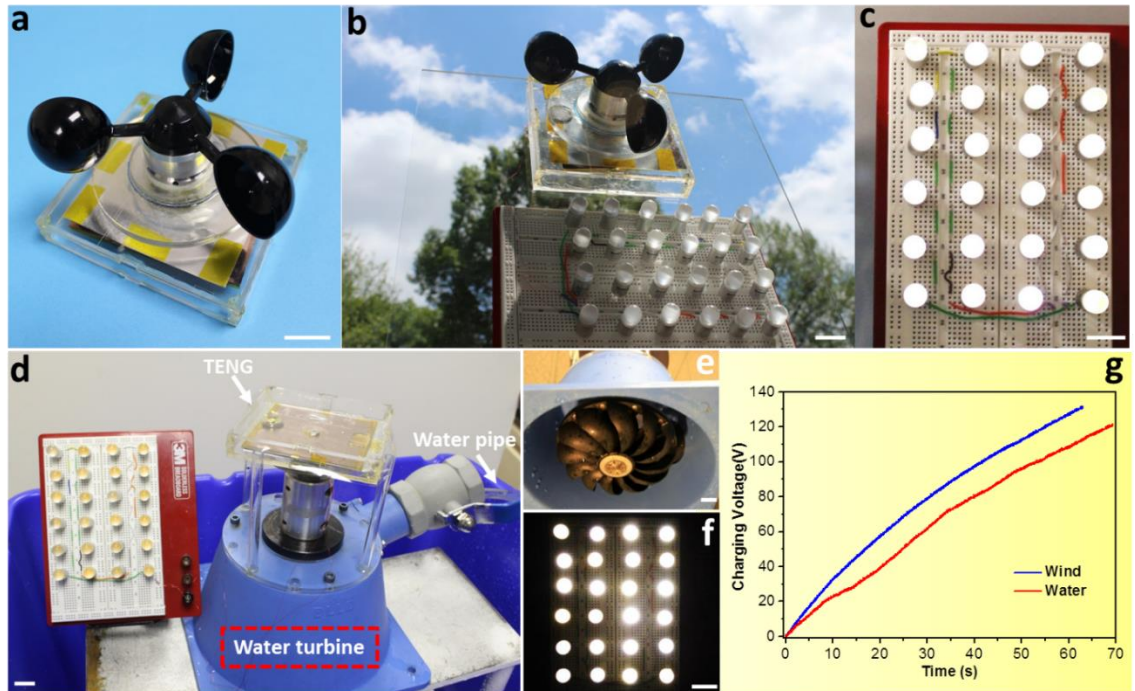
Figure 2.29 Demonstration of the AT-TENG for harvesting energy from ambient wind and water flow. (a) Photograph of the as-developed AT-TENG-based wind energy harvester. (b) A device in the ambient environment. (c) Harvesting energy from light wind at a flow speed of 6.5 m/s by the AT-TENG and an array of 24 spot lights were lighted up simultaneously. (d) Harvesting energy from the water flow at a flow rate of 5.5 L/min. (e) Photograph of the upward view of the water turbine. (f) An array of 24 spot lights were lighted up simultaneously. (g) Charging a commercial capacitor when the AT-TENG is driven by the above light wind and water flow. All the scale bars are 2 cm.[66]

Figure 2.29a is a photograph of the as-fabricated device, and Figure 2.29b shows

the device in the ambient environment. Drove by the light wind at a flow speed of 6.5 m/s,

the harvested energy by the AT-TENG is capable of simultaneously lighting up an array of

24 spot lights (0.6 W each) connected in series(Figure 2.29c). Furthermore, the AT-TENG

was also demonstrated to harvest energy from the environmental water flow. Figure 2.29d

and e are respectively the photographs showing the setup for water flow energy harvesting

and the upward view of the water turbine employed. At a flow rate of 5.5 L/min *via* a water

pipe, the harvested power can also be utilized to simultaneously light up an array of 24 spot

lights connected in series (Figure 2.29f). In the meanwhile, as shown in Figure 2.29g, the harvested energy from the wind and water flow by the AT-TENG was also capable of charging a capacitor up to more than 120 V in 60 seconds.
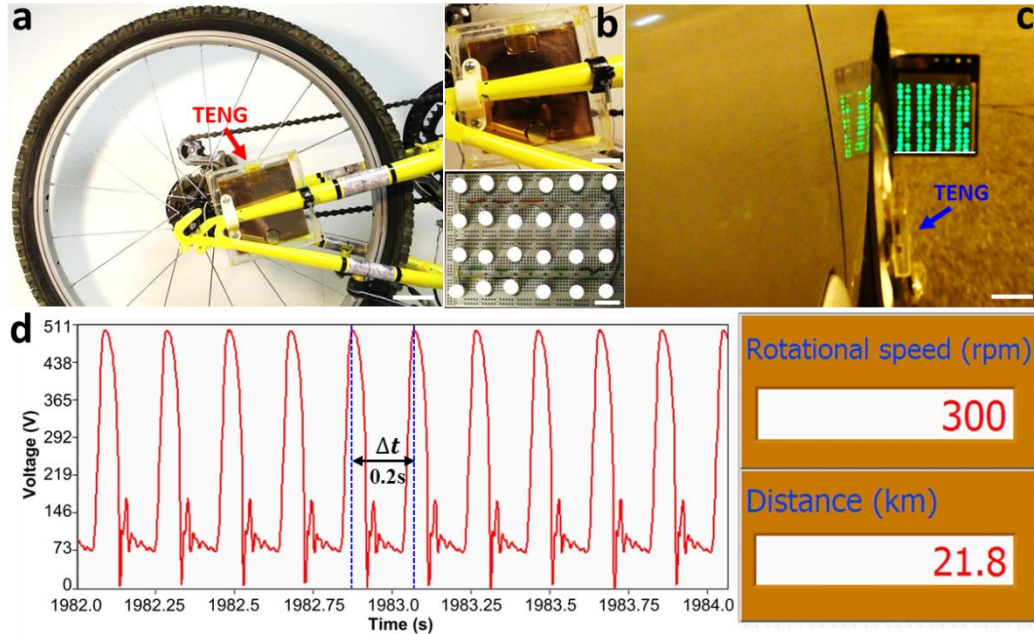
Figure 2.30 Demonstration of the AT-TENG for recycling mechanical energy from bicycling and moving car and acting as a self-powered active speedometer. (a) Photograph of the AT-TENG for harvesting energy from bicycling. The scale bar is 5 cm. (b) Up is an enlarged view of the installation of the AT-TENG onto a commercial bike. Down is a photograph showing that 24 spot lights are lighted up simultaneously when bicycling naturally. The scale bars are 2 cm. (c) Harvesting energy from a moving car at normal speed and about 104 LEDs were lighted up simultaneously. The scale bar is 10 cm. (d) A photograph showing the AT-TENG acting as a self-powered active sensor for both real-time moving speed detection and travelled distance measurement.[66]

The AT-TENG was also further demonstrated to recycle mechanical energy from bicycling and moving car. As shown in Figure 2.30a, an AT-TENG was equipped onto a commercial bicycle. An enlarged view of the installation is presented in Figure 2.30b. The harvested power is also capable of lighting up 24 spot lights simultaneously when a human rides a bike naturally. And still, the AT-TENG can also harvest energy from a moving car.

As shown in Figure 2.30c, about 104 LEDs were lighted up simultaneously when a car is running at normal speed.

In addition, owing to the unique output characteristic, the AT-TENG was also demonstrated to be a self-powered speedometer with ultra-high measurement accuracy, which can measure not only the wheel moving speed, but also the travelled distance in a real-time manner. Read the acquired electric signals from an N-segment AT-TENG, the rotational speed in rpm at this moment can be expressed as

$$R_t = 60/(N \cdot \Delta t) \tag{2.19}$$

where Δt is the time lag in second between two adjacent peaks in the acquired electric signals. And the travelled distance till this moment can be calculated by:

$$L = \int_0^t \pi D \cdot R_t dt \tag{2.20}$$

where R_t and L are respectively the real-time rotation rate in rpm and travelled distance, N is the segment number of the AT-TENG, D is the tire diameter of the moving object. It is worth noting that, the self-powered speed or distance measurement does not require a uniform motion of the wheel. It can move at arbitrary time-varying velocity, which renders it a very practical application. Figure 2.30d shows a real-time speedometer realized by Labview programming. Holding a novel but simple structural design, the ultra-robustness of the AT-TENG promises itself to have extensive applications in wheel-based transport systems for either energy harvesting or self-powered sensing purpose.

2.2.3 Rolling friction enhanced free-standing TENG

In the meanwhile, to avoid the material abrasion and the consequently generated heat for TENG, a free standing working mode of the TENG is also developed recently.[36] The created free-standing gap between the two triboelectric layers largely assures the superior robustness of the device as well as unprecedentedly high energy conversion efficiency. However, an awkward dilemma emerges due to a low output performance as well as unavoidable elastic charge dissipation, which also obstructed the TENG towards practical applications.[73]

Herein, we present an ultra-robust, high-performance route for rotational kinetic energy harvesting by fabricating a rolling friction enhanced free-standing mode triboelectric nanogenerator (RF-TENG).[74] Creatively utilizing the rolling friction from a metal rod, the awkward predicament of elastic charge dissipation in the free standing model TENG is well resolved with no compromising of the device robustness.

The device structure of the RF-TENG is schematically illustrated in Figure 2.31a, which consists of three parts, a rotator, a stator and an aluminum rod. The zoom-in illustration (middle left) demonstrates the functionality of the aluminum rod for charge replenishment *via* rolling friction with the rotator. An axial gap in between the rotator and stator, namely, the free-standing gap, is tunable. In the stator, a layer of copper electrodes, which are complementarily patterned and disconnected by fine trenches in between, were deposited onto the kapton film. While, in the rotator, a layer of paralleled identical copper stripes with equal space was uniformly deposited onto the FEP thin film. Photographs of the as-fabricated rotator and stator with a grating number of 30 were respectively demonstrated in Figures 2.31b and c.
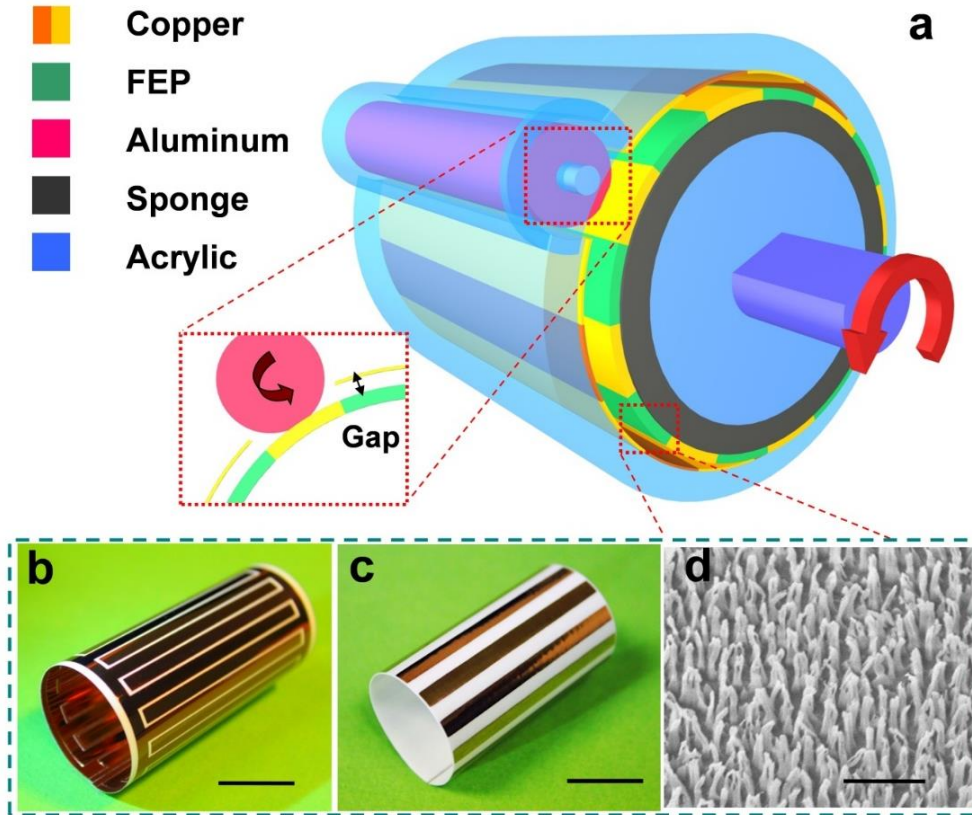
Figure 2.31 Structural design of the rolling friction enhanced free-standing triboelectric nanogenerator (RF-TENG), which consists of three parts, a rotator, a stator and an aluminum rod. (a) A schematic illustration of a RF-TENG. The zoom-in illustration (middle left) demonstrates the functionality of the aluminum rod for charge replenishment *via* rolling friction. (b) A photograph of the rollable stator. The scale bar is 1cm. (c) A photograph of the rotator, which is made of evenly-spaced metal gratings on a FEP thin film. The scale bar is 1cm. (d) A SEM image of the FEP polymer nanowires. The scale bar is 500 nm.[74]

In order to enhance the surface charge density of contact electrification, inductively coupled plasma (ICP) etching treatment was performed to create polymer nanowires array on the FEP surface. A scanning electron microscope (SEM) of the FEP nanowires is shown in Figure 2.31d, which indicates an average clustering diameter of FEP nanowires of 80 nm with an average length of 250 nm. To operate, the thin film of the rotator was aligned onto a layer of sponge foam before being supported by an Acrylic rod with a diameter of

2.54 cm. The soft sponge foam here was acting as a buffer layer to assure an intimate contact between the aluminum rod and FEP film.
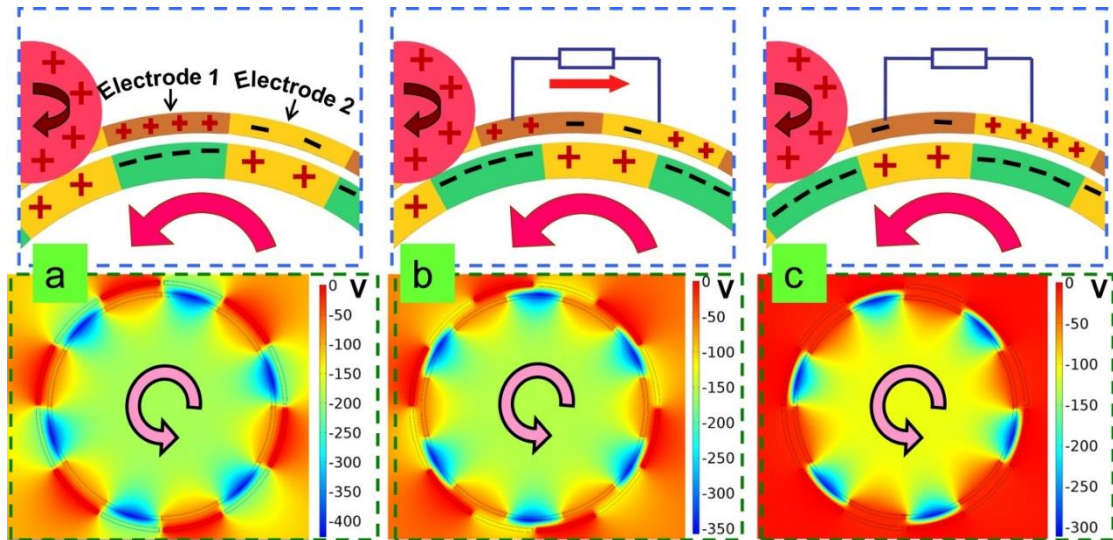
Figure 2.32 Schematics of the operating principle of the RF-TENG. Both two-dimensional schematic illustrations of the charge distribution (up) and potential distribution by COMSOL (down) were employed to elucidate the working principle of the RF-TENG in a half cycle. (a) The initial state. (b) The intermediate state. (c) The final state.[74]

The electricity generation of RF-TENG originates from a coupling effect of contact electrification and electrostatic induction,[75-77] as depicted in Figure 2.32. Here, both two-dimensional schematic illustrations of charge distribution (up) and potential distribution by COMSOL (down) were used for explanation. We define the initial state and the final state as the states when the FEP gratings of the rotator aligned with electrode 1 and electrode 2, respectively. While an intermediate state is the state when the rotator spins from the initial position to the final position. To begin with, when the rotator starts to spin, a rolling friction happens between the aluminum rod and FEP surface. And thus an equal amount of negative and positive charges will be respectively generated on the FEP parts and the metal parts due to a difference of the electron affinity between aluminum and FEP. The rolling friction

here can effectively avoid the sliding friction between the rod and FEP surface, which can not only assure the durability of the materials, but also provide an enduring charge density on the FEP surface, contributing to a time-lasting and constant output power.

In the meanwhile, the rotation of the stator will also lead to an intimate contact between the aluminum rod and the copper gratings, which ends up a redistribution of the positive charges on both the aluminum rod and the copper electrodes of the rotator, according to the principle of equipotential body. Subsequently, owning to electrostatic induction, the negatively charged FEP will induce the equal amount of positive charges in the electrode 1, while the positively charged copper will induce the equal amount of negative charges in the electrode 2 in the stator, as illustrated in Figure 2.32a. A continuous rotation will bring to the intermediate state, where the positive charge on electrode 1 will transfer to electrode 2 through the external circuit (Figure 2.32b) till it reaches the final state (Figure 2.32c). Further rotation beyond the final state induces both the open circuit voltage and short-circuit current to change in a reversed way because of the periodic structure.

To systematically investigate the performance of the RF-TENG in harvesting rotational kinetic energy, two key design parameters, the grating numbers and the free standing gap, are both experimentally and theoretically studied. To measure, the RF-TENG was anchored on a platform with one end was fixed by a bearing, and other end was connected to a programmable rotary motor. The center of the bearing and the rotary motor was tuned by a raising platform as well as a 3D-stage to guarantee a coaxial operation of the RF-TENG for a stable electric output. The motor is programmable for a quantitative measurement of the electric output, which was carried out under a relatively dry humidity

72

(RH=30%). To begin with, given a fixed free standing gap of 0.5 mm, the open circuit voltage shows a minor degradation with increasing the grating numbers, while a quasi-linear increasing trend was experimentally observed for the short circuit current, as demonstrated in Figure 2.33a. Then, a further electric output characterization was systematically performed when the free standing gaps were set at 1 mm, 2 mm, 3 mm and 6 mm, and the corresponding experimental observations were respectively presented in Figures 2.33b, c, d and e.
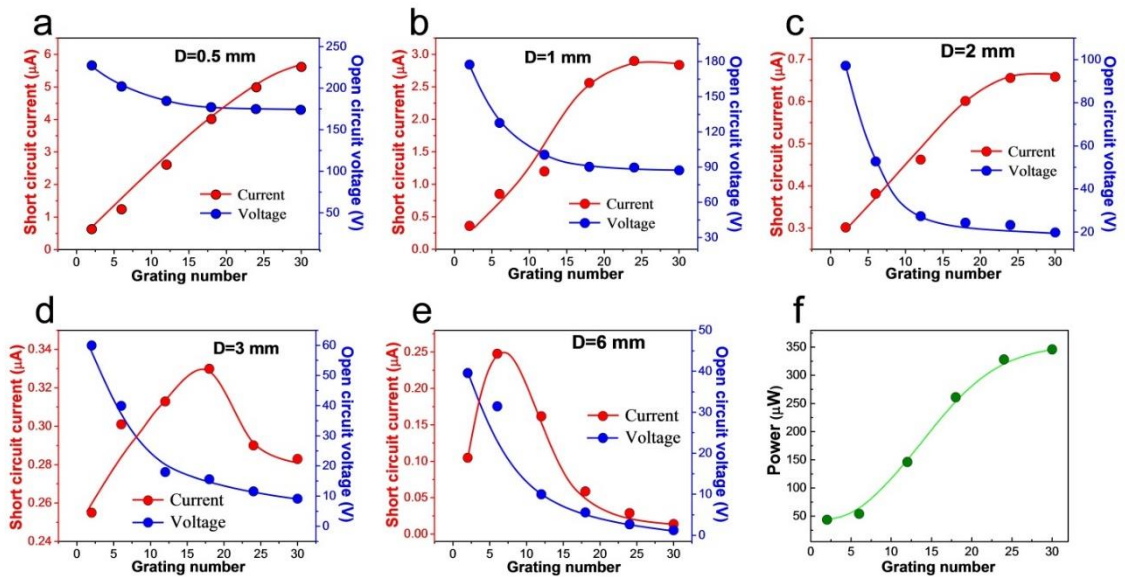
Figure 2.33 Electrical output characterization of the RF-TENG. Dependence of the short-circuit current and open-circuit voltage on the number of gratings under a various free standing gap distance D between the rotator and stator: (a) D=0.5 mm, (b) D=1 mm, (c) D=2 mm, (d) D=3 mm, (e) D=6mm. (f) Dependence of the maximum output power of the RF-TENG on the grating numbers at a fixed axial distance D = 0.5mm.[74]

From the evolution of the output signals regarding the increasing grating numbers at various gap distances, certain trends can be derived to clearly profile the reported RF-TENG. Firstly, current amplitudes are drastically increased with elevated grating numbers at a gap distances lower than 2 mm. Secondly, when the gap distance was larger than 2

73

mm, maximized current outputs emerge at an optimized grating numbers. And also, the maximized current points were shifted towards a larger grating numbers at smaller gap distances. Apparently, a monotone increasing relationship was no longer exhibited between the current output and the grating numbers for the RF-TENG. This is mainly attributed to the transferred charges across the electrodes were degraded with increasing of the grating numbers.[78]

For the in-plane sliding mode, due to the intimate contact between the two triboelectric layers, the generated static electric fields by the triboelectric charges are mutually locked. As a consequence, the transferred charges Q across electrodes will not be reduced with further subdivided gratings. The output current is proportional to dQ/dt. With constant charge transfer across electrodes, a faster charge transfer will be resulted from the subdivide grating, which contributes to an enhanced current output. However, in the RF-TENG, the static electric fields between triboelectric layer and electrode are no longer mutually locked due to the existence of a physical gap, which will lead to a reduced transfer charges across the electrodes. With further subdivided gratings, the increase of the output current due to a faster charge transfer will be undermined by the reduced amounts of the transferred charges. And the later will become more and more dominant on the current output with elevated subdivided gratings, which renders a maximized current output at an optimized grating number. In the meanwhile, this effect will also become more and more dominant at a fixed grating number with elevated gap distance, which contributes to a shifted peak current points towards a smaller grating numbers.[78] Thirdly, at all gap distance, the open-circuit voltage shows a decreasing trend with increasing the grating numbers. Especially, at larger gap distances, the output voltage is decreased much more obviously.

Fourthly, both the current and voltage are apparently decreased with elevated free standing gap distances. These observations are mainly attributed to that a larger gap distance leads to a weaker electrostatic induction effect. More importantly, a more confined electrostatic field will exist with smaller gap distance between the charged surfaces and the electrodes. Additionally, the symmetrical neutralizing effect of the potential will become stronger at a larger gap distance.

For a systematical study, a further step was taken to evaluate the output power of the RF-TENGs with elevated grating numbers. At a fixed gap distance of 0.5 mm, the output power density is obviously increased with grating numbers, as shown in Figure 2.33f. Here, each output power density is the maximized value at its optimized external load resistance. Furthermore, charge replenishment by a rod rolling friction is the driving force behind the enhanced electric output of the presented RF-TENG. To quantify the rolling induced performance improvement, both the open-circuit voltage and short-circuit current are measured with or without the rod under various rotating speeds, from 100 to 900 r/min. Here, the rotator of the tested RF-TENG has a diameter of 2.54 cm and a length of 10 cm. And the free standing gap is set to be 0.5 mm. As the experimental results presented in Figure 2.34a and b, both the open-circuit voltage and short-circuit current are doubled with the rolling friction induced charge replenishment. Absence of the rod rolling, the triboelectric charges on the FEP surface will decay continuously. After placing the aluminum rod, the output of the RF-TENG is obviously increased and keeps constant at a higher plateau. Not until removing of the metal rod, the electric output shows an obvious degradation. It is worth noting that the charge degradation rate is highly related to the ambient environment, such as temperature, humidity, pressure, floating particles in air and

so on. In the RF-TENG, the continuous charge replenishment will enable the device free from the environmental factors, rendering a consistent and constant electric output. This is also a critical advantage towards a sustainable practical power source.
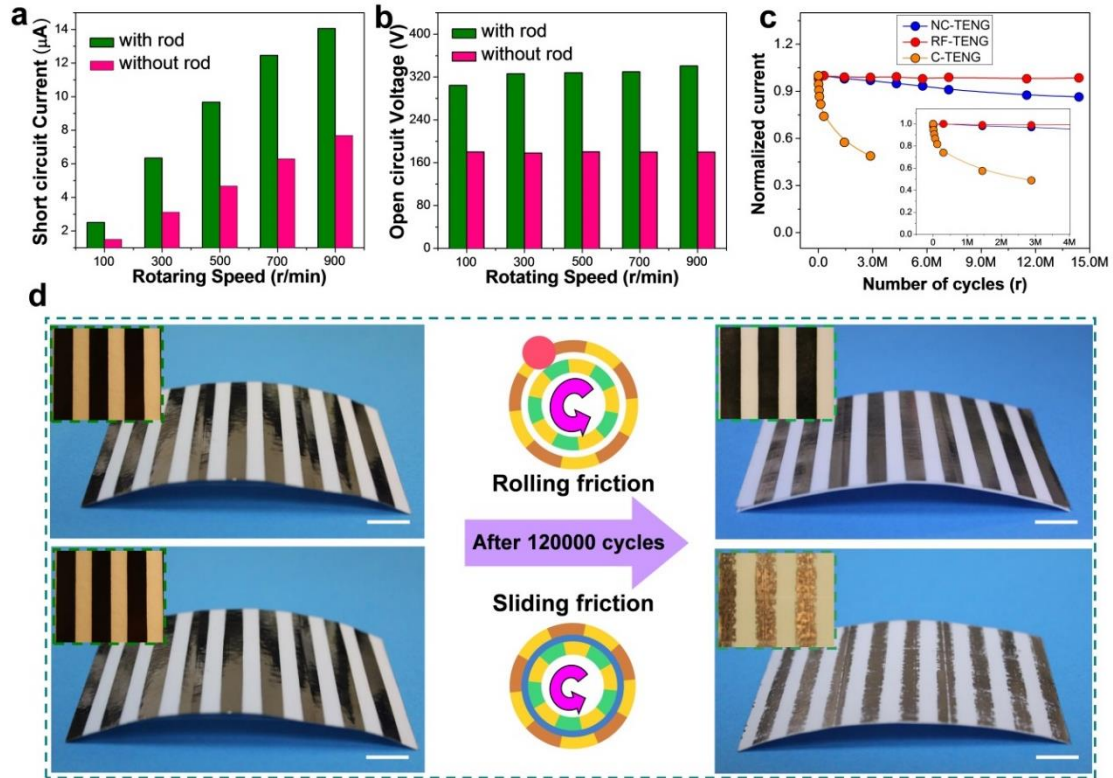
Figure 2.34 The rolling friction induced charge replenishment and device robustness. The current (a) and voltage (b) enhancement by introducing the aluminum rod rolling friction. (c) Mechanical robustness test of the RF-TENG. The output voltage only shows a minor fluctuation of less than 0.2% after 14.4 M cycles of rotations. (d) Comparison of the metal gratings surface morphology after the rolling friction and sliding friction up to 120000 cycles. The scale bars are 1 cm.[74]

The reliability is also a superior feature of the reported RF-TENG, which is primarily represented by its output stability and mechanical durability. On one hand, the output stability against the long-term continuous rotation has been investigated. To evaluate, a set of current output measurements were performed among three types of TENGs: RF-TENG, Non-contact free-standing mode TENG (NC-TENG), and Contact in-

plane sliding mode TENG (C-TENG). The output current data of each TENG was normalized as shown in Figure 2.34c, the output of RF-TENG only shows a minor fluctuation of less than ±0.2% after 14.4 million cycles of rotations while the output of NC-TENG decreased about 15%. Noticeably, the output of the C-TENG dropped to 45 % only after 2.8 million cycles' rotation.

On the other hand, to investigate, the mechanical durability is also evaluated by comparing the surface material abrasion after 0.12 million cycles' rotation. As exhibited in Figure 2.34d, the metal electrodes of the RF-TENG stay almost intact while those of the in-plane sliding mode TENG were almost worn out. The ultra-robustness of the RF-TENG is mainly attributed to the novel device structural design. In the operation of RF-TENG, there is no direct physical contact between the triboelectric layer and the electrode, and the rolling friction for the charges replenishment will hardly cause any damage to the durable FEP polymer surface. Moreover, the using of a soft sponge can largely reduce the rigid contact between aluminum rod and FEP, and it also can avoid the relative slip between aluminum rod and FEP film, which could further enhance the robustness of the device.

To demonstrate the capability of the RF-TENG as a robust and sustainable power source, firstly, the output power of an as-fabricated RF-TENG with a grating number of 30, diameter of 2.54 cm, length of 10 cm was quantified at the free standing gap of 0.5 mm. As shown in Figure 2.35a, the short-circuit current and open-circuit voltage (peak to peak) can respectively reach ~15 μA and ~ 320V. Resistors were utilized as external loads to further investigate the output power of the RF-TENG at a rotation rate of 1000 r/min. As displayed in Figure 2.35b, the current amplitude drops with increasing load resistances owing to the ohmic loss, while the voltage follows a reverse trend. As a result, the

instantanenous peak power is maximized at a load resistance of 20 MΩ, coresponding to a

peak power density of 250 mW/m^2. This long-term continuous output power is capable of

simultaneously powering 16 spot lights connected in parallel (Figure 2.35c), charging a

200 μF commercial capacitor to 120 V in 170 s as well as lighting up a G16 globe light

(Figure 2.35d).
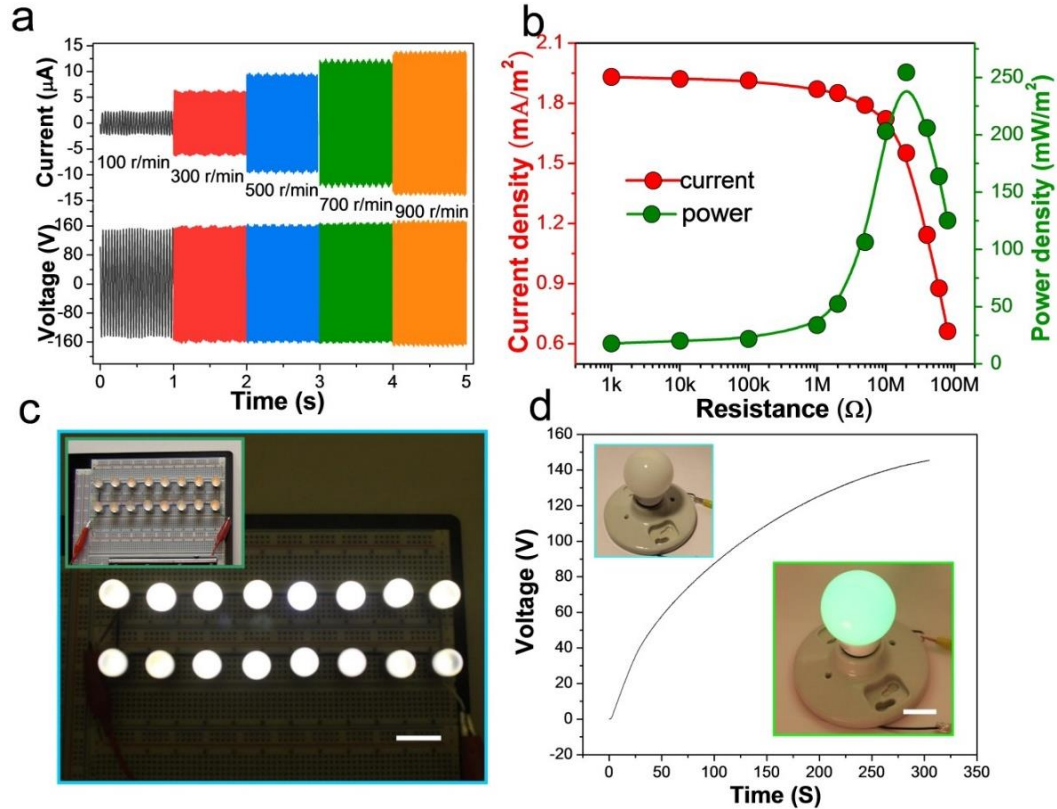
Figure 2.35 Demonstrations of the RF-TENG as a practical power source. (a) Electric
output characterization of a RF-TENG with a grating number of 30 and gap distance D =
0.5 mm. (b) Dependence of the output current and peak power of the RF-TENG on the
resistance of the external load, indicating the maximum power output is obtained at 20 MΩ.
The results were obtained under a fixed rotating speed of 900 r/min. (c) Photograph of 16
spot lights that are directly powered by the RF-TENG in complete darkness under a rotating
rate of 1500 r/min. The scale bar is 1 cm. (d) Demonstration of the RF-TENG charging a
200 μF commercial capacitor and simultaneously lighted up a G16 globe light. The scale
bar is 2 cm.[74]

2.3 TENG for acoustic energy harvesting

As a clean, ubiquitous and sustainable energy source, acoustic waves, such as various sound noises from any living activities, airports, construction sites and traffic, are one of the wasted energies that are abundant in our daily life. Sound energy is usually taken as unwanted noise that is polluting our living environment. Acoustic energy harvesting was not as popular as other types of energy harvesting, such as solar energy and thermal electric energy, possibly because not only sound waves having much lower power density but also the lacking of effective technology for harvesting such energy.

Harvesting acoustic energy has been demonstrated using approaches based on piezoelectric effect[79] and electrostatic effect,[80] but their performances are limited by low energy conversion efficiency, low power density, structure complexity and requirement of high-quality materials.[80] Furthermore, most of the presented devices generally work at high frequencies from a few kHz to MHz,[79, 80] while sound sources available in everyday life contain predominantly low frequency components, making the presented mechanisms unsuitable in most circumstances.[81] Therefore, harvesting sound wave energy remains a challenge.

2.3.1 Organic thin film based TENG

To scavenge ambient acoustic energy as a sustainable power source, we firstly reported the first organic thin-film based triboelectric nanogenerator.[82] Relying on a Helmholtz cavity with a size-tunable narrow neck on its back, the core of the nanogenerator is in a circular shape and embedded as the flexible front plate of the cavity, as schematically shown in Figure 2.36a. For a better illustration, a cross-sectional view of the core is shown

in Figure 2.36b, with a multilayered structure. Aluminum thin film with nanoporous surface plays dual roles as an electrode and a contact surface. A scanning electron microscopy (SEM) image of nanopores on the aluminum is presented in Figure 2.36c. The nanopores were uniformly distributed on the surface of aluminum with an average diameter of 57 ± 5 nm and a density of 210 per μm^2. A layer of polytetrafluoroethylene (PTFE) film with deposited copper was employed as another electrode. An SEM image of the PTFE nanowires is displayed in Figure 2.36d. The average diameter of PTFE nanowires is 54 ± 3 nm with an average length of 1.1 ± 0.4 μm.
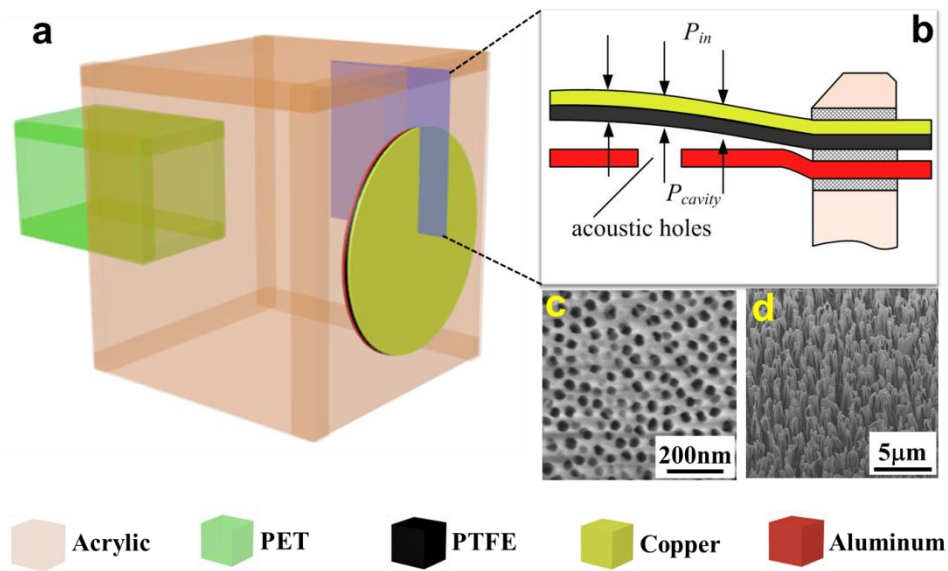
Figure 2.36 Structural design of the organic film nanogenerators. (a) A sketch and (b) Cross sectional view of the nanogenerator. (c) A SEM image of nanopores on aluminum electrode. (d) An SEM image of PTFE nanowires fabricated on the film surface by plasma etching, which largely increase the triboelectrification.[82]

When an external sound wave is incident on the core part of the nanogenerator, the air within the cavity is alternately compressed and expanded in responding to the magnitude and frequency of the sound wave, and thus the PTFE thin film will oscillate due to the initiated pressure difference on its two sides, while the aluminum film stays still.

Mathematically, the pressure difference can be expressed as [83]

$$\Delta p = 2p\sin(kd\cos\theta/2) \tag{2.21}$$

where k is the wavenumber, p is the incident acoustic pressure, d is the effective distance between the PTFE thin film and the opening of the neck, and θ is the sound wave incident angle, which is the angle between the sound propagation direction and the normal direction of the PTFE surface.

A MATLAB simulation for the deformation of the PTFE film under the acoustic pressure difference is shown in Figure 2.37a, where we assume that the uniformly distributed acoustic pressure difference is 0.1 Pa and the Young's Modulus of the cylindrical PTFE thin film (65 mm in diameter and 0.06 mm in thickness) is 420 MPa. The color represents the magnitude of the deformations of the PTFE thin film, of which a maximum displacement of 0.7 mm is obtained at the center. The average deformation is a monotonically increasing function of acoustic pressure difference throughout our experimental time window, as shown in Figure 2.37b.

A cycle of electricity generation process under acoustic pressure is schematically depicted in Figure 2.37c, using the numerically simulated electrostatic potential distribution arising from triboelectric charges (using COMSOL package). At original state, the PTFE is in contact with aluminum thin film. Because PTFE is much more triboelectrically negative than aluminum, electrons are injected from aluminum into PTFE, generating positive triboelectric charges on the aluminum side and negative charges on the PTFE side (Figure 2.37c Stage I). Due to the wave character of sound propagation, a resulted acoustic pressure separates the PTFE thin film away from the aluminum thin film. As a result, the positive triboelectric charges and the negative ones no longer coincide on

the same plane and an inner dipole moment between the two contact surfaces is consequently generated, which drives free electrons to flow from the copper electrode to the aluminum electrode to screen the local electric field, producing positively induced charges on the copper electrode (Figure 2.37c Stage II).
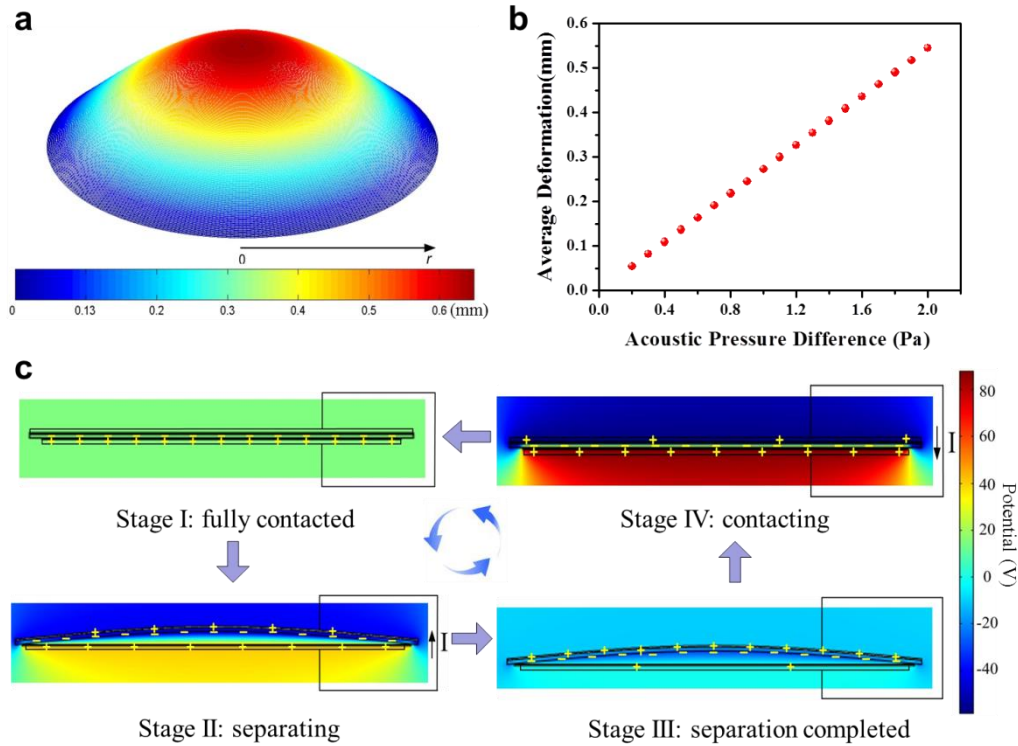
Figure 2.37 Working principle of the organic film nanogenerators. (a) Simulation result of PTFE thin film oscillating mode. (b) Relationship between the average deformation of the PTFE thin film and the acoustic pressure difference. (c) COMSOL simulation of the periodic potential change between the two electrodes upon acoustically induced cyclic deformation, showing the driving force for the back-and-forth charge flow generated by the nanogenerator.[82]

The flow of electrons lasts until the PTFE thin film reaches the highest point, where the corresponding separation is maximized (Figure 2.37c Stage III). Subsequently, due to the acoustic pressure difference change, the PTFE film is pushed back towards the aluminum film. In response to the reduced separation and thus the weakened potential drop, the free electrons in aluminum electrode flow back to the copper electrode until the two

surfaces come into contact, making a complete cycle of electricity generation (Figure 2.37c Stage IV). Then the PTFE thin film is bounced away from the aluminum thin film again after obtaining a momentum from the sound waves, starting another cycle of electricity generation. The output electric signal can be a power source or a sound sensor, as illustrated in follows.
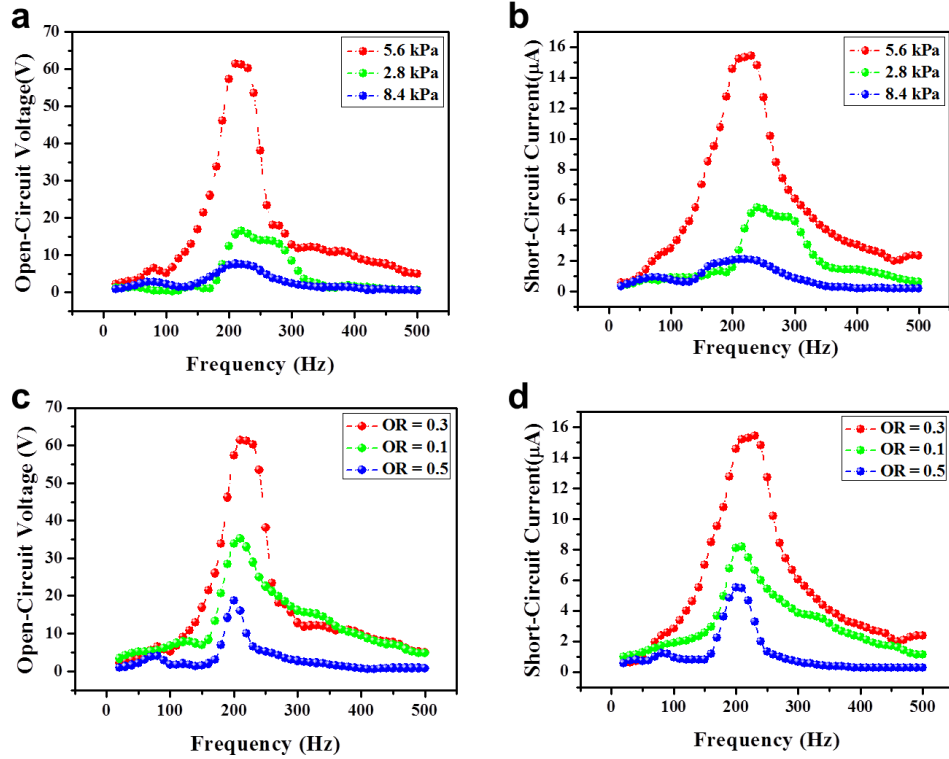
Figure 2.38 Electrical measurement of the organic film nanogenerators. (a) Open-circuit voltages (V_{OC}) and (b) Short-circuit currents (I_{SC}) as a function of acoustic frequency with different pre-stresses of 2.8 kPa, 5.6 kPa and 8.4 kPa. The curves are the fitted results. (c) V_{OC} and (d) I_{SC} as a function of acoustic frequency with different open ratios (ORs) of 0.1, 0.3 and 0.5. The curves are the fitted results.[82]

To investigate the performance of the proposed nanogenerator in harvesting acoustic energy, a loudspeaker (Fostex Inc.) that provides sinusoidal sound waves was used as an acoustic source with tunable frequency and amplitude. A sound level meter (Extech Inc.) with 2 dB accuracy and 0.1 dB resolution is used to measure the incident acoustic

pressure. The meter is located near the harvester at a distance far less than the acoustic wavelength. Displacements in the radial direction are prescribed at the outer circular boundary of the PTFE film to intentionally introduce the initial in-plane pre-stress in order to tune the resonance frequency of the film, thus render it acting as an elastic element to oscillate under acoustic wave excitation. Under pre-stresses of 2.8 kPa, 5.6 kPa and 8.4 kPa and a constant incident acoustic pressure of 110 dB$_{SPL}$, the reliance of open-circuit voltages (V_{oc}) and short-circuit currents (I_{sc}) on the input acoustic frequency is presented in Figures 2.38a and 2.38b, respectively. At the resonance frequencies, the V_{oc} under different pre-stresses are respectively 16.50 V, 60.50 V and 7.50 V, respectively. While I_{sc} are 5.50 μA, 15.10 μA and 2.10 μA, respectively. The output voltage shows an enhancement of 3.7 times for the device with a pre-stress of 5.6 kPa than that with the pre-stress of 2.8 kPa, and also an enhancement of 8.1 times is achieved compared to the device with pre-stress of 8.4 kPa. The results show that a suitable initial pre-stress can optimize the oscillation coupling between the air trapped in the cavity and PTFE thin film, and thus the electrical output.

Regarding the optimized design, namely, the device with pre-stress of 5.6 kPa, experimentally, both V_{oc} and I_{sc} are maximized at the acoustic frequency of 240 Hz, indicating that 240 Hz is the resonance frequency of the as-fabricated generator. Theoretically, if the dimensions of device are smaller than or comparable to the incident acoustic wavelength, its dynamic behavior can be modeled as a lumped system. And its resonant frequency can be expressed as[84]

$$f_R = \frac{c}{2\pi}\sqrt{\frac{S}{L'V}} \tag{2.22}$$

where S and L' are respectively the cross-sectional area and effective length of the neck. V

is the cavity volume and c is the speed of sound in air (343 m s^{-1}). Submitting the values into Equation (2.22), we can obtain the theoretical natural frequency of 238.8 Hz, which is consistent with the experimental result.

Besides the pre-stress has a marked impact on the electric output of the device, aimed at further improving the electric output, a serial of acoustic holes are punched through the aluminum electrode, which act as communicating vessels to integrate the air gap between two contact surfaces with the air in the cavity. The open ratio (OR) is defined as the area ratio of all acoustic holes' area to the surface area of the aluminum electrode, which largely influences the damping of the air. A larger value of OR results in a higher flow velocity and lower damping,[50] which will contribute to a larger deformation of the PTFE film under the same acoustic pressure excitation.

Under a constant acoustic pressure of 110 dB$_{SPL,}$ the V_{oc} and I_{sc} of the generator with different ORs of 0.1, 0.3 and 0.5 were respectively measured, as shown in Figures 2.38c and d. At the resonance frequencies, the V_{oc} for open ratio of 0.1, 0.3 and 0.5, are respectively 35.20 V, 60.50 V and 18.70 V, and the corresponding I_{sc} are 8.20 µA, 15.10 µA and 5.50 µA. The results indicate that an enhancement of 1.7 times of the electric output is obtained for the device with OR value of 0.3, compared to that of 0.1, and also an enhancement of 3.2 times is achieved compared to that of 0.5. This experimental observation is resulted from a tradeoff between the PTFE deformation and the effective contact area. Larger OR leads to a larger deformation of the PTFE thin film, and thus a higher electric output. However, increased OR will reduce the effective contact area for triboelectrification, and thus a lower electrical output. Consequently, an optimum OR is needed to maximize the electrical output.
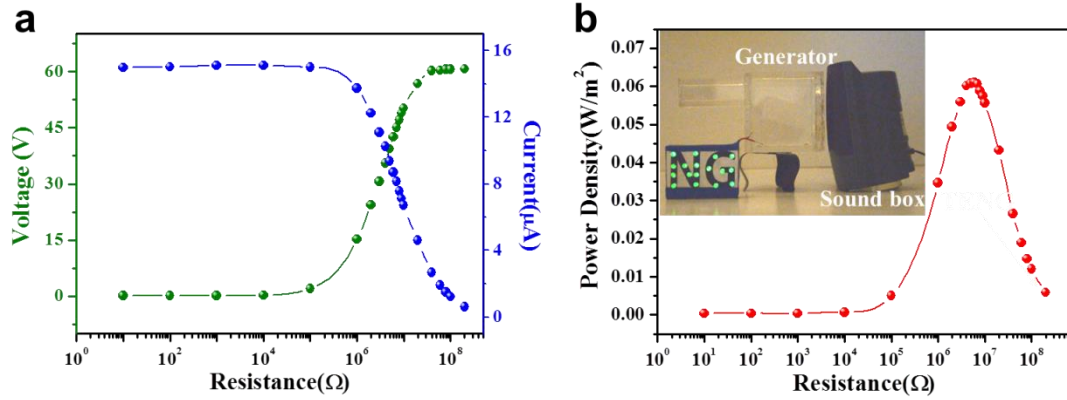
Figure 2.39 Demonstration of the organic film nanogenerator acting as a sustainable power source. (a) Dependence of the voltage and current output on the external load resistance. (b) Dependence of the peak power output on the resistance of the external load, indicating maximum power output at R = 6 MΩ. Inset is a photograph that shows nanogenerator works under the excitation from a sound box. Due to the external sound, 17 LEDs are being lighted up simultaneously. [82]

Resistors were utilized as external loads to further investigate the useful output power of the as-fabricated nanogenerator at the resonance frequency. As displayed in Figure 2.39a, the voltage amplitudes increase with increasing load resistance, while the current follows a reverse trend owing to the ohmic loss. As a result, the instantaneous peak power $(V^2/R)_{peak}$ is maximized at a load resistance of 6 MΩ, corresponding to a peak power density of 60.2 mWm^{-2} (Figure 2.39b). To prove the capability of the proposed nanogenerator as a sustainable power source, powered by a nanogenerator with the cavity dimensions of 8 cm × 8 cm × 8 cm under acoustic pressure of 110 dB$_{SPL}$ at the resonant frequency of 240 Hz, 17 commercial LED bulbs were lighted up simultaneously, as demonstrated in the inset of Figure 2.39b.

In a word, we developed a new type of acoustic energy harvester that scavenges energy using triboelectrification effect, a universal phenomenon upon contact between two materials with opposite triboelectric polarities. Rationally designed structure, coupled with

nanomaterial modification, the as-fabricated nanogenerator enables superior performance in harvesting ambient acoustic energy. It produced a maximum electric power density of 60.2 mW m^{-2}, which directly lighted up 17 commercial LEDs simultaneously. This work presents an adaptable, cost-effective and fundamentally new approach for ambient acoustic energy harvesting with potential applications in infrastructure monitoring, sensor networks, military surveillance and environmental noise reduction.

2.3.2 Ultrathin, rollable, paper-based TENG

The traditional acoustic energy harvester has a bulky structure due to the requirement of a resonance cavity, which greatly limited its wide-range application, such as harvesting acoustic energy from a commercial cell phone when playing music or from human talking on the phone. A further improved performance of the acoustic energy harvesting is on the basis of an ultrathin, rollable, and paper-based TENG, which innovatively employs arrays of micro holes for acoustic response enhancement.[85]

An ultrathin TENG has a multilayered structure composed of thin film materials that are vertically laminated. A layer of multiholed paper forms the structural backbone of the TENG, which was coated with copper acting as an electrification layer that generates triboelectric charges upon contacting with a thin polytetrafluoroethylene (PTFE) membrane, as schematically shown in Figure 2.40a. Papers were selected as the structural materials owing to its flexibility, lightweight, good machinability, low cost as well as biodegradability. Of course, instead of papers, other expensive organic thin films can be chosen as well.
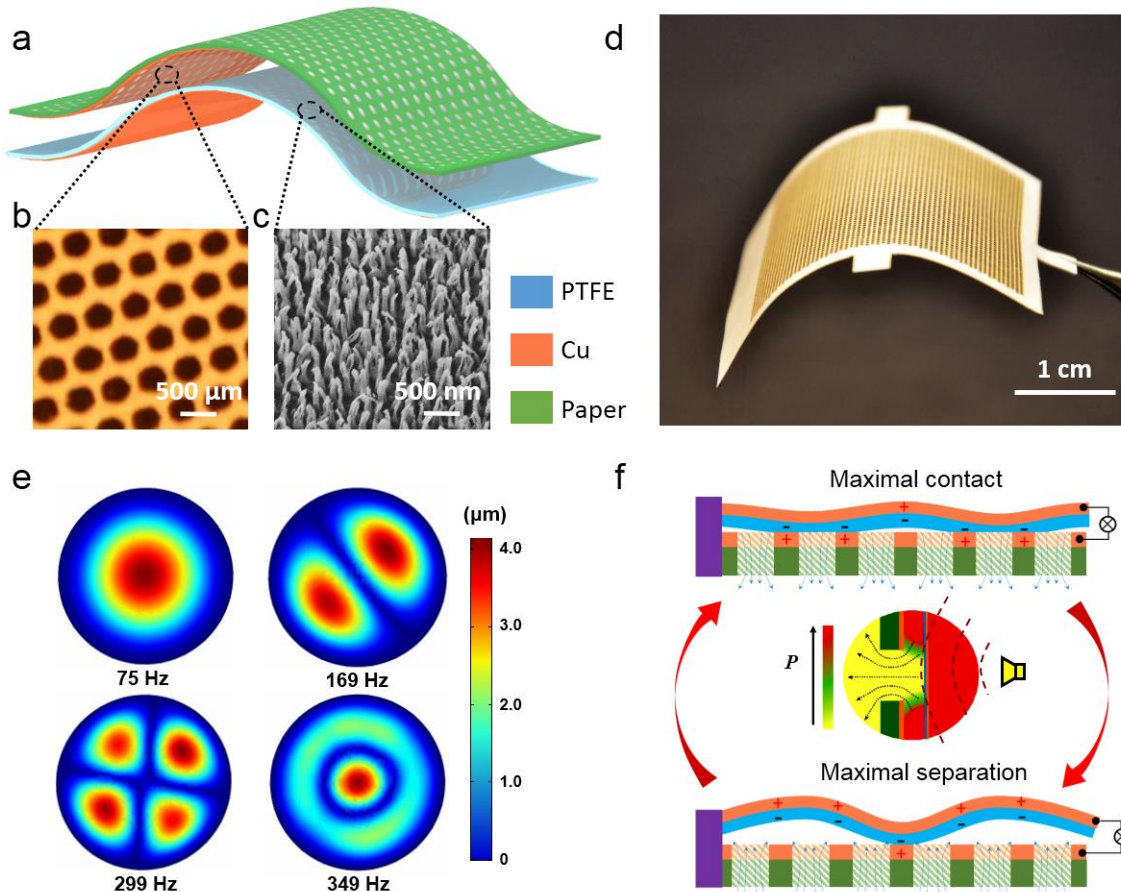
Figure 2.40 Structural design and operating principle of the ultrathin paper-based TENG. (a) Schematic illustrations of the paper-based TENG. (b) A photograph of the multi-hole paper electrode. (c) An SEM image of the PTFE polymer nanowires. (d) A photograph of an as-fabricated paper-based TENG. (e) The ANSYS software was employed to characterize the PTFE membrane vibrations under various sound frequencies. (f) An illustration to interpret the sound wave induced PTFE membrane vibration and electricity generation.[85]

For purpose of enhancing a broad-band acoustic response, holes with diameters of 400 μm were evenly punched and distributed on the paper substrate. A photograph of the multi-hole paper electrode is demonstrated in Figure 2.40b. In order to enhance the triboelectrification, the polymer nanowires array was purposely created onto the PTFE membrane, as the SEM image shown in Figure 2.40c. Figure 2.40d is a photograph of an as-fabricated paper-based TENG with a thickness less than 125 μm.

The working principle of the paper thin triboelectric nanogenerator can be elucidated from two aspects, namely, sound induced membrane vibration and vibration induced electricity generation. On one hand, when an external sound wave is continuously incident onto the paper thin TENG, the flexible PTFE membrane would vibrate accordingly. Namely, the propagation of the sound wave will cause a periodical air-pressure difference between two sides of the membrane, which leads to the membrane vibration. This vibrational mechanism is distinctly different from the traditional acoustic energy harvester that relies on a resonator cavity, for which the mechanical vibration is attributed to the alternative air compression-expansion within the cavity.[84, 86] An ANSYS software is employed to simulate the sound wave induced PTFE membrane vibration under various frequencies, as shown in Figure 2.40e, assuming that the acoustic pressure difference of 20 Pa is uniformly distributed over the 0.025 mm-thick PTFE membrane with Young's modulus of 440 MPa. As it can be observed from the simulation results, the deformation regions and magnitudes of the PTFE membrane are highly related to the external sound excitation frequencies, which can be attributed to different resonance frequencies under different vibration modes.

On the other hand, the vibration induced electricity generation is attributed to a coupling effect between contact electrification and electrostatic induction. A cycle of electricity generation process under external pressure is schematically depicted in Figure 2.40f. At its maximum contact state, sound wave induced contact between PTFE and copper will generate electrical charges. The two materials have a different affinity for electrons, with the PTFE attracting electrons from copper, resulting in positive triboelectric charges on the copper side and negative ones on the PTFE side. Subsequently, the acoustic

pressure will separate the PTFE from copper. As a result, an inner dipole moment between the two contact surfaces is consequently altered, which drives free electrons to flow from the copper electrode on the PTFE membrane to the multi-hole paper electrode till the maximum separation state is reached. And the free electrons will flow in a reverse direction in the process from maximum separation state towards maximum contact state, which completes a full cycle of electricity generation process.

The electric output of the as-fabricated paper thin TENG is highly related to the sound wave induced PTFE membrane vibration, while the air damping is acting as a negative impact, of which the influence on acoustic energy harvesting is still under-estimated.[87, 88] Introducing holes is a rational solution to minimizing the damping but it also reduces the effective contact area as a tradeoff. Thus, in order to obtain an optimized output for the paper thin TENG, arrays of micro holes are added, and the structural parameters of the holes, including shape, dimensions, and distributions, needs also to be systematically optimized.

Firstly, the influence of the hole shape on the output performance is studied at a constant void-to-surface ratio. The transmitting ability of air flow through the holes, namely, the acoustic pressure difference is highly dependent on the hole shapes. As demonstrated in Figure 2.41a, both the peak distribution and peak values are various with hole shapes. And a best output performance is obtained from the evenly-distributed micro holes in a circle shape. It is worth noting that, for all the three hole-shapes, the frequency-response curves hold a multi-peak characters with all the maximum peak output occurring at ~320 Hz, while the other peaks emerge at the frequencies around the integral multiples of ~80 Hz. This observation is mainly attributed to that the thin membrane vibrates in a multi-

modal manner under external acoustic pressure. And each vibration mode holds a natural frequency. At those resonance frequencies, a stable planar standing wave will form over the membrane to cause large deformations, corresponding to the peaks in the frequency-response curves.[89, 90]
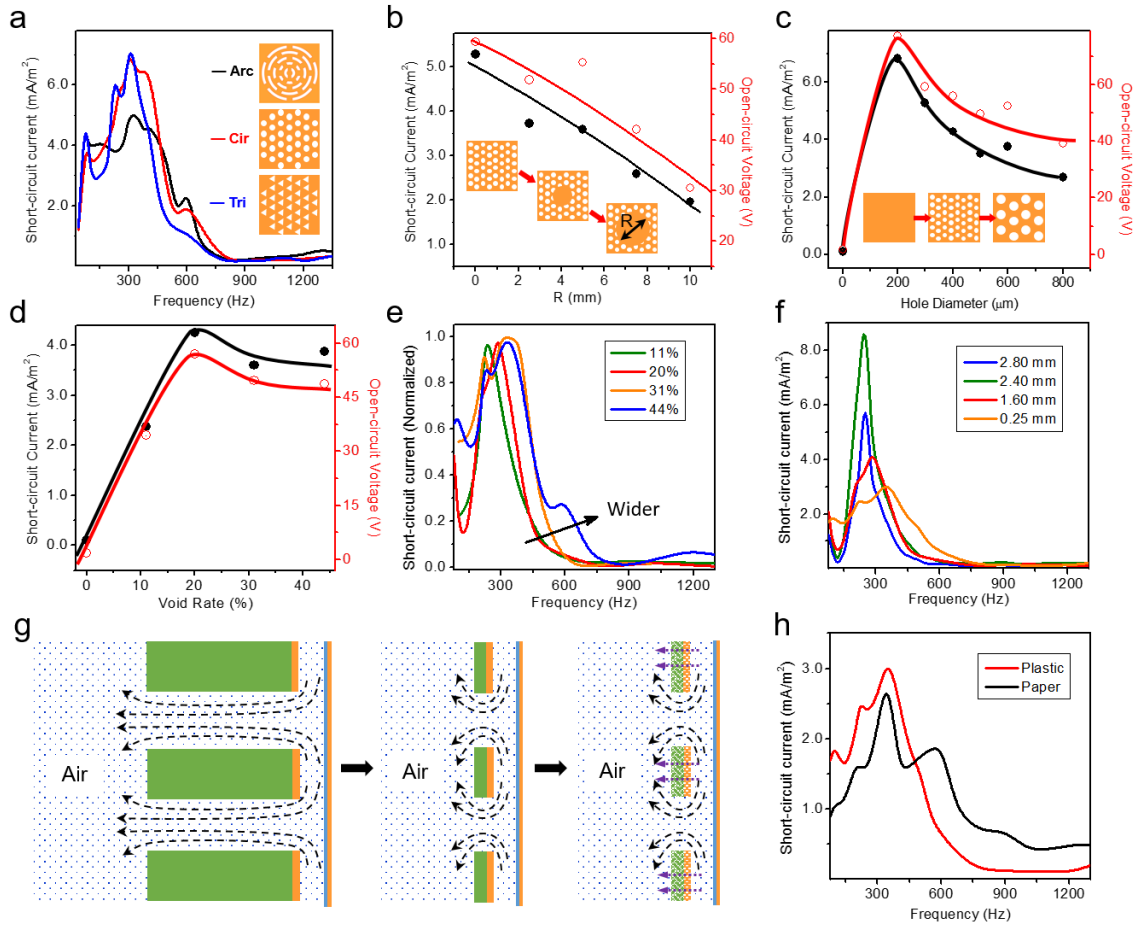
Figure 2.41 Factors that influence the electric output of the triboelectric nanogenerator without Helmholtz resonator. (a) Influence of the hole shapes on the multihole electrode with constant void-to-surface ratio. (b) Influence of the central holes distribution on the electrical output. (c) Influence of hole diameters with constant void-to-surface ratio of 20%. (d) Influence of void-to-surface ratio on the device electrical output. (e) Influence of void-to-surface ratio on the device frequency response. (f) Influence of the electrode thicknesses on the electrical output. (g) An illustration to interpret the influence of the electrode thickness. (h) Influence of electrode substrate materials on the electrical output. All of the measurements were under a constant sound pressure of 120 dB$_{SPL}$.[85]

Secondly, the center structure is another critical parameter that determines the

output performance. Since the added holes on the electrode will reduce the effective contact area, a circular area without holes is purposely reserved in the center of the multi-hole electrode. As shown in Figure 2.41b, at a fixed excitation frequency of 320 Hz, the maximum peak output decreases as the hole-free area increases, which is mainly attributed to the weakened membrane vibration due to the air dumping effect in the hole-free part. This also further validates that the air damping is a determining factor for the paper thin TENG without a resonator.

Thirdly, the influence of the hole diameter on the output performance is also systemically investigated at a constant void-to-surface ratio. As indicated in Figure 2.41c, experimentally, the peak output is an increasing function of the hole diameter in small hole range till an optimal hole diameter emerges (0.2 mm). And then, the output decreases as the hole diameter increases. Theoretically, the membrane vibration is an increasing function of the air-pressure difference across the PTFE membrane ($\Delta P_{membrane}$). At a certain sound pressure (P_{sound}), $\Delta P_{membrane}$ can be calculated as

$$\Delta P_{membrane} = P_{sound} - \Delta P_{hole} - P_{damping} \tag{2.23}$$

where $P_{damping}$ is the reduced pressure around PTFE due to air damping. Meanwhile, according to the Hagen-Poiseuille equation,[91] the average air-pressure difference across the multihole electrode (ΔP_{hole}) can be expressed as

$$\Delta P_{hole} = 8\mu LQ/(\pi r^4) \tag{2.24}$$

where, L is the thickness of the multihole electrode. μ and Q are the dynamic viscosity and volumetric flow rate of the air flow, respectively. r is the average radius of the hole. π is a mathematical constant. According to the equations (2.23) and (2.24), ΔP_{hole} increased with the decreasing of the hole diameters, while $P_{damping}$ follows a reverse trend. Consequently,

an optimal hole diameter will lead to a maximum $\Delta P_{\text{membrane}}$, thus an optimized output performance.

Fourthly, a further step was taken to study the influence of the void-to-surface ratio of multihole paper electrode on its output performance. As demonstrated in Figure 2.41d, the electric output is firstly-increasing and then decreasing function of the void-to-surface ratio and it is maximized at a value of ~20%. A larger void-to-surface ratio will lead to a smaller damping effect of the air, thus, a larger vibration of the PTFE membrane; however, a smaller effective contact area. The tradeoff of larger membrane vibration and smaller effective contact area requires an optimal void-to-surface ratio, as experimentally observed. It is worth noting that the void-to-surface ratio also shows an evident impact on the device working bandwidth, as demonstrated in Figure 2.41e. As the void-to-surface ratio increases, the frequency response is widened and expanded to a higher frequency range, which is essential to the paper thin TENG for self-powered active sensing.

Fifthly, the thickness of the multihole electrode is also another important design parameter that needs to be investigated. As shown in Figure 2.41f, a sharp and narrow output peak was observed for the device with thicker electrode, which is a typical character of a sound-response device based on Helmholtz resonator. However, the frequency-response curve turns into a broad multi-peak waveform when the electrode thickness becomes thinner. Especially, the output at a higher frequency ranging up to 700 Hz is obviously increased with thinner electrode. Theoretically, when the electrode thickness is relatively large, a Helmholtz resonator is formed, which can improve the output at the resonance frequency while narrowing the frequency response range as the tradeoff,[92, 93] as schematically shown in Figure 2.41g. Besides, according to the equations (2.23) and (2.24),

ΔP_{hole} increased with the increasing of the electrode thickness, while P_{damping} follows a reverse trend. Thus, there should be an optimized electrode thickness. And a thickness of 2.4 mm is observed experimentally.

Additionally, the paper based multi-hole electrode is capable of expanding the frequency response, comparing with the plastic sheet based multi-hole electrode with identical thickness, as indicated in Figure 2.41h. A possible reason is that the paper holds a micro textile structure with tiny communicating vessels, which would further weaken the air damping effect. In a word, in order to obtain a decent output for the acoustic energy harvester without a resonator, a paper thin electrode with evenly-distributed circular holes is highly desired.

Resistors were utilized as external loads to further investigate the output power of the structurally optimized paper thin TENG at acoustic frequency of 250 Hz with an acoustic pressure of 114 dB_{SPL}. As displayed in Figure 2.42a, the voltage amplitudes increase with increasing load resistance, while the current follows a reverse trend owing to the Ohmic loss. As a result, the instantaneous peak power is maximized at a load resistance of 800 KΩ, corresponding to a peak power density of 121 mW/m^2 (volume power density of 968 W/m^3), as shown in Figure 2.42b. Furthermore, the dependence of the electrical output on the incident sound pressures was also investigated and a direct proportional relationship was experimentally observed between the two, as indicated in Figure 2.42c. Holding a collection of compelling features, including paper thin, rollable, broad working bandwidth, independent of resonator, the proposed nanogenerator demonstrated its unique power in the field of acoustic energy harvesting. And it was demonstrated to recycle acoustic energy from a commercial cell phone when playing music, human talking on the

phone. As shown in Figure 2.42d, the recycled acoustic energy from a cell phone is capable of charging a commercial capacitor up to 1.8 V in about 12 seconds. Especially, when the paper thin triboelectric nanogenerator was installed on a wall or glass window, it can still recycle the environmental noise for electricity generation.
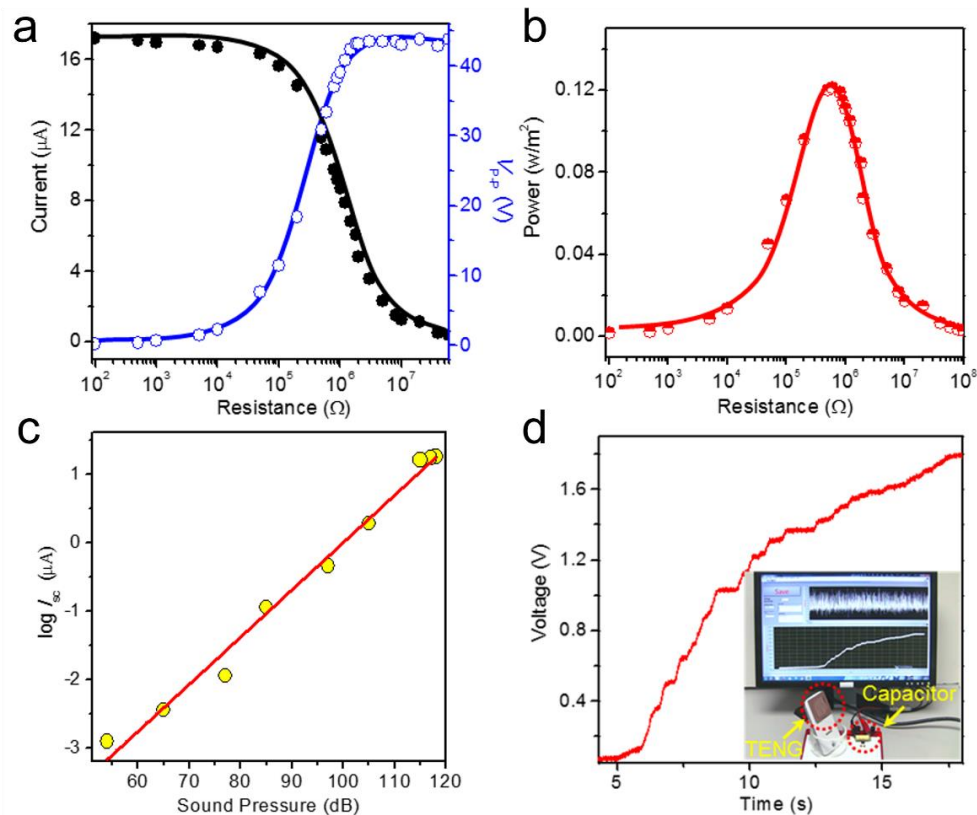
Figure 2.42 Performance evaluation of the paper thin triboelectric nanogenerator as a sustainable power source. (a) Dependence of the peak-to-peak voltage (Vp-p) and current output on the external load resistance. (b) Dependence of the peak power output on the resistance of the external load, indicating the maximum power output at R = 800KΩ. (c) Dependence of the electrical output on the input sound pressures. (d) Recycling the acoustic energy from the cell phone via charging a 2 μF capacitor. Inset is a photograph that shows a commercial cell phone equipped with a paper thin triboelectric nanogenerator for capacitor charging.[85]

Holding a collection of compelling features, including paper thin, rollable, broad working bandwidth, independent of resonator, the proposed nanogenerator demonstrated its unique power in the field of acoustic energy harvesting. Compared to other existing

95

technologies for acoustic energy harvesting, the paper based TENG distinguishes itself in many aspects and brings about a number of advantages.

From structure point of view, the traditional acoustic energy harvester has a bulky structure due to the requirement of a resonance cavity. Superiorly, the presented ultrathin triboelectric nanogenerator innovatively employs a multi-hole structure on the paper electrode, which effectively gets rid of the traditional resonator for acoustic energy harvesting. The paper thin TENG achieves a volume power density of ~1 kW/m^3 at a sound pressure of 117 dB$_{SPL}$.

From cost point of view, the ultrathin TENG is fabricated mainly based on low-cost, light-weight, and biodegradable paper materials with a simple structure. Besides, based on surface charging effect, the fabrication requires only very small amount of materials, which are conventional polymers or thin layer of metal as electrodes. Furthermore, the fabrication process of the paper-thin TENG is straightforward and compatible with possible large-scale manufacturing. Additionally, the backbone of paper thin TENG is made of commonly-used paper materials, which is biodegradable and greatly reduced the possible environmental costs. As a consequence, the paper-based TENG is extremely cost-effective, which is an unparalleled advantage compared to any other acoustic energy harvesting techniques.

CHAPTER 3

TENG TOWARD LARGE-SCALE BLUE ENERGY

Water wave, wind and solar irradiance, available in huge quantities, are clean and renewable energy sources with great potential.[1, 94-97] In comparison with solar and wind energy, energy from water wave in ocean may have several advantages. Widely distributed across the globe, water kinetic energy is one of the richest energy sources for large-scope applications. The energy provided by water wave has a much less dependence on season, day or night, weather and/or temperature. Although numerous studies have concluded that water wave power could contribute massive amounts to the overall energy consumption of the world, the utilization of water wave energy is way under explored.[90, 95, 97]

The general approach for harvesting mechanical kinetic energy is mainly based on electromagnetic effect, which, however, is likely to have possible limitations for harvesting water wave energy in ocean. First, the electromagnetic generator (EMG) is usually heavy and has a large mass density owing to the presence of magnets and metal coils, so it cannot naturally float on the surface of the water unless supported by a floater or a buoy platform. In ocean, the most dynamic energy presents at the surface of water. Secondly, the EMG is most effective to catch the power from a flowing stream, so that the wave energy of water cannot be effectively harvested. Lastly, the fabrication of EMG requires high-quality materials, so that it may not be cost-effective for applications at a large surface area.

3.1 Networks of TENG for blue energy harvesting

In this chapter, we presented a TENG network (TENG-NW) design as a potential

approach for harvesting large-scale water wave energy.[98] Relying on surface contact electrification effect between the conventional polymers and very thin layer of metal as electrodes, the TENG-NW is extremely light-weight, low-cost, high anticorrosion to the marine environment and capable of floating on the surface of water for wave energy harvesting. By using the collision of a rolling ball caused contact and separation, the TENG converts the slow, random and high-force all-directional oscillatory motions into electricity.

The basic unit of the TENG is arch-shaped top and bottom plates with a multilayer core, as schematically shown in Figure 3.1a. Both the top and bottom plates are made of polyethylene terephthalate, naturally bent by a heat treatment, which helps to carry out the action of effective charge separation and contact using the elasticity of the film. A photograph of an as-fabricated unit is shown in Figure 3.1b. Holding a sandwiched structure, both the upper layer and bottom layer of the functional core is polytetrafluoroethylene (PTFE) film with deposited copper as back electrodes. PTFE nanowires arrays were created on the exposed PTFE surface by a top-down method through reactive ion etching, which largely enhance the charge density of contact electrification. A scanning electron microscopy (SEM) image of vertically aligned PTFE nanowires is displayed in Figure 3.1c, which indicates that the average clustering diameter of FEP nanowires is 54 ± 3 nm with an average length of 1.5 ± 0.5 μm. Aluminum thin film with nanoporous surface is sandwiched between the top and bottom layers of the functional core, playing dual roles as an electrode and a contact surface. An SEM image of nanopores on the aluminum is presented in Figure 3.1d. The average diameter and depth of the aluminum nanopores are 57 ± 5 nm and 0.8 ± 0.2 μm, respectively, with a distribution density of 212 per μm^2.
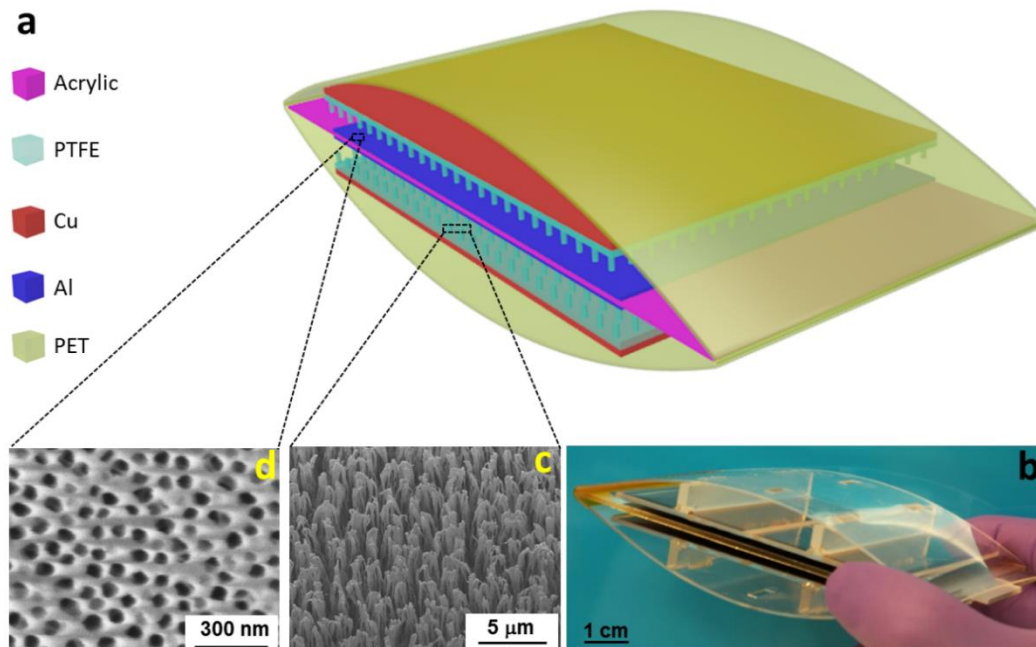
Figure 3.1 A single unit in a TENG. (a) Schematic illustration and (b) photograph of an as-fabricated minimum functional unit. (c) SEM image of PTFE nanowires. (d) SEM image of nanopores on aluminum electrode.[98]

The fundamental working principle of the reported TENG is based on the coupling between contact electrification and electrostatic induction,[99-107] as depicted in Figure 3.2. Here, both two-dimensional schematic illustrations of charge distribution (up) and potential distribution by COMSOL (down) were used for illustration. When an external force, for example, the collision from a rolling ball, is applied to the top plate of the minimum functional unit, which brings the two layers of PTFE into contact with middle aluminum simultaneously; charge transfer occurs at the contact interfaces. According to the triboelectric series, electrons are injected from aluminum into PTFE, since PTFE is much more triboelectrically negative than aluminum, generating positive triboelectric charges on the aluminum and negative ones on the PTFE (Figure 3.2a). Subsequently, if

the collision disappeared, the elasticity of the arch-shaped plates will lead to a separation between the PTFE and the aluminum.
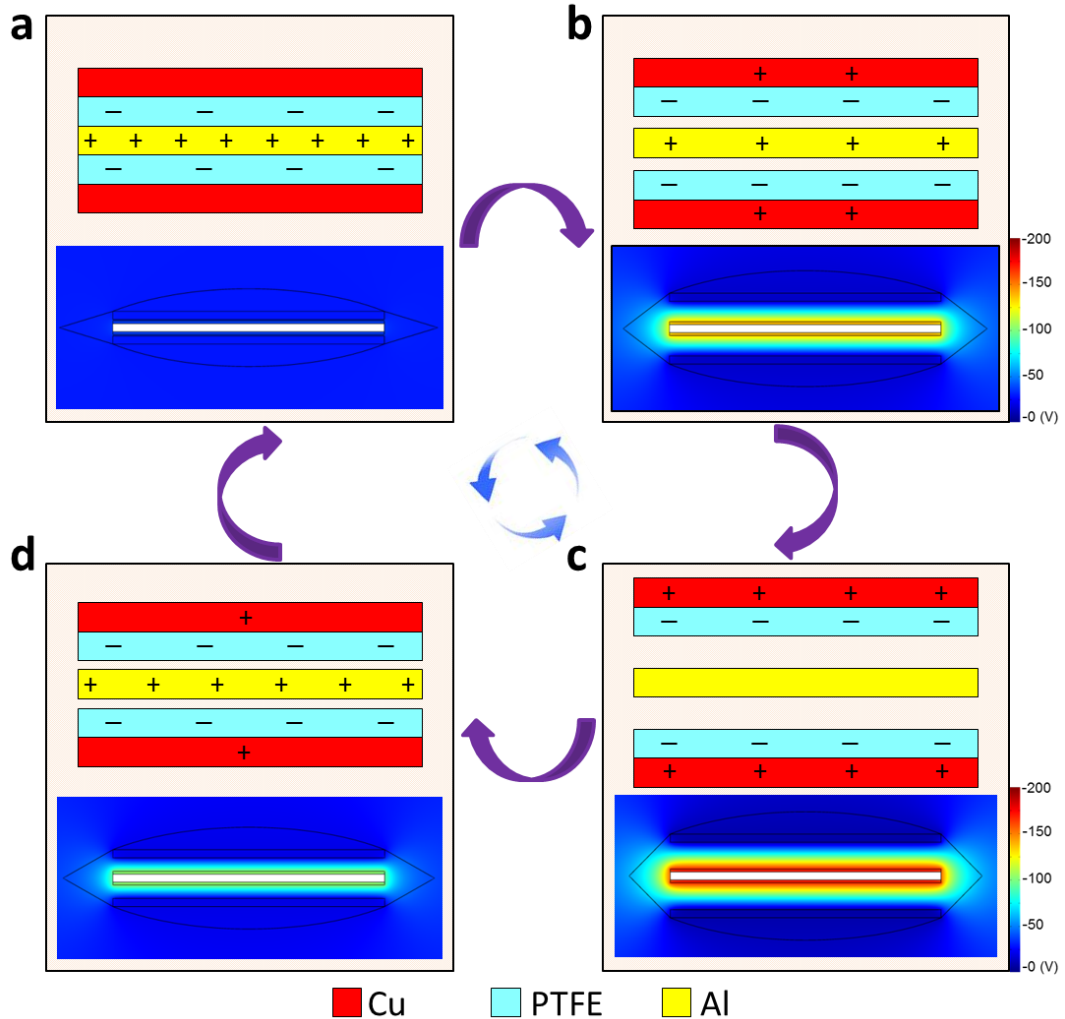
Figure 3.2 Schematics of operating principle of the TENG. Both two-dimensional schematic illustrations of the charge distribution (up) and potential distribution by COMSOL(down) were employed to elucidate the working principle of the minimum functional unit. (a) Initial state in which the PTFE is negatively charged after contact with aluminum. (b) When the PTFE and aluminum separates, electric potential difference drives the electrons from back electrodes to the contact electrode, screening the triboelectric charges and leaving behind the inductive charges. (c) With continuously increasing the separation, all the positive triboelectric charges almost entirely screened. (d) A reduced separation between the contact surfaces will drive the free electrons flow back to the copper electrode until the two contact surfaces come into contact. Notes: Aluminum nanopores and PTFE nanowires are not shown in the sketch for the simplification of illustration.[98]

As a result, the positive triboelectric charges and the negative ones no longer coincide on the same plane and generate an inner dipole moment between the two sets of contact surfaces. Such a dipole moment drives free electrons from the copper electrode to the aluminum electrode to balance out the electric field, producing positively induced charges on the copper electrode (Figure 3.2b). And the flow of electrons lasts until the upper plate reaches the highest point, where the corresponding separation is maximized (Figure 3.2c). Continuously, a reduced separation between the contact surfaces will weakened the dipole moment, free electrons flow back to the copper electrode until the two contact surfaces come into contact (Figure 3.2d), making a complete cycle of electricity generation process. Consequently, the kinetic energy from the water wave induced consecutive ball collisions result in a periodical-changing electric field that drives reciprocating flows of electrons between electrodes, producing alternating current in the external circuit.

We first study the performance of a single unit of TENG-NW for energy harvesting, a first step was to trigger the TENG by a ball collision as driven by gravity. A simple measurement platform was established, resort to that a 160-gram metal ball was controlled to collide at the center of the top plate with tunable acceleration and displacement. Dependence of the open circuit voltage and short circuit current on the acceleration and displacement of the ball collision are respectively exhibited in Figures 3.3a and 3.3b. As Figure 3.3a indicated, the voltage amplitude is an increasing function of the both acceleration and displacement of the rolling ball. Likewise, the current amplitude follows a same trend, as displayed in Figure 3.3b. And the open circuit voltage and short circuit

current, induced by the ball collision at acceleration of 10 m/s^2 and a displacement of 9 cm, shot up to 569.9 V and 0.93 mA, as respectively shown in the Figures 3.3c and 3.3d.
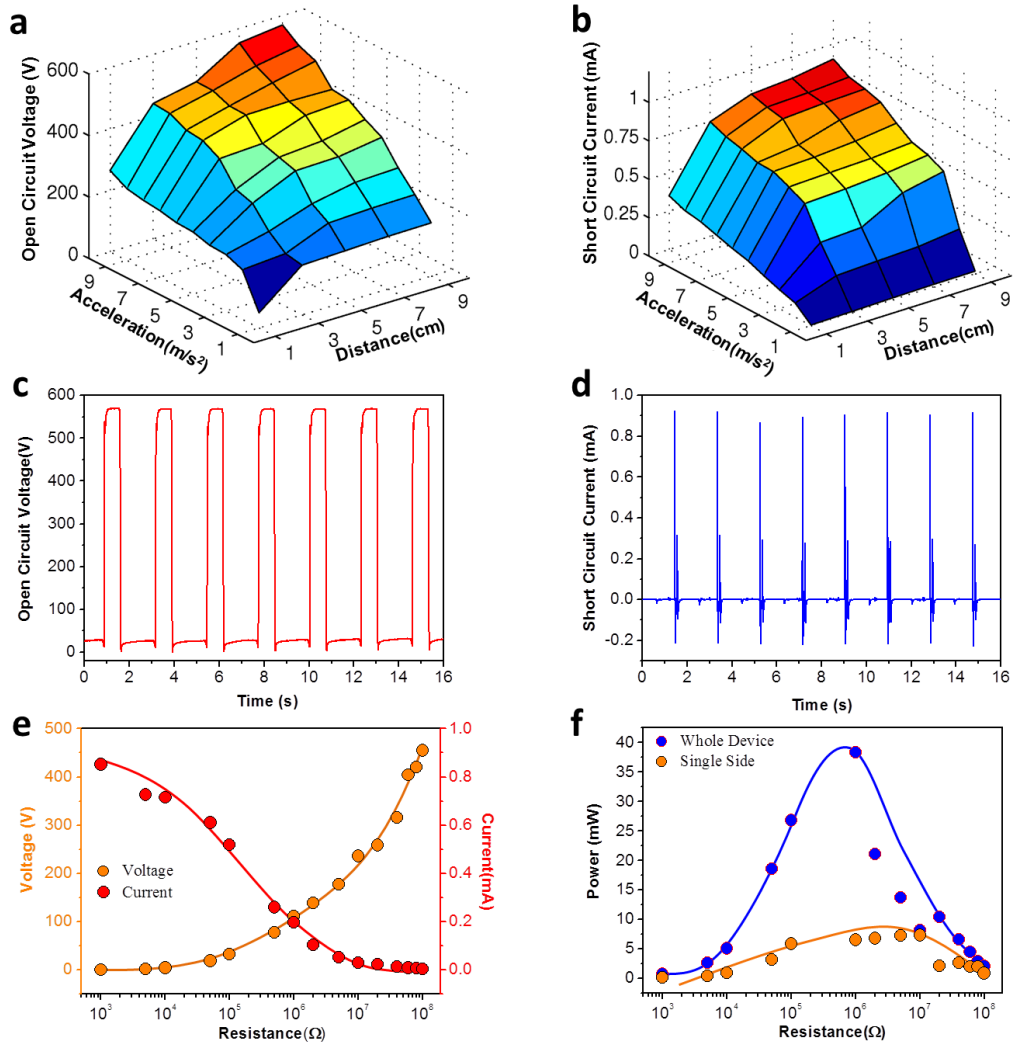
Figure 3.3 Electrical output characterization of a single unit of TENG. (a) Dependence of the open circuit voltage (a) and short circuit current (b) on the acceleration and displacement of a 160 grams metal ball collision. The open circuit voltage (c) and short circuit current (d) induced by the ball collision with an acceleration of 10 m/s^2 and a displacement of 9 cm. (e) Dependence of the voltage and current output on the external load resistance. The points represent peak value of electric signals while the lines are the fitted results. (f) Dependence of the peak power output on the resistance of the external load. Blue curve is for the whole device, indicating the maximum power output is obtained at 1 MW. The yellow curve is for the single side output, indicating the maximum power output is obtained at 5 MΩ.[98]

Resistors were utilized as external loads to further investigate the output power under the same condition. As displayed in Figure 3.3e, the current amplitude drops with increasing load resistance owing to the ohmic loss, while the voltage follows a reverse trend. As a result, the instantaneous peak power is maximized at a load resistance of 1 MΩ, corresponding to a peak power density of 0.26 mW/cm^2 (Figure 3.3f).
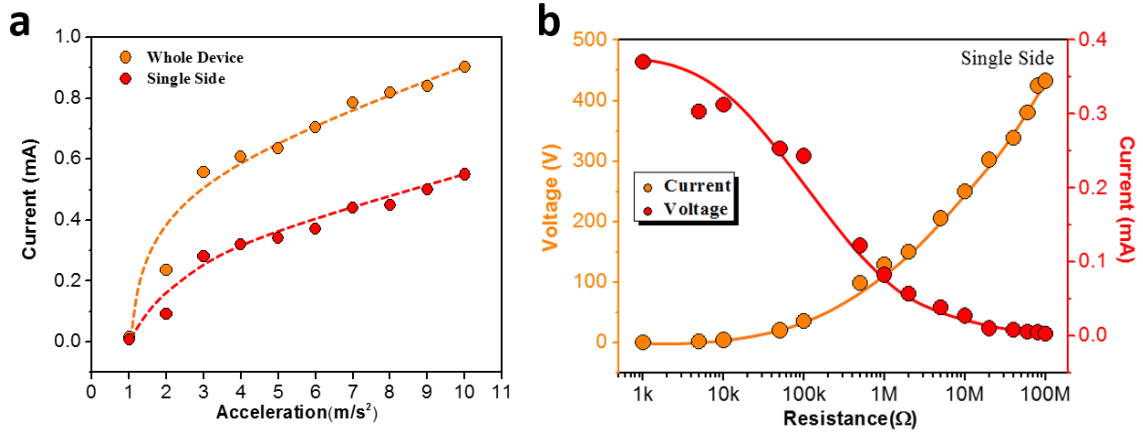
Figure 3.4 Electric output of the one side of the basic unit. (a) The current output comparison of the whole device with its single side, under a 160-gram metal ball collision from a displacement of 9 cm. (b) Dependence of the voltage and current output on the external load resistance. The points represent peak value of electric signals while the lines are the fitted results.[98]

Here, a further step was taken to investigate of the effectiveness of the synchronization for current output enhancement. Here, the basic unit of the TENG actually is made of two back-to-back functional units separated by a middle acrylic substrate. As shown in Figure 3.4a, under a same collision condition, the current output of the single side of the device is about half of that of the whole device. Likewise, the output power of the single side was also investigated. As demonstrated in Figure 3.4b, the voltage amplitude increases with increasing of the external load resistance, while the current follows a reverse trend. And thus, the instantaneous peak power of single side of the device is maximized at a load resistance of 10 MΩ, with a peak power density of 0.1mW/cm^2 (Figure 3.3f).

Consequently, the rational structure design effectively enhanced the current output as well as the energy conversion efficiency.
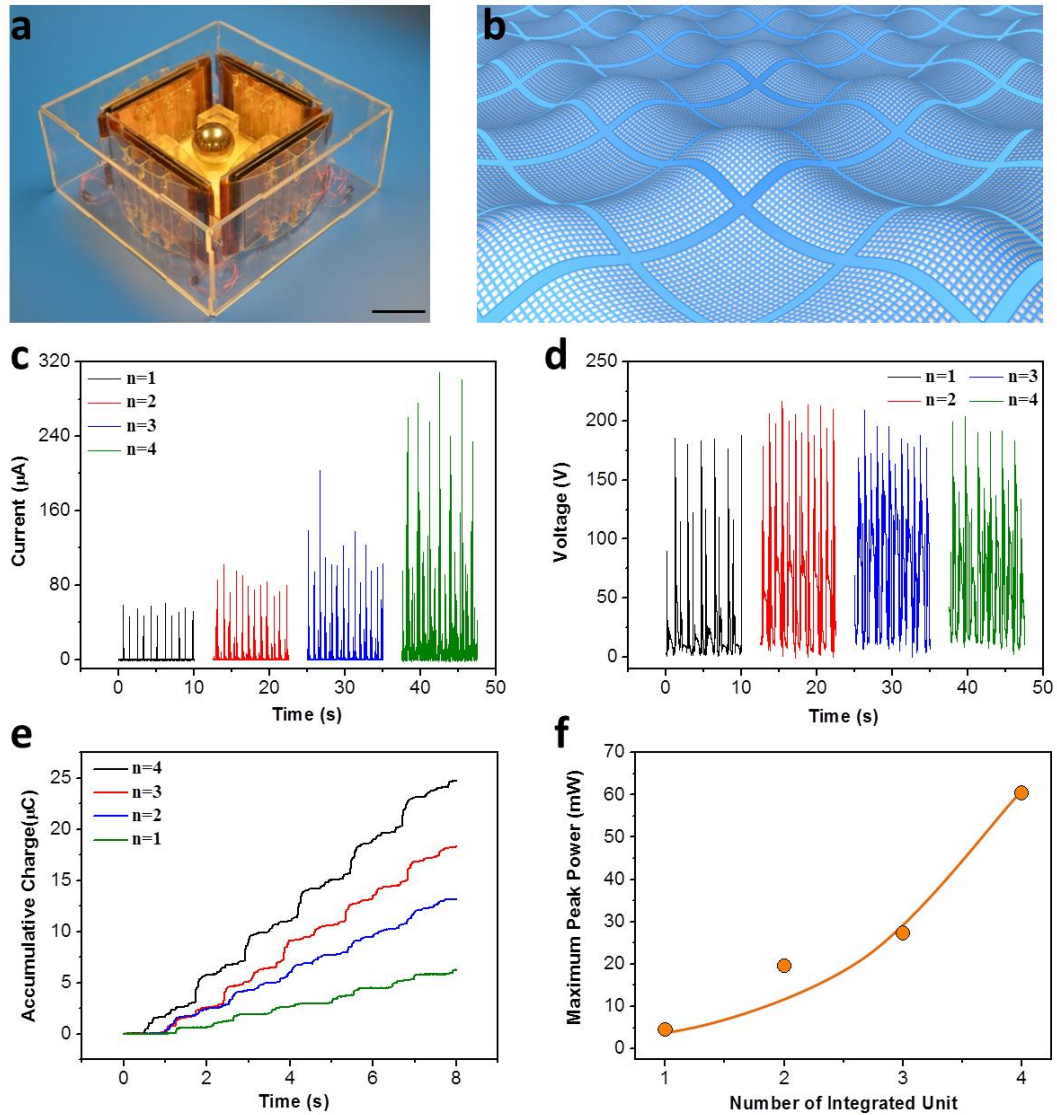
Figure 3.5 TENG-NW and its electrical output characterization for water wave energy harvesting. (a) Photograph of an as-fabricated single unit of the TENG-NW. The scale bar is 5 cm. (b) Schematic illustration of the TENG-NW that is consisted of thousands of single units. (c) Rectified short circuit current of the TENG-NWs with unit number n =1, 2, 3, 4. (d) Open circuit voltage of the TENG-NWs with unit number n =1, 2, 3, 4. (e) Accumulative induced charges generated by the TENG-NWs with unit number n =1, 2, 3, 4. (f) Dependence of the peak power output on the resistance of the unit numbers of TENGs. Here, all of the units are electrically connected in parallel.[98]

For wave energy harvesting, four basic units, vertically anchored, wall a metal ball to form a TENG, as the photograph shown in Figure 3.5a. Triggered by the water wave motion, the ball at the center of the single unit will collide with the walls, namely, the standing basic units. To develop a TENG-NW, thousands of TENGs will be electrically connected and wove into a network, as the sketch showing in Figure 3.5b. To deduce and demonstrate the law of the TENG-NW for blue energy harvesting, a further study was taken to investigate the output performance on the unit numbers. With this regards, four units were fabricated and wove into a small-scale network. The output characteristics regarding the scale of the TENG-NW were demonstrated in Figures 3.5c-3.5f. The output current and voltage of the TENG-NW with unit number n = 1, 2, 3, 4 were respectively demonstrated in Figure 3.5c and 3.5d. From the evolution of the output signals regarding the increasing unit numbers, certain trends can be derived for the TENG-NW.

Firstly, current amplitudes are drastically increased with elevated unit numbers. The average current amplitude at n = 1 is about 50.44 μA, which is greatly increased to 301.95 μA at n = 4, as indicated in Figure 3.5c. Secondly, the peak density of current output is also obviously increased when the unit number increased from 1 to 4. Thirdly, the peak density of voltage signals is still an increasing function of the unit number. Here the average voltage peak amplitudes hold almost constant with elevated unit numbers, which is attributed to the electrically parallel-connected units. Based on the above observations, it can be inferred that a quasi-direct/ direct output signal could be obtained if thousands of units working together as a TENG-NW. And also the output power frequency is totally controllable and tunable by configuration design of the TENG-NW. With a diode bridge, the total accumulative induced charges can also be measured, as show in Figure 3.5e. And

a directly proportional relationship was found between the unit number and the charging

accumulation rate. This is because more units in the TENG-NW means more collisions are

launched in a unit period of time, thus faster of triboelectric charges generation, and higher

charging accumulation rate is expected. Additionally, further effort was committed to

investigate the dependence of the peak power output on the resistance of the TENG-NW

unit numbers. As demonstrated in Figure 3.5f, the peak output power of the TENG-NW is

exponentially increased with the elevated unit numbers.

To extrapolate the capability of the TENG-NW for large scale blue energy

harvesting, the TENG-NW with a single unit was considered. The generated average power

E_0 in a single current peak can be calculated as:

$$E_0 = \alpha \cdot I_{sc} \cdot V_{oc} \cdot \Delta t \tag{3.1}$$

where I_{sc} and V_{oc} are the average short-circuit current and open-circuit voltage for the single

unit, which are 50 µA and 180 V, respectively. Δt is the peak width of the short-circuit

current with a value of 0.0184 s. And α is a factor in a range of 0 to 1. For a rough

estimation, assuming $\alpha = 0.5$. Submit all the value into eq 1, E_0 is calculated to be 82.8 µJ.

Regarding a single unit of the TENG-NW, one collision will generate two current

peaks with identical $I_{sc} \cdot \Delta t$, consequently, the generated average power E_c in one collision

can be estimated as:

$$E_c = 2 \, E_0 \tag{3.2}$$

And the generated power per second per unit volume E_{cv} can be expressed as:

$$E_{cv} = f \cdot \beta \cdot \frac{E_c}{V_o} \tag{3.3}$$

where β is the volume ratio of TENG-NW, since all of the units in the TENG-NW is not

close packing. Here, β is designed to be 0.6. V_o as the effective volume of a single unit.

According to the experimental design, V_o = 6cm· 12cm ·12cm= 864 cm^3. f is the ball collision frequency, assuming an average collision frequency is 2 Hz for the ocean wave. Thus, E_{cv} is estimated to be 0.23 J/m^3.

Features as extremely light-weight, high anticorrosion to the marine environment, it is reasonable to construct the TENG-NW with a depth of 5 meters in the ocean, then, the generated energy in a water area of 1 square kilometer per second could be estimated as :

$$E = 5m \cdot 1 \text{ km}^2 \cdot E_{cv} \tag{3.4}$$

Submit equation (3.3) into (3.4), E is thus calculated to be 1.15 MJ.

Consequently, an average power output of 1.15 MW was expected in a water area of 1 kilometer square for the reported TENG-NW. To demonstrate its feasibility as a practical power source, a small scale TENG-NW was developed with four units connected in parallel. As displayed in Figure 3.6a, a small TENG-NW with 4 units is floating on the water surface of a home swimming pool. As a light wind passed by, the aroused gentle wave can start to drive the TENG-NW, which is capable of realizing a self-powered SOS system for ocean emergency, as shown in Figure 3.6b.

Figure 3.6c is a schematic illustration of the configuration of the TENG-NW for practical applications. Here, a multi-layer electrical connection is proposed. In a foot layer, thousands of single units are electrically connected in parallel to form a community, which could effectively enhance the output current. In the upper layer, thousands of communities could be electrically connected in series to obtain an enhanced output voltage. As a result, both the current and voltage, amplitude and peak density, will be greatly boosted up to a high level for practical applications. Compared with current technologies for wave energy harvesting, the TENG-NW holds unprecedented advantages towards large-scale ocean

wave energy harvesting. Firstly, TENG-NW is suitable to harvest wave energy in a wide

range of wave motions, from subtle to strong, transverse wave to lateral wave.
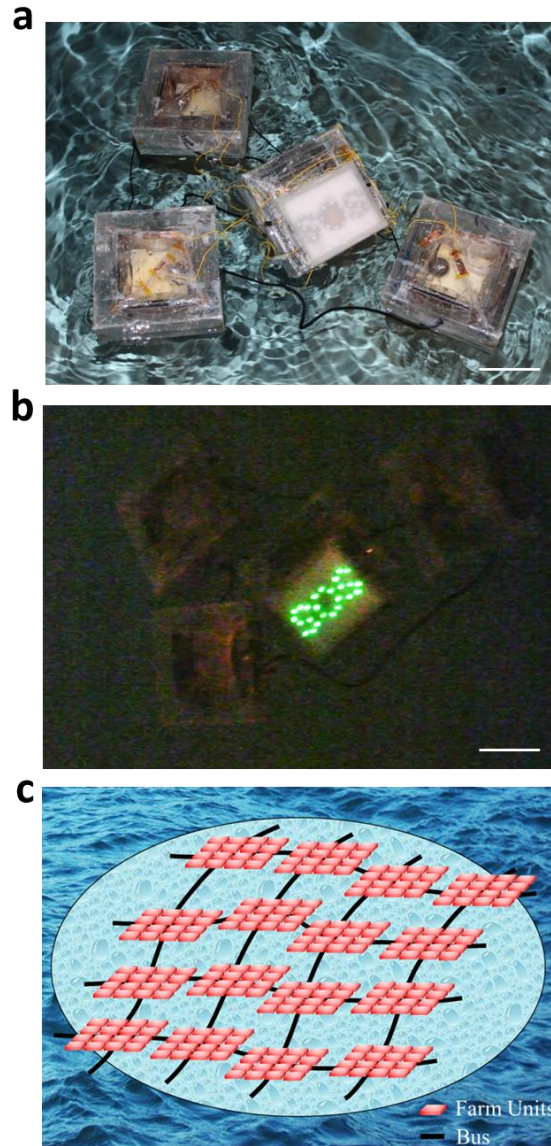
Figure 3.6 Demonstration of a small scale TENG-NW as a sustainable power source. (a) Photograph of a small scale TENG-NW with 4 units in a swimming pool. The scale bar is 10 cm. (b) Photograph shows the TENG-NW works and is capable of realizing a self-powered SOS system for ocean emergency. The scale bar is 10 cm. (c) Schematic illustration of the configuration of the proposed TENG-NW for practical applications.[98]

Furthermore, not like the electromagnetic effect based wave energy harvesting, which mainly relies on the undercurrents, the TENGs will show great potential in

harvesting energy from both the undercurrent and the surface waves. In addition, most of the wave motions are multidirectional, the TENG-NW, with a rationally designed structure, renders an innovative and effective approach to fully utilize the wave motion from all-directions. And it can not only be applied in the epicontinental sea, but also can easily be implemented in almost all of the water area.

Secondly, since the TENGs are mostly made from polymer materials without magnets, the load of the total device is expected to be decreased greatly compared to current electromagnetic generators, which are made from heavy materials (such as metals). Moreover, relying on the surface charging effect, only small amount of materials are needed. The TENG-NW is thus cost-effective as well as light-weight, which makes it possible high anticorrosion to the marine environment and floating on the water surface for wave energy harvesting, which will greatly eliminate the needs of building poles or towers for holding traditions electromagnetic generators for wave energy harvesting.

Thirdly, with the network architecture and packaging of individual TENG, the failure rate of the structure could be greatly decreased compared to the state-of-art technologies. And besides, in a case if any of a single unit in the TENG-NW was broken, the entire network can tolerate the failed one and the working status of the rest of the TENGs will not be affected.

In a word, with a distinctive working mechanism and rational designed device structures, the TENG-NW will distinguish itself in the field of energy harvesting with unique applicability, especially playing a complementary role in current development of wave energy harvesting.

CHAPTER 4

TENG AS SELF-POWERED ACTIVE SENSORS

Self-powered sensors can be generally realized by using the actively generated electrical signals in response to a stimulation/triggering from the ambient environment. Owing to the low-frequency sensitivity of TENG, it is ideally suited for sensing vibration and biological signals related to human health. The magnitude, frequency, number of periods and fine details in the voltage and current signals are directly determined by input mechanical behaviors. The voltage signal is a measure of the motion amplitude, and the current signal characterizes the dynamic processes of the mechanical motions. This Chapter systematically presents the applications of TENG for detection of sound waves, human cardiac signals as well as the ambient chemicals.

4.1 TENG as active acoustic sensors

In the previous section of 2.3, both organic thin-film based TENG and paper-thin based TENG were demonstrated to effectively recycle ambient acoustic energy. Actually, they are also capable of acting as self-powered active acoustic sensors with superior performance.

4.1.1 Helmholtz-cavity-based acoustic sensor

To justify the capability of organic thin-film based TENG as acoustic sensors, a first step is made towards investigating the response of the device to applied acoustic power

and frequency. To test, the acoustic frequencies are spreading from 0 Hz to 500 Hz. And

corresponding acoustic pressure ranging from 70 dB$_{SPL}$ to 110 dB$_{SPL}$ in a step of 5 dB$_{SPL}$

is controlled and measured by the sound level meter. The electric output is highly related

to the input acoustic pressures and frequencies, as demonstrated in Figures 4.1a and b.
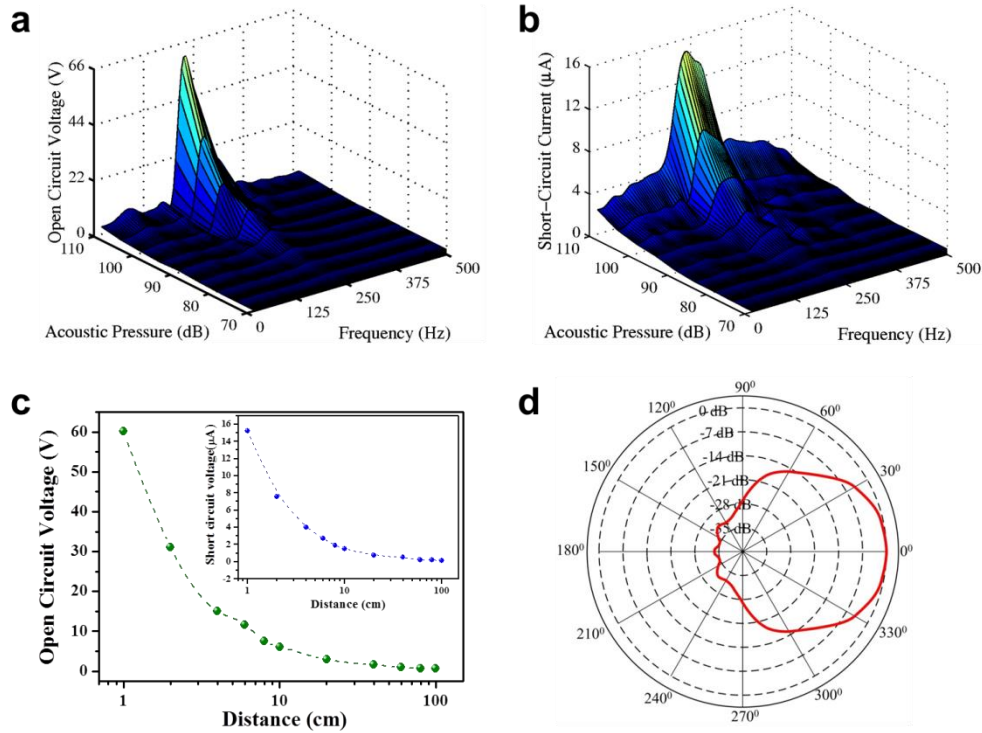
Figure 4.1 Electrical and acoustical performance evaluation of the organic film nanogenerators. (a) V_{OC} and (b) I_{SC} as a function of acoustic pressures and frequencies. (c) Nanogenerator acts as an active acoustic sensor for distance measurement as well as ambient acoustic source detection. When a sound source approaching the nanogenerator, the output signal is exponentially increased. (d) Directional pattern of the nanogenerator.[82]

As shown, at the resonant frequency of 240 Hz, with the decreasing of acoustic

pressure from 110 dB$_{SPL}$ to 70 dB$_{SPL}$, the V_{oc} is decreased from 60.50 V to 0.73 V, and the

short-circuit current is decreased from 15.10 µA to 0.19 µA. Based on the experimental

results, a MATLAB fitting renders a linear relationship between the open-circuit voltage

(V_{oc}) and the applied acoustic pressure P_{in} (in Pascal), which can be expressed as:

$$V_{oc} = 9.54 \cdot P_{in} + 0.13 \hspace{6cm} (4.1)$$

The sensitivity of the generator as a pressure sensor was 9.54 V Pa^{-1} in the acoustic pressure range from 0.063 Pa (70 dB$_{SPL}$) to 6.32 Pa (110 dB$_{SPL}$) at the frequency of 240 Hz. Furthermore, the acoustic waves decay in the course of propagation, thus the distance of the measured device to the acoustic source shows a tremendous impact on the electric output for acoustic energy harvesters. At a fixed acoustic pressure of 110 dB$_{SPL}$ and resonant frequency of 240 Hz, a distance depended electric output is measured, as shown in Figure 2.29C. The open-circuit voltage is decreased from 60.50 V to 0.81V, with short-circuit current decreasing from 15.10 µA to 0.21 µA, when the distance is increased from 1 cm to 100 cm. It is worth noting that the electric output attenuates at a rate of 6 dB each time when the distance from the acoustic source doubles.

For a comprehensive study of the proposed acoustic energy harvester, we still make a further step to evaluate the directional dependence (directivity) pattern of the as-fabricated devices. Anchor the device onto a rotary stage, then gradually increase the rotating angle from 0 to 360°, and measure the V_{oc} at the resonant acoustic frequency of 240 Hz. The corresponding directional pattern is obtained by normalizing relative to the peak response of voltage, as illustrated in Figure 4.1d. The test results show that the pattern is in shape of Cardioid and smooth as a function of rotating angle, and the -3 dB points are at +26^0 and -26^0 off axis, producing a total response angle of 52^0. At an angle of 90^0, the sound pressure level is reduced to -28 dB from the maximum value on-axis. The acoustic response of the device has a dependence on the incident angle of the sound waves, which is actually the stage rotating angle in the measurement. As a sound filter, the as-fabricated device is sensitive to the sound coming from directions within the response angle and

rejects the contribution from other angles, which renders it a great potential in the application of directional microphones.

A series of practical applications were demonstrated to show the capability of the TENG as active self-powered acoustic sensors. The first demonstration for the nanogenerators is to work as a self-powered microphone. The natural frequencies of the devices can be designed by parameters configuration, and their corresponding frequency bands are able to overlap with each other, rendering us a broadened working bandwidth. Here, as demonstrated in Figure 4.2a, four nanogenerators, NG_1, NG_2, NG_3 and NG_4, respectively with varying resonance frequencies of 350 Hz, 650 Hz, 1100 Hz and 1400 Hz, were employed to widen the overall working bandwidth from 10 Hz to 1700 Hz, which assured the superior performance of the nanogenerators as a self-powered microphone for sound recording. For experimental measurement, a multi-channel signal acquisition implant was designed by LabVIEW to collect the electric outputs at a sampling rate of 44.1 kHz. Figures $4.2b_1$ and $4.2b_2$ are respectively the time domain waveforms of the recorded sounds from NG_1 and NG_4.

Although NG_1 and NG_4 share the same sound source, the waveforms of the two apparently exhibit different characteristics, which is attributed to a different frequency response ranges of the two. With a natural frequency of 350 Hz, the waveform of NG_1 is smoother owing to its dominant response to lower frequency components from 10 Hz to 600 Hz, as shown in Figure $4.2b_3$, which is the corresponding Short-Time Fourier Transform (STFT). While the waveform of NG_4 with a natural frequency of 1400 Hz is rougher, due to its dominant response to the higher frequency components from 1100 Hz to 1700 Hz, as demonstrated in Figure $4.2b_4$ of its corresponding STFT.
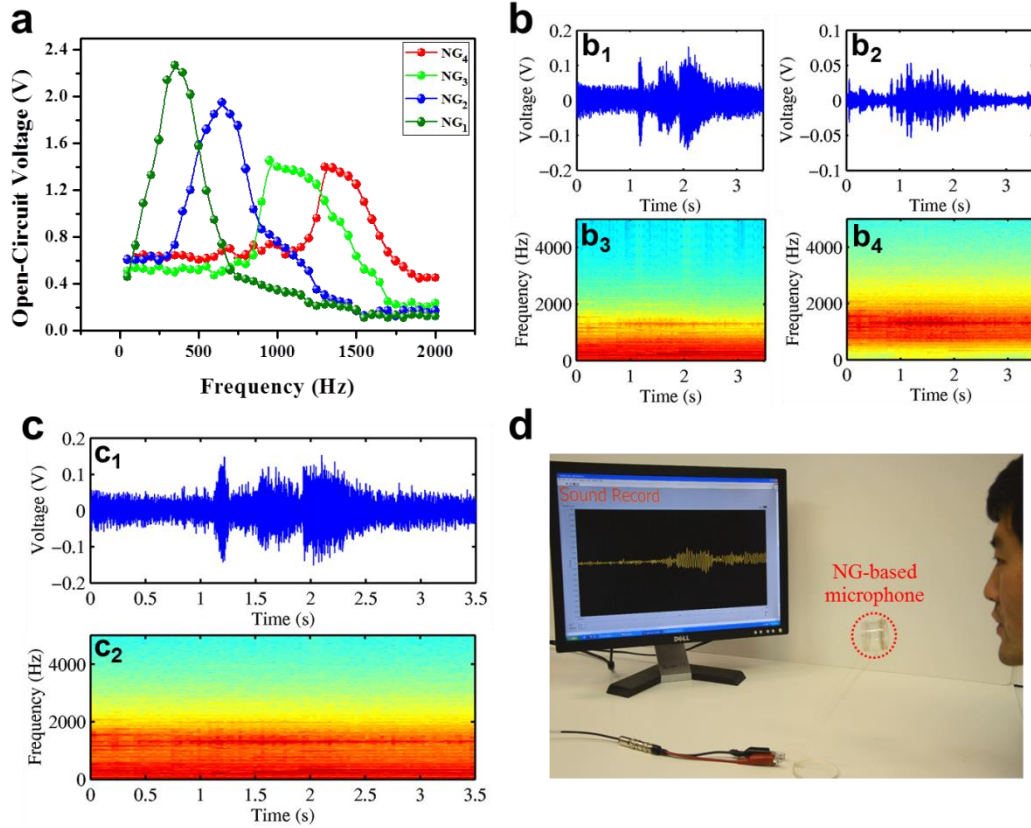
Figure 4.2 Demonstration of the organic film nanogenerator acting as a self-powered microphone. (a) Frequency responses from the nanogenerators array, which consists of four NGs with various designed natural frequencies, aimed to enhance the overall working bandwidth. (b$_1$, b$_2$)Sound waveforms of the signals acquired by NG$_1$ and NG$_2$, respectively; (b$_3$, b$_4$) Short-Time Fourier Transforms of the acquired signals by NG$_1$ and NG$_2$, respectively. (c) Sound waveform and corresponding Short-Time Fourier Transform of the signals acquired by the array of the NGs. (d) Photograph that shows a NG is working as a self-powered microphone for sound recording.[82]

In order to reconstruct the original sound, the acquired acoustic signals of the array are weighted according to the relative amount of information available from each source. The reconstructed signal S_{re} can be mathematically expressed as:

$$S_{re} = \sum_{i=1}^{4} a_i s_i \tag{4.2}$$

114

where a_i is a weighting factor, which is a function of speech-to-noise following a rule of

$$\sum_{i=1}^{4} a_i = 1.$$ And s_i is the acquired output acoustic signal from NG_i ($i = 1, 2, 3, 4$).

The waveform of the reconstructed signal by equation (4.2) and its corresponding STFT are illustrated in Figures 4.2c$_1$ and 4.2c$_2$, respectively. The frequency components of the reconstructed signal cover all the frequencies ranging from 10 Hz to 1700 Hz, as demonstrated in Figure 4.2c$_2$. As a practical demonstration, two songs are recorded and reconstructed by the array of as-fabricated nanogenerators. Figure 4.2d shows an as-fabrication nanogernator is working as a self-powered microphone for sound recording.

The second demonstration of the nanogenerator for sensing purpose is to act an acoustic source localization sensor. Experimentally, three as-fabricated nanogenerators arranged in an L shape, and anchored in a 2-dimensional (2D) plane with dimensions of 2 m by 1.8 m, as schematically shown in Figure 4.3a and a corresponding photograph in Figure 4.3b. The sound was created by bursting a small balloon in the 2D plane as acoustic sources. A customized triple-channel data acquisition system based on LabVIEW was used to collect the sensing signals from the acoustic sensors (ASs). Figure 4.3c elucidates the acoustic signals acquired by the ASs when a balloon burst at the center of the 2D plane. When another balloon bursting spot is settled with various distances to the ASs, the three acoustic signals show obvious discrepancies in response starting time and magnitude.

The acoustic localization algorithm presented in this work is based on the estimation of the time difference of arrival (TDOA) at pairs of acoustic sensors. Let $\mathbf{S}_k = [X_k, Y_k]^T$ denote the location of kth AS with $k = 1, 2, 3$. And $\mathbf{P} = [x, y]^T$ represents the location of the acoustic source. Then, the distance $d(\mathbf{P}, \mathbf{S}_k)$ between acoustic source and the kth sensor can be expressed as:

$$d(\mathbf{P}, \mathbf{S}_k) = \|\mathbf{S}_k - \mathbf{P}\| \tag{4.3}$$

And the time delay in TDOA at $\mathbf{S}_i$ and $\mathbf{S}_j$ is given by:

$$\tau_{ij}(\mathbf{P}) = \left(d(\mathbf{P}, \mathbf{S}_i) - d(\mathbf{P}, \mathbf{S}_j) \right) / c \tag{4.4}$$

where $i, j = 1, 2, 3$, and $i \neq j$. The in-pair evaluating TDOA of acquired signals by ASs can be achieved by computing the cross-correlation function of these two signals. Let $z_i(n)$ and $z_j(n)$ denote the signals acquired by AS_i and AS_j, respectively, where n is the sample time index. Then, the cross-correlation function $R_{z_i,z_j}(\tau)$ between AS_i and AS_j is defined as:

$$R_{z_i,z_j}(\tau) = \sum_{n=1}^{N} z_i(n) z_j(n + \tau_{ij}) \tag{4.5}$$

where N is the number of the sample points. The time difference between the two acquired signals is estimated by the time lag at the highest peaks of their cross-correlation functions.

Two correlation functions of the three acquired acoustic signals in Figure 4.3c were derived from equation (4.5), as shown in Figure 4.3d. It is worth noting that the time lags of the two cross-correlation functions between AS_1 and AS_2 as well as AS_2 and AS_3 are zero, indicating the same distance is travelled by the sound from the acoustic source to the ASs, which is well consistent with the real experimental case. Give the distances between the three acoustic sensors and also the in-pair time delay information, the acoustic source can be localized/positioned as the intersection of the two hyperbolic curves by virtue of the speed of sound and geometry.

Experimentally, positioning within an average error circle of 7 cm in diameter is achieved based on multiple measurements, which mainly depends on the signal-to-noise ratio (SNR), if the SNR of the acquired signals is comparable with each other, and the error will stay within a same average error circle even if the distance between the source and the

ASs is more than hundreds of meters. The proposed acoustic sensors in this work have extensive applications in the fields such as military surveillance and reconnaissance, intruder detection, sniper localization, underwater acoustics, and auto talker detection in a web conferencing.
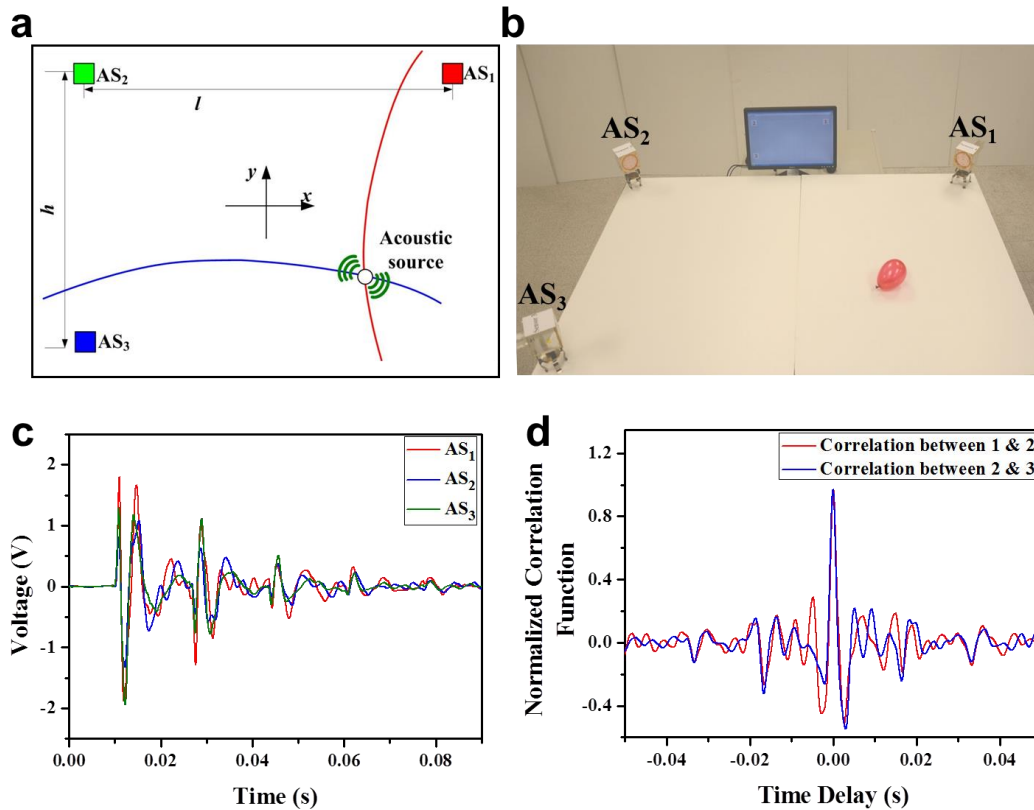
Figure 4.3. Demonstration of the organic film nanogenerator acting as an active sensor for acoustic source localization. (a) Schematic illustrations and (b) photograph showing the working mechanism of nanogenerators for sound localization. (c) Acquired acoustic signals from the three nanogenerators when a balloon burst. (d) Correlation functions of the acquired acoustic signals from AS_1, AS_2 and AS_3.[82]

In summary, the as-fabricated Helmholtz-cavity-based organic thin film TENG was proved to be active self-powered acoustic sensors for both self-powered sound recording and acoustic source localization. This work presented a milestone progress in TENG-based active sensors.

4.1.2 Ultrathin paper-based acoustic sensor

The bulky structure of the Helmholtz resonance cavity greatly limited the wide-range application of the TENG as an acoustic sensor. A further improved performance of the acoustic sensor is on the basis of an ultrathin, rollable, and paper-based TENG, which innovatively employs arrays of micro holes for acoustic response, as detailed described in the Section 2.3.2.

With a broad working bandwidth, the as-fabricated paper thin TENG is also capable of acting as an active self-powered microphone for sound recording.[85] As demonstrated in Figure 4.4a, a low-cost ultra-thin self-powered microphone was developed, which can efficiently convert the human voice into electrical signals for the recording purpose. Compared to other existing technologies for acoustic energy harvesting, the paper based TENG distinguishes itself in many aspects and brings about a number of advantages, such as ultrathin, rollable, low-cost, environmentally friendly and extremely high volume power density.

Owing to the superior advantages of structurally ultrathin and flexible, the paper based TENG is rollable. And, for the first time, a novel rolled type device is demonstrated. Figure 4.4b and 4.4c are the schematic illustrations to show the measurement of the directional patterns of the flat and rolled paper thin TENG with insets being the photographs of the as-fabricated devices. Figure 4.4d shows the corresponding shape dependent directional patterns of the TENG with flat and rolled structure, respectively. And a butterfly shaped directional pattern with mirror symmetry was observed for the flat type paper thin TENG. While the directional pattern of the rolled type is a highly symmetric circle, which indicates the output is independent of the sound wave incident direction. This is mainly attributed to the rigorous structural symmetry.
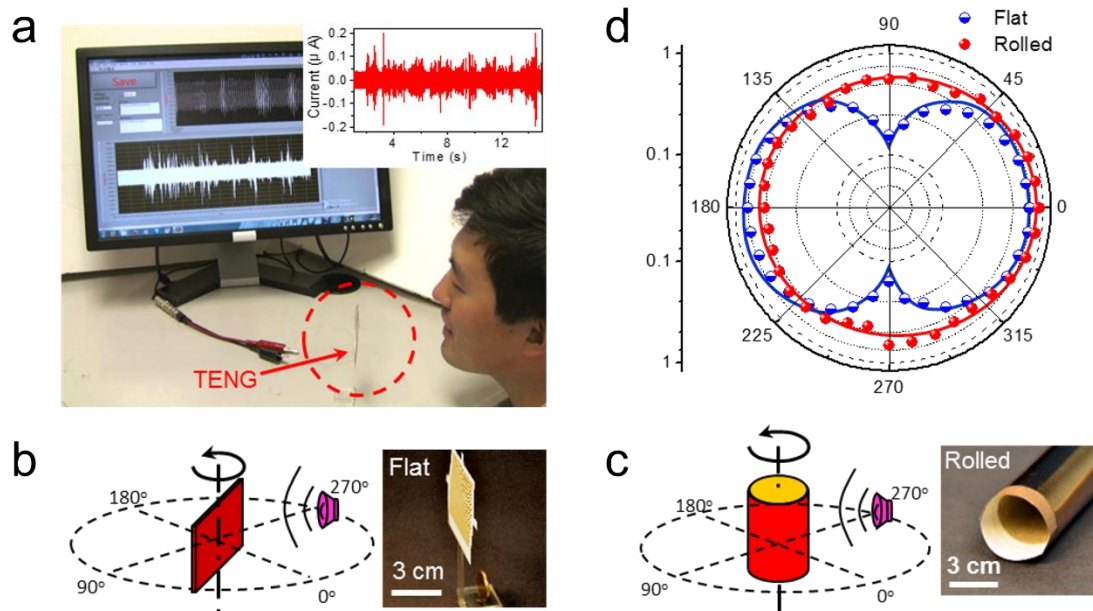
Figure 4.4 Demonstration of the paper thin TENG for self-powered sound recording. Schematic illustration to show the measurement of the directional patterns of the (a) flat and (b) rolled paper thin TENG. Right sides are the photographs of the as-fabricated devices. The scale bars are 2.5cm. (c) Shape dependent directional patterns of the paper thin TENG. (d) Photograph that shows a paper thin TENG is working as a self-powered microphone for sound recording. Inset is the acquired electrical signals.[85]

Holding the advantage of directional independence, the paper thin TENG is suitable to a wide range of circumstances for self-powered acoustic sensing purposes, such as theatric stage omnibearing live recording, military surveillance and so on.

4.2 An intelligent keyboard

Computer keyboard is one of the most common, reliable, accessible and effective approaches used for human-machine interfacing and information exchange. Although keyboard has been used for hundreds of years for advancing human civilization, studying human behavior by keystroke dynamics using smart keyboard remains a great challenge.

Here we report a self-powered, non-mechanical-punching keyboard enabled by contact electrification, a ubiquitous but underexplored phenomenon,[108-111] between human fingers and keys, which converts mechanical stimuli applied onto the keyboard into local electronic signals without applying an external power.

The key functional element (KFE) of the IKB is composed of vertically-stacked transparent thin film materials.[112] A layer of polyethylene terephthalate (PET) sits between two layers of ITO that are the bottom and the top electrodes. Then, a layer of fluorinated ethylene propylene (FEP) is applied onto the ITO surface as an electrification layer that generates triboelectric charges upon contact with human fingers, as schematically shown in Figure 4.5a. FEP nanowires arrays were created on the exposed FEP surface by a top-down method through reactive ion etching.

A scanning electron microscopy (SEM) image of vertically aligned FEP nanowires is displayed in Figure 4.5b, which indicates that the average clustering diameter of FEP nanowires is 104 ± 21 nm with an average length of 0.8 ± 0.2 μm. The static contact angle of the FEP surface was measured by a sessile droplet method with a 2 μl water droplet. Inset of Figure 4.5b is the contour of the resting droplet, which indicates a contact angle of 160° by Young-Laplace fitting. Meanwhile, a tilting base method was employed to investigate the surface sliding angle of the IKB. The superhydrophobicity of the IKB surface assures its self-cleaning property, which can effectively keep the keyboard free of dirt and grime.
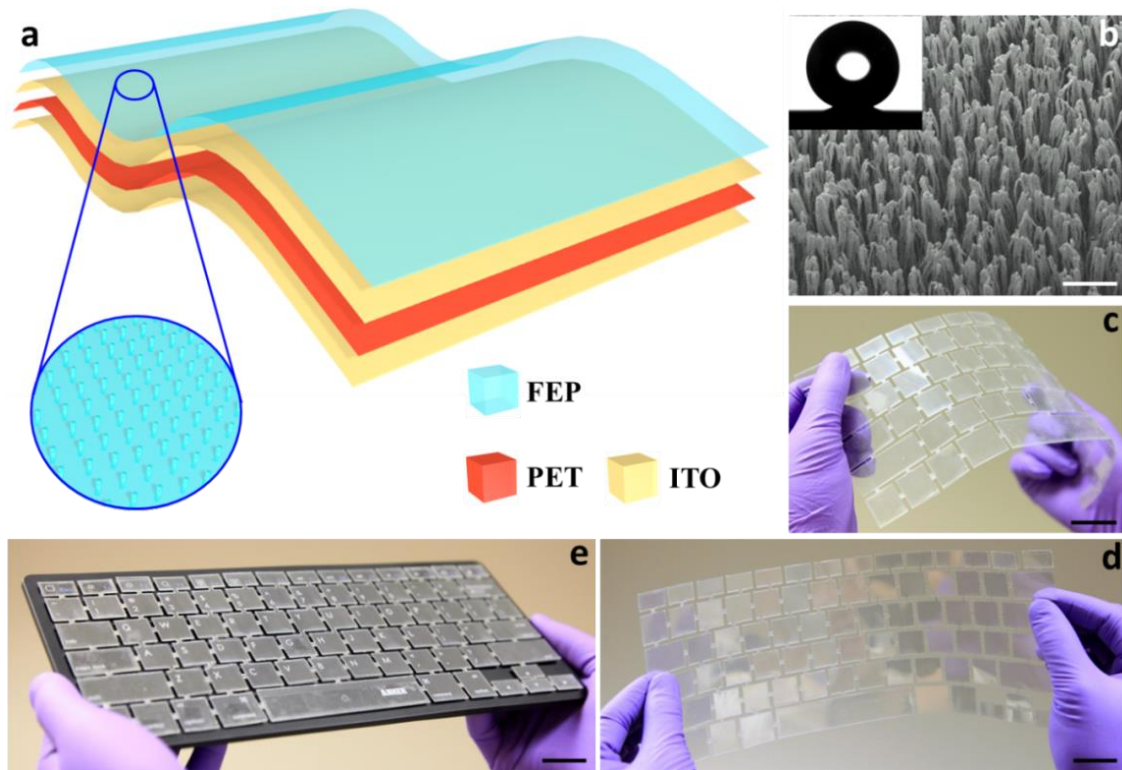
Figure 4.5 Structural design of the KFE of the intelligent keyboard. (a) Schematic illustrations of the KFE. Inset: enlarged schematic of FEP nanowires on the top surface. It is noted that these drawings do not scale. (b) SEM image of FEP nanowires. Inset is the contour of resting droplet for surface static contact angle measurement. The scale bar is 500 nm. (c, d) Photograph of a flexible and transparent KFE. The scale bars are 3 cm. (e) Photograph of an as-fabricated IKB, which is system integration of KFE and a commercial keyboard. The scale bars are 3 cm.[112]

A photograph of an as-fabricated KFE is shown in Figures 4.5c and d, plainly demonstrating its flexibility, transparency and one-piece structure without mechanical punching. Figure 4.5e is a photograph of an IKB after assembling the KFE with a commercial keyboard.

The basic working principle of the IKB is based on the coupling between contact electrification and electrostatic induction rather than the traditional mechanical switching. An electricity generation process from a key unit is depicted in Figure 4.6. Here, both two-

dimensional schematic illustrations of charge distribution (up) and three-dimensional

potential distribution by COMSOL (down) were used for illustration.
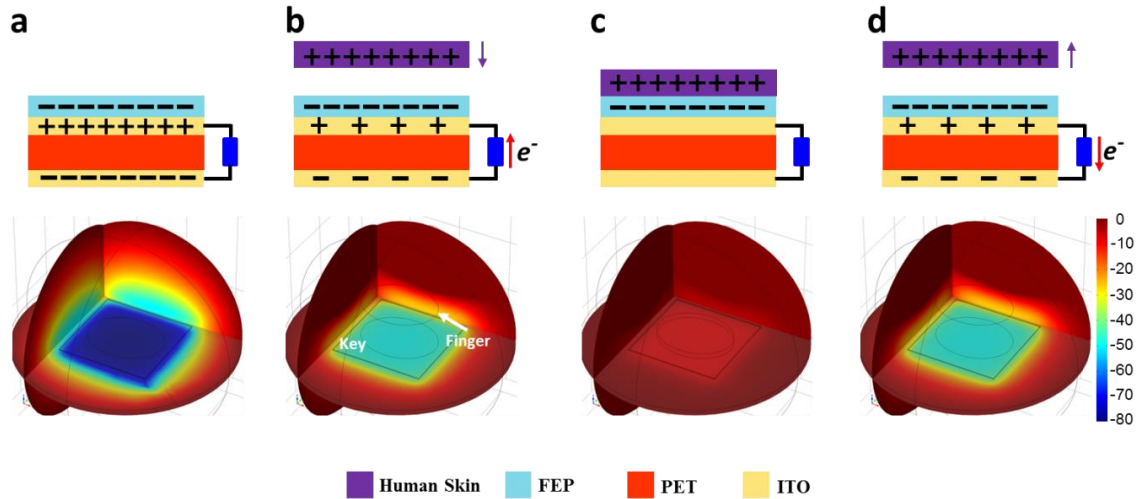
Figure 4.6 Schematics of operating principle of the intelligent keyboard. Both two-dimensional schematic illustrations of charge distribution (up) and three-dimensional potential distribution by COMSOL (down) were employed to elucidate the working principle of IKB. (a) Initial state in which the FEP is negatively charged after contact with human finger. (b) When a keystroke is initiated, the approach of positively charged human finger results in free electrons flowing from bottom ITO electron to top electrode. (c) The current in the external circuit lasts until the human finger fully contacts with FEP. (d) When the finger is up and a separation occurs, it produces another current in the external circuit flowing from the bottom electrode to top electrode.[112]

When a human finger is brought into contact with FEP, charge transfer at the

contact interface occurs. According to the triboelectric series,[113] electrons are injected from

human skin into FEP, since FEP is much more triboelectrically negative than human skin,

generating positive triboelectric charges on the human skin and negative ones on the FEP.

Subsequently, if the human finger moves away, the negative charges on the FEP side will

induce positive charges on the top ITO electrode and thus equal amount of negative charges

on the bottom electrode (Figure 4.6a). Once a keystroke is initiated, the positively charged

human finger approaches the keyboard, the induced positive charges on the top electrode

are expelled, resulting in a flow of free electrons from the bottom electrode to top electrode

(Figure 4.6b) until the finger and the key are in contact (Figure 4.6c). When the finger separates, free electrons flow backward from the top electrode to the bottom electrode (Figure 4.6d). This is a full cycle of the electricity-generating process. It is worth noting that the triboelectric charges don't dissipate but remain on the FEP surface for an extended period of time. Consequently, consecutive keystrokes result in a periodical-changing electric field that drives reciprocating flows of electrons between electrodes.

Intelligent keyboard was firstly demonstrated as a self-securing wireless warning system by integrating with a signal-processing circuit. The circuit diagram of the complete IKB based self-securing system is shown in Figure 4.7. This customized circuit for the IKB holds two unique advantages. First, a designed trigger voltage threshold of 5 V enables the IKB to work stably even in a high electrical noise environment. Second, the alarm time is controllable and tunable by the signal processing circuit.

Figure 4.7 Circuit diagram of the complete self-securing system. It consists of an IKB and a signal processing circuit.[112]

Once a finger gently strokes a key, the generated voltage signal triggers an IC timer that controls a wireless transmitter and remotely switches a siren between a panic state and a silence state.

Figure 4.8 Keys classification in the intelligent keyboard. The keys in the keyboards are classified into seven kinds according to their dimensions.[112]

The keys in the keyboards are categorized into seven regions (Figure 4.8) according to their dimensions to compare their output voltages. The obtained results are shown in Figure 4.9a. An increasing function between key dimensions and the output voltage is observed. The reason is that contact electrification is a surface charging effect, a larger amount of triboelectric charges will contribute to a higher voltage output.[114] Figure 4.9b is an enlarged view of the output voltage when the smallest key is gently touched. Even this lowest voltage was capable of triggering the siren that produced a sharp alarm with flashing light (Figure 4.9c). Furthermore, a customized multi-channel data acquisition system was designed for the IKB to individually address the electric signal from each key (Figure 4.9d). Consequently, the real-time tracing and recording during typing can be realized. Every channel was electrically but independently connected to a key in the keyboard as a functional unit, and each unit was connected to the ground through a 1 MΩ resistor.
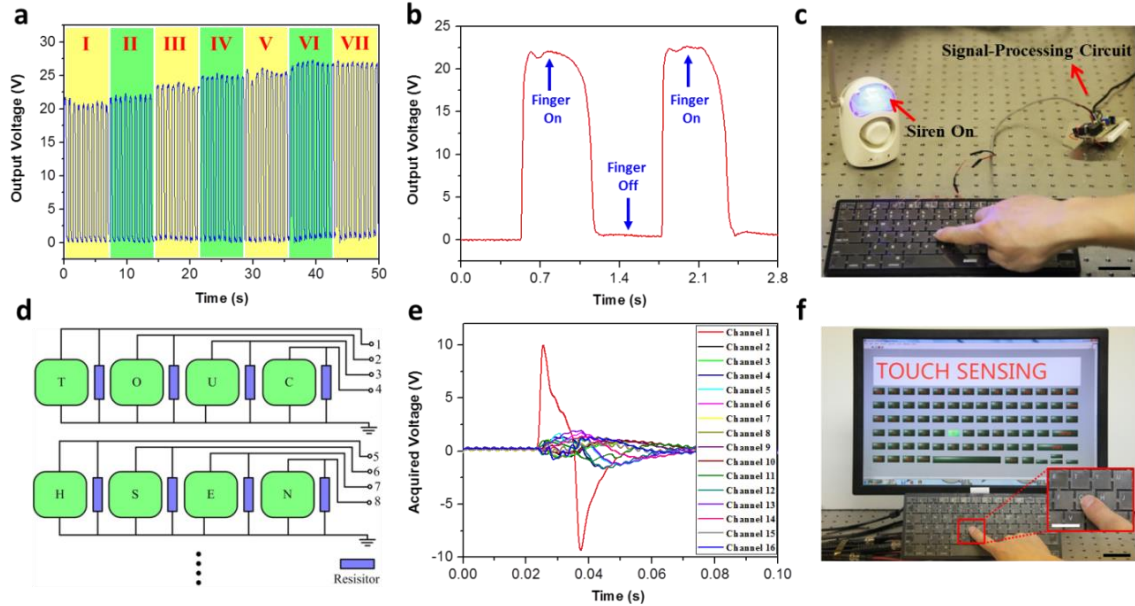
Figure 4.9 Intelligent keyboard as a self-securing system. (a) Measured output voltage is an increasing function of the key dimensions when a gentle keystroke was applied. (b) An enlarged view of obtained output voltage when the smallest key is gently touched. (c) Triggering a wireless alarm system by gentle finger tapping on the IKB. The scale bar is 5 cm. (d) Schematic diagram of keyboard based multi-channel data acquisition system for keystroke tracing and real-time recording. (e) The system acquired output voltage signals when the key "T" was stroked. (f) A photograph demonstrated the IKB for the real-time keystroke tracing and recording. A continuously typing string "TOUCH SENSING" was recorded in real time without uncomfortable delay. The scale bar is 5 cm. Inset: an enlarged view of the key "G" was stroked. The scale bar is 2 cm.[112]

When a keystroke was initiated on a particular key, "T" for example, a peak output voltage up to 10 V was acquired from the corresponding channel, while signals from other keys were less than 2.5 V (Figure 4.9e). Theoretically, the signals from untouched keys should be 0. However, a certain voltage signals were observed experimentally, which is mainly due to the coupling among all of the channels in the data acquisition system.[115, 116] For recognition purpose, the maximum peak value of the output voltage from channel i, V_{pi}, was extracted. Then the threshold voltage V_{th} can be analytically expressed by the following equation using Pauta Criterion Method.

$$V_{\mathrm{th}} = \frac{1}{n}\sum_{i=1}^{n} V_{\mathrm{pi}} + \frac{3}{\sqrt{n}}\sqrt{\sum_{i=1}^{n} V_{\mathrm{pi}}(V_{\mathrm{pi}} - 1)} \qquad (4.6)$$

where n is the total number of channels, and i is integral from 1 to n. Once the extracted V_{pi} is higher than V_{th}, the key corresponding to this particular channel is considered to be stroked. Figure 4.9f demonstrates the real-time keystroke tracing and recording. When a phrase "TOUCH SENSING" was continuously typed, it was simultaneously recorded and displayed without noticeable delay.

Typing patterns based on dimensional keystroke timing vector, lacking of uniqueness and permanence, largely hinder the practicality and acceptability of behavioral biometric of keystroke dynamics as effective identifier to current authentication system. The IKB in this work provides a superior route in creating accurate, unique, and permanent typing patterns for verification and identification purposes. As demonstrated in Figure 4.10, three sets of original typing patterns (in red curves) were respectively obtained for three typists Tom, Mike, and Alex, who independently typed the word "touch" for more than four times on the IKB in each accustomed manner. Each set of typing pattern corresponds to two subsets of characteristic signals (voltage and current), which are time-series data. These electric signals correlate to a variety of information, including the manner and rhythm of the keystroke, typing habit, finger size, individual bioelectricity, and applied typing force. Thus, they can not only characterize the keystroke timing, but also quantitatively record the concrete dynamic changes in the course of typing. The as-collected electric signals look apparently different from each other. For quantitative differentiation, Discreet Fourier Transformation (DFT) was performed to obtain frequency features of the electric signals. Wavelet transformation was carried out to simultaneously obtain both time domain and frequency domain features of the typing patterns.
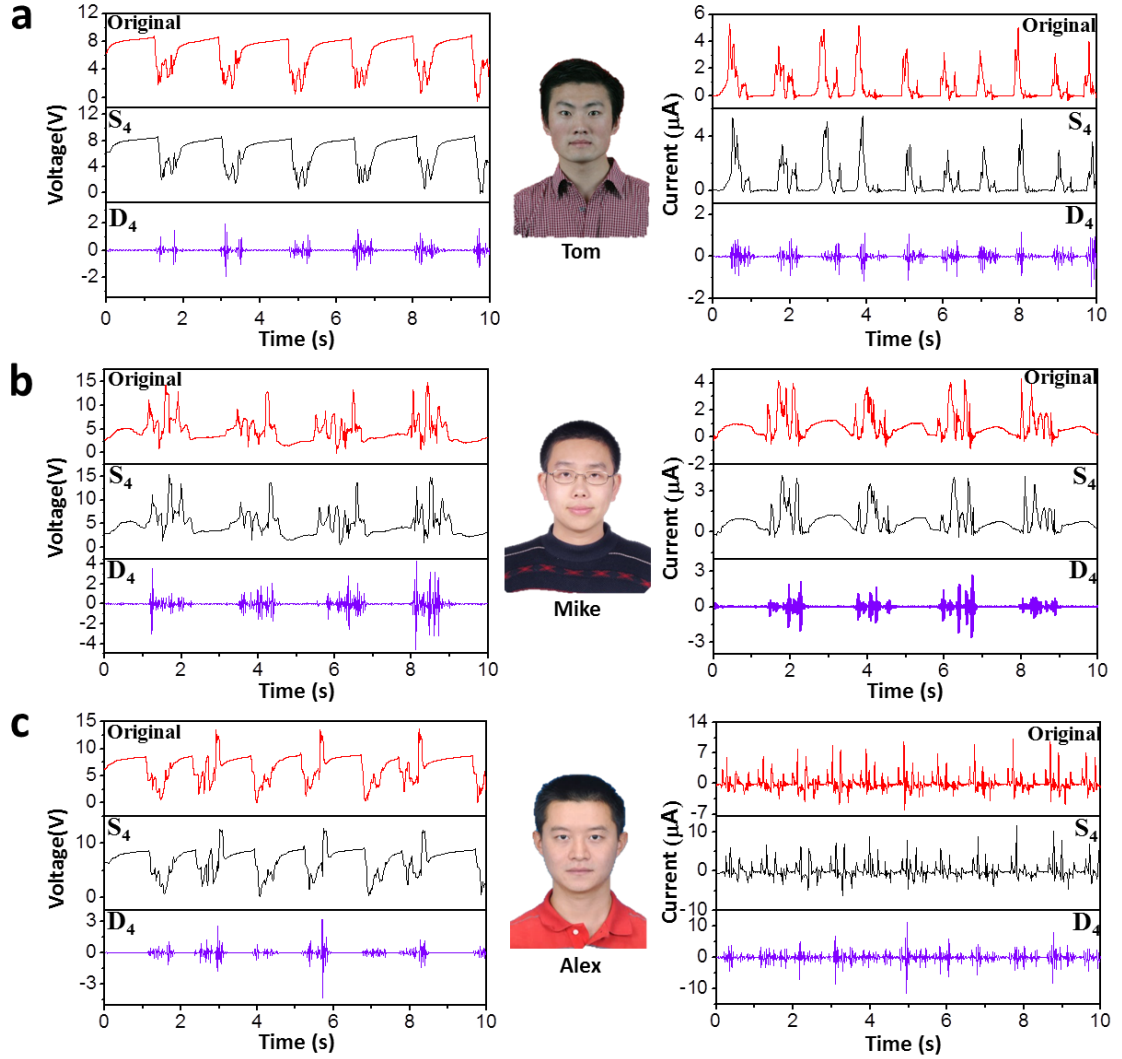
Figure 4.10 Personality identified keystroke dynamics using intelligent keyboard. Typing patterns obtained when (a) Tom, (b) Mike, (c) Alex, were continuously typing the word "touch" more than four times into the computer *via* the IKB. S_4 and D_4 are the corresponding wavelet components after DB4 transformation.[112]

Based on DB4, the typing patterns in the form of electric signals can be expressed by the following formula *via* multiresolution analysis

$$f(t) = S_4(t) + D_4(t) + D_3(t) + D_2(t) + D_1(t) \tag{4.7}$$

and $S_4 = \sum_k s_{4,k}\, \varphi_{4,k}(t) \tag{4.8}$

$$D_j = \sum_k d_{j,k}\, \psi_{j,k}(t) \tag{4.9}$$

where $s_{4,k}$ and $d_{j,k}$ are the wavelet coefficients, j =1, 2, 3, 4. k is the number of translations of the wavelet for any given scale. $\varphi_{4,k}(t)$ and $\psi_{j,k}(t)$ are respectively the father wavelets and mother wavelets. f (t) is either voltage or current signal of the typing patterns. S_4 is smooth. Wavelet details D_4, D_3, D_2 and D_1 represent a set of voltage or current components that provide representations of the original signals at different resolution levels.

The S_4 and D_4 of the original typing patterns after DB4 are presented in Figure 2.37, respectively for different individuals. On the basis of DB4 results, the corresponding higher resolution wavelet components of three individuals are significantly different from each other. Still, Pearson correlation coefficient was utilized to quantitatively measure the correlation between the wavelet components by the following equation:[117]

$$\gamma = \frac{\sum_{i=1}^{n}(t_i-\bar{t})(x_i-\bar{x})}{\sqrt{\sum_{i=1}^{n}(t_i-\bar{t})^2}\sqrt{\sum_{i=1}^{n}(x_i-\bar{x})^2}} \tag{4.10}$$

where n is the length of compared date sequence, and x is either the voltage or the current sequences after DB4. The obtained Pearson correlation coefficient of D4 and S4 components are respectively tabulated in Table 4.1.

TABLE 4.1. Pearson Correlation Coefficients between the Wavelet Components.

Voltage	Tom		Mike		Alex		Current	Tom		Mike		Alex	
	S_4	D_4	S_4	D_4	S_4	D_4		S_4	D_4	S_4	D_4	S_4	D_4
Tom	0.91	0.92	0.43	0.45	0.45	0.43	Tom	0.92	0.89	0.44	0.41	0.42	0.39
Mike	0.43	0.45	0.86	0.87	0.42	0.34	Mike	0.42	0.41	0.85	0.85	0.36	0.35
Alex	0.45	0.43	0.42	0.34	0.88	0.89	Alex	0.42	0.39	0.36	0.35	0.88	0.89

All of the Pearson correlation coefficients of the voltage or current components from each individual are larger than 0.85, suggesting superior permanence of the typing patterns, while other Pearson correlation coefficients are less than 0.45 that is indicative of

excellent uniqueness among individuals. Therefore, the Pearson correlation coefficient can be harnessed to express the uniqueness and permanence among individual typing patterns. In the meanwhile, the correlation coefficient can also act as a threshold to separate the genuine typing patterns from the impostor typing patterns, if a verification system is established using behavioral biometric of keystroke dynamics.

To evaluate the performance of the triboelectrification enabled behavioral biometric of keystroke dynamics as an effective identifier, 104 participants were invited to independently type the word "touch" for more than four times on the IKB in each accustomed manner. All the participants are the randomly and diversely selected with an age span from 14 to 69 years old, male and female people from different countries.

Subsequently, a collection of 104 individual typing patterns were divided into 52 client patterns and 52 impostor patterns. In the whole testing set of 104 typing patterns, user template is composed of the 52 client patterns. And the performance of the authentication biometrics is characterized through two error rates: False Rejection Rate (FRR) and False Acceptance Rate (FAR).

The FRR and FAR are variables depending on the classification threshold. By tuning the threshold, the FRR and FAR can typically be traded off against each other to achieve the preferable classification result. In this regard, the Pearson correlation coefficient was selected as the classification threshold to evaluate the behavioral biometric authentication system using triboelectrification enabled keystroke dynamics. The variation of FAR and FRR in relation to the threshold is shown in Figure 4.11. The FRR is increasing with the elevated threshold, while FAR follows a reverse trend. However, the FRR and FAR intersect at a certain threshold value, which indicates the EER point.
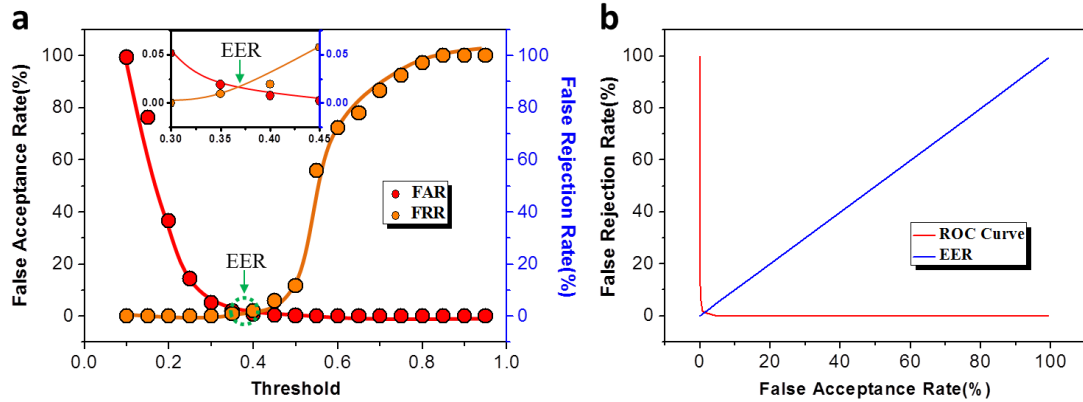
Figure 4.11 Evaluation of the performance of the biometric authentication system using triboelectrification enabled keystroke dynamics. (a) The variation of FAR and FRR is in relation to the threshold. Inset is an enlarged view of the EER point, which indicates a remarkably low EER value of 1.34% at the threshold of 0.37. (b) Receiver operating characteristic (ROC) curve of the biometric authentication system using triboelectrification enabled keystroke dynamics. The false rejection curve is plotted as a function of the false acceptance curve.[112]

The inset of Figure 4.11 is an enlarged view of the EER point of the presented behavioral biometric authentication system. Compared with the state of the art biometric techniques, the presented biometric authentication system achieves a remarkably lower EER value of 1.34% at the threshold of 0.37. In the meanwhile, the Receiver Operating Characteristic (ROC) curve is demonstrated in the Figure 4.11b. In addition, to prove the capability of the IKB as an additional layer of stronger security to current authentication systems, a practical application was demonstrated. When four different individuals typing the password "touch" into the computer through IKB, only the genuine owner with matched typing pattern can access into the computer. Given its exceptional authentication ability, the IKB is able to identify the personal character of typing individuals, making it practical for developing a highly secured authentication system based on behavioral biometrics.

In addition, the intelligent keyboard can be applied to capturing wasted energy. To systematically investigate the performance of the IKB in harvesting typing energy, two typing modes, intermittent and continuous typing, were both evaluated. For the intermittent model, a key in zone "II" was repeatedly tested because keys in this zone are the mostly used. The open-circuit voltage and the short-circuit current are exhibited in Figure 4.12a and 4.12b, respectively, with a peak value of 26.8 V and 23.5 μA.
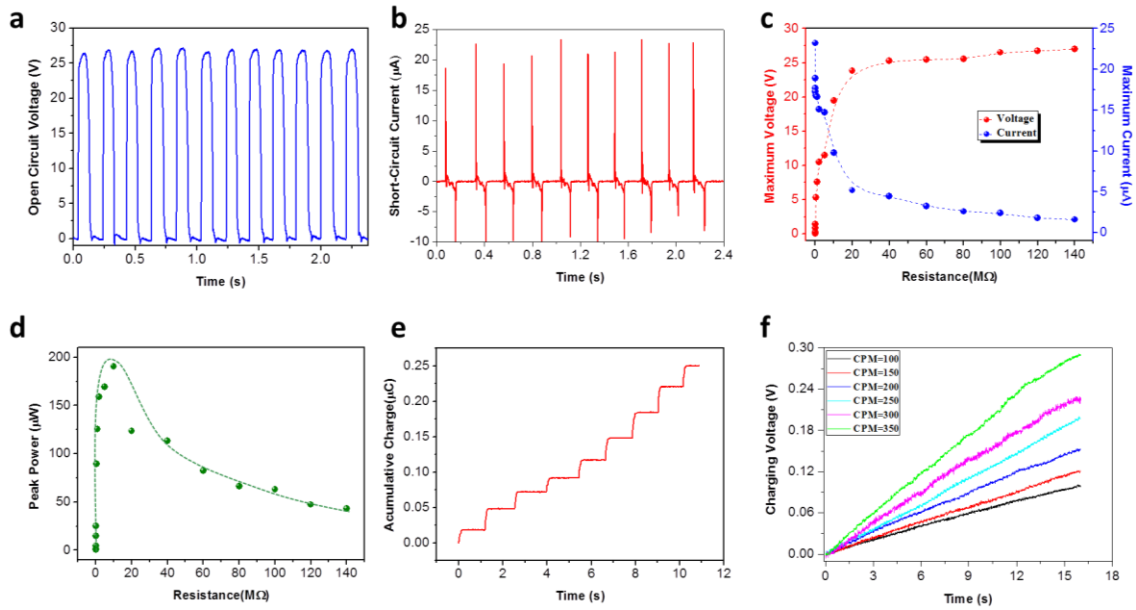
Figure 4.12 Intelligent keyboard as a self-powered system. (a) Measured open-circuit voltage and (b) short-circuit current of the IKB under the intermittent typing model. (c) Dependence of the voltage and current output on the external load resistance. The points represent the peak values of electrical signals while the lines are the fitted results. (d) Dependence of the peak power output on the external load resistance, indicating maximum power output when R = 9MΩ. (e) Accumulative induced charges generated by the IKB. Each step represents an output current resulting from a keystroke. (f) The IKB can effectively capture the wasted typing energy for charging portable electronics in a wide range of typing speed. And a directly proportional relationship was found between the typing speed and the charging rate.[112]

As shown in Figure 4.12b, the output current is asymmetric. It was found that the larger positive peaks correspond to the process when the key was being pressed, while the smaller ones are produced when the key was being released. Given the same amount of

total transported charges, the faster pressing process is expected to generate larger current peaks than the slower releasing process. Resistors were utilized as external loads to further investigate the output power of the IKB. As displayed in Figure 4.12c, the current amplitude drops with increasing load resistance, while the voltage follows a reverse trend. As a result, as demonstrated in Figure 4.12d, the instantaneous peak power is maximized at a load resistance of 9 MΩ, which corresponds to a peak power density of 69.6 μWcm^{-2} and a peak specific power of 2.05mwg^{-1}. This output performance leads previous reports by at least 141 times enhancement.

With a diode bridge, the total accumulative induced charges can also be measured, as show in Figure 4.12e. Each step represents an output current resulting from a keystroke, producing 37 nC of induced charges on average. Correspondingly, the area density of triboelectric charges is calculated to be 134 μC/m^2. Such solid achievements are mainly attributed to the following two reasons. First, human skin and FEP have a large difference in triboelectric polarity, which assures large amount of triboelectric charges generated in keystroke. Second, the vertically standing FEP nanowires enables tremendous enhancement of effective contact area as well as triboelectric charges, and thus superior output performance. A detailed interpretation and description of the mechanism behind the nanowires improved contact area was rendered in the following Contact Area Improvement section.

Meanwhile, the energy harvesting capability of IKB was also evaluated under the continuously typing working mode, which is the mostly used mode for computer users. As demonstrated in Figure 4.12f, the IKB can effectively capture the wasted typing energy for charging portable electronics in a wide range of typing speeds, which almost covers all

kinds of users in daily life. And a directly proportional relationship was found between the typing speed and the charging rate. This is because a faster typing means more keystrokes are launched in a unit period of time, thus faster of triboelectric charges generation, and higher charging rate is expected. Under a moderate typing speed of 350 CPM, a charging rate of 0.019 Vs^{-1} was achieved for a commercial capacitor.

Aimed at optimizing the output performance when a keystroke is initiated, FEP nanowires arrays were purposely created to enhance the effective contact area between the human finger and FEP surface. Without FEP nanowires, the contact between the human skin and FEP is possibly confined at certain points due to the surface asperities. With an average clustering diameter of 104 ± 21 nm and a length of 0.8 ± 0.2 μm, the FEP nanowires are likely to be readily bent and become adaptive to the morphology of the human finger due to a dimensional matching. Such a conformable structural interaction can result in an improvement of the real contact area.

A further step was taken to investigate the relationship between electric output and the applied contacting force. A dual-range force sensor was employed to quantitatively control the applied typing force. As demonstrated in the Figure 4.13a, for both IKBs, with or without FEP nanowires as surface modification, the current output is clearly increasing with elevated contact forces. However, different increasing trends were found. Firstly, at a fixed applied force, the output of IKB with FEP nanowires is always larger than that of the IKB without FEP nanowires. Secondly, the output has different force sensitivities. Thirdly, a faster saturation was observed for the IKB without FEP nanowires. These observations are mainly attributed to the increased contact area at larger forces. The surface of human finger skin and FEP are neither absolutely flat nor smooth. At small contacting

133

force, the surface roughness leads to some areas untouched between the FEP and human skin, while a larger pressure could bring the two surfaces a fully intimate contact. The reliance of output on the applied contact force further validates that the enhanced effective contact area is attributed to the structural coupling of FEP nanowires and human skin hierarchical roughness.
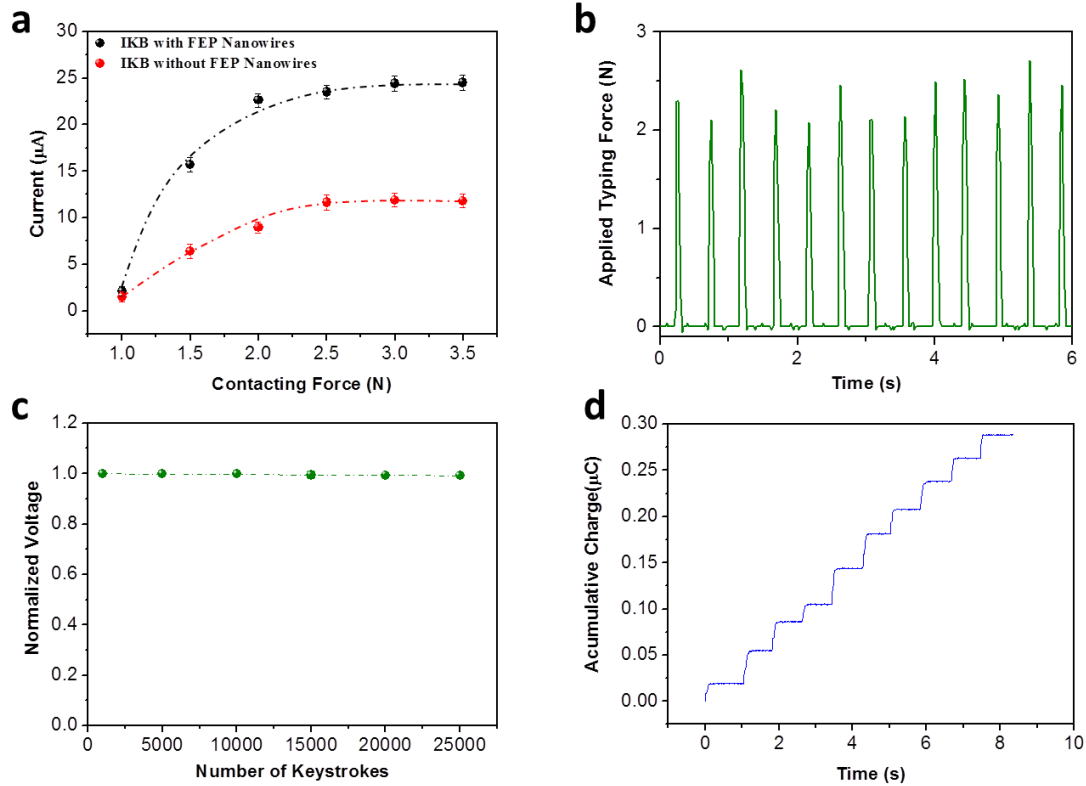
Figure 4.13 Force depended output performance of IKB and its reliability test. (a) Investigate the relationship between electric output and the applied contacting force for IKBs with or without FEP nanowires. (b)The applied typing force to the IKB by an index finger for the mechanical durability test. (c) Mechanical durability test of the IKB. The output voltage only shows a minor fluctuation of less than 0.8% after 25000 cycles of repetitive keystroke. (d) Accumulative induced charges generated by the intelligent keyboard with wearing a pair of Latex gloves.[112]

The reliability of the IKB is primarily represented by its mechanical durability and output stability. Firstly, mechanical durability against the applied pressure during the iterative keystrokes has been investigated. The applied typing force by an index finger was

134

fixed at a value of 2.3 ± 0.2 N, as shown in Figure 4.13b. As shown in Figure 4.13c, the output voltage only shows a minor fluctuation of less than 0.8% after 25000 cycles of repetitive keystrokes. This mechanical robustness along with the output stability is mainly attributed to its robust structure that is consisted of durable thin film materials.

Additionally, it is worth noting that contact electrification is a universal effect that exists for almost all of the materials. The IKB can effectively respond to either insulating or conductive materials of any kinds, even a glove-wearing intrusion or imposture could be effectively detected. Figure 4.13d shows the accumulative induced charges generated by the intelligent keyboard with hands wearing a pair of Latex gloves. Each step represents an output current resulting from a keystroke, generating 39 nC of induced charges on average, which is comparable, and even better than the results obtained by bare hands directly typing.

Enabled by the contact electrification and electrostatic induction between human fingers and the keys, an intelligent self-powered keyboard was innovatively reported in this work. Given its exceptional properties of self-securing, self-powering and self-cleaning, as well as cost-effectiveness and unique applicability resulting from distinctive mechanism and one-piece non-mechanical punching structure, the IKB is a practical approach in converting typing motions for either sensing or energy harvesting purposes. Moreover, it is worth noting that, as the most comment input tool nowadays, keyboard widely exists in our daily life, from cash register to ATM, from music instrument to even game machines. The justified concepts and demonstrations in this work can be immediately and extensively adopted in a variety of applications, and come into effect of improving the way of our living.

4.3 Eardrum inspired bionic membrane sensor

By capturing human physiological or behavioral characteristics, wearable electronic sensors in biomonitoring and biometric systems carry significant importance in daily life such as in personalized health monitoring and assessment, disease diagnosis, entrance and mobile control, secured financial transactions and others.[118-122] A lightweight and self-powered technology is highly desired for simultaneously acquiring multifunctional characteristics. Here, we report the first self-powered bionic membrane sensor (BMS), which is wearable, lightweight, cost-effective, easy to fabricate and capable of working in a multi-modal manner for either health-monitoring or authentication purposes.[123] Innovatively coupling the contact electrification effect with a structure inspiration by a human eardrum, the as-fabricated BMS holds a superior sensitivity of 51 mVPa^{-1} with a fast response time less than 6 ms as well as a pressure detection limit down to 2.5 Pa.

A BMS has a multilayered structure with a thin layer of polyethylene terephthalate (PET) in an oval shape as the bottom supporting substrate, as schematically shown in Figure 4.14a. The oval shape was inspired from the human tympanic membrane, enabling the BMS to monitor the external dynamic pressure with wide frequency range. A layer of ITO coated Nylon thin film was laminated onto the PET substrate with the ITO acting as the back electrode and the Nylon functioning as one electrification layer. Mimicked a human eardrum, a layer of polytetrafluoroethylene (PTFE) tympanic membrane is tented outwards at the level of the tip of an umbo, which was centered at a Nylon layer with a size of Φ 0.6 mm $\times$ 0.4 mm.
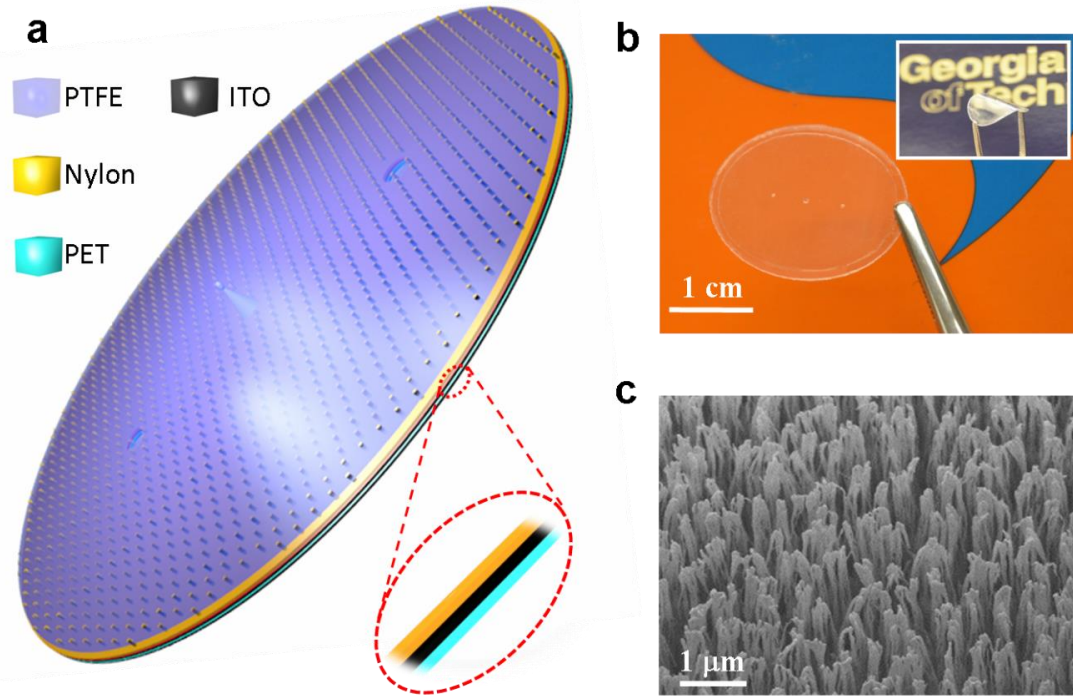
Figure 4.14 Structural design of the bionic membrane sensor. (a)Schematic illustrations of the bionic membrane sensor. (b) Photograph of an as-fabricated flexible and transparent bionic membrane sensor. The scale bar is 1.0 cm. (c) A SEM image of surface-etched PTFE nanowires. The scale bar is 1 μm.[123]

The polyester (PET) was chosen as the material of the umbo, whose two ends were tightly attached with the PTFE membrane and the Nylon layer, respectively. The height of umbo will determine the pressure detection limit as well as detection range of the as-fabricated BMS. By peripherally being anchored, the tensed oval PTFE tympanic membrane, acting as another electrification layer, is extremely sensitive to external dynamic pressure over a wideband frequency range like human eardrum. The formed slightly conical cavity between the PTFE and Nylon serves as an air spacer for the charge generation and transfer. And two circular acoustic holes with diameters of 0.5 mm are punched through the PET, ITO and Nylon three layers, acting as communicating vessels to integrate the conical cavity with the ambient air. A photograph of an as-fabricated flexible

and transparent BMS is shown in Figure 4.14b. In order to enhance the triboelectrification, vertically aligned polymer nanowires were created onto the PTFE surface for an intimate contact with Nylon. A scanning electron microscopy (SEM) image of PTFE nanowires is displayed in Figure 4.14c, which indicates that the average clustering diameter of nanowires is 110 nm with an average length of 0.8 μm. In general, the surfaces of a Nylon and a PTFE film consist of milli/micro/nano hierarchical structure. Without PTFE nanowires, the contact between the Nylon and PTFE is not compact at certain points due to the surface morphology and structures. While with PTFE nanowires, the nanowires are likely to be readily bent and become adaptive to the surface morphology of the Nylon for an intimate contact. Such a conformable interaction can result in an improvement of the effective contact area, thus improving the output performance.

Designed to mimic a human eardrum, the working principle of the BMS can be elucidated in two aspects, namely, membrane mechanical vibration and vibration induced electricity generation. On one hand, the mechanical vibration patterns of the PTFE tympanic membrane in response to external pressure at various frequencies spanning from 100 Hz to 5 kHz were simulated by a Finite Element Analysis, as demonstrated in Figure 4.15a. The simulation is carried out based on an assumption that the applied pressure is uniformly distributed and holds at a constant of 0.6 kPa. Meanwhile, the Young's modulus and Poisson's ratio of the PTFE tympanic membrane are assumed to be 480 MPa and 0.46, respectively. As it can be observed from the simulation results, the deformation regions and magnitudes of PTFE tympanic membrane are highly related to the external excitation frequencies. And it shows that an extremely wide working bandwidth of 3200 Hz was

achieved, which affirms the validity of the BMS structural design mimicking from human eardrum.
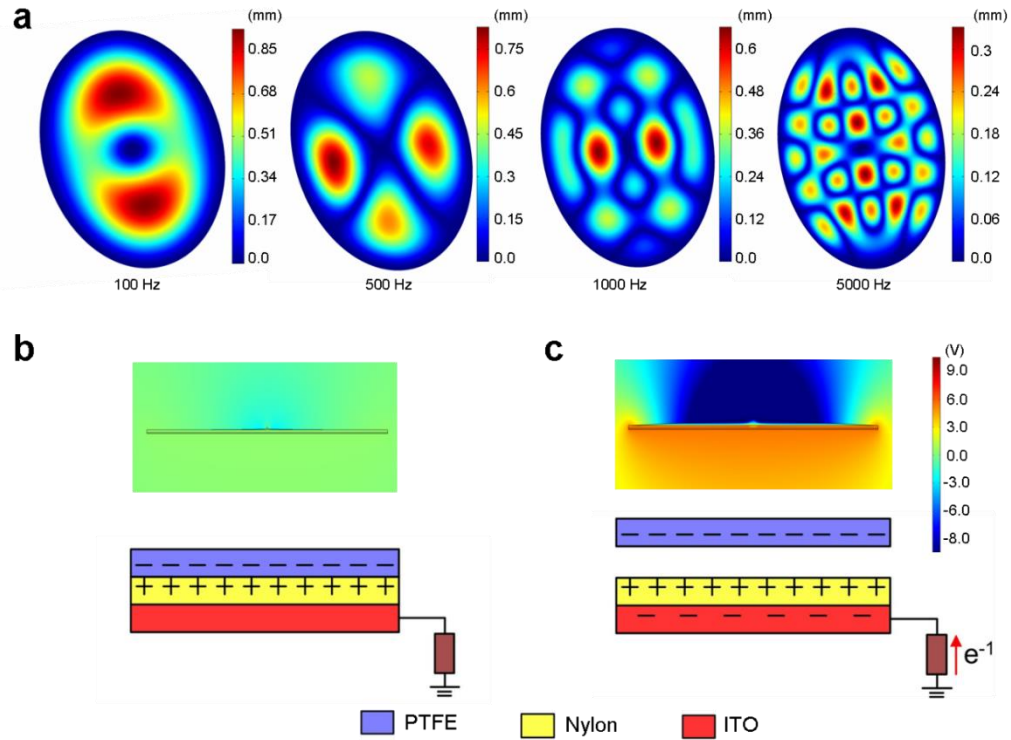
Figure 4.15 Demonstration of the working principle of the bionic membrane sensor. (a)The ANSYS software was employed to characterize the PTFE membrane vibrations under various applied pressures at frequencies of 100 Hz, 500 Hz, 1000 Hz and 5000 Hz, respectively. A PTFE membrane vibration induced electricity generation process was simulated via COMSOL. (b) Contact state in which the PTFE is negatively charged while the Nylon is positively charged. (c) When the elastic PTFE membrane is released, an emerged potential difference drives free electrons to flow from the ground to ITO electrode through the external circuit.[123]

On the other hand, the vibration induced electricity generation is attributed to a coupling between contact electrification and electrostatic induction. A cycle of electricity generation process under external pressure is schematically depicted in Figure 4.15b-c, which is a two-dimensional charge potential distribution by COMSOL. To begin with, when the external pressure brings the PTFE to in contact with Nylon, since these two materials have a different affinity for electrons, with the PTFE eager to grab electrons and

the Nylon able to give them up, positive triboelectric charges on the Nylon side and negative ones on the PTFE side will be produced. In the current contact state, the generated charges are balanced by their opposite counterparts due to electrostatic induction. Consequently, there is neither potential difference across the two layers nor between the ITO electrode and ground (Figure 4.15b). Once the pressure is released, the PTFE tympanic membrane will immediately rebound back away from the Nylon due to its elasticity. A gap will emerge between the two layers, which results in a potential drop across them due to triboelectric charges, so does between the ITO electrode and ground. This is the separation state (Figure 4.15c). The emerged potential difference drives free electrons to flow from the ground to ITO electrode through the external circuit until it is fully offset.

To characterize the sensing performances of a BMS, a computer-controlled linear motor and a force gauge were employed to provide a well-defined load. At one side of the BMS, a small glass plate with same dimension was placed between the PET substrate and tip of the force gauge. Meanwhile, at another side of the BMS, a polydimethylsiloxane (PDMS) pad was anchored to a linear motor tip to apply the pressures uniformly onto the PTFE tympanic membrane. To begin with, we measured the electrical outputs of a BMS as a function of applied dynamic pressure with a constant frequency of 0.3 Hz. In a cycle of the dynamic pressure, increasing and decreasing pressure were realized through a linear motor. The forward and backward voltage-pressure curves of BMS are demonstrated in Figure 4.16a. It is worth noting that both pressure response curves exhibit two distinct regions with different slopes. In the low pressure region (< 1.2 kPa), well behaved liner variation in the output voltage with pressure gives a superior pressure sensitivity of 51 mVPa^{-1} and a detection limit of 2.5 Pa. While in the high pressure region (> 1.2 kPa), a

lower pressure sensitivity was experimentally observed. The different sensitivities are attributed to a difference of contact area change upon pressure in two distinct regions, that is, in lower pressure region, an equal amount of pressure change results in a larger contact area change, which leads to a higher output voltage increase. Most importantly, relying on an innovative working principle and an unique bio-inspired structure, the BMS distinguishes itself in term of the sensitivity together with the observed broad dynamic range (51 mVPa^{-1}, in a range of 2.5-1200 Pa), compared with that of other sensors based on capacitive (0.55 kPa^{-1} in unites of relative capacitance, in a range of 0.5-2 kPa)[124] and piezoelectric (0.79 mVPa^{-1}, in a range of 0.1-12 Pa).[125] Furthermore, for all applied pressures, forward and backward pressure sweep, the forward and backward curves do not show significant hysteresis.

To present a direct view, a 3 mg-human-hair was employed to test the ultrasensitiveness of the BMS, as demonstrated in Figure 4.16b. The as-fabricated BMS can reliably detect the placement or removal of the human hair on or from the covered sensor area of 3.2 mm^2, corresponding to 13 Pa in contact pressure. Furthermore, a further step was taken to examine the response time of BMS to external forces. In Figure 4.16c, a real-time profile of the applied pressure with its corresponding voltage output was demonstrated. Inset are the enlarged views of the loading and unloading process in one cycle, which are respectively elucidated in (up) and (down), rendering a response time of less than 6 ms. This achievement demonstrates a prompt response of the BMS, and is superior to other approaches of its kind in the literature.[120, 124, 126-128] A high sensitivity with a fast response time justifies the practicability of BMS for detecting minuscular dynamic

pressure, which is of paramount importance for various further applications, such as electronic skin and soft robotics.
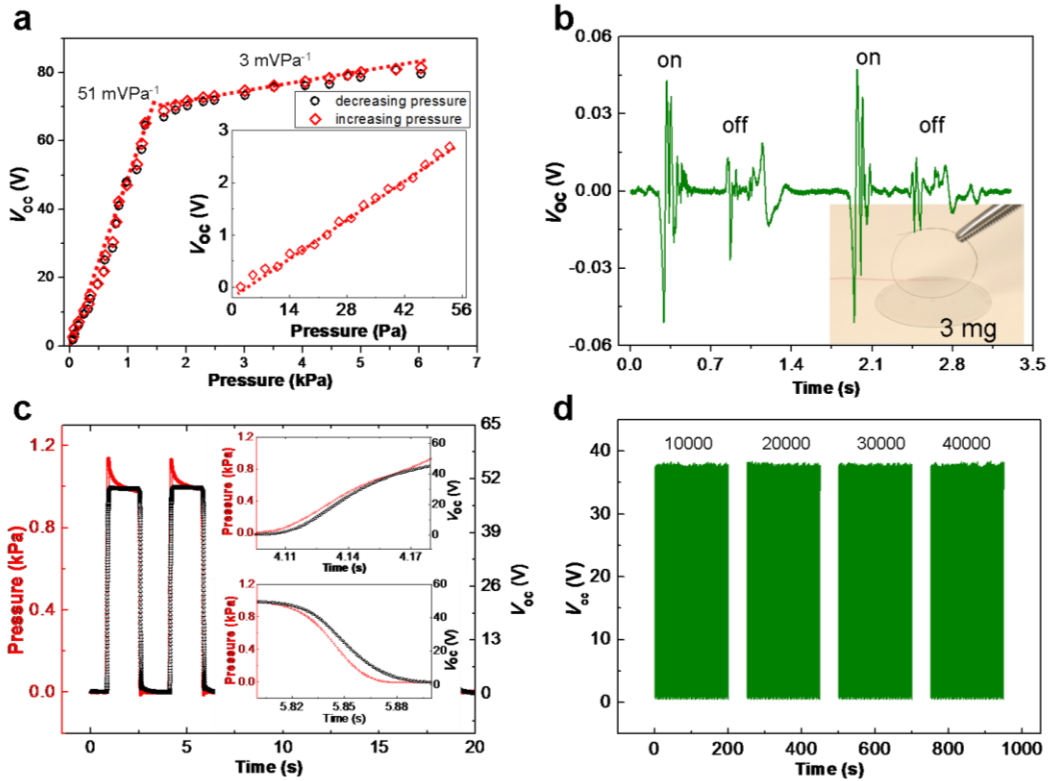
Figure 4.16 Electrical and mechanical characterization of the bionic membrane sensor. (a) The electrical characterization of the bionic membrane sensor in response to applied pressure. Inset: enlarged view in small-pressure region from 2.5 Pa to 55 Pa. (b) The bionic membrane sensor is able to sense the application of tiny pressures. Shown is the output voltage change on placing and removing a human hair (3 mg). (c) Time-resolved sensor response. Periodic pressure changes are utilized to determine the response time taken for the sensor. The enlarged views of the loading and unloading process in one cycle are respectively elucidated in (up) and (down), which renders a response time of less than 6 ms. (d) The mechanical durability characterization of the bionic membrane sensor. Under a pressure of 0.8 kPa at a frequency of 2 Hz for 40,000 cycles, no degradation of the output voltage is experimentally observed.[123]

In addition, to further investigate the stability of the BMS, a pressure of 0.8 kPa with a frequency of 2 Hz was applied. The voltage was recorded after each 10,000 loading/ unloading cycles and 400 cycles of data were presented in each recording, as shown in

Figure 4.16d. The voltage amplitudes exhibit negligible changes after a total 40,000 cycles, revealing a high repeatability, stability, and durability of the BMS.

4.3.1 Self-powered noninvasive arterial pulse measurement

The worldwide leading causes of death are from cardiovascular diseases. Intensive research is focused on early detection and prevention of such diseases, with a special emphasis on arterial compliance capability. Arterial pulse wave propagation in the arterial tree can provide essential information about the arterial physical situation. The BMS in this work provides a superior route in acquiring the human arterial pulse wave in a self-powered and noninvasive manner. For a real-time monitoring of the arterial pulse, the BMS was attached onto the carotid, wrist and chest, just over the artery as it is usually done in arterial tonometry. The arterial pulse wave corresponds to the dynamic pressure change on the skin surface, which can be characterized by the electrical output of the attached BMS.

Figure 4.17a-b respectively show the recorded real-time voltages over several pulse periods when a BMS was placed over the carotid arteries of a 30-year-old man and a 70-year-old man. Insets are the enlarged views of one cycle for a detailed information delivery. A typical characteristic pulse wave shape was obtained with three clearly distinguishable determinants for both the 30-year-old and 70-year-old men: Systolic peak (P_S), Point of inflection (P_i) and Dicrotic wave (P_D), which are known to be respectively resulted from the blood ejected from the left ventricle, the reflected pulse wave and the ejected blood back to the left ventricle. A comparison of the pressure pulse waves of a young man with that of an old man indicates apparent differences between the two, especially that P_i occurs after the P_S for the younger one, while the P_i appears before the P_S for the older one.
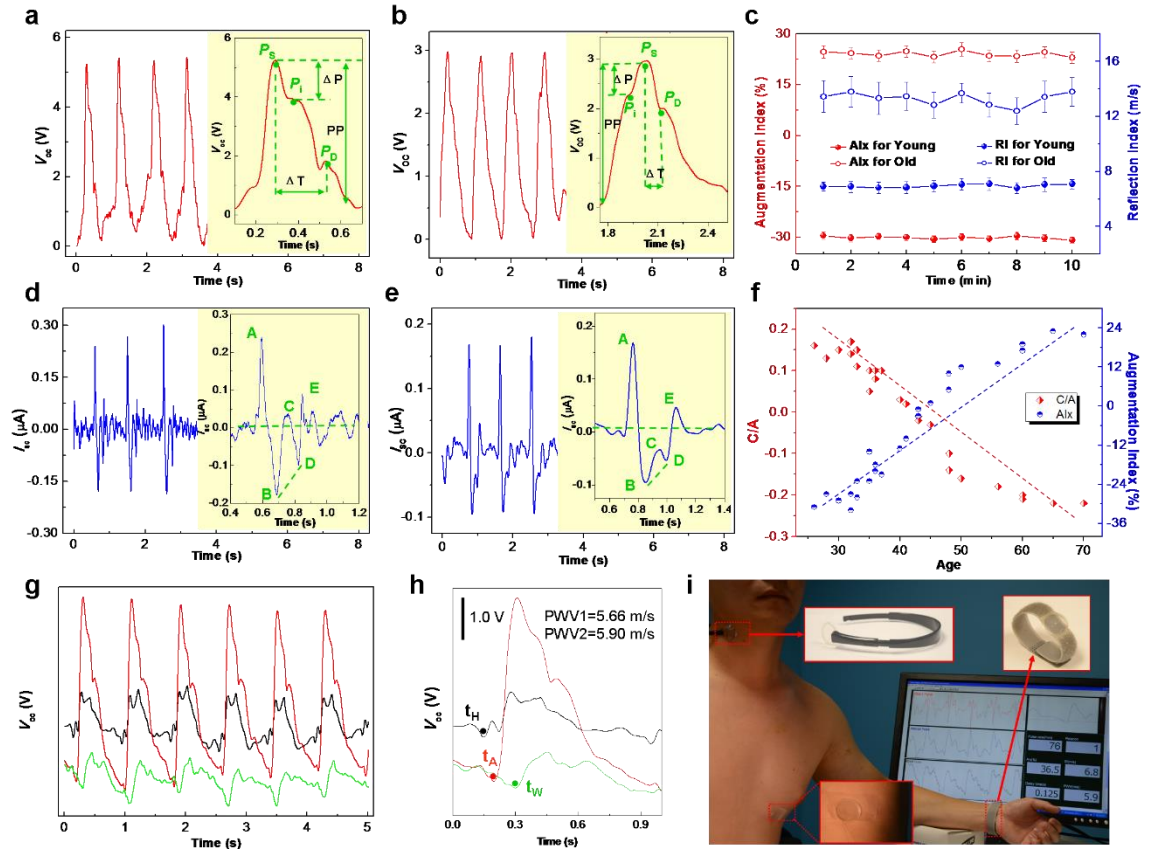
Figure 4.17 Bionic membrane sensor measured the arterial pulse wave for noninvasive self-powered human health monitoring. (a) and (b) The real-time voltage outputs when the sensors are placed over the carotid arteries of a 30-year-old man and a 70-year-old man, respectively. The inset is an enlarged view of one cycle, which is a graphic representation of the augmentation index (AIx), defined as AIx(%)=±(P_S-P_i)/PP. PP is the absolute pulse amplitude. ΔT is the time delay between the systolic P_S and diastolic peak P_D. And thus the reflection index (RI) of carotid artery can be obtained from subject height divided by the time delay. (c) Quantitative comparison of the AIx and RI between the 30-year-old man and the 70-year-old one. (d) and (e) The corresponding real-time current outputs of the 30-year-old man and the 70-year-old man, respectively. The inset is an enlarged view of one cycle of the current signal, whose waveform comprises of five main parts, labeled as A-wave to E-wave: initial positive (A-wave), early negative (B-wave), re-increasing (C-wave), late re-decreasing (D-wave) and diastolic positive (E-wave). (f) Relationship between the C/A ratio and AIx in the carotid arteries of 25 subjects age from 26 to 70 years' old. The C/A ratio decreased with age, while AIx followed a reverse trend. (g) The pulse waves acquired from three different sites of a participant: carotid artery, left wrist and the chest. (h) An enlarged view of a cycle of output signals corresponding to three positions. And the dots indicate their start points of each cycle. (i) A photograph showing the bionic membrane sensors were directly attached to simultaneously monitor the pulse waves of the participant from his carotid artery, chest and wrist.[123]

144

The differences are significantly related to the physiological condition of human cardiovascular system, which can be quantified by two of the most commonly used parameters: the augmentation index $\text{AIx}\,(\%)=\pm\left(P_\text{s}-P_\text{i}\right)/\text{PP}$, and the reflection index $\text{RI}=h/\Delta t$, where h is the subject height, Δt is the time delay between P_S and P_D, while PP is the absolute pulse wave magnitude.[129, 130] In order to accurately evaluate the physiological conditions of the two peoples' cardiovascular systems, a time period of ten minutes was taken to continuously record their arterial pulse waves. Based on the acquired waveforms, a statistical result of the AIx and RI was respectively obtained for the young and old, as shown in Figure 4.17c. For the younger one, average values of -30 % and 6.8 m/s were respectively obtained for the parameters AIx and RI, while for the older one, values of 24.8 % and 13.3 m/s were respectively obtained. A distinct difference of AIx and RI between the two subjects is mainly attributed to that, for the young man with better arterial compliance capability, the pulse wave is spread through the arteries at a lower velocity and also the reflected wave arrives back to the aorta after the late systole, resulting in a negative AIx and a smaller RI. In contrast, for the old man with stiffer arteries, the blood pulse velocity is higher and the reflected wave arrives back to the aorta in the early systole, leading to a positive AIx and a larger RI.

Figure 4.17d-e respectively show the corresponding real-time current outputs of the 30-year-old man and the 70-year-old man. The inset is an enlarged view of one cycle of the current signal, whose waveform comprises of five main parts, labeled as a-wave to e-wave: initially positive (A-wave), early negative (B-wave), re-increasing (C-wave), late re-decreasing (D-wave) and diastolic positive (E-wave). The height of each wave was measured from the baseline, with the values above the baseline being positive and those

under it negative. A comparison of the current signal waveform of the young man with that of the old man indicates obvious differences between the two, especially that a positive C-wave is observed for the young man, while a negative C-wave for the old one. In order to quantify the difference, a parameter (C/A) was employed, which was defined by the ratio of the height of the C-wave to that of the A-wave. The C/A and AIx values were measured from 25 people with ages spanning from 26 to 70 years' old, as shown in Figure 4.17f. It is interesting to find that the C/A index decreases with age, while AIx follows a reverse trend. These two parameters are reported to independently but complementarily indicate the vascular stiffness, that is, the AIx increases with the increasing of arterial stiffness, while the C/A index decreases. These statistical results highlight that the measured output voltage and current by BMS can reflect the condition of the cardiovascular system as well as the risk of cardiovascular disease. Thus, it can be utilized for non-invasive medical diagnosis. The acquired voltage and current signals independently but complementarily give a comprehensive picture of the arterial physical situation.

Meanwhile, in order to obtain more information for cardiovascular risk estimation, a further step was made to measure the pulse wave velocity (PWV) by using multiple BMSs to monitor human pulse waves over different artery sites. The PWV is highly related to the vascular compliance and can be determined by measuring the pulse propagation time from the pressure waveforms at different sites along a vascular segment. A stiffer vessel will conduct the pulse wave faster than a more compliant one. Figure 4.17g presents the simultaneously acquired voltage signals when three BMSs were respectively attached to the carotid artery, left wrist and the chest. Figure 4.17h is enlarged views of a cycle of output signals, and the characteristic dots indicate their cycle start points. It is worth noting

that the start point of the signal acquired from chest comes first, which is 53 and 163 ms earlier than the start points of the signals from the carotid artery and left wrist, respectively. Here, the PWV is derived by dividing the pulse wave propagation distance between the two testing sites by the time delay over that distance. For the test subject, PWV1 = 5.66 m/s (along chest to carotid artery) and PWV2 = 5.9 m/s (along chest to left wrist) were experimentally obtained, which are characteristic values expected for a healthy adult.

To prove the capability of the BMS for self-powered noninvasive arterial pulse measurement, a set of practical applications was demonstrated, as shown in Figure 4.17i. Three BMSs were directly attached to simultaneously monitor the pulse waves of the participant from his carotid artery, chest and wrist, and all of the essential information about the arterial physical situation, including pulse rate, PWV, AIx, and RI, were systematically obtained for a further medical diagnosis.

4.3.2 Self-powered throat microphone

Throat microphone is becoming more and more popular since it can effectively pick up speech even in extremely noisy or windy environments, such as for a parachute jumper from sky, on a motorcycle or in a pandemoniac street, while it is beyond the capability of other types of microphones due to high levels of background noise and the limitation of current technology. Here, the reported BMS is also capable of acting as superior throat microphone, which is lightweight, small volume, portable, extremely low cost, easy to fabricate, more importantly, it can work without external power. When the BMS was worn against the neck without speaking, a series of pulse waves with low frequency of 1.1 Hz were observed, corresponding to the silent state in Figure 4.18a.

147
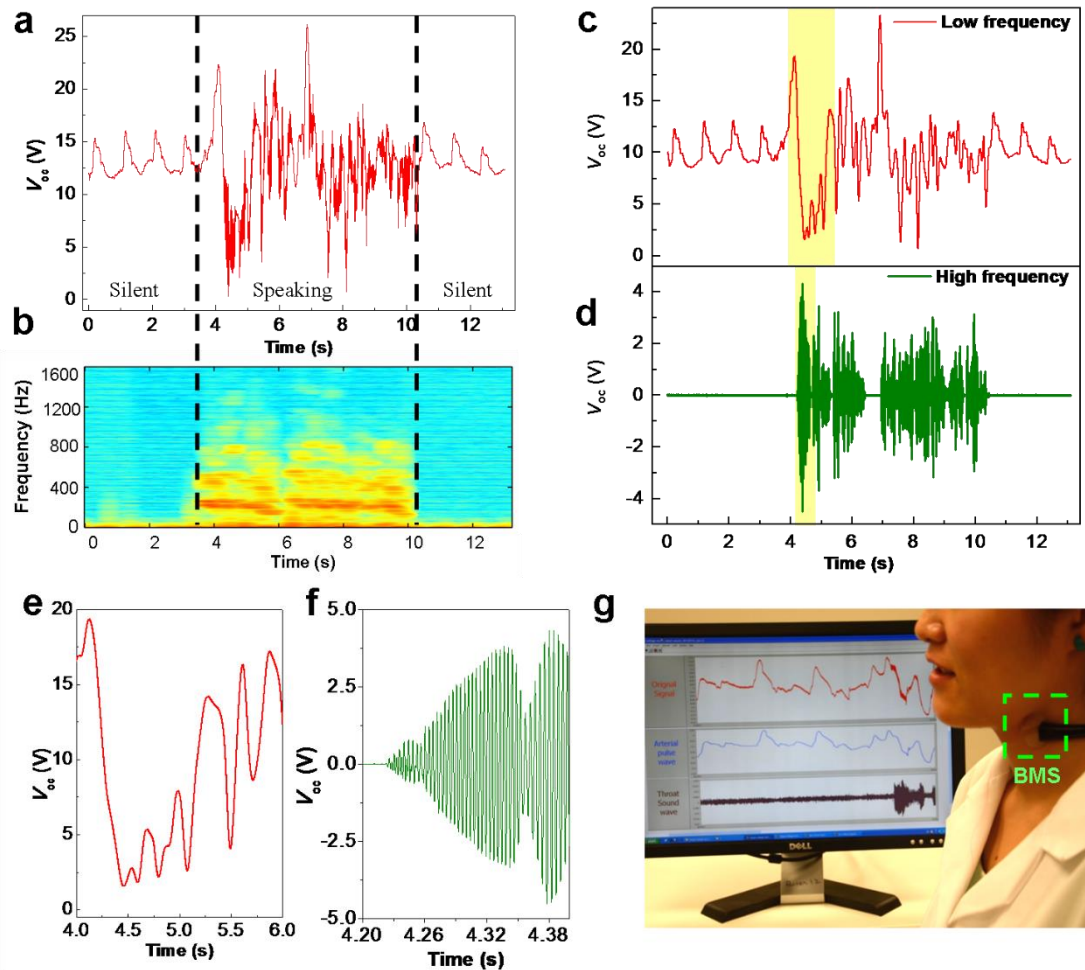
Figure 4.18 Bionic membrane sensor as a superior anti-interference, self-powered and throat-attached microphone. (a) The real-time voltage output in response to the throat vibration during speaking when the sensor is worn against the neck. (b) Short-Time Fourier Transform of the acquired output voltage, which indicates a majority of the frequency components spanning from 45 to 1500 Hz. The low frequency components (c) and high frequency components (d) of the voltage signal, which are obtained respectively via a 10 Hz-cutoff-frequency low pass filter and a ban-pass filter with pass-band from 45 to 1500 Hz. The partial enlarged view of the low frequency component (e) and high frequency component (f) elaborately illustrates the rich output signals responding to the concrete dynamic change in the speaking, which assures the superior performance of the bionic membrane sensor as a throat microphone. (g) A photograph showing the BMS was worn against the participant's neck acting as a self-powered throat microphone.[123]

While plentiful high frequency components were emerged and superimposed when the participant spoke the sentence "This is a self-powered throat microphone", which were reflected by the acquired voltage signals in the speaking state in Figure 4.18a. From the

148

Short-Time Fourier spectrum of the recorded data, the acquired voltage signal was analyzed, obviously indicating a majority of the frequency components spanning from 45 to 1500 Hz when peaking, as shown in Figure 4.18b. Then, according to the frequency distribution, a 10 Hz cutoff-frequency low-pass finite impulse response digital filter was further used to get the low frequency components from the acquired voltage signal (Figure 4.18c). While a ban-pass finite impulse response digital filter with a pass-band from 45 to 1500 Hz was applied to resolve the throat sound from the acquired voltage signal (Figure 4.18d). The partial enlarged view of the low frequency component (Figure 4.18e) and high frequency component (Figure 4.18f) elaborately illustrate the rich output signals responding to the concrete dynamic change in the speaking, which exhibits plenty high frequency detailed information and thus can be harnessed to rebuild/recover the speaking content.

To prove the capability of the BMS as a superior self-powered throat microphone, a practical application was demonstrated, as shown in Figure 4.18g. When the tester worn the BMS against her neck and spoke in a noisy environment, the speaking content can be successfully recovered. This is the first invention that a single self-powered sensor can exhibit a multi-functionality of simultaneously acting as a throat microphone and a non-invasive arterial pulse wave monitor, which will attract extensive attentions, especially for astronaut, soldier, motorcycle rider, and those who has to keep quiet while communicating with others at a distance, such as during covert military operations.

4.3.3 Single-sensor multi-modal biometric authentication

Biometric recognition, an automatic identification and verification of a person based on the physiological or behavioral characteristics, is getting increasing research attention for that the current authentication system cannot be easily separated from the genuine owner. A biometric system that relies only on a single physiological or behavioral characteristic in making a personal identification is often not able to meet the desired performance requirements. Identification based on multiple biometrics represents an emerging trend. Here, relying on the superior sensing performance of BMS, a multimodal biometric authentication system was established using a single BMS, which, for the first time, integrates the pulse wave recognition and voice recognition in making a personal identification.

To demonstrate the capability of BMS for multi-modal biometric authentication, a first step was taken here to show its functionality for voice recognition, since the capability of BMS for pulse wave recognition was justified in the previous section. Figure 4.19a-b show the originally recorded voltage signals when two participants were continuously saying "one world" more than three times in each accustomed manner. Figure 4.19c-d are their corresponding high frequency components of the recorded voltage signals via a 45-to-1500-Hz band-pass filter, which correspond to the throat sound signals according to the frequency distribution. Enlarged views of one cycle of the voice signal for saying "one world" of two participants are respectively shown in Figure 4.19e-f. It is clearly noted that these throat sound waves look apparently different from each other, which is mainly attributed to the differences of anatomy (e.g., size and shape of the throat) and behavioral patterns (e.g., voice pitch, speaking style).
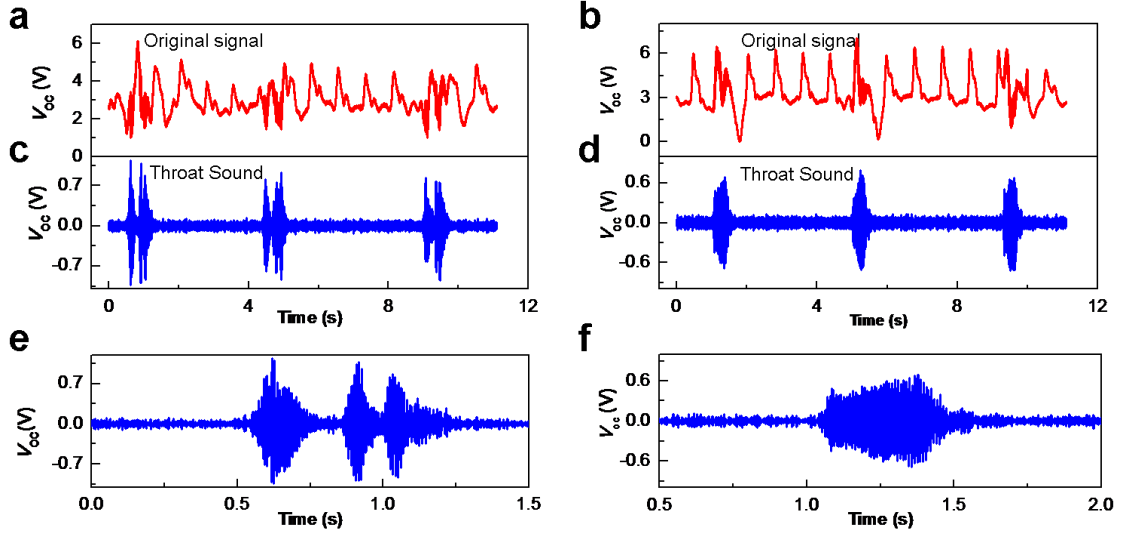
Figure 4.19 Bionic membrane sensor measured throat sound for biometric recognition. (a) and (b) The recorded voltage signals when Alex and Tom were continuously saying "one world" more than three times, respectively. (c) and (d) The high frequency components of the recorded voltage signals from Alex and Tom via a ban-pass filter, respectively. (e) and (f) The enlarged views of a cycle of the high frequency components from Alex and Tom, respectively.[123]

Pearson correlation coefficient was utilized to quantitatively measure the difference between two throat sounds signals. Let $\mathbf{X}=[x_1, x_2,\ldots,x_N]$ and $\mathbf{Y}=[y_1, y_2,\ldots,y_N]$ denote two throat sound signals from two different individuals, the Pearson correlation coefficient between signals $\mathbf{X}$ and $\mathbf{Y}$ can be defined as:

$$r = \frac{\sum_{i=1}^{N}(x_i - \bar{x})(y_i - \bar{y})}{\sqrt{\sum_{i=1}^{N}(x_i - \bar{x})^2}\sqrt{\sum_{i=1}^{N}(y_i - \bar{y})^2}} \tag{4.11}$$

To evaluate the performance of the BMS for voice recognition, 120 participants were invited to independently say the phrase "one world" for more than four times in each accustomed manner with the BMS wearing against the necks. A calculation of the Pearson correlation coefficient between any two of the throat sound signals of 120 participants was

performed, and the results were demonstrated in Figure 4.20a. It is worth noting that most of the Pearson correlation coefficients from individual self-comparing are larger than 0.7, while the Pearson correlation coefficients from comparison among individuals are less than 0.7, which is indicative of that Pearson correlation coefficient can be harnessed to act as a threshold to separate the genuine voice from the impostor voice, if a verification system is thus established.
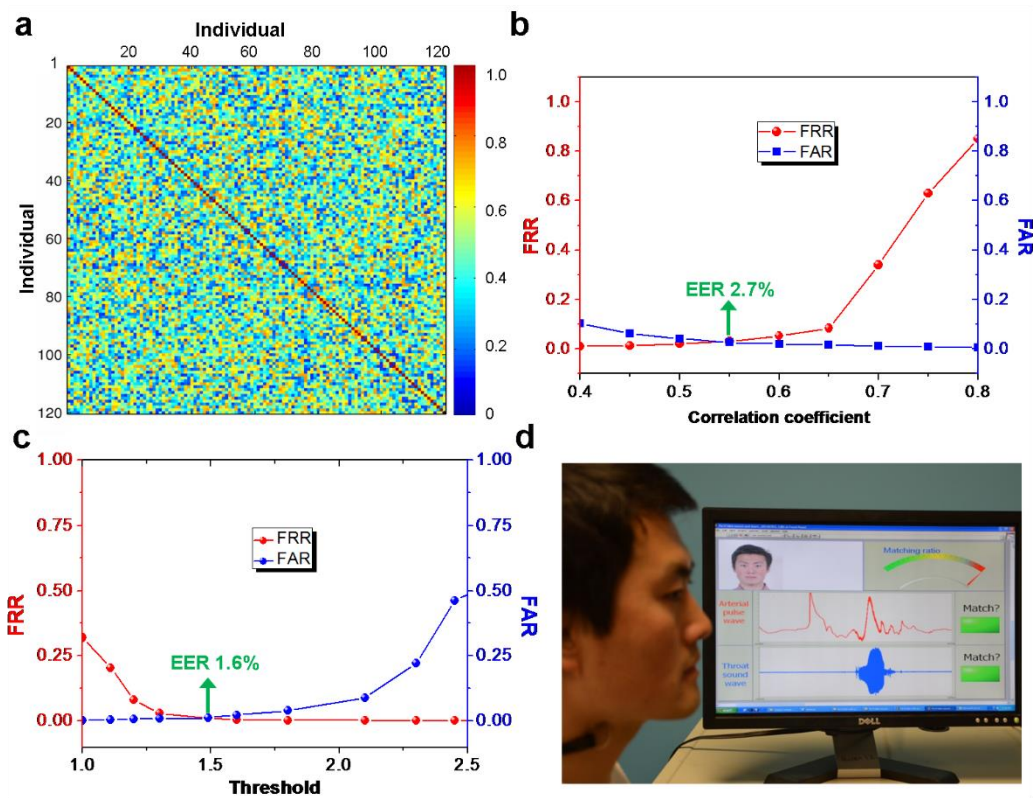
Figure 4.20 Bionic membrane sensor simultaneously recorded the arterial pulse and throat sound for single-sensor multi-modal biometric authentication. (a) Calculated correlation coefficients of the throat sounds among different individuals as well as the same individual. (b) Performance evaluation of the measured throat sound profiles for biometric authentication, which indicates a low EER value of 2.7% at the threshold of 0.55. (c) Performance evaluation of the presented multi-modal biometric authentication system. The variation of FAR and FRR in relation to the threshold, which indicates a remarkably low EER value of 1.6% at the threshold of 1.5. (d) A photograph showing the bionic membrane sensor was worn against the participant's neck to simultaneously record the arterial pulse and throat sound for a single-sensor multi-modal biometric authentication.[123]

The variation of FAR and FRR in relation to the threshold is shown in Figure 4.20b. The presented BMS based voice authentication system achieves an EER value of 2.7% at the threshold of 0.55. For an enhanced authentication performance, identification based on the integration of the pulse wave and voice recognition was evaluated as a multi-modal biometric. The new feature representation for the multi-modal biometric authentication system is a combination of EM of the FDPWs ($d_{\mathbf{XY}}$) from the pulse wave recognition and Pearson correlation coefficient (r) from the voice recognition. And the new feature representation is mathematically expressed by a feature vector $\mathbf{T}=[d_{\mathbf{XY}i}, r_i]$, where $i = 1, 2, 3, ..., u$, denoting the index of the user (u is total number of users in the system database). A new threshold relying on the feature vector can be defined as:

$$TSM_i = w_1 \times 0.0018\, / d_{\mathbf{XY}i} + w_2 r_i \tag{4.12}$$

The weight coefficients w_1 and w_2 are proportional to the authentication performance of the two uni-modal systems with a constraint of $w_1 + w_2 = 1$. A larger value of TSM_i indicates a larger similarity between the user templates and client templates. As demonstrated in Figure 4.20c, a remarkably low EER value of 1.6% was achieved for the presented multi-modal biometric authentication system at a threshold value of 1.5. As demonstrated in Figure 4.20d, the BMS was utilized for a multi-modal biometric authentication, by simultaneously recording the arterial pulse and throat sound, and only the genuine owner with matched both arterial pulse wave and throat sound can access into the computer.

Given its authentication ability, a BMS is capable of simultaneously identifying personal characters physiologically as well as behaviorally. The results demonstrate that the identity established by such an integrated system is much more reliable than the identity

established by a single biometrics, making it unique and practical for developing a highly secured biometrics authentication system.

4.4 Tribosensor for self-powered phenol treatment

Phenol is corrosive to human eyes, skins, and the respiratory tract due to its high toxicity. Repeated or prolonged human contact with phenol may cause harmful effects on the liver, kidneys, heart and central nervous system, resulting in dysrhythmia, seizures and coma.[131] In almost all cases, phenol is damaging not only to individual species and populations, but also to the natural biological communities. Disturbingly, with plenty of discharging sources, such as chemical plants, pharmaceutical plants and petroleum refineries, phenol is one of the most serious and persistent organic pollutants widely existed in ambient environment, especially in the surface water.[132] Considerable efforts have been committed to develop various techniques for phenol detection and degradation, including chromatographic,[133] spectrophotometric,[134] photocatalytic,[135] adsorptive,[136] and electrochemical analyses.[137] However, widely adoption of these techniques may be shadowed by the limitations such as sophisticated and expensive instruments, complex and time-consuming procedures, high energy consumption as well as high operating cost.[138]

Here, for the first time, we report a unique route that uses the energy harvested via the β-cyclodextrin (β-CD) enhanced triboelectricfication for a self-powered phenol treatment, which consisted of two steps, detection and degradation.[139]

154

4.4.1 Self-powered phenol detection

Regarding phenol detection, the as-fabricated nanosensor holds a multilayered structure with acrylic as supporting substrates, as schematically shown in Figure 4.21a. On the upper substrate, a layer of polytetrafluoroethylene (PTFE) film was adhered acting as one contact surface with coated copper as the back electrode. On the lower substrate, a layer of Ti foil with surface grown TiO_2 nanowires is laminated as another contact surface. TiO_2 nanowires on the Ti foil were prepared via a coupling of hydrothermal route in alkali solution with ion-exchange process.[140, 141] A scanning electron microscopy (SEM) image of grown TiO_2 nanowires on the Titanium foil is presented in Figure 4.21b with measured average nanowire diameter and length of 73.4 nm and 1.92 μm, respectively. And the corresponding X-ray diffraction (XRD) pattern of TiO_2 nanowires is shown in Figure 4.21c. β-CD molecules were then assembled onto the TiO_2 nanowires as a surface chemical modification. Figure 4.21d illustrates the charges transfer from the hydroxyl groups of β-CD to TiO_2 nanowires. Here, β-CD plays dual roles of a phenol recognition element and an electrical performance enhancer. A detailed description of the function of β-CD is presented in the following working principle section. A photograph of the as-fabricated phenol nanosensor is shown in Figure 4.21e and the device has a dimension of 4cm×4cm.

Designed to use β-CD as the phenol recognition element as well as the electrical performance enhancer, the working principle of the devices based on β-CD enhanced triboelectrification can be elucidated in two aspects, namely, β-CD as surface chemical modification, and triboelectrification for phenol detection and degradation. On one hand, β-CD is cyclic oligosaccharides of seven α-D-glucose units connected through glycosidic α-1, 4 bonds, which are composed of hydrophobic internal cavity and hydrophilic external

surface. This special molecular structure allows it to form host/guest inclusion complex via various guest molecules with suitable polarity and dimension. The cavity diameter of β-CD has been found to be the most appropriate size for selective adsorption of phenol, which explains the β-CD as surface chemical modification for phenol recognition.[142, 143]
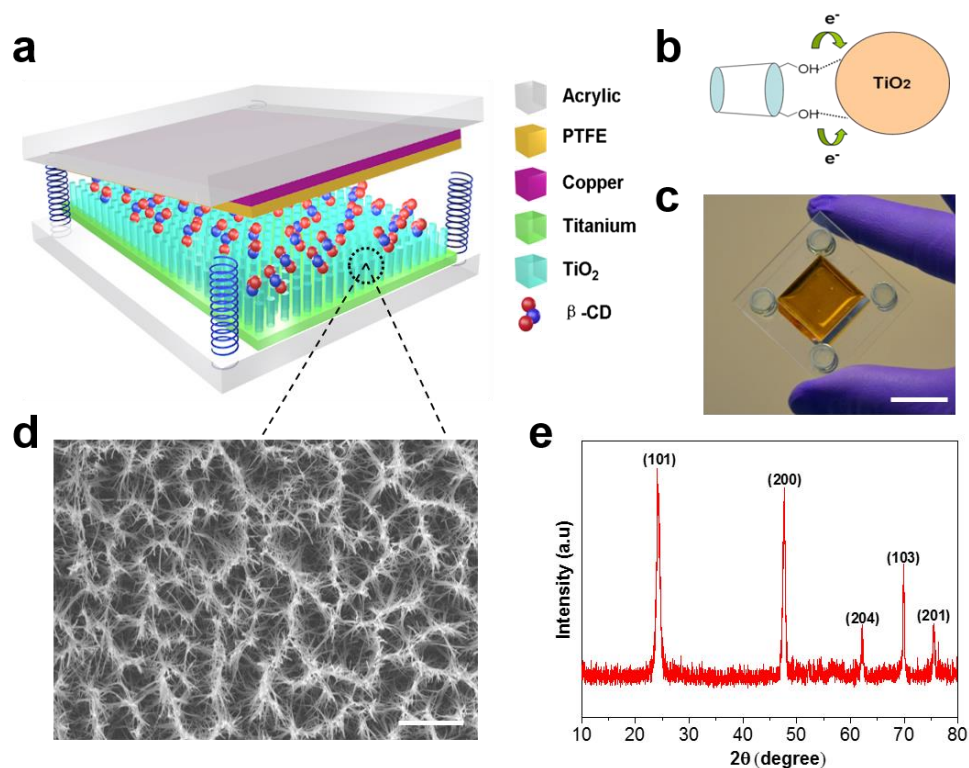
Figure 4.21 (a) A sketch of the triboelectrification with β-CD surface modification for phenol detection. (b) A SEM image of the TiO_2 nanowires. The scale bar is 5μm. (c) The XRD spectra of the grown TiO_2 nanowires. (d) Schematic diagram for illustrating the charges transfer from the hydroxyl groups of β-CD to TiO_2 nanowire. (e) A photograph of the as-fabricated β-CD enhanced triboelectrification for phenol detection. The scale bar is 2 cm.[139]

On the other hand, the triboelectrification for phenol detection is a two-way coupling of triboelectric effect and electrostatic induction. The periodic contact and separation of the oppositely charged plates can create a dipole layer and a potential drop, which drives the flow of electrons between electrodes in responding to the mechanical

vibration. Given a consistent and cyclical operation of the two plates of the as-fabricated nanosensor at a fixed surface concentration of β-CD, the acquired output electrical signals in the external circuit is determined by the phenol concentration absorbed by the β-CD on the surface of TiO_2 nanowires, which is the cornerstone of the β-CD enhanced triboelectrification for phenol detection. Furthermore, the electrical signals generated by the β-CD enhanced triboelectrification can also act as a direct power source to electrochemically degrade the phenol in the wastewater. Since the electricity is converted from the motion of wastewater wave, which renders a self-powered manner for phenol degradation.
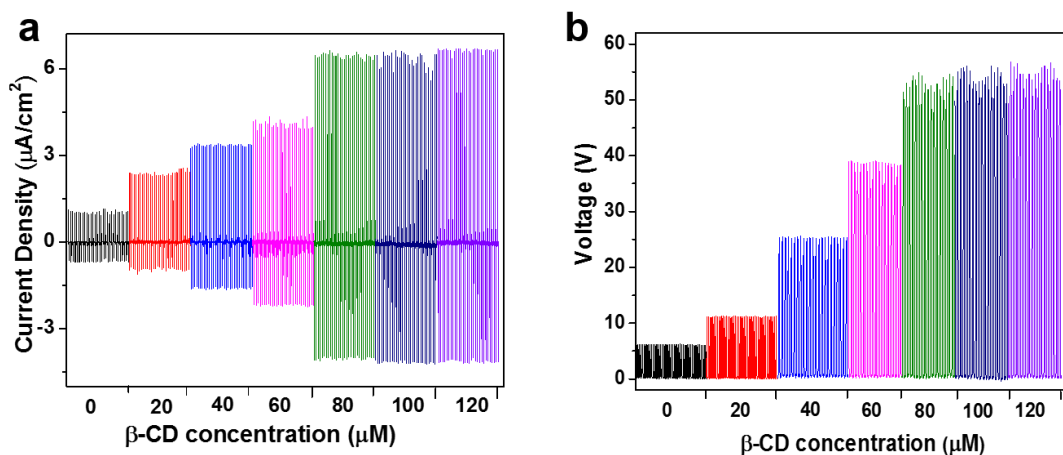
Figure 4.22 (a) Dependence of the current output on the β-CD concentrations. (b) Dependence of the voltage output on the β-CD concentrations.[139]

In order to investigate reasoning behind the β-CD functioning as an electrical performance enhancer, a series of electrical outputs was experimentally measured under various β-CD concentrations, as demonstrated in Figures 4.22a and b. And both the current and voltage signals are increasingly in proportional to the surface concentrations of β-CD

till a saturation point was reached, which was 80 μM by experimental observation. An output plateau emerges with further increasing the concentrations beyond 80 μM. The binding of β-CD to TiO_2 nanowire surface is ascribed to the adhesion of the hydroxyl groups, which derives from physical adsorption or H-bonding interactions. Besides, charge-transfer complex between the β-CD hydroxyl groups and surface Ti atoms of TiO_2 nanowire was also formed owning to coordination effect between ligand and metal under visible light irradiation.[144-147] Charges will transfer from the hydroxyl groups of β-CD to TiO_2 nanowires upon the triboelectrification between the PTFE and TiO_2. Consequently, β-CD is capable of acting as an effective chemical surface modification, which can enhance the triboelectrification, and thus the device output performance.

After looking into the impact of β-CD concentrations on the electrical output, a further step was taken to evaluate the performance of β-CD enhanced triboelectrification for self-powered phenol detection. Under a fixed β-CD concentration of 80 μM, phenol solutions with various concentrations but constant volumes (20 μL) were dropped onto the β-CD modified TiO_2 nanowires surface. Prior to the further electrical measurement, the phenol treated nanosensors were dried at ambient temperature. The dependence of current and voltage outputs on the phenol concentrations are presented in Figures 4.23a and 4.23b, respectively. In a certain phenol concentration region of 10 – 100 μM, both the current and voltage outputs are a monotonically decreasing function of phenol concentrations throughout the experimental time windows. The decrease is mainly attributed to a modified surface triboelectric behavior due to the adsorbed phenol molecules. The phenol will replace the position of TiO_2 to contact with PTFE. In comparison to TiO_2, the phenol molecules have lower tendency to transfer the electrons to PTFE, resulting in a phenol

158

concentrations depended electrical output.
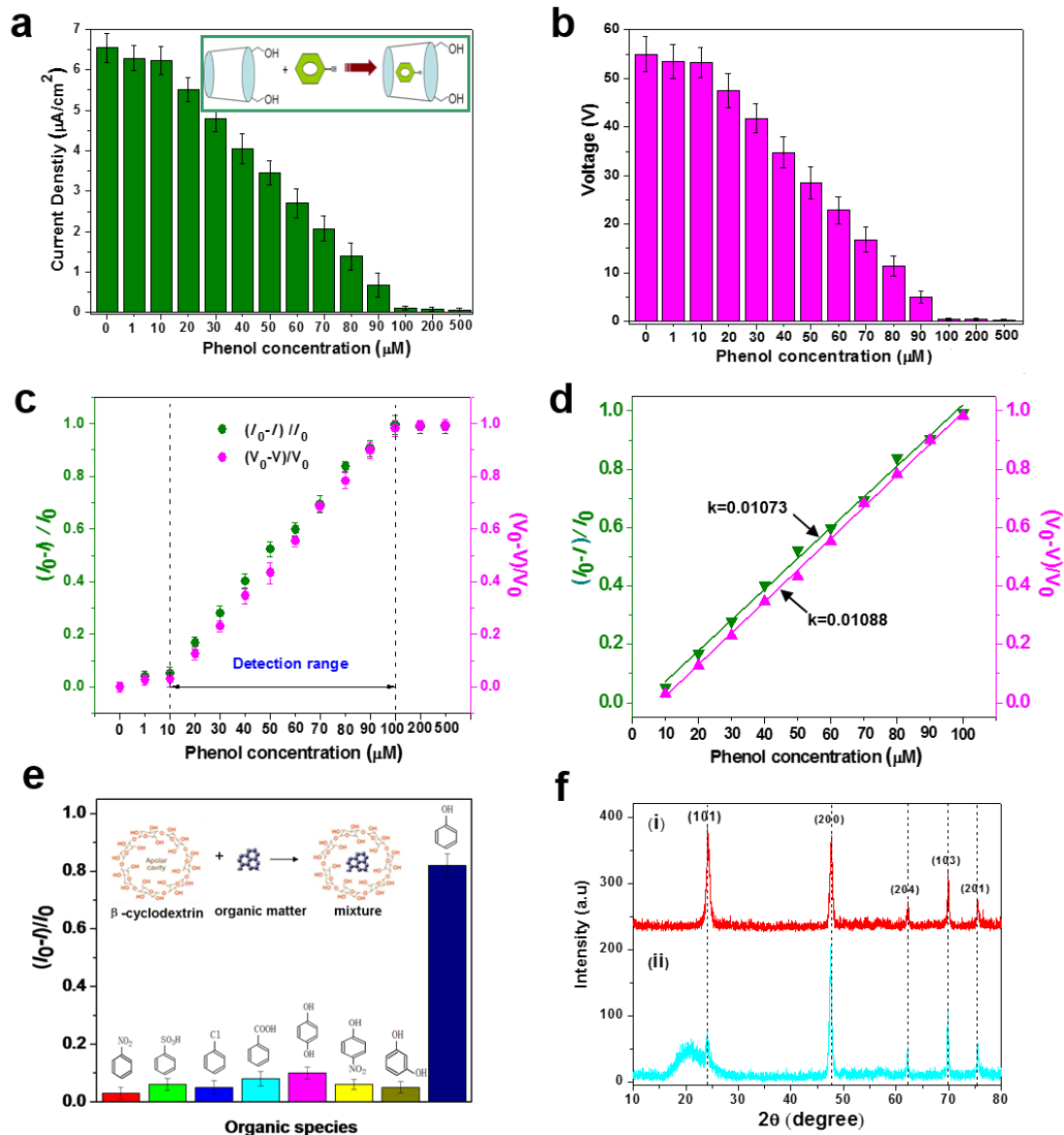
Figure 4.23 Under a fixed 80 µM β-cyclodextrin surface modification, dependence of the current (a) and voltage (b) output on the phenol concentrations. Inset is an illustration of the reaction mechanism between β-cyclodextrin and phenol molecule. (c) The sensitivity and detection range of the as-developed β-CD enhanced triboelectrification for phenol detection in term of both current and voltage output. (d) A sensitivity of 0.01/µM was simultaneously achieved from both current and voltage signals with a detection range of 10 – 100 µM. (e) Selectivity of the as-developed β-CD enhanced triboelectrification for phenol detection. Inset is an illustration of the reaction mechanism between β-cyclodextrin and different kinds of organic species. (f) A comparison of the XRD pattern of the TiO_2 nanowires: (i) as-grown (ii) refurbished with 20 mL ethyl alcohol after phenol detection.[139]

159

In order to render a direct view of the sensing performance of the β-CD enhanced triboelectrification for phenol detection, both the current ratio $((I_0-I)/I_0)$ and voltage ratio $((V_0-V)/V_0)$ were plotted versus the phenol concentrations, as shown in Figures 4.23c and 4.23d. These results reveal the designed nanosensor is sensitive to the phenol molecules with a sensitivity of 0.01/μM in the sensing range of 10 – 100μM.

Furthermore, control experiments were carried out to test the selectivity of the as-developed β-CD enhanced triboelectrification toward phenol detection as compared to other organic species. With a constant concentration of 50 μM for all the testing organic species, the obtained current ratio from the phenol absorbed nanosensor was far larger than other organic species (Figure 4.23e), which indicated that the β-CD enhanced triboelectrification is an effective means for phenol detection with excellent selectivity. Additionally, the β-CD enhanced triboelectrification based nanosensor is reusable and can be refurbished by ethyl alcohol rinsing after phenol detection. Both the XRD pattern (Figure 4.23f) and SEM image shows no chemical composition or surface morphology change after refurbishment, which proves a good reusability of the device for phenol detection.

4.4.2 Self-powered phenol electrochemical degradation

For a systematical treatment of ambient phenol, a further action was taken to degrade the phenol after it was detected. Here, a β-CD enhanced triboelectrification based energy harvester was developed as a power source to electrochemically degrade the phenol in the wastewater by using the kinetic impact energy from water waves.
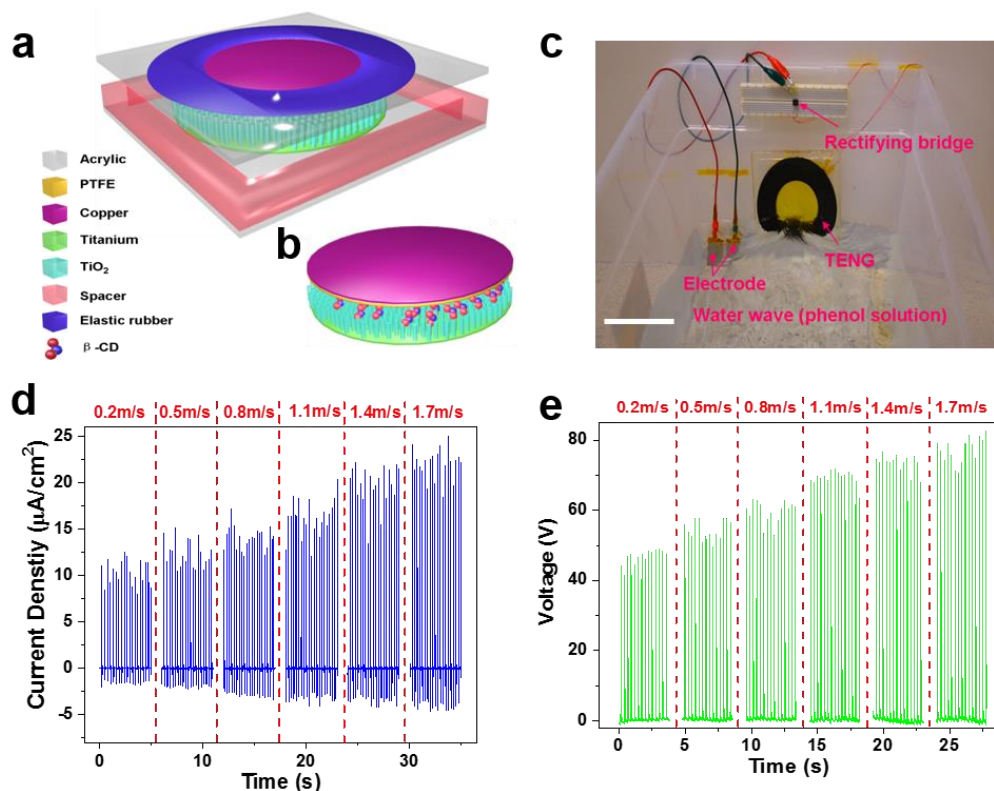
Figure 4.24 (a) Structural design of the β-CD enhanced triboelectrification for self-powered phenol degradation by using kinetic impact energy from water waves. (b) An illustration of the core part the β-CD enhanced triboelectrification for phenol degradation. (c) Demonstration of an integrated self-powered phenol degradation system by harnessing water waves. The scale bar is 15 cm. The dependence of the current (d) and voltage (e) output of the β-CD enhanced triboelectrification on the wave velocities.[139]

A schematic illustration of the water wave energy harvester is shown in Figure 4.24a, which has a multilayered structure with acrylic as supporting substrates. An annular ring shaped elastic rubber was employed to bridge the top plate of the "core" with the central-holed acrylic substrate, and thus it is capable of converting the water wave impact into the contact-separation of the two contact surfaces, PTFE and β-CD modified TiO_2 surface, thus convert the wave energy into electricity as a sustainable power source for phenol degradation. Figure 4.24b is a close view of the "core" of the as-developed wave energy harvester. An integrated self-powered phenol degradation system by harnessing wastewater wave energy is demonstrated in Figure 4.24c. An as-fabricated wave energy

harvester equipped with a Ti/PbO$_2$ anode and a Ti cathode was vertically fixed in a wastewater container.

With surface concentration of 80 μM β-CD on the TiO$_2$ nanowires, a quantitative characterization of the output performance responding to various water wave velocities were systematically investigated. In order to quantitatively control the water waves, a linear motor was used to introduce a periodical impact onto the water. The water waves were propagating at different velocities by controlling the frequency and impulse length of the linear motor. And a directly proportional relationship was experimentally observed between the two, as shown in Figure 4.24d and e. At a water wave velocity of 1.4m/s, the generated current density and voltage are as high as 20 μA/cm^2 and 70 V, respectively. The performance of the phenol degradation based on β-CD enhanced triboelectrification was evaluated at a fixed wave velocity of 1.4 m/s.

And the UV-Visible absorption spectra of the phenol in the wasted water, measured under fixed time intervals, were shown in Figure 4.25a. With the increasing of electrochemical degradation time, the characteristic absorption peak intensity of phenol in the wastewater decreases evidently, indicating the effectiveness of the route for self-powered phenol degradation. Inset of Figure 4.25a is the calibration curve of phenol concentration at the wavelength of 269 nm, which is the wavelength corresponding to the characteristic absorption peaks. In order to further validate the decrease of phenol absorption peak intensity is attributed to the electrochemical degradation, a control experiment was conducted without triboelectrification or external power sources. Since electricity is a must for the electrochemical degradation of phenol. Without electricity, the phenol cannot be degraded itself over time.
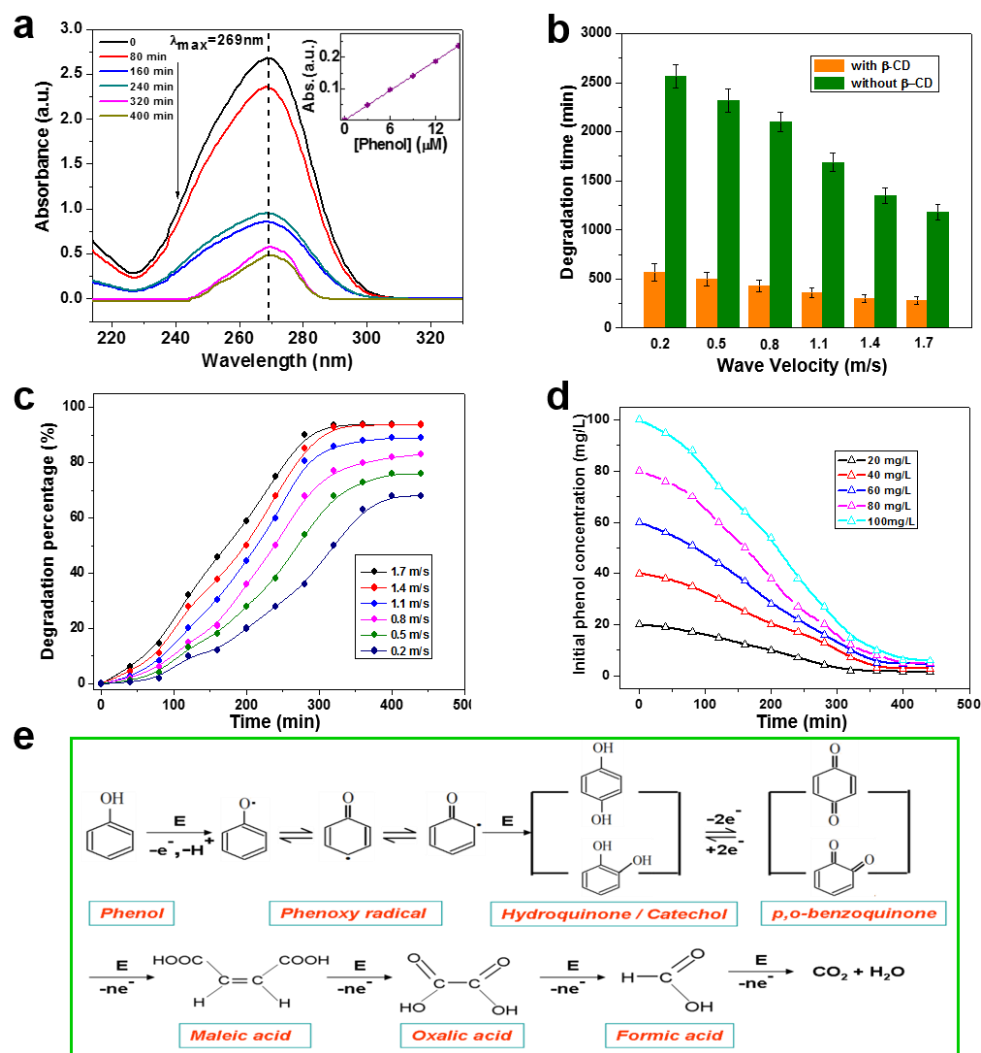
Figure 4.25 Performance evaluation of the β-CD enhanced triboelectrification for phenol degradation. (a) UV-Visible absorption spectra of the phenol in the wasted water with increasing of the electrochemical degradation time by the β-CD enhanced triboelectrification. Inset is the calibration curve of the phenol concentration from absorption spectra at a wavelength of 269 nm. (b) Comparison of the phenol degradation time versus the water waves velocity when the degradation percentage reaches 90%, without and with an 80 μM β-cyclodextrin surface modification. (c) Comparison of the phenol degradation percentage versus the degradation time under different propagating speeds of water waves. (d) Comparison of the initial phenol concentration versus the degradation time under fixed water waves velocity of 1.4 m/s. (e) The proposed reaction mechanisms of the phenol electrochemical degradation.[139]

Factors, especially the β-CD surface modification, wave velocity and the phenol initial concentration, can largely influence the effectiveness of the proposed routes for

phenol electrochemical degradation. A systematical investigation upon the three factors was made to comprehensively evaluate the performance of the β-CD enhanced triboelectrification based self-powered phenol degradation. First, the influence of β-CD surface modification on the degradation performance was studied via a comparison of the time needed for reaching a phenol degradation percentage of 90% under various wave velocities at a fixed initial phenol concentration of 80 mg/L. Technically, in an electrochemical degradation processing, the degradation efficiency is proportional to the applied power. As shown in Figure 4.25b, without β-CD surface modification, the phenol still degrades over time, but the degradation efficiency is very low due to a relatively smaller electrical output of the devices. However, after surface modification with β-CD, the β-CD enhanced triboelectrification, which contributes to a larger electrical output of the devices, largely boosts the speed of phenol electrochemical degradation and shortens the time required for completely mineralizing the phenol in the wastewater.

Secondly, as an important factor to the electrical output, the influence of water wave velocity on the degradation performance was also studied at a fixed initial phenol concentration of 80 mg/L. As demonstrated in Figure 4.25c, to reach the same phenol degradation percentage, a shorter time is needed with a larger wave velocity. Likewise, given a fixed degradation time interval, a larger wave velocity will contribute to a larger phenol degradation percentage in the wastewater. Specifically, given a wave velocity of 1.4 m/s, the degradation percentage of phenol in the wastewater is up to 90% in 320 min. Furthermore, in the beginning the phenol concentration in wastewater is high. The amount of phenol that can be degraded per unit time is more, which corresponds to a higher degradation rate. As the degradation reaction proceeded, the phenol concentration in

wastewater continues to decrease. And this will inevitably lead to a low degradation efficiency. That's why the degradation rate increases at first place (before 320 min), then keeps constant over time.

Additionally, initial phenol concentration in the wastewater is also another factor that needs to be explored for a systematical evaluation of the degradation performance. It is observed in Figure 4.25d that, under a fixed wave velocity of 1.4 m/s, more time is required for the electrochemical degradation starting with higher initial phenol concentration. And, what is more, though the initial phenol concentration varies, the residual content of phenol remains almost the same after a continuous degradation for 360 min. And it is encouraging to find out that the electrochemical degradation process is more effective at higher initial phenol concentrations, which renders the proposed route very practical and promising for the industrial wastewater treatment.

Experimentally, the phenol electrochemical degradation initiated at the Ti/PbO_2 anode electrode, where the color of the solution changed from initial colorless to yellow (40-260min), and lastly to colorless (300min). The proposed reaction mechanisms of the phenol electrochemical degradation were illustrated in Figure 4.25e. In electrochemical oxidation process, the phenol pollutants can not only be mineralized by the hydroxyl radicals produced on the anode surface, but also can be directly oxidized and degraded on the surface of anodes. Phenol was first transformed into phenoxy radical, and then the hydroxyl radicals produced on the anode surface attack benzene rings to produce hydroquinone and catechol. The hydroquinone and catechol were further degraded to benzoquinone, which turns the solution from colorless to yellow.[137, 138, 148] Subsequently, the ring was broken and the benzoquinone was degraded into various carboxylic acids such

as maleic acid, oxalic acid and formic acid. Finally, these organic acid intermediates were mineralized into CO_2 and H_2O, and thus the solution became colorless again.

In summary, we demonstrate a unique route that creatively harnessed the β-cyclodextrin (β-CD) enhanced triboelectricfication for both self-powered phenol detection and electrochemical degradation. Relying on the β-CD as the recognition element, the as-fabricated nanosensors can selectively capture and detect the phenol molecules in ambient environment. A detection sensitivity of 0.01/μM was experimentally read from calibrating both the current and voltage signals in a sensing range of 10 – 100 μM. The presented nanosenors are proved reusable after being refurbished with ethyl alcohol. Additionally, the β-cyclodextrin enhanced triboelectricfication was designed to harvest kinetic impact energy from water waves to electrochemically degrade the phenol in a self-powered manner without supplying an external power. At a fixed wave velocity of 1.4 m/s and initial phenol concentration of 80 mg/L, the generated power is capable of cleaning up to 90% of the phenol in the wastewater in 320 min. The justified concept of self-powered phenol treatment by using triboelectricfication is a green and alternative to traditional methods, which could arouse a broad range of audience, especially from the fields of wastewater treatment, ecological sanitation, environmental degradation, monitoring, assessment and sustainability. And it can not only be applied to the ambient phenol detection and degradation, but also can be extended to other common organic pollutants in the wastewater, such as methylbenzene, benzaldehyde, chlorobenzene, aniline, benzoic acid and so on, which is promising and could possible change the way of current wastewater treatment.

CHAPTER 5

CONCLUSIONS

Mechanical motion is of great abundance and ubiquitousness in ambient environment with a wide-range of scales and a variety of forms. It is also obtainable from human body. Harvesting mechanical energy is an important route in obtaining cost-effective, clean and sustainable electric energy. In the past decades, increasing research efforts have been committed to develop renewable energy technologies to convert the ambient motions into electricity. The triboelectric effect is known for many centuries and it is the cause of many charging phenomena. However, it has not been utilized for energy harvesting until very recently. Triboelectric nanogenerator (TENG), a creative invention based on triboelectric effect has been launched as a new and renewable energy technology in 2012. In the past four year's PhD study in Georgia Tech and as presented in this dissertation, I devoted myself to developing the TENG from fundamentals, devices, to applications. The concept and design presented in this dissertation research can greatly promote the development of TENG as both sustainable power sources and self-powered active sensors. In this chapter, my research achievements and technological innovations are summarized, and several suggestions for advancing this research filed are posed.

5.1 TENG as a new energy technology

To promote the development of TENG as a new energy technology, my efforts were committed from the following five aspects in my four years' PhD study at the Georgia Institute of Technology.

167

Fundamental Model Study: I and my co-workers invented a fundamentally new principle of TENG based on in-plane sliding electrification. It can be applied to TENGs of different configurations that accommodate the needs of harvesting energy and/or sensing from diverse mechanical motions, such as contacted sliding, lateral translation and rotation/rolling. It presented a versatile solution to harvest energy from diverse forms of mechanical motions, including rolling wheels, wind flow and water flow.

Vibration Energy Harvesting: I and my co-workers for the first time introduced a fundamentally new working principle into the field of vibration energy harvesting by fabricating a harmonic-resonator-based TENG. And we systematically built up the new field via a series of continuous projects. Featured as cost-effectiveness, scalable device sizes, abundant choices of low density triboelectric materials such as polymers, varieties of working modes, wide adaptability on structural design for various applications, the TENG based vibration energy harvesting overcome the challenges of the traditional approaches and will greatly benefit the whole scientific research community.

Rotary Energy Harvesting: I and my co-workers firstly reported a two-dimensional planar-structured TENG for producing energy from rotary surfaces with unprecedented performance. With an average output power of 1.5 W, corresponding to an area power density of 19 mWcm^{-2}, the radial-arrayed rotary TENG represented a gigantic leap in terms of output power by orders of magnitude compared to previous reports. In the meanwhile, the robustness of TENG for rotary energy harvesting remains a great challenge owning to the requirement of surface friction for a decent output. In this regards, I and my coworkers also developed techniques that achieves a high output performance without compromising the device robustness through either rolling friction based charge

replenishment or an automatic transition between a contact working state and a non-contact working state.

Acoustic Energy Harvesting: I and my co-workers introduced a new working principle into the field of acoustic energy harvesting by firstly fabricating an organic thin-film based TENG with an energy conversion efficiency up to 60%. And then, we innovatively employed a multi-hole structure on the paper electrode to developed an ultrathin, rollable paper based TENG, which can effectively get rid of the traditional resonator for acoustic energy harvesting. These two works present an adaptable, cost-effective and fundamentally new approach for ambient acoustic energy harvesting, which can be further applied in a variety of circumstances for either energy-harvesting or sensing purposes, e.g. aeroacoustic sensing, jet engine noise reduction, military surveillance and reconnaissance as well as wireless technology applications.

Large-Scale Blue Energy Harvesting: I and my coworkers, paved a new way in the field of blue energy exploitation by presenting a TENG network (TENG-NW) design. This approach distinguishes itself from several aspects. Firstly, TENG-NW is suitable to harvest wave energy in a wide range of wave motions, from subtle to strong, transverse wave to lateral wave. Furthermore, not like the electromagnetic effect based wave energy harvesting, which mainly relies on the undercurrents, the TENG-NW is capable of harvesting energy from both the undercurrent and the surface waves. Besides, most of the wave motions are multidirectional, the TENG-NW, with a rationally designed structure, renders an innovative and effective approach to fully utilize the wave motion from all-directions. And it can not only be applied in the epicontinental sea, but also can easily be implemented in almost all of the water area.

In addition, relying on the surface charging effect, only small amount of materials are needed. The TENG-NW is thus cost-effective as well as light-weight, which makes it possible high anticorrosion to the marine environment and floating on the water surface, which will greatly eliminate the needs of building poles or towers for holding traditions electromagnetic generators for wave energy harvesting.

Based on these research, it is safe to conclude that TENG is a fundamentally new energy technology, featured as being simple, reliable, cost-effective as well as high efficiency. And it is a green and alternative to traditional methods for ambient mechanical energy harvesting and also potentially for large-scale blue energy harvesting.

5.2 TENG as self-powered active sensors

As a sustainable power source, TENG can convert the mechanical input into electrical output signals, reversely, TENG can also be a high sensitive self-powered sensors for detecting mechanical triggering, stimulation and movement. The electric current and voltage signals generated by TENG represent the dynamic and static information, respectively, regarding a mechanical action. Part of my dissertation research was also involved in developing TENG into self-powered active sensing systems for human health monitoring, ambient phenol / heavy metal ions / alcohol detection, as well as the self-powered human-machine interfacing.

Self-powered Acoustic Sensing: A triboelectrification based thin-film nanogenerator was first developed as an acoustic sensor which can not only act as self-powered microphone, but also can act an acoustic source localization sensor within an average error circle of 7 cm in diameter. Subsequently, an ultrathin, rollable, paper-based

microphone was also developed. The rolled device is directional independence, which can be used for self-powered all-sounding recording without an angular dependence. The proposed acoustic sensors have extensive applications in the fields such as military surveillance and reconnaissance, intruder detection, sniper localization, underwater acoustics, and auto talker detection in a web conferencing.

Self-powered Human-Machine Interfacing: Computer keyboard is one of the most common, reliable, accessible and effective approaches used for human-machine interfacing and information exchange. I and my coworkers reported a self-powered, non-mechanical-punching keyboard enabled by contact electrification between human fingers and keys, which converts mechanical stimuli applied onto the keyboard into local electronic signals without applying an external power. The intelligent keyboard (IKB) can not only sensitively trigger a wireless alarm system once gentle finger tapping occurs but also be capable of tracing and recording typing contents by detecting both the dynamic time intervals between and during inputting letters and the force used for each typing action. Such features promise its use as a smart security system that can realize detection. The IKB can be potentially applied not only to self-powered electronics but also to artificial intelligence, cyber security, and computer or network access control.

Self-powered Biomedical Monitoring: Measurements of human physiological or behavioral characteristics are the main designing functions of wearable and interactive electronics. And I and my co-workers reported the first bionic membrane sensor (BMS) based on triboelectrification for self-powered physiological and behavioral measurements such as local internal body pressures. Enabled by the unique sensing mechanism and an eardrum-inspired structure, the self-powered bionic membrane sensor holds a collection of

superior performances, including fast response time (< 6 ms), low pressure detection limit down to 2.5 Pa, high sensitivity (>51 mVPa^{-1}), high stability (>40,000 loading and unloading cycles), as well as an exceptional wide working bandwidth. The BMS can be utilized to measure rapidly-changing pressure over an exceptional wide frequency ranges from 0.1 Hz to 3.2 kHz, which enables it to not only continuously monitor the human low-frequency arterial pulse wave, but also to acquire and recover the high-frequency throat sound using a single device. As a demonstration, by measuring the distinguishable dynamic pressure patterns of human cardiovascular system, the BMS is capable of acting as a wearable, mobile, user-friendly and self-powered arterial pulse wave monitor for continuous and noninvasive human health assessment and monitoring.

Self-powered Chemical Sensing: Chemical pollutants, such as phenol, heavy metal ions, widely existed in ambient environment, especially in the waste waters. The treatment of them is of special concern due to their recalcitrance and persistence in the environment, which also places a permanent damage to the underground water system once invaded. In this regard, I and my coworkers, for the first time introduced the triboelectric effect into the field of wastewater treatment. And the chemicals pollutants, such as phenol, heavy metal ions, was demonstrated to be detected and removed. With a collection of compelling features, such as high detection sensitivity and degradation efficiency, extremely low cost, simplicity and reusability, the presented works not only provide a new and efficient pathway for environmental chemical treatment, but also a solid "green" advancement in the fields of industrial waste management, ecological sanitation, environmental degradation, monitoring, assessment and sustainability.

5.3 Future works

The discovery of the triboelectric nanogenerator is a major milestone in the field of converting mechanical motions into electricity for building self-powered systems. TENGs have experienced a very rapid development both in fundamental understanding and technological improvements in the last four years. As toward the future applications, some problems still remain to be solved to make this technology applicable as commercial products, as listed in the following.

First and foremost, the fundamental mechanism of contact electrification still needs clarification. Although triboelectrification is a widely existed phenomenon around us in daily life, the underlying physics is still unexplored.[16, 17, 108-111] Why do electrons transfer at the interfaces when two materials are brought into contact with each other? As the cornerstone of TENG, a clarification of the contact electrification processing will be great beneficial to optimize the TENG output performance.

Besides, a general challenge of TENG is its relatively low current output. How to effectively and efficiently manage the output power of TENG that can be used for practical applications is of great importance. This is a critical step towards TENG based self-powered systems.

Moreover, device durability and output reliability is also a disturbing concern that needed to be addressed. A requirement of the surface friction between two contact materials for a decent output renders the TENGs a common challenge that the material abrasion and the concomitantly generated heat will make the device nondurable under long-term continuous working and reduce the energy conversion efficiency. As a consequence, durable fabrication materials and rational device structural design are

necessary for achieving a high output performance without compromising the device robustness.

Furthermore, since the TENG output performance is highly subjected to environmental factors, such as temperature, humidity, pressure, particle contaminations and so on.[149-153] Packaging is highly desirable for long-term device operation, especially in some harsh environment.

Last but not least, based on a surface charging effect, the TENG based sensing application is challenged when the device dimension is miniaturized, which greatly hinders its further development into the micro-electro-mechanical systems. More advanced device design and fabrication techniques are highly desired to accomplish a higher spatial resolution of the TENG based active sensors.

REFERENCES

1. Painuly, J. P. *Renewable Energy* **2001,** 24, 73-89.

2. Panwar, N. L.; Kaushik, S. C.; Kothari, S. *Renewable and Sustainable Energy Reviews* **2011,** 15, 1513-1524.

3. Weisser, D.; Garcia, R. S. *Renewable Energy* **2005,** 30, 1299-1308.

4. Abed, I.; Kacem, N.; Bouhaddi, N.; Bouazizi, M. L. *Smart Materials and Structures* **2016,** 25, 025018.

5. Beeby, S. P.; Torah, R. N.; Tudor, M. J.; Glynne-Jones, P.; Donnell, T. O.; Saha, C. R.; Roy, S. *Journal of Micromechanics and Microengineering* **2007,** 17, 1257.

6. Shearwood, C.; Yates, R. B., in *Electronics Letters*, Institution of Engineering and Technology, **1997,** 33, 1883-1884.

7. Mitcheson, P. D.; Miao, P.; Stark, B. H.; Yeatman, E. M.; Holmes, A. S.; Green, T. C. *Sensors and Actuators A: Physical* **2004,** 115, 523-529.

8. Beeby, S.; A Tudor, M.; A White, N. *Measurement Science and Technology* **2006,** 17, R175-R195.

9. Janicek, V.; Husak, M. *Journal of Electrostatics* **2013,** 71, 214-219.

10. Qin, Y.; Wang, X.; Wang, Z. L. *Nature* **2008,** 451, 809-813.

11. Wang, X.; Song, J.; Liu, J.; Wang, Z. L. *Science* **2007,** 316, 102-105.

12. Wang, Z. L.; Song, J. *Science* **2006,** 312, 242-246.

13. Xu, S.; Hansen, B. J.; Wang, Z. L. *Nature Communications* **2010,** 1, 93.

14. Xu, S.; Qin, Y.; Xu, C.; Wei, Y.; Yang, R.; Wang, Z. L. *Nature Nanotechnology* **2010,** 5, 366-373.

15. Yang, R.; Qin, Y.; Dai, L.; Wang, Z. L. *Nature Nanotechnology* **2009,** 4, 34-39.

16. Horn, R. G.; Smith, D. T. *Science* **1992,** 256, 362-364.

17. Horn, R. G.; Smith, D. T.; Grabbe, A. *Nature* **1993,** 366, 442-443.

18. Fan, F.-R.; Tian, Z.-Q.; Lin Wang, Z. L. *Nano Energy* **2012,** 1, 328-334.

19. Bae, J.; Lee, J.; Kim, S.; Ha, J.; Lee, B.-S.; Park, Y.; Choong, C.; Kim, J.-B.; Wang, Z. L.; Kim, H.-Y.; Park, J.-J.; Chung, U. I. *Nature Communications* **2014,** 5,4929.

20. Bai, P.; Zhu, G.; Lin, Z.-H.; Jing, Q.; Chen, J.; Zhang, G.; Ma, J.; Wang, Z. L. *ACS Nano* **2013,** 7, 3713-3719.

21. Bai, P.; Zhu, G.; Liu, Y.; Chen, J.; Jing, Q.; Yang, W.; Ma, J.; Zhang, G.; Wang, Z. L. *ACS Nano* **2013,** 7, 6361-6366.

22.Yang, Y.; Zhang, H.; Chen, J.; Lee, S.; Hou, T.-C.; Wang, Z. L. *Energy & Environmental Science* **2013,** 6, 1744-1749.

23. Yang, Y.; Zhang, H.; Lin, Z.-H.; Liu, Y.; Chen, J.; Lin, Z.; Zhou, Y. S.; Wong, C. P.; Wang, Z. L. *Energy & Environmental Science* **2013,** 6, 2429-2434.

24. Yang, Y.; Zhang, H.; Lin, Z.-H.; Zhou, Y. S.; Jing, Q.; Su, Y.; Yang, J.; Chen, J.; Hu, C.; Wang, Z. L. *ACS Nano* **2013,** 7, 9213-9222.

25. Zhu, G.; Zhou, Y. S.; Bai, P.; Meng, X. S.; Jing, Q.; Chen, J.; Wang, Z. L. *Advanced Materials* **2014,** 26, 3788-3796.

26. Wang, S.; Lin, L.; Wang, Z. L. *Nano Letters* **2012,** 12, 6339-6346.

27. Zhu, G.; Lin, Z.-H.; Jing, Q.; Bai, P.; Pan, C.; Yang, Y.; Zhou, Y.; Wang, Z. L. *Nano Letters* **2013,** 13, 847-853.

28. Zhu, G.; Pan, C.; Guo, W.; Chen, C.-Y.; Zhou, Y.; Yu, R.; Wang, Z. L. *Nano Letters* **2012,** 12, 4960-4965.

29. Wang, Z. L.; Chen, J.; Lin, L. *Energy & Environmental Science* **2015,** 8, 2250-2282.

30. Wang, Z. L. *ACS Nano* **2013,** 7, 9533-9557.

31. Wang, Z. L. *Faraday Discussions* **2014,** 176, 447-458.

32. Wang, S.; Lin, L.; Xie, Y.; Jing, Q.; Niu, S.; Wang, Z. L. *Nano Letters* **2013,** 13, 2226-2233.

33. Zhu, G.; Chen, J.; Liu, Y.; Bai, P.; Zhou, Y. S.; Jing, Q.; Pan, C.; Wang, Z. L. *Nano Letters* **2013,** 13, 2282-2289.

34. Yang, Y.; Zhang, H.; Chen, J.; Jing, Q.; Zhou, Y. S.; Wen, X.; Wang, Z. L. *ACS Nano* **2013,** 7, 7342-7351.

35. Yang, Y.; Zhou, Y. S.; Zhang, H.; Liu, Y.; Lee, S.; Wang, Z. L. *Advanced Materials* **2013,** 25, 6594-6601.

36. Wang, S.; Xie, Y.; Niu, S.; Lin, L.; Wang, Z. L. *Advanced Materials* **2014,** 26, 2818-2824.

37. Beeby, S. P.; Tudor, M. J.; White, N. M. *Measurement Science and Technology* **2006,** 17, R175.

38. Shen, D.; Park, J.-H.; Noh, J. H.; Choe, S.-Y.; Kim, S.-H.; Wikle Iii, H. C.; Kim, D.-J. *Sensors and Actuators A: Physical* **2009,** 154, 103-108.

39. Kulah, H.; Najafi, K. *Sensors Journal, IEEE* **2008,** 8, 261-268.

40. Chen, J.; Zhu, G.; Yang, W.; Jing, Q.; Bai, P.; Yang, Y.; Hou, T.-C.; Wang, Z. L. *Advanced Materials* **2013,** 25, 6094-6099.

41. Fang, H.; Wu, W.; Song, J.; Wang, Z. L. *The Journal of Physical Chemistry C* **2009,** 113, 16571-16574.

42. Tang, L.; Yang, Y. *Applied Physics Letters* **2012,** 101, 094102.

43. Wang, X. Y.; Palagummi, S.; Liu, L.; Yuan, F. G. *Smart Materials and Structures* **2013,** 22, 055016.

44. Ashraf, K.; Khir, M. H. M.; Dennis, J. O.; Baharudin, Z. *Smart Materials and Structures* **2013,** 22, 049601.

45. Yang, J.; Chen, J.; Yang, Y.; Zhang, H.; Yang, W.; Bai, P.; Su, Y.; Wang, Z. L. *Advanced Energy Materials* **2014,** 4, 1301322.

46. Yang, W.; Chen, J.; Zhu, G.; Wen, X.; Bai, P.; Su, Y.; Lin, Y.; Wang, Z. L. *Nano Research* **2013,** 6, 880-886.

47. Fan, F.-R.; Lin, L.; Zhu, G.; Wu, W.; Zhang, R.; Wang, Z. L. *Nano Letters* **2012,** 12, 3109-3114.

48. Hu, Y.; Zhang, Y.; Xu, C.; Lin, L.; Snyder, R. L.; Wang, Z. L. *Nano Letters* **2011,** 11, 2572-2577.

49. Yang, W.; Chen, J.; Jing, Q.; Yang, J.; Wen, X.; Su, Y.; Zhu, G.; Bai, P.; Wang, Z. L. *Advanced Functional Materials* **2014,** 24, 4090-4096.

50. Yang, W.; Chen, J.; Zhu, G.; Yang, J.; Bai, P.; Su, Y.; Jing, Q.; Cao, X.; Wang, Z. L. *ACS Nano* **2013,** 7, 11317-11324.

51. Yang, P.-K.; Lin, Z.-H.; Pradel, K. C.; Lin, L.; Li, X.; Wen, X.; He, J.-H.; Wang, Z. L. *ACS Nano* **2015,** 9, 901-907.

52. Zhang, X.-S.; Han, M.-D.; Wang, R.-X.; Zhu, F.-Y.; Li, Z.-H.; Wang, W.; Zhang, H.-X. *Nano Letters* **2013,** 13, 1168-1172.

53. Zhong, J.; Zhong, Q.; Fan, F.; Zhang, Y.; Wang, S.; Hu, B.; Wang, Z. L.; Zhou, J. *Nano Energy* **2013,** 2, 491-497.

54. Lin, L.; Wang, S.; Niu, S.; Liu, C.; Xie, Y.; Wang, Z. L. *ACS Applied Materials & Interfaces* **2014,** 6, 3031-3038.

55. Lin, L.; Wang, S.; Xie, Y.; Jing, Q.; Niu, S.; Hu, Y.; Wang, Z. L. *Nano Letters* **2013,** 13, 2916-2923.

56. Xie, Y.; Wang, S.; Lin, L.; Jing, Q.; Lin, Z.-H.; Niu, S.; Wu, Z.; Wang, Z. L. *ACS Nano* **2013,** 7, 7119-7125.

57. Yang, Y.; Zhang, H.; Wang, Z. L. *Advanced Functional Materials* **2014,** 24, 3745-3750.

58. Zhang, C.; Zhou, T.; Tang, W.; Han, C.; Zhang, L.; Wang, Z. L. *Advanced Energy Materials* **2014,** 4, 1301798.

59. Zhu, G.; Chen, J.; Zhang, T.; Jing, Q.; Wang, Z. L. *Nature Communications* **2014,** 5, 3426.

60. Niu, S.; Liu, Y.; Wang, S.; Lin, L.; Zhou, Y. S.; Hu, Y.; Wang, Z. L. *Advanced Materials* **2013,** 25, 6184-6193.

61. Kim, Y. K.; Chang, C. A.; Schrott, A. G. *Journal of Applied Physics* **1990,** 67, 251-254.

62. Zi, Y.; Lin, L.; Wang, J.; Wang, S.; Chen, J.; Fan, X.; Yang, P.-K.; Yi, F.; Wang, Z. L. *Advanced Materials* **2015,** 27, 2340-2347.

63. Xie, Y.; Wang, S.; Niu, S.; Lin, L.; Jing, Q.; Su, Y.; Wu, Z.; Wang, Z. L. *Nano Energy* **2014,** 6, 129-136.

64. Meng, X. S.; Li, H. Y.; Zhu, G.; Wang, Z. L. *Nano Energy* **2015,** 12, 606-611.

65. Du, W.; Han, X.; Lin, L.; Chen, M.; Li, X.; Pan, C.; Wang, Z. L. *Advanced Energy Materials* **2014,** 4, 1301592.

66. Chen, J.; Yang, J.; Guo, H.; Li, Z.; Zheng, L.; Su, Y.; Wen, Z.; Fan, X.; Wang, Z. L. *ACS Nano* **2015,** 9, 12334-12343.

67. Zhong, Q.; Zhong, J.; Hu, B.; Hu, Q.; Zhou, J.; Wang, Z. L. *Energy & Environmental Science* **2013,** 6, 1779-1784.

68. Zhong, J.; Zhang, Y.; Zhong, Q.; Hu, Q.; Hu, B.; Wang, Z. L.; Zhou, J. *ACS Nano* **2014,** 8, 6273-6280.

69. Shin, S.-H.; Kwon, Y. H.; Kim, Y.-H.; Jung, J.-Y.; Lee, M. H.; Nah, J. *ACS Nano* **2015,** 9, 4621-4627.

70. Seung, W.; Gupta, M. K.; Lee, K. Y.; Shin, K.-S.; Lee, J.-H.; Kim, T. Y.; Kim, S.; Lin, J.; Kim, J. H.; Kim, S.-W. *ACS Nano* **2015,** 9, 3501-3509.

71. Lee, K. Y.; Chun, J.; Lee, J.-H.; Kim, K. N.; Kang, N.-R.; Kim, J.-Y.; Kim, M. H.; Shin, K.-S.; Gupta, M. K.; Baik, J. M.; Kim, S.-W. *Advanced Materials* **2014,** 26, 5037-5042.

72. Han, M.; Zhang, X.-S.; Meng, B.; Liu, W.; Tang, W.; Sun, X.; Wang, W.; Zhang, H. *ACS Nano* **2013,** 7, 8554-8560.

73. Lin, L.; Xie, Y.; Niu, S.; Wang, S.; Yang, P.-K.; Wang, Z. L. *ACS Nano* **2015,** 9, 922-930.

74. Guo, H.; Chen, J.; Yeh, M.-H.; Fan, X.; Wen, Z.; Li, Z.; Hu, C.; Wang, Z. L. *ACS Nano* **2015,** 9, 5577-5584.

75. Jeong, C. K.; Baek, K. M.; Niu, S.; Nam, T. W.; Hur, Y. H.; Park, D. Y.; Hwang, G.-T.; Byun, M.; Wang, Z. L.; Jung, Y. S.; Lee, K. J. *Nano Letters* **2014,** 14, 7031-7038.

76. Bai, P.; Zhu, G.; Zhou, Y.; Wang, S.; Ma, J.; Zhang, G.; Wang, Z. L. *Nano Research* **2014,** 7, 990-997.

77. Bai, P.; Zhu, G.; Jing, Q.; Yang, J.; Chen, J.; Su, Y.; Ma, J.; Zhang, G.; Wang, Z. L. *Advanced Functional Materials* **2014,** 24, 5807-5813.

78. Niu, S.; Wang, Z. L. *Nano Energy* **2015,** 14, 161-192.

79. Cha, S. N.; Seo, J.-S.; Kim, S. M.; Kim, H. J.; Park, Y. J.; Kim, S.-W.; Kim, J. M. *Advanced Materials* **2010,** 22, 4726-4730.

80. Que, R.; Shao, Q.; Li, Q.; Shao, M.; Cai, S.; Wang, S.; Lee, S.-T. *Angewandte Chemie International Edition* **2012,** 51, 5418-5422.

81. Mei, J.; Ma, G.; Yang, M.; Yang, Z.; Wen, W.; Sheng, P. *Nature Communications* **2012,** 3, 756.

82. Yang, J.; Chen, J.; Liu, Y.; Yang, W.; Su, Y.; Wang, Z. L. *ACS Nano* **2014,** 8, 2649-2657.

83. Sessler, G. M.; West, J. E. *The Journal of the Acoustical Society of America* **1969,** 46, 1081-1086.

84. Hu, X.; Ho, K.-M.; Chan, C. T.; Zi, J. *Physical Review B* **2008,** 77, 172301.

85. Fan, X.; Chen, J.; Yang, J.; Bai, P.; Li, Z.; Wang, Z. L. *ACS Nano* **2015,** 9, 4236-4243.

86. Červenka, M.; Šoltés, M.; Bednařík, M. *The Journal of the Acoustical Society of America* **2014,** 136, 1003-1012.

87. Yu, K.; Zijlstra, P.; Sader, J. E.; Xu, Q.-H.; Orrit, M. *Nano Letters* **2013,** 13, 2710-2716.

88. Zhou, J.; Bhaskar, A.; Zhang, X. *Journal of Sound and Vibration* **2014,** 333, 1972-1990.

89. Goll, E.; Dalhoff, E. *The Journal of the Acoustical Society of America* **2011,** 130, 1452-1462.

90. Kashy, E.; Johnson, D. A.; McIntyre, J.; Wolfe, S. L. *American Journal of Physics* **1997,** 65, 310-313.

91. Holt, J. K.; Park, H. G.; Wang, Y.; Stadermann, M.; Artyukhin, A. B.; Grigoropoulos, C. P.; Noy, A.; Bakajin, O. *Science* **2006,** 312, 1034-1037.

92. Fusheng, H.; Gary, S.; Yuyuan, Z.; Barry, G. *Journal of Physics D: Applied Physics* **2003,** 36, 294.

93. Murray, A. R. J.; Summers, I. R.; Sambles, J. R.; Hibbins, A. P. *Journal of the Acoustical Society of America* **2014,** 136, 980-984.

94. Salter, S. H. *Nature* **1974,** 249, 720-724.

95. Falcão, A. F. d. O. *Renewable and Sustainable Energy Reviews* **2010,** 14, 899-918.

96. Falnes, J. *Marine Structures* **2007,** 20, 185-201.

97. Kofoed, J. P.; Frigaard, P.; Friis-Madsen, E.; Sørensen, H. C. *Renewable Energy* **2006,** 31, 181-189.

98. Chen, J.; Yang, J.; Li, Z.; Fan, X.; Zi, Y.; Jing, Q.; Guo, H.; Wen, Z.; Pradel, K. C.; Niu, S.; Wang, Z. L. *ACS Nano* **2015,** 9, 3324-3331.

99. Lin, Z.-H.; Cheng, G.; Wu, W.; Pradel, K. C.; Wang, Z. L. *ACS Nano* **2014,** 8, 6440-6448.

100. Lin, Z.-H.; Cheng, G.; Lin, L.; Lee, S.; Wang, Z. L. *Angewandte Chemie International Edition* **2013,** 125, 12777-12781.

101. Lin, Z.-H.; Cheng, G.; Lee, S.; Pradel, K. C.; Wang, Z. L. *Advanced Materials* **2014,** 26, 4690-4696.

102. Liang, Q.; Yan, X.; Gu, Y.; Zhang, K.; Liang, M.; Lu, S.; Zheng, X.; Zhang, Y. *Scientific Reports* **2015,** 5, 9080.

103. Hu, Y.; Yang, J.; Jing, Q.; Niu, S.; Wu, W.; Wang, Z. L. *ACS Nano* **2013,** 7, 10424-10432.

104. Fan, F. R.; Luo, J.; Tang, W.; Li, C.; Zhang, C.; Tian, Z.; Wang, Z. L. *Journal of Materials Chemistry A* **2014,** 2, 13219-13225.

105. Cheng, G.; Lin, Z.-H.; Lin, L.; Du, Z.-l.; Wang, Z. L. *ACS Nano* **2013,** 7, 7383-7391.

106. Cheng, G.; Lin, Z.-H.; Du, Z.-l.; Wang, Z. L. *ACS Nano* **2014,** 8, 1932-1939.

107. Chen, S.; Gao, C.; Tang, W.; Zhu, H.; Han, Y.; Jiang, Q.; Li, T.; Cao, X.; Wang, Z. L. *Nano Energy* **2015,** 14, 217-225.

108. Terris, B. D.; Stern, J. E.; Rugar, D.; Mamin, H. J. *Physical Review Letters* **1989,** 63, 2669-2672.

109. Henniker, J. *Nature* **1962,** 196, 474-474.

110. Grzybowski, B. A.; Winkleman, A.; Wiles, J. A.; Brumer, Y.; Whitesides, G. M. *Nature Materials* **2003,** 2, 241-245.

111. Baytekin, H. T.; Patashinski, A. Z.; Branicki, M.; Baytekin, B.; Soh, S.; Grzybowski, B. A. *Science* **2011,** 333, 308-312.

112. Chen, J.; Zhu, G.; Yang, J.; Jing, Q.; Bai, P.; Yang, W.; Qi, X.; Su, Y.; Wang, Z. L. *ACS Nano* **2015,** 9, 105-116.

113. Diaz, A. F.; Felix-Navarro, R. M. *Journal of Electrostatics* **2004,** 62, 277-290.

114. Niu, S.; Liu, Y.; Wang, S.; Lin, L.; Zhou, Y. S.; Hu, Y.; Wang, Z. L. *Advanced Functional Materials* **2014,** 24, 3332-3340.

115. Gang, F.; Jun, F. *Electromagnetic Compatibility, IEEE Transactions on* **2010,** 52, 699-711.

116. Yoo, J.; Long, Y.; El-Damak, D.; Altaf, M. A. B.; Shoeb, A. H.; Chandrakasan, A. P. *Solid-State Circuits, IEEE Journal of* **2013,** 48, 214-228.

117. Weichao, X.; Chunqi, C.; Hung, Y. S.; Kwan, S. K.; Chin Wan Fung, P. *Signal Processing, IEEE Transactions on* **2007,** 55, 5552-5563.

118. Ma, Z. *Science* **2011,** 333, 830-831.

119. Wu, W.; Wen, X.; Wang, Z. L. *Science* **2013,** 340, 952-957.

120. Schwartz, G.; Tee, B. C. K.; Mei, J.; Appleton, A. L.; Kim, D. H.; Wang, H.; Bao, Z. *Nature Communications* **2013,** 4, 1859.

121. Dagdeviren, C.; Su, Y.; Joe, P.; Yona, R.; Liu, Y.; Kim, Y.-S.; Huang, Y.; Damadoran, A. R.; Xia, J.; Martin, L. W.; Huang, Y.; Rogers, J. A. *Nature Communications* **2014,** 5, 4496.

122. Hammock, M. L.; Chortos, A.; Tee, B. C. K.; Tok, J. B. H.; Bao, Z. *Advanced Materials* **2013,** 25, 5997-6038.

123. Yang, J.; Chen, J.; Su, Y.; Jing, Q.; Li, Z.; Yi, F.; Wen, X.; Wang, Z.; Wang, Z. L. *Advanced Materials* **2015,** 27, 1316-1326.

124. Mannsfeld, S. C. B.; Tee, B. C. K.; Stoltenberg, R. M.; Chen, C. V. H. H.; Barman, S.; Muir, B. V. O.; Sokolov, A. N.; Reese, C.; Bao, Z. *Nature Materials* **2010,** 9, 859-864.

125. Persano, L.; Dagdeviren, C.; Su, Y.; Zhang, Y.; Girardo, S.; Pisignano, D.; Huang, Y.; Rogers, J. A. *Nature Communications* **2013,** 4, 1633.

126. Pang, C.; Lee, G.-Y.; Kim, T.-i.; Kim, S. M.; Kim, H. N.; Ahn, S.-H.; Suh, K.-Y. *Nature Materials* **2012,** 11, 795-801.

127. Wang, X.; Gu, Y.; Xiong, Z.; Cui, Z.; Zhang, T. *Advanced Materials* **2014,** 26, 1336-1342.

128. Gong, S.; Schwalb, W.; Wang, Y.; Chen, Y.; Tang, Y.; Si, J.; Shirinzadeh, B.; Cheng, W. *Nature Communications* **2014,** 5.

129. Alberto, P. A.; Mark, B.; Andrew, W. *Physiological Measurement* **2010,** 31, R1.

130. Nichols, W. W. *American Journal of Hypertension* **2005,** 18, 3S-10S.

131. Mier, P. D.; Van Den Hurk, J. J. M. A. *British Journal of Dermatology* **1975,** 93, 1-10.

132. Wang, J.; Lu, J.; Ly, S. Y.; Vuki, M.; Tian, B.; Adeniyi, W. K.; Armendariz, R. A. *Analytical Chemistry* **2000,** 72, 2659-2663.

133. Zhao, T.; He, J.; Wang, X.; Ma, B.; Wang, X.; Zhang, L.; Li, P.; Liu, N.; Lu, J.; Zhang, X. *Journal of Pharmaceutical and Biomedical Analysis* **2014,** 98, 311-320.

134. Han, X. X.; Chen, L.; Kuhlmann, U.; Schulz, C.; Weidinger, I. M.; Hildebrandt, P. *Angewandte Chemie International Edition* **2014,** 53, 2481-2484.

135. Mukthar Ali, M.; Sandhya, K. Y. *Carbon* **2014,** 70, 249-257.

136. Ma, W.; Li, J.; Tao, X.; He, J.; Xu, Y.; Yu, J. C.; Zhao, J. *Angewandte Chemie International Edition* **2003,** 42, 1029-1032.

137. Li, H.; Chen, Y.; Zhang, Y.; Han, W.; Sun, X.; Li, J.; Wang, L. *Journal of Electroanalytical Chemistry* **2013,** 689, 193-200.

138. Ma, W.; Cheng, Z.; Gao, Z.; Wang, R.; Wang, B.; Sun, Q. *Chemical Engineering Journal* **2014,** 241, 167-174.

139. Li, Z.; Chen, J.; Yang, J.; Su, Y.; Fan, X.; Wu, Y.; Yu, C.; Wang, Z. L. *Energy & Environmental Science* **2015,** 8, 887-896.

140. Lin, Z.-H.; Xie, Y.; Yang, Y.; Wang, S.; Zhu, G.; Wang, Z. L. *ACS Nano* **2013,** 7, 4554-4560.

141. Liao, J.-Y.; Lei, B.-X.; Chen, H.-Y.; Kuang, D.-B.; Su, C.-Y. *Energy & Environmental Science* **2012,** 5, 5750-5757.

142. Chen, X.; Cheng, X.; Gooding, J. J. *Analytical Chemistry* **2012,** 84, 8557-8563.

143. Feng, J.; Miedaner, A.; Ahrenkiel, P.; Himmel, M. E.; Curtis, C.; Ginley, D. *Journal of the American Chemical Society* **2005,** 127, 14968-14969.

144. Wu, T.; Liu, G.; Zhao, J.; Hidaka, H.; Serpone, N. *The Journal of Physical Chemistry B* **1998,** 102, 5845-5851.

145. Zhao, J.; Wu, T.; Wu, K.; Oikawa, K.; Hidaka, H.; Serpone, N. *Environmental Science & Technology* **1998,** 32, 2394-2400.

146. Kim, S.; Choi, W. *The Journal of Physical Chemistry B* **2005,** 109, 5143-5149.

147. Zhou, Y.; Antonietti, M. *Journal of the American Chemical Society* **2003,** 125, 14960-14961.

148. Chen, G. *Separation and Purification Technology* **2004,** 38, 11-41.

149. Zhang, H.; Yang, Y.; Su, Y.; Chen, J.; Hu, C.; Wu, Z.; Liu, Y.; Ping Wong, C.; Bando, Y.; Wang, Z. L. *Nano Energy* **2013,** 2, 693-701.

150. Nguyen, V.; Yang, R. *Nano Energy* **2013,** 2, 604-608.

151. Guo, H.; Chen, J.; Tian, L.; Leng, Q.; Xi, Y.; Hu, C. *ACS Applied Materials & Interfaces* **2014,** 6, 17184-17189.

152. Wen, X.; Su, Y.; Yang, Y.; Zhang, H.; Wang, Z. L. *Nano Energy* **2014,** 4, 150-156.

153. Su, Y.; Chen, J.; Wu, Z.; Jiang, Y. *Applied Physics Letters* **2015,** 106, 013114.

VITA

JUN CHEN

JUN CHEN received his B.S. and M.S. in Electrical Engineering from the School of Electronic Information and Communications at Huazhong University of Science and Technology in 2007 and 2010, respectively, and a second M.S. in Biological Engineering from the College of Engineering at The University of Georgia in 2012. He then went to begin his doctoral research and study in School of Materials Science and Engineering at Georgia Institute of Technology, under the supervision of Prof. Zhong Lin Wang. His doctoral research focuses primarily on nanomaterial-based energy harvesting, energy storage, active sensing and self-powered micro-/nano-systems. He has already published 58 papers in total and 31 of them as first-author in prestigious scientific journals, such as *Nature Communications, Advanced Materials, Nano Letters, ACS Nano*, and so on. And still, he filed 8 US patents and 15 Chinese patents. His research on triboelectric nanogenerators has been reported by worldwide mainstream media over 400 times in total, including *Nature, PBS, The Wall Street Journal, Washington Times, Scientific American, NewScientist, Phys.org, ScienceDaily, Newsweek*, and so on. Jun also received the 2015 Materials Research Society Graduate Student Award, and the 2015 Chinese Government Award for Outstanding Students Abroad. His current H-index is 30.